



SAKARYA ÜNİVERSİTESİ

FEN BİLİMLERİ ENSTİTÜSÜ DERGİSİ

Sakarya University Journal of Science (SAUJS)



SAKARYA
ÜNİVERSİTESİ

e-issn: 2147-835X

Volume: 28

Issue: 5

October 2024

VOLUME: 28 ISSUE: 5
E-ISSN 2147-835X

October 2024
<https://dergipark.org.tr/tr/pub/saufenbilder>

SAKARYA UNIVERSITY JOURNAL OF SCIENCE



SAKARYA
ÜNİVERSİTESİ

The Owner on Behalf of Sakarya University

Prof. Dr. Hamza Al
Sakarya University, Sakarya-Türkiye

Publishing Manager

Hüseyin Özkan Toplan
Department of Metallurgical and Materials Engineering
Sakarya University, Sakarya-Türkiye
toplano@sakarya.edu.tr

Editor in Chief

Ömer Tamer
Department of Physics
Sakarya University, Sakarya-Türkiye
omertamer@sakarya.edu.tr

Associate Editors

İhsan Hakan Selvi
Department of Information Systems Engineering
Sakarya University, Sakarya-Türkiye
ihselvi@sakarya.edu.tr

Editorial Board

Asude Ateş
Department of Environmental Sciences and
Engineering
Sakarya University
Sakarya - Türkiye
aates@sakarya.edu.tr

Bahadır Respect
Department of Nuclear Physics
Ankara University
Ankara - Türkiye
bsaygi@ankara.edu.tr

Berrin Denizhan
Department of Industrial Engineering
Sakarya University
Sakarya - Türkiye
denizhan@sakarya.edu.tr

Hüseyin Aksoy
Department of Biology
Sakarya University
Sakarya - Türkiye
haksoy@sakarya.edu.tr

Mehmet Uysal
Department of Metallurgical and
Materials Engineering
Sakarya University
Sakarya - Türkiye
mehmetu@sakarya.edu.tr

Muhammed Fatih Adak
Department of Computer Science and Engineering
Sakarya University
Sakarya - Türkiye
fatihadak@sakarya.edu.tr

Muhammet Hilmi Nişancı
Department of Electrical and Electronics Engineering
Sakarya University
Sakarya - Türkiye
nisanci@sakarya.edu.tr

Mustafa Gülfen
Department Analytical Chemistry
Sakarya University
Sakarya - Türkiye
mgulfen@sakarya.edu.tr

Osman Sönmez
Department of Civil Engineering
Sakarya University
Sakarya - Türkiye
osonmez@sakarya.edu.tr

Serap Coşansu
Department of Food Engineering
Sakarya University
Sakarya - Türkiye
scosansu@sakarya.edu.tr

Tahsin Turgay
Department of Architecture
Sakarya University
Sakarya - Türkiye
turgay@sakarya.edu.tr

Ufuk Durmaz
Department of Mechanical Engineering
Sakarya University
Sakarya - Türkiye
udurmaz@sakarya.edu.tr

Section Editor (Civil Engineering)

Elif Ağcakoca
Department of Civil Engineering
Sakarya University
Sakarya - Türkiye
elifd@sakarya.edu.tr

Faruk Fırat Çalım
Department of Civil Engineering
Adana Alparslan Türkeş
Science and Technology University
Adana - Türkiye
ffcalim@atu.edu.tr

Issa Al-Harthy
Department of Civil and Architectural Engineering
Sultan Qaboos University
Oman
aissa@squ.edu.om

Jamal Khatib
Department of Civil Engineering
University of Wolverhampton
United Kingdom
jmkhatib@wlv.ac.uk

Khalifa Al-Jabri
Department of Civil and Architectural Engineering
Sultan Qaboos University
Oman
aljabri@squ.edu.om

Hakan Alp
Department of Geophysical Engineering
İstanbul University-Cerrahpaşa
İstanbul - Türkiye
hakanalp@iuc.edu.tr

Tuba Tatar
Department of Civil Engineering
Sakarya University
Sakarya - Türkiye
ttatar@sakarya.edu.tr

Gökhan Dok
Department of Civil Engineering
Sakarya University of Applied Sciences
Sakarya - Türkiye
gokhandok@subu.edu.tr

Section Editor (Chemistry)

Can Serkan Keskin
Department of Chemistry
Sakarya University
Sakarya - Türkiye
ckeskin@sakarya.edu.tr

Gražyna Simha Martynková
Department of Chemistry Education Vsb-Technical
University of Ostrava
Czech Republic
grazyna.simha@vsb.cz

Murat Tuna
Department of Chemistry
Sakarya University
Sakarya - Türkiye
tuna@sakarya.edu.tr

Aligholi Niaie
Department Chemical Engineering
University of Tabriz
Iran
aniaei@tabrizu.ac.ir

Nahit Gencer
Department of Biochemistry
Balıkesir University
Sakarya - Türkiye
ngencer@balikesir.edu.tr

Section Editor (Biology)

Cansu Akbulut
Department of Biology
Sakarya University
Sakarya - Türkiye
cansua@sakarya.edu.tr

Luis Materon
Department of Biology
University of Texas Rio Grande Valley
USA
luis.materon@utrgv.edu

Nazan Deniz Yön Ertuğ
Department of Biology
Sakarya University
Sakarya - Türkiye
nkoc@sakarya.edu.tr

Nihan Akıncı Kenanoğlu
Department of Biology
Çanakkale Onsekiz Mart University
Çanakkale - Türkiye
nakinci@comu.edu.tr

Oğuz Kurt
Department of Biology
Manisa Celal Bayar University
Manisa - Türkiye
oguz.kurt@cbu.edu.tr

Sezgi Somuncu
Department of Biology
Sakarya University
Sakarya - Türkiye
sezgisomuncu@sakarya.edu.tr

Sezen Toksoy Köseođlu
Department of Biology
Sakarya University
Sakarya - Türkiye
sezentoksoy@sakarya.edu.tr

Section Editor (Mathematics)

Murat Güzeltepe
Department of Mathematics
Sakarya University
Sakarya - Türkiye
mguzeltepe@sakarya.edu.tr

Murat Sarduvan
Department of Mathematics
Sakarya University
Sakarya - Türkiye
msarduvan@sakarya.edu.tr

Ali Demir
Department of Mathematics
Kocaeli University
Kocaeli - Türkiye
ademir@kocaeli.edu.tr

Luan Hoang
Department of Mathematics
Texas Tech University
USA
luan.hoang@ttu.edu

Selma Özçađ
Department of Mathematics
Hacettepe University
Ankara - Türkiye
sozcag@hacettepe.edu.tr

Necati Olgun
Department of Mathematics
Gaziantep University
Gaziantep - Türkiye
olgun@gantep.edu.tr

Section Editor (Computer Science and Engineering)

Fahrettin Horasan
Computer Science and Engineering
Kırıkkale University
Kırıkkale - Türkiye
fhorasan@kku.edu.tr

Kevser Ovaz Akpınar
Computer Science and Engineering
Rochester Dubai Institute of Technology
Dubai
kxocad1@rit.edu

Muhammed Maruf Öztürk
Computer Science and Engineering
Süleyman Demirel University
Isparta - Türkiye
muhammedozturk@sdu.edu.tr

Mustafa Akpınar
Computer Science and Engineering
High Tech Collages
United Arab Emirates
mustafakpınar@gmail.com

Section Editor (Physics)

Ceren Tayran
Department Physics
Gazi University
Ankara - Türkiye
c.tayran@gazi.edu.tr

Grzegorz Jaworski
Department Physics
University of Warsaw
Poland
grzegorz.jaworski@pwr.edu.pl

Section Editor (Industrial Engineering)

Feyza Gürbüz
Department Industrial Engineering
Erciyes University
Kayseri - Türkiye
feyza@erciyes.edu.tr

Caner Erden
Department Industrial Engineering
Sakarya University of Applied Sciences
Sakarya - Türkiye
cerden@subu.edu.tr

Hatice Esen
Department Industrial Engineering
Kocaeli University
Kocaeli - Türkiye
hatice.eris@kocaeli.edu.tr

Mehmet Emin Aydın
Department Industrial Engineering
University of The West of England Bristol
England
mehmet.aydin@uwe.ac.uk,

Barış Yüce
Department Industrial Engineering
University of Exeter
United Kingdom
b.yuce@exeter.ac.uk

Benjamin Durakovic
Department Industrial Engineering
International University of Sarajevo
Bosnia and Herzegovina
bdurakovic@ius.edu.ba

Section Editor (Mechanical Engineering)

Elif Eker Kahveci
Department of Mechanical Engineering
Sakarya University
Sakarya - Türkiye
eeker@sakarya.edu.tr

Erman Aslan
Department of Mechanical Engineering
Kocaeli University
Kocaeli - Türkiye
erman.aslan@kocaeli.edu.tr

Mohammad Sukri Bin Mustapa
Department of Mechanical Engineering
University Tun Hussein Onn Malaysia
Malaysia
sukri@uthm.edu.my

Raja Mazuir Bin Raja Ahsan Shah
Department of Mechanical Engineering
Coventry University
United Kingdom
ac9217@coventry.ac.uk

Seong Jin Park
Department of Mechanical Engineering
Pohang University of Science and Technology
Korea
sjpark87@postech.ac.kr

Abderrahmane Benbrik
Department of Mechanical Engineering
M'hamed Bougara University
Egypt
abderrahmane.benbrik@univ-boumerdes.dz

Ali Cemal Benim
Department of Mechanical Engineering
Düsseldorf University of Applied Sciences
Germany
alicemal@prof-benim.com

Herman Nied
Department of Mechanical Engineering
Lehigh University
USA
hfn2@lehigh.edu

Shi-Chune Yao
Department of Mechanical Engineering
Carnegie Mellon University
USA
sy0d@andrew.cmu.edu

Tauseef Aized
Department of Mechanical Engineering
Uet Lahore
Pakistan
tauseef.aized@uet.edu.pk

Section Editor (Environmental Sciences and Engineering)

Ece Ümmü Deveci
Department of Environmental Sciences and
Engineering
Niğde Omer Halisdemir University
Niğde - TÜRKİYE
eudeveci@ohu.edu.tr

Senay Çetin Doğruparmak
Department of Environmental Engineering
Kocaeli University
Kocaeli - Türkiye
senayc@kocaeli.edu.tr

Section Editor (Food Science)

Aslı Uçar
Department of Food Sciences
Ankara University
Ankara - Türkiye
aucar@ankara.edu.tr

Edgar Perez Esteve
Department of Food Sciences
Polytechnic University of Valencia
Spain
edpees@upv.es

Syed Abbas
Department of Cereal Technology, Food Microbiology
Curtin University
Australia
s.abbas@curtin.edu.au

Section Editor

(Electrical and Electronics Engineering)

Abdullah Oğuz Kızılçay
Department of Electrical and Electronics Engineering
Zonguldak Bülent Ecevit University
Zonguldak - Türkiye
oguzkizilcay@yyu.edu.tr

İbrahim Bahadır Başığit
Department of Electrical and Electronics Engineering
Isparta University of Applied Sciences
Isparta - Türkiye
bahadirbasyigit@isparta.edu.tr

Francesco De Paulis
Department of Electrical and Electronics Engineering
L'Aquila University
Italy
francesco.depaulis@univaq.it

Mesut Baran
Department of Electrical and Electronics Engineering
North Carolina State University
USA
baran@ncsu.edu

Ozan Erdinç
Department of Electrical and Electronics Engineering
Yıldız Technical University
İstanbul - Türkiye
oerdinc@yildiz.edu.tr

Rıfki Terzioğlu
Department of Electrical and Electronics Engineering
Bolu Abant İzzet Baysal University
Bolu - Türkiye
rifkiterzioğlu@ibu.edu.tr

Section Editor (Architecture)

İsmail Hakkı Demir
Department of Architecture
Sakarya University
Sarkaya - Türkiye
idemir@sakarya.edu.tr

Section Editor (Materials Science)

Miraç Alaf
Department Metallurgical and Materials Engineering
Bilecik Şeyh Edebali University
Bilecik - Türkiye
mirac.alaf@bilecik.edu.tr

Kamaruzzaman Sopian
Department Metallurgical and Materials Engineering
Universiti Kebangsaan
Malaysia
ksopian@ukm.edu.my

English Language Editor

Seçkin Arı
Department of Computer Engineering
Sakarya University, Sakarya-Türkiye
ari@sakarya.edu.tr

Editorial Assistant

Evrım Yüksel
Department of Environmental Engineering
Institute of Sciences, Sakarya University
Sakarya-Türkiye
eyuksel@sakarya.edu.tr

Statistical Editor

Önder Gökmen Yıldız
Department of Mathematics
Bilecik Şeyh Edebali University, Bilecik-Türkiye
ogokmen.yildiz@bilecik.edu.tr

Managing Editor

Hüseyin Yasin Uzunok
Department of Physics
Sakarya University, Sakarya-Türkiye
hyuzunok@sakarya.edu.tr

Technical Editor

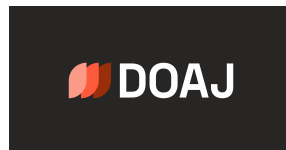
Hatice Vural
Department of Electrical and Electronics Engineering
Amasya University, Amasya-Türkiye
hatice.vural@amasya.edu.tr

Layout Editor

Mehmet Emin Çolak
Scientific Journals Coordinatorship
Sakarya University
Sakarya-Türkiye
mehmetcolak@sakarya.edu.tr

Yakup Beriş
Scientific Journals Coordinatorship
Sakarya University
Sakarya-Türkiye
yakupberis@sakarya.edu.tr

Indexing



Contents

Research Article

- 1 A Decision Support System For Early Stage Parkinson's Diagnosis from EEG Data Using Symbolic Mutual Information and KAC Features
Neslihan Baki, Nurhan Gürsel Özmen 912-923
- 2 Effect of Different Parameters on Enzymatic Hydrolysis of Hazelnut Shells
Özcan Gezen, İrem Deniz 924-929
- 3 The Effect of Various Parameters in the Sulfuric Acid Leaching of Low Grade Zinc Oxide Ore of Niğde-Türkiye
Özlem Kaya, Gürol Uysal 930-936
- 4 Comparison of the Bactericidal Effect of the UV and Blue-Light Regions on Selected Escherichia Coli and Staphylococcus Aureus Strains
Can Saç 937-944
- 5 An Analysis of Tiny Houses through a Viewpoint on Preferences, Satisfaction, and Expectations of Residents
Miray Gür, Elif Çay 945-958
- 6 Cost Minimization with Project Crashing: Comparison of the Traditional Solution and Genetic Algorithm Approach
Semih Caglayan, Sadik Yiğit 959-977
- 7 Additions to the Knowledge of the Flat Wasps Fauna of Türkiye (Hymenoptera, Bethyridae)
İlyas Can, Serdar Tezcan, Jeroen De Rond 978-983
- 8 Eco-Friendly Green Synthesis of Zinc Oxide Nano/Microparticles Using Aqueous Leaf Extract of Polygonum cognatum Meisn. Plant
Erdem Akça 984-999
- 9 Role of Mechanical Activation in Enhancing Li and Co Recovery from Spent Li-ion Batteries through Citric Acid Leaching
Hasan Algül, Figen Algül 1000-1009
- 10 Ultraviolet Protection and Antibacterial Properties of Polylactic Acid Nonwoven Fabrics Coated with Water-Borne Polyurethane/Zinc Oxide Composite Coatings
Gülçin Baysal 1010-1021
- 11 Improved Singlet Oxygen Production of Zinc Phthalocyanine Bearing Pyridine-4-Thiol Groups Using Sonochemistry and Comparison with Photochemistry
Öznur Dülger Kutlu 1022-1030
- 12 Analysis of Electrochemical Deposition of Polyaniline and Polyaniline Composites in Sodium Tungstate and Sodium Molybdate Solutions
Asuman Ünal 1031-1039
- 13 Comparison of MCM6 rs4988235 Polymorphism Allele and Genotype Frequencies in Professional Football Players and a Sedentary Control Group
Beste Tacal Aslan, Tolga Polat, Özlem Özge Yılmaz, Aleyna Muhan, Rukiye Ziya, Korkut Ulucan 1040-1046
- 14 Investigation of Spintronic Properties of Transition Metal Doped ZnO Thin Films Produced by Sol-Gel Spin Coating
Zafer Gültekin, Cengiz Akay, Nuray Altınölçek 1047-1058

15	New Integrated and Differentiated Sequence Spaces $\int b_p^{r,s}$ and $db_p^{r,s}$ <i>Kübra Topal</i>	1059-1069
16	Experimental and Theoretical Characterization, In Silico and In Vitro Studies of (E)-1-(5-Nitrothiophen-2-yl)-N-(2-(Trifluoromethyl)Phenyl)Methanimine <i>Seyhan Öztürk</i>	1070-1085
17	Air Fixation and AFM: A Comparative Study of Nanoparticle-Induced Topographical Changes in Lung Cells <i>Gamze Yeşilay</i>	1086-1092
18	A Study of q-Deformed Bosons, and Their Implications to Quantum Optics <i>Mustafa Şenay</i>	1093-1102
19	Shear Capacity Prediction of Extremely-Loaded Box Culvert on Elastic Soil Using Artificial Neural Network <i>Yesim Tuskan, Dilay Yıldırım Uncu</i>	1103-1114
Review		
20	A Review of Structural Systems to be Built on Planets <i>Serra Çelik Kıratlı, Ali Osman Kuruşçu</i>	1115-1131



A Decision Support System For Early Stage Parkinson's Diagnosis from EEG Data Using Symbolic Mutual Information and KAC Features

Neslihan Baki^{1*} , Nurhan Gürsel Özmen² 

¹ Karadeniz Technical University, Health Sciences Institute, Department of Medical Informatics and Biostatistics, Trabzon, Türkiye, neslihanbaki520@gmail.com

² Karadeniz Technical University, Faculty of Engineering, Department of Mechanical Engineering, Trabzon, Türkiye, gnurhan@ktu.edu.tr

*Corresponding Author

ARTICLE INFO

ABSTRACT

Keywords:
Parkinson
Electroencephalography
Weighted Symbolic Mutual Information (wSMI)
Kolmogorov Algorithmic Complexity (KAC)
Extreme gradient boosting algorithm

Parkinson's disease (PD) is a serious neurological disease that is threatening the whole world population. The devolution of the neurons located in the substantia nigra of the brain causes, bradykinesia, rigidity and resting tremor, which are characteristic motor symptoms, occurring in advanced stages. Currently, there is not an effective treatment for PD, it is just controlled by some prescriptions. Early detection of this disease affects the choice of treatment. Recent studies on early diagnosis by analyzing electroencephalography (EEG) recordings have provided a glimmer of hope. Therefore, in this study, an efficient PD detection method from EEG data by using a new set of features is searched. An opensource resting state data of 28 subjects divided as Parkinson and control groups were analyzed. PSDs of the EEG frequency bands that are delta, theta, alpha, beta and gamma and Median Spectral Frequency (MSF), Spectral Entropy (SE), Kolmogorov Algorithmic Complexity (KAC) and Weighted Symbolic Mutual Information (wSMI) were extracted as features. The performance of the PD and control group was evaluated with Gradient Boosting (GB), Gaussian Naive Bayes (GNB), and K-nearest Neighbor (KNN), Support Vector Machines (SVM), Logistic Regression (LR), Categorical Boosting (CatBoost) and Extreme Gradient Boosting (XGBoost) Algorithms. A 85% accuracy was achieved with the XGBoost algorithm, using 31 channels and 13 features which outperforms the results of previous studies using this dataset in the literature.

Article History:

Received: 28.09.2023

Accepted: 26.08.2024

Online Available: 14.10.2024

1. Introduction

Parkinson's disease (PD) is a progressive, neuronal degeneration disorder that is caused by genetic and environmental factors and affects considerable amount of people all around the world [1]. Many research were done on the symptoms, causes, and the treatments of PD till now [2]. Various motor and non-motor symptoms due to damage of nigrostriatal dopaminergic nerve cells and other nerve cells are observed. Basic motor symptoms include bradykinesia, rigidity, postural instability, tremor

and non-motor symptoms include cognitive, behavioral, sleep, and autonomic disorders [3-6].

It is often difficult to diagnose PD in its primer stage. A neurologist generally makes the diagnosis based on a clinical examination of the patient and an assessment of the patient's medical history. Since the symptoms are not specific to the disease, there may be misdiagnosis or delays [7]. These delays impose enormous costs on both the people and the health systems of countries. Early diagnosis of the disease affects the choice of treatment. Initiation of neuroprotective treatment to protect the nerves before too much

loss of nerve cells in the substantia nigra may slow the progression of PD.

In recent years, electroencephalography (EEG) recordings are being used for diagnosing PD [8-10]. Since a clear temporal resolution of the cortical electrical activity of EEG is achieved, it is mostly preferred for clinical and research use. Moreover, it is cheaper and easy to use, compared to MEG.

Recent EEG studies on PD, showed that the amplitudes of theta and alpha brain waves change significantly with the slowing actions [10]. In order to reveal the hidden information about the differences during PD needs more attention to implement new methods in the analysis of EEG. These studies may also contribute to the discovery of other functions and dysfunctions of the brain. It is stated that if there is any deformation in the substantia nigra neurons, it will affect the information transfer between the cortex and the basal ganglia. These changes can also be revealed from EEG recordings [11, 12]. During PD, the EEG spectrum slows down [13, 14]. Based on these changes, classification of PD and healthy control (HC) groups can be detected. Moreover, decision support systems can be developed.

Research on PD diagnosis from EEG data mostly focus on the development of new signal processing methods for feature extraction [15]. Linear features acquired from different frequency bands have achieved around 75-82% accuracy [16] whereas, nonlinear methods have also been used to extract information from EEG for PD diagnosis [17, 18] where around 80-95% classification accuracy rates were calculated. Besides feature extraction methods, the use of different machine learning methods and comparison of their performances are also searched [19].

Chaturvedi et al. compared high-resolution EEG measurements of 50 PD patients and 41 HC and found that the theta power in the left temporal region and the alpha1/theta ratio in the mid left region were the most effective variables in classification. Among machine learning methods, 56%, 78%, 74% and 68% accuracy

results were obtained with Logistic Regression (LR), Random Forest, Support Vector Machines (SVM) and Decision Tree, respectively [20]. Betrouni et al. achieved 84% and 88% classification accuracy using Power Spectral Density (PSD) features with SVM and K-nearest Neighbor Algorithm (KNN) methods in classifying the level of cognitive impairment in PD [21]. Anjum et al. achieved 85.7% accuracy in their classification with a linear predictive coding for PD detection from EEG [22].

Loh et al. transformed EEG data into spectrograms to train a two-dimensional convolutional neural network model by applying Gabor transform to resting state EEG data from 16 individuals with HC and 15 individuals with PD, achieving 99.46% classification accuracy [23]. Lee et al. proposed a prediction method with 89.3% accuracy in classification using Hjorth parameter features and Gradient Boosting (GB) algorithm [24]. Suuronen et al. investigated how the number and placement of electrodes affect PD and HC subjects. Using a special budget-based search algorithm to select optimized channel sets for classification, they achieved an accuracy of 76% [25]. Karakaş et al. achieved 85.7% accuracy in the Iova data and 63.25% accuracy in the Turku data sets using beta activity and amplitude reduction in EEG signals associated with PD [26].

Onay et al. used triaxial accelerometer signals collected during a pedaling task in 13 HC, 13 PD and 13 FoG symptomatic individuals, the perceptual latency from the movement command to the start of the movement was estimated for each session. Features of the distributions of the latencies of each participant were extracted and 69.2% success was achieved with SVM [27]. Orkan Olcay et al. used entropy and connectivity properties of chemosensor-derived EEG signals together to discriminate PD and HC with odor stimuli with over 80% classification performance [28].

Moreover, some deep learning studies in the literature have achieved higher classification results [29, 30]. The main drawback is that, they require high processing time and large data. On the other hand, a successful classification

performance can be achieved by using classical machine learning methods due to the limited data size.

Most of the studies in the literature analyze EEG data of whole channels. Fewer studies searched for the regional and number of electrodes based differences. In this study, the data of 63 channels and 31 channels were analyzed by excluding Pz as it is the reference channel. The 31 channels analyzed in this study consist of Fp1, AF3, F7, F3, FC1, FC5, T7, C3, CP1, O1, Oz, O2, CP5, P3, P7, PO3, PO4, P4, P8, CP6, CP2, C4, T8, FC6, FC2, F4, F8, AF4, Fp2, Fz, Cz.

This study proposes novel features to extract prominent features of EEG signals that can be used as biomarkers to identify Parkinson's patients with the help of machine learning algorithms. In this study, wSMI, KAC and SE features were used for the first time in PD classification in resting state EEG data. The classical and new established ensemble learning algorithms are used to diagnose PD. GB, Gaussian Naive Bayes (GNB), KNN, SVM, LR, Categorical Boosting Algorithm (CatBoost) and, Extreme Gradient Boosting Algorithm (XGBoost) are used with different metrics.

In classification studies for PD diagnosis based on EEG, generally the accuracy metric is included. In these studies, 69.77% of the data used consisted of balanced classes, and the remaining percentage did not show a balanced distribution. Training data with unbalanced classes can lead to prediction errors and poor generalizations. In studies with patients, especially for the diagnosis of a disease, sensitivity, specificity, and accuracy measures are very useful in evaluating the results of the model, as they provide a measure of true positives. In this study, classification results were evaluated according to Accuracy, Precision, Recall, F1 score and AUC. The average number of electrodes in studies in the literature is 43.34 ± 62.18 [19, 31].

The next section of the study continues with the "Material - Method" section, where data sets and signal processing methods are introduced. In this section, the features and classifiers are briefly described. In the third section, the results

obtained using different classifiers are presented comparatively for different performance measures. Related discussions are summarized here. The last section summarizes the conclusions of the study.

2. Materials and Methods

2.1. Methods

The open-source EEG dataset from the Narayanan Laboratory at the University of Iowa is used [32]. The dataset contains resting state EEG recordings of 14 PD and 14 HC groups. The EEG recordings were done by using Brain Vision 64-channel electrodes system placed on the head according to the international 10-20 system. The HC group was recruited from physically and mentally healthy subjects who were demographically matched with PD in terms of gender and age and had no history of neuropsychiatric disorders. All of the participants signed the written informed consent form. In Table 1, demographic information of the dataset is given. EEG recordings contains 2 minutes eyes open data with 500 Hz sampling frequency and a sampling rate of 0.1-100 Hz. The 64 channels 10-20 EEG electrode locations are shown in Figure 1. The Pz channel was selected as the reference channel.

Table 1. Iowa dataset demographic information for PD and HC groups

Status	PD and HC groups	
	<i>PD</i>	<i>HC</i>
Number	14	14
Gender (male/female)	8f/6m	8f/6m
Age (mean years \pm SD)	70.5 ± 8.7	70.5 ± 8.7
NAART	–	–
MMSE	–	–
MOCA	25.9 ± 2.7	27.2 ± 1.7
UPDRS	13.4 ± 6.6	–
PD years of	5.6 ± 3.2	–

The mean PSD changes of 28 subjects and 31 channels are given in Figure 2.

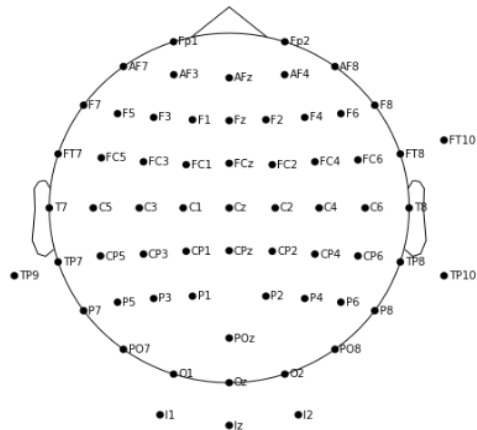


Figure 1. EEG 10-20 Electrode Placement System for 64 channels

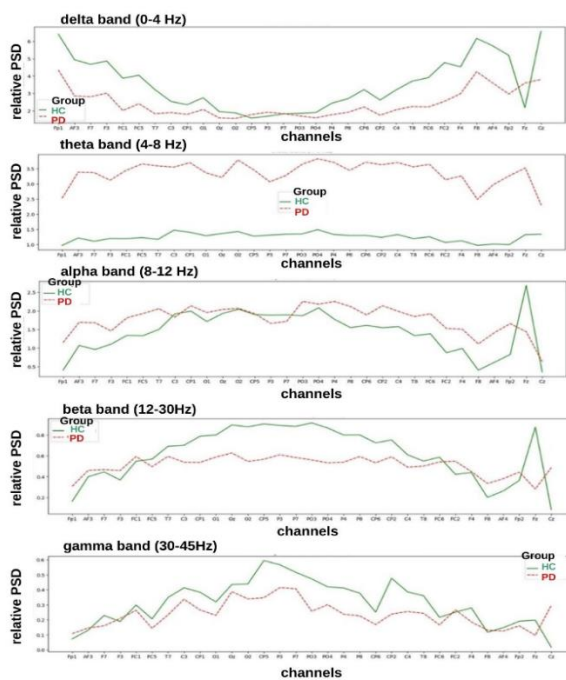


Figure 2. PD and HC relative PSD of 28 contacts and 31 channel frequency bands

In Figure 2, delta, theta, alpha, beta, and gamma frequency bands are given per channel. There is a clear difference both between PD and HC groups, that is, they have different relative PSD values. A reduction of beta rhythm in frontal and central regions, and another reduction of gamma rhythm in central, parietal, and temporal regions was observed, rather than the Fp2, AF3 channels.

In Figures 3-4, EEG topographic maps of PD and HC groups are given. Most of them are in gamma and beta bands, and slightly in alpha, more activation is observed in the HC group compared to PD. These differences are in accordance with the existing literature [1, 8-9].

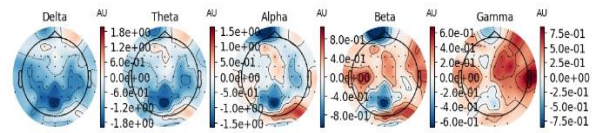


Figure 3. Topographic maps of band power in five frequency bands of the HC group

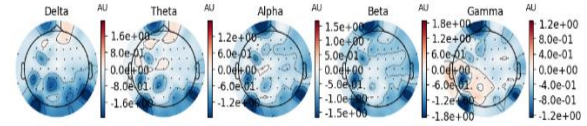


Figure 4. Topographic maps of band power in five frequency bands of the PD group

2.2. Preprocessing

All stages of data analysis were performed with Python using CPU in the Google Colab environment. In order to process EEG data with Python, many libraries such as mne, numpy, pandas, matplotlib, etc. were installed and configured in the Google Colab Python environment.

Since EEG data was recorded in the Brain Vision System, raw EEG files with vhdr extension were transferred to the Google Colab environment by converting them into raw objects with the mne library so that they can be processed in Python language. The data was transferred from other libraries. The data was first bandpass filtered between 0.5 Hz low and 45 Hz high frequencies and notch filtered at 60 Hz and 100 Hz. After filtering, these signals were divided into a non-overlapping time window length of twenty seconds. Then, MSF, PSD theta, wSMI theta, wSMI beta features were extracted and binary classification was performed using CatBoost, XGBoost, GNB, KNN, SVM, GB and LR algorithms. In Figure 5, data analysis steps are depicted.

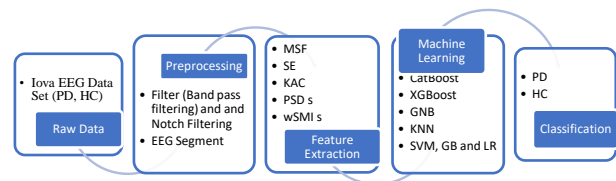


Figure 5. EEG data analysis scheme

2.3. Feature extraction

Feature extraction is the transformation of the unprocessed data into digital values with a reduced size of dimension to lessen the complexity of processing information in which, the original signal characteristics are correctly decoded and evaluated with a well-performing classifier [33]. There are various studies that used PSD parameters from the subbands of decomposed EEG signals which obtained successful classification results [22]. In this study, the PSD of the five bands of the EEG signal, wSMI Delta, wSMI Theta, wSMI alpha, wSMI Beta, wSMI Gama and MSF, SE, KAC, are selected as the feature vector.

2.3.1. Power spectral density

PSD is the measure of the power content of a signal with respect to frequency. It allows time-varying signals to be transferred to the frequency domain, resulting in power distributions of the frequency ranges of the signal [34]. The power distribution of a random signal at different frequencies is calculated by Fourier transform. The PSD equation is given in equation (1).

$$S(f) = \int_{-\infty}^{\infty} R(t)e^{-2\pi if} dt = F(R(t)) \quad (1)$$

2.3.2. Calculation of weighted symbolic mutual information

The Weighted Symbolic Mutual Information (wSMI) measure is increasingly applied to EEG [35, 36]. It is based on the interactions between two signals and the non-linear coupling between them. In a selected tau time k samples of the signal are selected. The magnitudes of the samples are defined by a set of symbols based on the order relation which represents the temporal separation of the signals. In this data set, wSMI is calculated for the joint probability of each pair of symbols. In order to decrease the false correlations between two signal groups, the joint probability matrix P, is multiplied by binary weights. The wSMI can be calculated with the statement in equation (2), where X, and Y represent two different signals.

$$wSMI(X, Y) = \frac{1}{\log k!} \sum_{x \in X} \sum_{y \in Y} w(x, y) p(x, y) \log \left(\frac{p(x, y)}{p(x)p(y)} \right) \quad (2)$$

2.3.3. Median spectral frequency

The Median Spectral Frequency (MSF) is commonly used to show spectral change. It represents the midpoint of the power distribution of the compressed EEG spectral array. It is a measure of the frequency above and below 50% of the total power in the EEG. MSF is also defined as half of the total power [37]. The definition of MSF is given in equation (3):

$$\sum_{j=1}^{MDF} P_j = \sum_{j=MDF}^M P_j = 1/2 \sum_{j=1}^M P_j \quad (3)$$

2.3.4. Spectral entropy

Spectral Entropy is the spectral power distribution of a signal based on Shannon entropy [38]. It indicates the flatness or complexity of the signal spectrum [39]. In the following, SE is calculated by equation (4).

$$H(x, fs) = - \sum_{f=0}^{fs/2} P(f) \log_2 [P(f)] \quad (4)$$

Where P is the normalized PSD and fs is the sampling frequency.

2.3.5. Kolmogorov algorithmic complexity

The Algorithmic Complexity or Kolmogorov complexity (KAC) is related to the minimum description length. The KAC of a sequence s is the length of the shortest run that computes s. It expresses the concepts of simplicity and complexity. If the length d(s) of an array s with the fewest bits is the minimum, this is the minimum description of s. Here d(s) is the Kolmogorov complexity of s and is represented by K(s) [40]. It is represented by equation (5).

$$K(s) = |d(s)| \quad (5)$$

2.4. Classification

The EEG dataset contains a total of 28 data sets belonging to 14 PD and 14 HC groups. 10-fold cross-validation is used for classification. With this technique, the total data set is divided into k approximately equal parts. Machine learning structures are trained and tested k times. Each time, the part of the data to be tested is taken from the k chunks and all the remaining data is used for training the machine learning structure. The

PSD features of five frequency bands (MSF, KAC, wSMI Delta, wSMI Theta and wSMI Alpha) are selected and the performance of different classifiers on PD and HC group data is evaluated using Accuracy, Precision, F1 score, Recall, ROC-AUC metrics. Binary classification was performed with CatBoost, XGBoost, GNB, KNN, SVM, LR and GB algorithms in Python Google Colab environment.

2.4.1. Gradient boosting algorithm

GB algorithm is a method in which new models are created that account for the error in the previous model and then the residuals are added to make the final prediction. It creates prediction models similar to decision trees (Random Forests) for regression and classification problems. The GB algorithm does not create nodes after each tree to make an improvement. Instead, it starts with a leaf. This leaf represents an initial estimate for all weights. The first estimate here is the average value. Then Gradient Boost creates a tree. Boosting differs from other classification algorithms in that it often compensates for the lack of weak learners [41]. GB algorithms can be customized according to the needs of the application, such as learning according to different loss functions. When used for classification, Log-Loss is used as the cost function.

2.4.2. K Nearest neighbor algorithm

KNN is a well-known supervised learning algorithm commonly preferred in classification. This algorithm searches for the closest points to the new point. K is the number of nearest neighbors of the unknown point which is usually chosen as an odd number. In the K-NN method, the output is the class membership. An object is attained to the selected label by a majority vote of its neighbors [42].

2.4.3. Gaussian naive bayes classifier

Naive Bayes Classification, is a simplified version of Bayes' theorem with the independence premise. Bayes' theorem is expressed in equation (6); normal distribution of features

$$P(A|B) = \frac{P(B|A)P(A)}{P(B)} \quad (6)$$

$P(A|B)$ denotes the probability of event A when event B occurs, $P(B|A)$ denotes the probability of event B when event A occurs. $P(A)$ and $P(B)$ show the a priori probabilities of events A and B, adding subjectivity to Bayes' theorem [43]. Naive Bayes classifiers perform well especially with a small set of training data to estimate the necessary parameters.

2.4.4. Support vector machines

SVM is a supervised learning method with three main components that are statistical learning theory, optimization algorithm and kernel functions [44]. In SVM, the most appropriate line separation is the one with equal and maximum distance to the data classes. While creating this maximum distance, called the margin, the samples that are closest to the separating line among the samples belonging to the data classes are used. These examples are called support vectors. In multidimensional space, lines are replaced by hyperplanes [45].

2.4.5. Logistic regression

LR, binary logistic model or logit model is a statistical approach that models the probability of a problem occurring between two alternatives by taking the logarithm of the rates for a problem. In this method, mathematical modeling is performed in order to define the relationship between independent variables and two or multi-class categorical dependent variables [46]. When all independent variables are continuous, the logistic model is calculated with an expression given in equation (7);

$$\ln \frac{\Pr(x_1, \dots, x_p)}{1 - \Pr(x_1, \dots, x_p)} = \beta_0 + \sum_{j=1}^k \beta_j x_{ij} \quad (7)$$

2.4.6. Categorical boosting algorithm

CatBoost is a new ensemble learning method derived from the GB and Decision Tree algorithms proposed by Yandex and shown to have the ability to deal well with heterogeneous data [47]. Moreover, CatBoost uses balanced forgetful trees as base predictors. Thus, it

overcomes the problems of overlearning. In general, it exhibits superior classification performance compared to other ensemble learning algorithms.

2.4.7. Extreme gradient boost algorithm

XGBoost is a high performance version of the GB algorithm that is optimized with various adjustments. It is quick, has high predictive power, can avoid overlearning, can manage empty data. The first step in XGBoost, is to make the first prediction. The prediction can be any number as it will converge with the operations to be performed in the next steps and the correct result will be reached. The first tree is completed by constructing the trees that predict the errors, calculating the similarity and gain scores for the trees, pruning and obtaining the model outputs [48].

3. Results and Discussion

For all machine learning algorithms used in this study, k-layer cross-validation was used to evaluate the overall accuracy, as it provides much better and more reliable results than conventional training methods (e.g. 75% training data, 25% test data) [49]. Based on the classical and newly used features, PSD of five frequency bands, SE, MSF, KAC, wSMI Delta, wSMI Theta, wSMI Alpha, wSMI Beta, wSMI Gamma the performance of different classifiers on the PD and HC group data was evaluated using Accuracy, Precision, F1 score, Recall, ROC-AUC metrics. The classification results are shown in Table 2 and Table 3 respectively, analyzing 63 channels and 31 channels.

Table 2. 10-fold cross-validation results of 63 channels

Classifier	Accuracy	Precision	Recall	F1 Score
XGBoost	0.63 (+/- 0.16)	0.45 (+/- 0.25)	0.57 (+/- 0.19)	0.48 (+/- 0.21)
CatBoost	0.83 (+/- 0.16)	0.70 (+/- 0.31)	0.77 (+/- 0.23)	0.72 (+/- 0.28)
GNB	0.58 (+/- 0.32)	0.50 (+/- 0.37)	0.57 (+/- 0.33)	0.51 (+/- 0.35)
KNN	0.51 (+/- 0.21)	0.36 (+/- 0.26)	0.52 (+/- 0.20)	0.40 (+/- 0.23)
GB	0.63 (+/- 0.22)	0.47 (+/- 0.29)	0.57 (+/- 0.25)	0.50 (+/- 0.27)
SVM	0.56 (+/- 0.30)	0.52 (+/- 0.34)	0.57 (+/- 0.31)	0.51 (+/- 0.32)
LR	0.46 (+/- 0.26)	0.42 (+/- 0.33)	0.52 (+/- 0.28)	0.42 (+/- 0.28)

Table 3. 10-fold cross-validation results of 31 channels

Classifier	Accuracy	Precision	Recall	F1 Score
XGBoost	0.85 (+/- 0.18)	0.85 (+/- 0.22)	0.87 (+/- 0.16)	0.83 (+/- 0.24)
CatBoost	0.81 (+/- 0.18)	0.78 (+/- 0.26)	0.82 (+/- 0.19)	0.77 (+/- 0.22)
GNB	0.75 (+/- 0.27)	0.68 (+/- 0.34)	0.72 (+/- 0.30)	0.69 (+/- 0.32)
KNN	0.58 (+/- 0.29)	0.48 (+/- 0.34)	0.57 (+/- 0.29)	0.49 (+/- 0.31)
GB	0.68 (+/- 0.18)	0.57 (+/- 0.28)	0.65 (+/- 0.22)	0.57 (+/- 0.25)
SVM	0.66 (+/- 0.25)	0.58 (+/- 0.33)	0.65 (+/- 0.27)	0.58 (+/- 0.30)
LR	0.46 (+/- 0.26)	0.41 (+/- 0.33)	0.55 (+/- 0.26)	0.42 (+/- 0.28)

The XGBoost algorithm achieved the highest accuracy among the seven classifiers. The confusion matrixes and ROC-AUC results of the classifiers are shown in Figure 6 and Figure 7. XGBoost correctly predicted 12 and incorrectly predicted 2 of the 14 HC groups and correctly predicted 12 and incorrectly predicted 2 of the 14 PD groups as given in Figure 6. The second best performing classifier is the CatBoost classifier, with 12 correct and 2 incorrect predictions of the 14 HC groups. Whereas, 11 correct and 3 incorrect predictions of the 14 PD groups. The amount of True Positives and True Negatives is decreasing with GNB, KNN, SVM, GB and LR algorithms, respectively.

The ROC curves and AUC values are seen in Figure 7. It is observed from the figure that, the XGBoost has the best separation capability for the proposed features. However, SVM, LR and GB have lower AUC values. Although they use the same feature sets, the best separation methodologies of the Machine Learning Algorithms bring this difference.

The present study has 13 features, belonging to PSD of five frequency bands, and SE, MSF, KAC, wSMI Delta, wSMI Theta, wSMI Alpha, SMI Beta, wSMI Gamma. A successful classification accuracy was achieved compared to the machine learning results in the literature.

The wSMI feature, KAC and SE features in this study were used for the first time in detecting PD from the resting state EEG data. The study in [50], is expanded with channel reduction and cross-validation parameters.

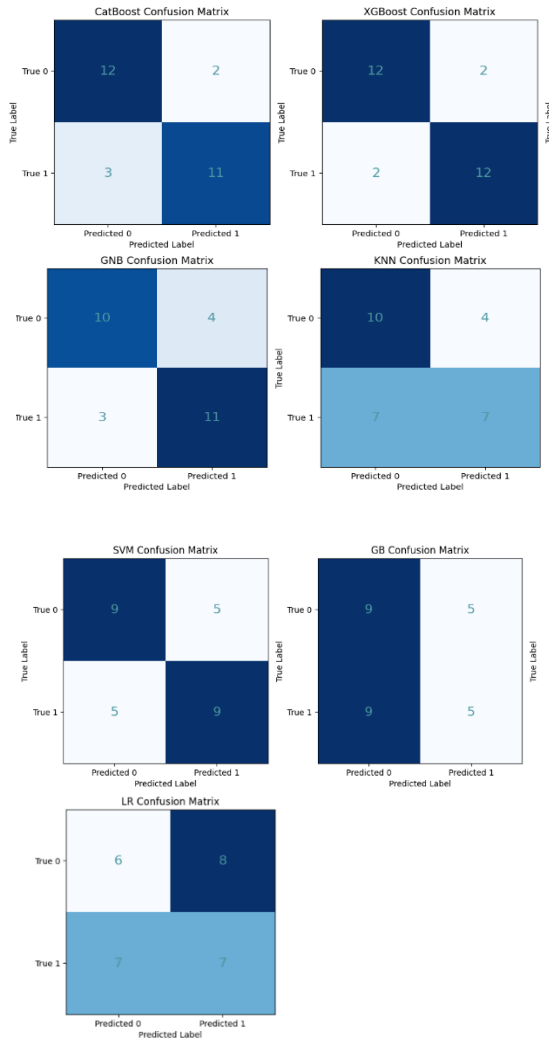


Figure 6. Confusion matrixes of classifiers

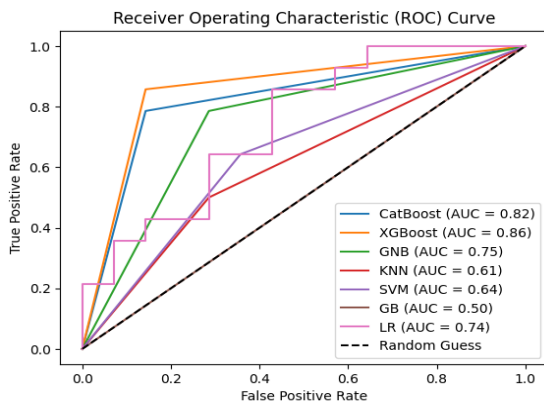


Figure 7. ROC curve and AUC values for classifiers

In the literature, accuracy metric is generally used in PD detection studies from EEG [19, 31]. In this study, precision, sensitivity, F1 score, AUC metrics were used. It is seen that the results are supporting each other. Resting EEG or magnetoencephalogram (MEG) activity in PD patients undergoes a general loss of complexity compared to controls [51, 52]. The KAC features

used in this paper are in accordance with that result. Studies have shown that beta and gamma band power is decreased in PD [53, 54]. Abnormalities in the beta band have been shown to be associated with dyskinesia (involuntary movements) in PD [55]. Therefore, the use of band power features are consistent with this view. New feature sets and channel-based studies will be continued to examine degeneration in different regions of the brain for future work.

4. Conclusion

In this study, new features wSMI, KAC, SE, MSF and subband PSDs were extracted from 63 channels and 31 channels of EEG data. They were analyzed by several machine learning algorithms for two different set of channels. According to the results, the 31 channel accuracies and AUC performances are higher than the 63 channels with all algorithms. The use of fewer channels reduces the processing time for online applications. A successful classification accuracy (85.00%) and 0.86 AUC value were obtained with XGB algorithm. Compared to the literature, a successful classification result was obtained. The use of novel features yielded a successful classification that can be a tool for PD diagnosis.

Article Information Form

Funding

The author (s) has no received any financial support for the research, authorship or publication of this study.

Authors' Contribution

The authors contributed equally to the study.

The Declaration of Conflict of Interest/ Common Interest

No conflict of interest or common interest has been declared by the authors.

The Declaration of Ethics Committee Approval

This study does not require ethics committee permission or any special permission.

The Declaration of Research and Publication Ethics

The authors of the paper declare that they comply with the scientific, ethical and quotation rules of SAUJS in all processes of the paper and that they do not make any falsification on the data collected. In addition, they declare that Sakarya University Journal of Science and its editorial board have no responsibility for any ethical violations that may be encountered, and that this study has not been evaluated in any academic publication environment other than Sakarya University Journal of Science.

Copyright Statement

Authors own the copyright of their work published in the journal and their work is published under the CC BY-NC 4.0 license.

References

- [1] J. Valls-Sole, F. Valdeoriola, "Neurophysiological correlate of clinical signs in parkinson's disease," *Clinical Neurophysiology*, vol. 113, no. 6, pp. 792–805, 2002.
- [2] J. Parkinson, "An essay on the shaking palsy," *The Journal of Neuropsychiatry and Clinical Neurosciences*, vol. 14, no. 2, pp. 223–236, 2002.
- [3] I. G. McKeith, D. Galasko, K. Kosaka, E. K. Perry, D. W. Dickson, L. A. Hansen, D.P. Salmon, J. Lowe, S.S. Mirra, E.J. Byrne, G. Lennox, N.P. Quinn, J.A. Edwardson, P.G. Ince, C. Bergeron, A. Burns, B.L. Miller, S. Lovestone, D. Collerton, E.N.H. Jansen, C. Ballard, R.A.I. de Vos, G.K. Wilcock, K.A. Jellinger, R.H. Perry, "Consensus guidelines for the clinical and pathologic diagnosis of dementia with Lewy bodies (DLB)," *Neurology*, vol. 47, no. 5, pp. 1113–1124, 1996.
- [4] J. Q. Trojanowski, "Neurodegeneration: The Molecular Pathology of Dementia and Movement Disorders," in D.W. Dickson (Ed.), ISN Press, Basel, 2003, pp. 11-13.
- [5] J. Jankovic, "Pathophysiology and assessment of parkinsonian symptoms and signs," in *Handbook of Parkinson's Disease*, 3rd ed., R. Pahwa, K. Lyons, and W.C. Koller, Eds. Taylor and Francis Group, LLC, New York, pp. 79-104, 2007.
- [6] C. H. Waters, "Diagnosis and Treatment of Parkinson's Disease," translated by B. Büyükkal, Turgut Publishing and Trade Co. Ltd., Istanbul, 2000.
- [7] H. Braak, K. Del Tredici, H. Bratzke, J. Hamm-Clement, D. Sandmann-Keil, U. Rüb "Staging of the intracerebral inclusion body pathology associated with idiopathic parkinson's disease (preclinical and clinical stages)," *Journal of Neurology*, vol. 249, no. 0, pp. 1–1, 2002.
- [8] C. Pappalettera, F. Miraglia, M. Cotelli, P. M. Rossini, F. Vecchio, "Analysis of complexity in the EEG activity of parkinson's disease patients by means of approximate entropy," *GeroScience*, vol. 44, no. 3, pp. 1599–1607, 2022.
- [9] D. Stoffers, J. L. W. Bosboom, J. B. Deijen, E. C. Wolters, H. W. Berendse, C. J. Stam, "Slowing of oscillatory brain activity is a stable characteristic of parkinson's disease without dementia," *Brain*, vol. 130, no. 7, pp. 1847–1860, 2007.
- [10] S. Kan, K. Satoshi, M. Akihiko, H. Motohiko, M. Tomohiko, Y. Hirokazu, Y. Mai, T. Jun, H. Kaname, "Comparison of quantitative EEGs between parkinson disease and age-adjusted normal controls," *Journal of Clinical Neurophysiology*, vol. 25, no. 6, pp. 361–366, 2008.
- [11] N. Fogelson, D. Williams, M. Tijssen, G. van Bruggen, H. Speelman, P. Brown, "Different functional loops between cerebral cortex and the subthalamic area in parkinson's disease," *Cerebral Cortex*, vol. 16, no. 1, pp. 64–75, 2006.
- [12] E. Lalo, S. Thobois, A. Sharott, G. Polo, P. Mertens, A. Pogosyan, P. Brown, "Patterns of bidirectional communication between cortex and basal ganglia during movement in patients with parkinson disease," *The*

- Journal of Neuroscience, vol. 28, no. 12, pp. 3008–3016, 2008.
- [13] J. L. W. Bosboom, D. Stoffers, C.J. Stam, B.W. van Dijk, J. Verbunt, H.W. Berendse, E.Ch. Wolters, “Resting state oscillatory brain dynamics in parkinson’s disease: An MEG study,” *Clinical Neurophysiology*, vol. 117, no. 11, pp. 2521–2531, 2006.
- [14] H. Tanaka, T. Koenig, R. D. Pascual-Marqui, K. Hirata, K. Kochi, D. Lehmann, “Event-related potential and EEG measures in parkinson’s disease without and with dementia,” *Dementia and Geriatric Cognitive Disorders*, vol. 11, no. 1, pp. 39–45, 2000.
- [15] R. Yuvaraj, P. Thagavel J. Thomas, J. Fogarty, F. Ali, “Comprehensive Analysis of Feature Extraction Methods for Emotion Recognition from Multichannel EEG Recordings,” *Sensors*. 23(2):915, vol. 23, no. 2, pp. 915, 2023.
- [16] G. Liu, Y. Zhang, Z. Hu, X. Du, W. Wu, C. Xu, X. Wang, S. Li, “Complexity analysis of electroencephalogram dynamics in patients with parkinson’s disease,” *Parkinson’s Disease*, vol. 2017, pp. 1–9, 2017.
- [17] T. M. McKenna, T. A. McMullen, M. F. Shlesinger, “The brain as a dynamic physical system,” *Neuroscience*, vol. 60, no. 3, pp. 587–605, 1994.
- [18] C. Lainscsek, M. E. Hernandez, J. Weyhenmeyer, T. J. Sejnowski, H. Poizner, “Non-linear dynamical analysis of EEG time series distinguishes patients with parkinson’s disease from healthy individuals,” *Frontiers in Neurology*, vol. 4, 2013.
- [19] A. M. Maitin, A. J. García-Tejedor, J. P. Munoz, “Machine learning approaches for detecting parkinson’s disease from EEG Analysis: A systematic review,” *Applied Sciences*, vol. 10, no. 23, p. 8662, 2020.
- [20] M. Chaturvedi, F. Hatz, U. Gschwandtner, J. G. Bogaarts, A. Meyer, P. Fuhr, V. Roth, “Quantitative eeg (QEEG) measures differentiate parkinson’s disease (PD) patients from healthy controls (HC),” *Frontiers in Aging Neuroscience*, vol. 9, Jan. 2017.
- [21] N. Betrouni, A. Delval, L. Chaton, L. Defebvre, A. Duits, A. Moonen, A. F. G. Leentjen, K. Dujardin, “Electroencephalography-based machine learning for cognitive profiling in parkinson’s disease: Preliminary results,” *Movement Disorders*, vol. 34, no. 2, pp. 210–217, Oct. 2018.
- [22] Md F. Anjum, S. Dasgupta, R. Mudumbai, A. Singh, J. F. Cavanagh, N. S. Narayanan, “Linear predictive coding distinguishes spectral EEG features of parkinson’s disease,” *Parkinsonism and amp; Related Disorders*, vol. 79, pp. 79–85, Oct. 2020.
- [23] H. W. Loh, C. P. Ooi, E. Palmer, P. D. Barua, S. Dogan, T. Tuncer, M. Baygin, U. R. Acharya, “GaborPDNet: Gabor Transformation and Deep Neural Network for parkinson’s disease detection using EEG signals,” *Electronics*, vol. 10, no. 14, p. 1740, Jul. 2021.
- [24] S. B. Lee, Y. J. Kim, S. Hwang, H. Son, S. K. Lee, K. I. Park, Y. G. Kim, “Predicting parkinson’s disease using gradient boosting decision tree models with Electroencephalography signals,” *Parkinsonism and amp; Related Disorders*, vol. 95, pp. 77–85, Feb. 2022.
- [25] I. Suuronen, A. Airola, T. Pahikkala, M. Murtojarvi, V. Kaasinen, H. Railo, “Budget-based classification of parkinson’s disease from resting state EEG,” *IEEE Journal of Biomedical and Health Informatics*, vol. 27, no. 8, pp. 3740–3747, Aug. 2023.
- [26] M. F. Karakaş, F. Latifoğlu, “Distinguishing parkinson’s disease with GLCM features from the Hankelization of

- EEG Signals,” *Diagnostics*, vol. 13, no. 10, p. 1769, May 2023.
- [27] F. Onay, B. Karaçalı, “Accelerometer-based timing analysis for parkinson’s disease classification,” 2023 31st Signal Processing and Communications Applications Conference (SIU), Jul. 2023.
- [28] B. O. Olcay, F. Onay, G. Akın Öztürk, A. Öviz, M. Özgören, T. Hummel, Ç. Güdücü “Using chemosensory-induced EEG signals to identify patients with de Novo Parkinson’s disease,” *Biomedical Signal Processing and Control*, vol. 87, p. 105438, Jan. 2024.
- [29] S. L. Oh, Y. Hagiwara, U. Raghavendra, R. Yuvaraj, N. Arunkumar, M. Murugappan, U. Rajendra Acharya, “A deep learning approach for parkinson’s disease diagnosis from EEG signals,” *Neural Computing and Applications*, vol. 32, no. 15, pp. 10927–10933, 2018.
- [30] L. Qiu, J. Li, J. Pan, “Parkinson’s disease detection based on multi-pattern analysis and multi-scale convolutional Neural Networks,” *Frontiers in Neuroscience*, vol. 16, 2022.
- [31] A. M. Maitin, J. P. Romero Munoz, A. J. Garcia-Tejedor, “Survey of machine learning techniques in the analysis of EEG signals for parkinson’s disease: A systematic review,” *Applied Sciences*, vol. 12, no. 14, p. 6967, 2022.
- [32] “Narayanan lab,” Datasets | Narayanan Lab, <https://narayanan.lab.uiowa.edu/article/datasets> (accessed Sep. 18, 2023).
- [33] S. Krishnan, Y. Athavale, “Trends in biomedical signal feature extraction,” *Biomedical Signal Processing and Control*, vol. 43, pp. 41–63, 2018.
- [34] “Power_spectral_density,” Wikipedia, https://en.wikipedia.org/wiki/Spectral_density#Power_spectral_density (accessed Sep. 18, 2023).
- [35] J. R. King, J. D. Sitt, F. Faugeras, L. Cohen, L. Naccache, L. Cohen, L. Naccache, S. Dehaene, “Information sharing in the brain indexes consciousness in noncommunicative patients,” *Current Biology*, vol. 23, no. 19, pp. 1914–1919, 2013.
- [36] J. D. Sitt, J. R. King, I. E. Karoui, B. Rohaut, F. Faugeras, A. Gramfort, L. Cohen, M. Sigman, S. Dehaene, L. Naccache, “Large scale screening of neural signatures of consciousness in patients in a vegetative or minimally conscious state,” *Brain*, vol. 137, no. 8, pp. 2258–2270, 2014.
- [37] A. Phinyomark, P. Phukpattaranont, C. Limsakul, “Feature reduction and selection for EMG Signal Classification,” *Expert Systems with Applications*, vol. 39, no. 8, pp. 7420–7431, 2012.
- [38] H. Helakari, J. Kananen, N. Huotari, L. Raitamaa, T. Tuovinen, V. Borchardt, A. Rasila, V. Raatikainen, T. Starck, T. Hautaniemi, T. Myllyla, O. Tervonen, S. Rytty, T. Keinanen, V. Korhonen, V. Kiviniemi, H. Ansakorpi, “Spectral entropy indicates electrophysiological and hemodynamic changes in drug-resistant epilepsy a multimodal MREG study,” *NeuroImage: Clinical*, vol. 22, p. 101763, 2019.
- [39] A. Vakkuri, A. Yli Hankala, P. Talja, S. Mustola, H. Tolvanen-Laakso, T. Sampson, H. Viertiö-Oja, “Time-frequency balanced spectral entropy as a measure of anesthetic drug effect in central nervous system during sevoflurane, propofol, and thiopental anesthesia,” *Acta Anaesthesiologica Scandinavica*, vol. 48, no. 2, pp. 145–153, Jan. 2004.
- [40] “Kolmogorov_complexity,” Wikipedia, https://en.wikipedia.org/wiki/Kolmogorov_complexity (accessed Sep. 18, 2023).
- [41] A. Natekin, A. Knoll, “Gradient Boosting Machines, a tutorial,” *Frontiers in Neurorobotics*, vol. 7, 2013.

- [42] “K-nearest neighbors algorithm,” Wikipedia, https://en.wikipedia.org/wiki/K-nearest_neighbors_algorithm (accessed Sep. 18, 2023).
- [43] “Naive Bayes Classifier,” Wikipedia, https://tr.wikipedia.org/wiki/Naive_Bayes_s%C4%B1n%C4%B1fland%C4%B1r%C4%B1c%C4%B1s%C4%B1 (accessed Sep. 18, 2023).
- [44] V. N. Vapnik, *The Nature of Statistical Learning Theory*. Cham: Springer International Publishing.
- [45] C. J. C. Burges, “Data Mining and Knowledge Discovery,” vol. 2, no. 2, pp. 121–167, 1998.
- [46] W. Menard, Scott. *Logistic regression: From introductory to advanced concepts and applications*. Sage, 2010.
- [47] L. Prokhorenkova, G. Gusev, A. Vorobev, A. V. Dorogush, A. Gulin, “CatBoost: unbiased boosting with categorical features.” *Advances in neural information processing systems* 31, 2018.
- [48] V. Morde, “XGBoost algorithm: Long may she reign!” *Medium*, <https://towardsdatascience.com/https-medium-com-vishalmorde-xgboost-algorithm-long-she-may-rein-edd9f99be63d> (accessed May 26, 2024).
- [49] E. Alpaydin. *Introduction to machine learning*. MIT press, 2020.
- [50] N. Baki, N. Gürsel Özmen, “An early diagnosis approach for parkinson patients without cognitive disorder from EEG Data,” 2022 Medical Technologies Congress (TIPTEKNO), Antalya, Turkey, 2022, pp. 1-4, doi: 10.1109/TIPTEKNO56568.2022.996020. Oct. 2022.
- [51] C. Gomez, K. T. E. Olde Dubbelink, C. J. Stam, D. Abasolo, H. W. Berendse, R. Hornero, “Complexity analysis of resting-state MEG activity in early-stage parkinson’s disease patients,” *Annals of Biomedical Engineering*, vol. 39, no. 12, pp. 2935–2944, 2011.
- [52] G. S. Yi, J. Wang, B. Deng, X. L. Wei, “Complexity of resting-state EEG activity in the patients with early-stage Parkinson’s disease,” *Cognitive Neurodynamics*, vol. 11, pp. 147-160, 2017.
- [53] L. Pezard, R. Jech, E. Ruzicka, “Investigation of non-linear properties of multichannel EEG in the early stages of Parkinson’s disease,” *Clinical Neurophysiology*, vol. 165, no. 1, pp. 38–45, 2001, PMID: 11137659.
- [54] J. Bosboom, D. Stoffers, C. Stam, B. Dijk, J. Verbunt, H. Berendse, E.Ch. Wolters, “Resting state oscillatory brain dynamics in Parkinson’s disease: An MEG study,” *Clinical Neurophysiology*, vol. 117, no. 11, pp. 2521–2531, 2006.
- [55] Q. Wang, L. Meng, J. Pang, X. Zhu, D. Ming, “Characterization of EEG data revealing relationships with cognitive and motor symptoms in Parkinson's disease: A systematic review,” *Frontiers in Aging Neuroscience*, cilt 12, sayı 587396, 2020.



Effect of Different Parameters on Enzymatic Hydrolysis of Hazelnut Shells

Özcan Gezen , İrem Deniz 

Manisa Celal Bayar University, Faculty of Engineering, Bioengineering Department, Manisa, Türkiye,
ozcangezen71@gmail.com, iremdenz@gmail.com

*Corresponding Author

ARTICLE INFO

ABSTRACT

Keywords:

Lignocellulosic biomass
Hazelnut shells
Alkaline pre-treatment
Enzymatic hydrolysis

In the last few decades, the increasing levels of environmental pollution have prompted a shift towards alternative energy sources and biobased solutions, such as lignocellulosic biomass. Lignocellulosic biomass (LB) is primarily derived from plants and is composed mainly of polysaccharides, namely cellulose, hemicellulose, and the aromatic polymer lignin. Hazelnut shells (HS), with a high lignin content of 43%, hemicellulose of 30%, and cellulose of 26%, hold promise as a valuable source of LB. In order to process those LB, lignin and hemicellulose are separated using various treatment methods. However, instead of being used solely for combustion, lignin-containing materials can be valorized for a range of purposes, from biomedical applications to the energy sector. In this study, the enzymatic hydrolysis of HS was conducted over different time periods (24, 48, 72, and 96 hours), at different temperature values with varying enzyme concentrations (0.05, 0.1, and 0.25 mL of cellulase/xylanase enzyme cocktail). To enhance the enzymatic hydrolysis, an alkaline pretreatment method using sodium hydroxide (NaOH) was employed. The results demonstrate that the maximum sugar concentration was achieved at 50°C, after 72 hours, and with a cellulase/xylanase cocktail concentration of 0.1 mL.

Article History:

Received: 06.11.2023

Accepted: 26.08.2024

Online Available: 14.10.2024

1. Introduction

Over the past few decades, researchers have come to realize that the use of fossil fuel resources is increasingly posing a threat to Earth's ecosystems through the emission of CO₂, resulting in rising sea levels and the potential loss of biodiversity. In the worst-case scenario, given the non-renewable nature of fossil fuels, their depletion could lead to a complete collapse of the global energy security system. However, this problem, along with even more dire scenarios, can be avoided by strategically planning the systematic replacement of fossil fuels with renewable, sustainable, environmentally friendly, and high-energy potential alternatives.

One key element in this transition is the utilization of lignocellulosic biomass (LB), a renewable and abundant resource derived from

plants, characterized by its polysaccharide and aromatic polymer composition. LB mainly consists of cellulose, hemicellulose, and lignin [1]. To facilitate effective enzymatic hydrolysis and achieve higher bioconversion of fermentable monosaccharides, it has been reported that a pretreatment step is necessary [2].

This pretreatment aims to weaken the naturally heterogeneous and multi-scale structure of the plant cell wall, which poses a challenge for enzymatic hydrolysis of LB [2, 3]. The choice of suitable reagents for pretreatment depends on achieving higher enzymatic hydrolysis of cellulose while maintaining a moderate cost in comparison to potassium hydroxide (KOH) [4, 5]. Alkaline sodium hydroxide (NaOH) pretreatment is a commonly used reagent that effectively removes lignin, thereby eliminating a major obstacle to the structure's recalcitrance and

enabling better accessibility of enzymes to cellulose and hemicellulose. Lignin is connected to hemicellulose through lignin carbohydrate complexes (LCC) [6, 7].

In herbaceous biomass, the LCC is composed of arabinoxylan and ferulic acid. The location of ferulic acid may vary depending on the specific lignocellulosic sources, but generally, it forms an ester linkage along the hemicellulose backbone. NaOH pretreatment specifically targets the ether and ester bonds within lignin-carbohydrate complexes [5, 8-12]. Ester bond between ferulic acid and the carbohydrate is highly susceptible to alkaline degradation, as the hydroxide ion (resulting from NaOH dissociation) enhances the rate of hydrolysis compared to water [13-15].

There are studies on enzyme hydrolysis for LB, however the values of temperature, enzyme concentration and operation time have not reached a common ground [16, 17]. Although those parameters depend on the enzyme type, enzyme source, enzyme structure along with the LB structure, the optimization of the parameters is necessary to pave the way for further studies. There are several studies that investigate the effects of temperature, enzyme concentration and operation time of enzymatic hydrolysis for basket willow [18], corn starch [19], cotton stalk [20], sugarcane bagasse [21] and crude cellulose [22].

In this study, the optimization of three different parameters to improve enzymatic hydrolysis was investigated. Enzyme concentration (2, 10, and 20 FPU/g), temperature (30, 40, 50, and 60°C), and operation time (24, 48, 72 and 96h) were individually adjusted using the one-variable-at-a-time (OVAT) approach, and the total sugar analysis was considered as the output for evaluation, corresponding to maximum enzyme activity. This is the first paper that examine the enzyme hydrolysis conditions for hazelnut shells.

2. Materials and Methods

2.1. Materials

HS were sourced from the local market in Turkey and grinded (Lavion HC-100 Cereal Grinder).

Sodium hydroxide (NaOH) was purchased from Sigma-Aldrich Supelco (CAS1310732), while *Trichoderma reesei* cellulase and *Trichoderma viride* xylanase were obtained from Sigma-Aldrich with enzyme activities of 700 U/g (CAS9012548) and xylanase activity ranging from 100-300 units/mg (CAS9025574), respectively.

2.2. Sample preparation and pre-treatment

For performing alkaline pretreatment, 2.5 g of HS was weighed and dissolved in 2% NaOH-water and NaOH-glycerol solutions. Subsequently, a 0.05 M acetate buffer with a pH of 4.8 was added to stabilize the pH. The mixture was then transferred to falcon tubes and incubated at 60°C for 2 hours. After the incubation period, the samples were centrifuged at 5000 rpm for 5 minutes, and the supernatant was carefully transferred to new pre-weighed falcon tubes. The solid residue obtained from the centrifugation was used for enzymatic hydrolysis.

2.3. Enzymatic hydrolysis

For the enzymatic hydrolysis process, 1g of pre-treated HS was added to 50 mL falcon tubes containing 10 mL of 0.05M acetate buffer at pH 4.8. The enzyme cocktail consisting of cellulase, and xylanase was loaded at a volume of 0.1 mL, which corresponds to approximately 20 FPU/g cellulose and xylan. The enzymatic hydrolysis was carried out under different parameters while maintaining a constant stirring speed of 150 rpm. Enzyme concentration (2, 10, and 20 FPU/g), temperature (30, 40, 50, and 60°C), and operation time intervals (24, 48, 72 and 96h) were selected based on a previous study by [1].

Different enzyme loads were tested, including 0.05, 0.1, and 0.25 mL (equivalent to 2, 10, and 20 FPU/g) of the cellulase and xylanase cocktail. Each sample was incubated for 72 hours at 50°C with continuous stirring at 150 rpm. The spectrophotometric analysis was performed at 490 nm to determine the total sugar concentration.

After determining the optimal enzyme concentration, the study proceeded to investigate the effect of different temperatures. The temperatures considered were 30°C, 40°C, 50°C, and 60°C. The parameters held constant during these experiments were a shaking speed of 150 rpm, a hydrolysis time of 72 hours, and an enzyme concentration of 0.1 mL. Furthermore, the impact of different hydrolysis times was examined. The durations tested were 24 hours, 48 hours, 72 hours, and 96 hours. The temperature, enzyme concentration, and shaking speed remained constant at 50°C, 0.1 mL, and 150 rpm, respectively.

2.4. Total sugar analysis

To determine the total sugars, phenol-sulfuric acid method was used [23] and a calibration curve was created by measuring increasing glucose concentrations. For each sample, 0.5 mL of the supernatant was transferred to glass test tubes, followed by the addition of 0.5 mL of 5% phenol solution and 2.5 mL of concentrated sulfuric acid (H₂SO₄). The tubes were then placed in a water bath for 15 minutes. After cooling down, the samples were analyzed spectrophotometrically at a wavelength of 490 nm. All results are the means of three samples and error bars represent the variability of data. Total sugar analysis was performed as an indirect indicator for specific enzyme activities.

3. Results and Discussion

3.1. Effect of increasing enzyme concentration

In this study, samples were enzymatically hydrolyzed at 150 rpm, 72 h, with varying enzyme concentrations 0.05 mL, 0.1 mL, 0.25 mL and Figure 1 shows the effect of increasing enzyme concentration.

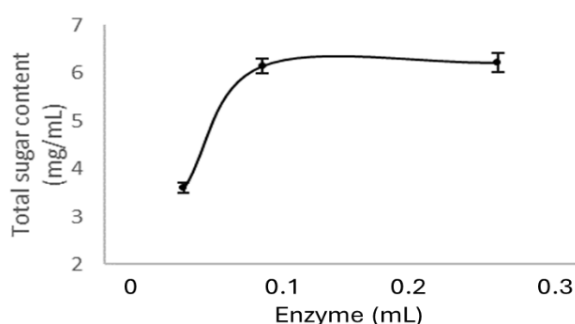


Figure 1. Effect of increasing enzyme concentration on enzymatic hydrolysis

Enzyme concentrations between 0.05 and 0.10 mL, the increase of sugar content was very sharp and at higher enzyme concentrations the total sugar content tended to stay constant. Moreover, the higher concentration of 0.25 mL increases the total sugar content slightly. However, in the long term this can be resulted as unnecessary enzyme consumption. Similar results were shown with different LB [24-26].

3.2. Effect of temperature

Temperature is an important factor for enzymatic reactions. Generally, cellulase and xylanase operate at different temperatures of 45-55 °C and 60°C, respectively [15]. However, cellulase and xylanase optimum temperatures can vary depending on the biomass structure and source adaptations [25]. Beyond the optimum operation temperatures, enzymes start to denature. As shown in Figure 2, temperatures up to 50°C, increasing temperature led to increased sugar release and between 40-50°C, ability to release saccharides of enzyme cocktail exponentially increased. At higher temperatures than 50°C, cellulase enzyme activity restricted due to the denaturation, while xylanase activity relatively increased and maximum concentration of total sugar obtained at 50°C as 11.19 mg/mL.

Figure 2 indicates that a temperature of 50 °C has a substantial impact, as the total sugar concentration observed was approximately 50–80% higher compared to temperatures of 40 °C and 60 °C. Increasing the temperature beyond the optimal range can lead to enzyme denaturation, thereby halting sugar production. Conversely, lowering the temperature below the optimal level may reduce the enzyme's energy, hindering its ability to interact with the substrate. Similar sharp changes in enzyme activity with temperature variations have been documented in other studies [26, 27]. Moreover, in a previous study where the effect of different parameters on enzymatic hydrolysis of wheat straw was reported, the optimum temperature was found to be 55 °C and the higher and lower temperature values was reported to decrease the enzymatic hydrolysis by 1/3 fold [24].

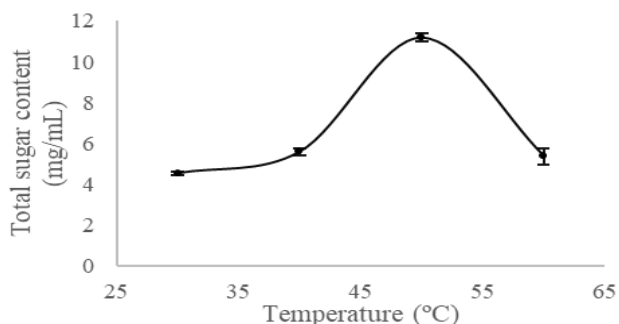


Figure 2. Effect of increasing temperature on enzymatic hydrolysis

3.3. Effect of different operation times

After the optimum temperature and enzyme concentrations were determined, the pre-treated nutshells mixed with enzyme cocktail was operated for 24 to 96 hours in order to examine the effect of operation time. Results were presented in Figure 3. It was shown that up to 48 h, total sugar concentration was increased two-fold and slightly increased to 11.19 mg/mL at 72h. After the first 72h, total sugar content was gradually decreased which can be explained by the accumulation of hydrolysis products resulting in enzymatic inhibition. Similar results were obtained elsewhere [24] which investigate alkaline pretreatment on wheat straw and enzymatic hydrolysis.

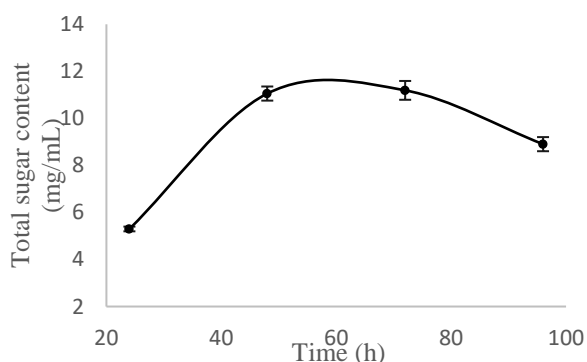


Figure 3. Effect of different process time on enzymatic hydrolysis

4. Conclusion

Efficient enzymatic hydrolysis achieved by highly accessible substrates to enzymes cellulase and xylanase. Main factor that affects hydrolysis is the accessible surface area of substrates, lignin content of LB and crystallinity. The main purpose of pretreatment is removing lignin and hemicellulose, while doing that, accessible

substrate surface of cellulose tremendously increased, crystallinity of cellulose decreased, porosity increased and as a result of this total sugar content increased.

Our results showed that the optimum operation conditions for the alkaline pretreatment integrated enzymatic hydrolysis were 0.10~10FPU/g for 72 h incubation at 50°C while stirring at 150 rpm. This research will serve as a reference guide for further studies on enzymatic hydrolysis of hazelnut shells.

Article Information Form

Funding

The author (s) has no received any financial support for the research, authorship or publication of this study.

Authors' Contribution

The authors contributed equally to the study.

The Declaration of Conflict of Interest/ Common Interest

No conflict of interest or common interest has been declared by the authors.

The Declaration of Ethics Committee Approval

This study does not require ethics committee permission or any special permission.

The Declaration of Research and Publication Ethics

The authors of the paper declare that they comply with the scientific, ethical and quotation rules of SAUJS in all processes of the paper and that they do not make any falsification on the data collected. In addition, they declare that Sakarya University Journal of Science and its editorial board have no responsibility for any ethical violations that may be encountered, and that this study has not been evaluated in any academic publication environment other than Sakarya University Journal of Science.

Copyright Statement

Authors own the copyright of their work published in the journal and their work is published under the CC BY-NC 4.0 license.

References

- [1] M. Chang, D. Li, W. Wang, D. Chen, Y. Zhang, H. Hu, X. Ye, “Comparison of sodium hydroxide and calcium hydroxide pretreatments on the enzymatic hydrolysis and lignin recovery of sugarcane bagasse,” *Bioresource Technology*, vol. 244(1), 1055-1058, 2017.
- [2] A. Zoghalmi, G. Paës, “Lignocellulosic Biomass: Understanding Recalcitrance and Predicting Hydrolysis,” *Frontiers in Chemistry*, vol. 7, 874, 2019.
- [3] N. Akhtar, K. Gupta, D. Goyal, A. Goyal, “Recent advances in pretreatment technologies for efficient hydrolysis of lignocellulosic biomass,” *Environmental Progress and Sustainable Energy*, no 35, pp. 489–511, 2016.
- [4] J. Y. Park, R. Shiroma, M. I. Al-Haq, Y. Zhang, M. Ike, Y. Arai-Sanoh, A. Ida, M. Kondo, K. Tokuyasu, “A novel lime pretreatment for subsequent bioethanol production from rice straw-calcium capturing by carbonation (CaCCO) process,” *Bioresource Technology*, 101, pp. 6805–6811, 2010.
- [5] C. I. S. Rodrigues, J. J. Jackson, M. D. Montross, “A molar basis comparison of calcium hydroxide, sodium hydroxide, and potassium hydroxide on the pretreatment of switchgrass and miscanthus under high solids conditions,” *Industrial Crops and Products*, vol. 92, pp.165–173, 2016.
- [6] A. U. Buranov, G. Mazza, “Lignin in straw of herbaceous crops,” *Industrial Crops and Products*, vol.28, no. 3, pp. 237-259, 2008.
- [7] J. H. Grabber, “How do lignin composition, structure, and cross-linking affect degradability? A review of cell wall model studies,” *Crop Science*, vol. 45, no. 3, pp. 820-831, 2005.
- [8] J. S. Kim, Y. Y. Lee, T. H. Kim, “A review on alkaline pretreatment technology for bioconversion of lignocellulosic biomass,” *Bioresource Technology*, 199, pp. 42–48, 2016.
- [9] P. Yadav, J. Maharjan, S. Korpole, G.S. Prasad, G. Sahni, T. Bhattarai, L. Sreerama, “Production, Purification, and Characterization of Thermostable Alkaline Xylanase from *Anoxybacillus kamchatkensis* NASTPD13”. *Frontiers in Bioengineering and Biotechnology*, vol 156, pp. 65, 2018.
- [10] S. D. Zhu, Y. X. Wu, Z. N. Yu, Q. M. Chen, G. Y. Wu, F. Q. Yu, C. W. Wang, S. W. Jin, “Microwave-assisted Alkali Pretreatment of Wheat Straw and its Enzymatic Hydrolysis.” *Biosystems Engineering*, vol. 4, pp. 437–442, 2006.
- [11] E. Bertrand, L. P. S. Vandenberghe, C. R. Soccol, J. C. Sigoillot, C. Faulds, “First Generation Bioethanol,” *Green Fuels Technology: Biofuels; Green Energy and Technology*; C.R. Soccol, S.K. Brar, C. Faulds, L.P. Ramos, Eds.; Springer International Publishing: Cham, Switzerland, pp. 175–212, 2016.
- [12] P. Y. Bruice, “Organic Chemistry (4th ed.)”. Upper Saddle River, N.J.: Prentice Hall, 2004.
- [13] A. F. Murawski de Mello, L. Porto de Souza Vandenberghe, K. K. Valladares-Diestra, G. Amaro Bittencourt, W. J. Martinez Burgos, C. R. Soccol, “Corn First-Generation Bioethanol Unities with Energy and Dried Grains with Solubles (DDGS) Production,” *Liquid Biofuels: Bioethanol; Biofuel and Biorefinery Technologies*; C.R. Soccol, G. Amarante Guimarães Pereira, C. G. Dussap, L. Porto de Souza Vandenberghe, Springer International Publishing: Cham, Switzerland, pp. 109–132, 2022.
- [14] S. K. Mohanty, M. R. Swain, “Chapter 3—Bioethanol Production from Corn and Wheat: Food, Fuel, and Future.” In

- Bioethanol Production from Food Crops; R.C. Ray, S. Ramachandran, Eds.; Academic Press: Cambridge, MA, USA, 2019; pp. 45–59, 2019.
- [15] Y. M. Tao, X. Z. Zhu, J. Z. Huang, S. J. Ma, X. B. Wu, M. N. Long, & Q. Chen, “Purification and properties of endoglucanase from a sugar cane bagasse hydrolyzing strain, *Aspergillus glaucus* XC9,” *Journal of Agricultural and Food Chemistry*, vol. 58, no. 10, pp. 6126–6130, 2010.
- [16] J. J. Stickel, R. T. Elander, J. D. Mcmillan,” *Enzymatic Hydrolysis of Lignocellulosic Biomass.*” Roman Brunecky Book, Book Editor(s): V.S. Bisaria, A. Kondo, 2014, pp. 77-103, 2014.
- [17] K. Vasić, Ž. Knez, M. Leitgeb, “Bioethanol Production by Enzymatic Hydrolysis from Different Lignocellulosic Sources.” *Molecules*, vol. 26,3, pp. 753, 2021.
- [18] R. Łukajtis, P. Rybarczyk, K. Kucharska, D. K. Łyskawa, E. Ślupek, K. Wychodnik, M. Kamiński,” *Optimization of Saccharification Conditions of Lignocellulosic Biomass Under Alkaline Pre-Treatment and Enzymatic Hydrolysis*” *Energies*, vol. 11, 4, pp. 886, 2018.
- [19] V. Rana,” *Optimization of enzymatic hydrolysis of lignocellulosic biomass,*” Ph.D. dissertation, Washington State University, 2013.
- [20] O. Yildirim, D. Tunay, B. Ozkaya,” *Optimization of Enzymatic Hydrolysis Conditions of Chemical Pretreated Cotton Stalk Using Response Surface Methodology for Enhanced Bioethanol Production Yield.*” *Biomass Conversion and Biorefinery*, vol. 13, pp. 6623-6634, 2023.
- [21] E. B. Moya, B. Syhler, J. O. Manso, G. Dragone, S.I. Mussatto,” *Enzymatic Hydrolysis Cocktail Optimization for the Intensification of Sugar Extraction from Sugarcane Bagasse.*” *International Journal of Biological Macromolecules*, vol. 242, 2023.
- [22] J. Zhou, Y. H. Wang, J. Chu, L.Z. Luo, Y. P. Zhuang, S. L. Zhang,” *Optimization of Cellulase Mixture for Efficient Hydrolysis of Steam-Exploded Corn Stover by Statistically Designed Experiments.*” *Bioresource Technology*, vol. 100, 2, pp. 819-825, 2009.
- [23] S. S. Nielsen, “*Phenol-Sulfuric Acid Method for Total Carbohydrates.*” *Food Analysis Laboratory Manual*, pp. 47-53, 2009.
- [24] L. Han, J. Feng, S. Zhang, Z. Ma, Y. Wang & X. Zhang,” *Alkali Pretreated of Wheat Straw and Its Enzymatic Hydrolysis.*” *Brazilian Journal of Microbiology*, vol. 43, 1, pp. 53–61, 2012.
- [25] M. J. Liszka, M. E. Clark, E. Schneider, D. S. Clark, “*Nature versus nurture: Developing enzymes that function under extreme conditions.*” *Annual Review of Chemical and Biomolecular Engineering*, vol. 3, pp. 77–102, 2012.
- [26] N. A. S. M. Rosdee, N. Masngut, S. M. Shaarani, S. Jamek, M. S. M. Sueb, “*Enzymatic hydrolysis of lignocellulosic biomass from pineapple leaves by using endo-1,4-xylanase: Effect of pH, temperature, enzyme loading and reaction time,*” *IOP Conf. Ser.: Mater. Sci. Eng.*, vol. 736, 022095, 2020.
- [27] D. K. A. Fortkamp, “*High Xylanase Production by Trichoderma viride Using Pineapple Peel as Substrate and Its Application in Pulp Biobleaching,*” *African Journal of Biotechnology*, pp. 2249-2259, 2014.

The Effect of Various Parameters in the Sulfuric Acid Leaching of Low Grade Zinc Oxide Ore of Niğde-Türkiye

Özlem Kaya^{1*}, Gürol Uysal²

¹ Sivas Cumhuriyet University, Faculty of Engineering, Department of Metallurgical and Materials Engineering, Sivas, Türkiye, okaya@cumhuriyet.edu.tr

² ETİ Electrometallurgy Inc., Muğla, Türkiye, g.uysal@etimet.com

*Corresponding Author

ARTICLE INFO

ABSTRACT

Keywords:

Leaching
Low grade zinc oxide ore
Zinc extraction

The aim of this study was to investigate the main parameters affecting the leaching of low grade zinc oxide ores with sulfuric acid. The influence of leaching time (5 to 480 minutes), sulfuric acid concentration (25 to 125 g/L), leaching temperature (25 to 90 °C), particle size (-104 µm, -82 µm, -60 µm, -49 µm) and solid/liquid ratio (1/10, 1/7.5, 1/5, 1/4) was investigated. The effects of these process parameters were studied with to achieve maximum zinc extraction with minimum iron extraction and acid consumption. The optimum parameters for sulfuric acid leaching of zinc ore were determined to be 60 min leaching time, 75 g/L sulfuric acid concentration, 80 °C leaching temperature, 1/10 solid/liquid ratio and -60 µm particle size. Under these optimum conditions, Zn extraction (%), Fe extraction (%) and acid consumption (ton H₂SO₄/ dissolved ton Zn) were obtained 88.68%, 25.83% and 5.47 ton H₂SO₄/ dissolved ton Zn respectively.

Article History:

Received: 29.12.2023

Accepted: 18.08.2024

Online Available: 14.10.2024

1. Introduction

Zinc is a versatile non-ferrous metal that is widely utilized in various industries including galvanization, cosmetics, die casting, and battery manufacturing. Oxidized zinc ores such as smithsonite (ZnCO₃), zincite (ZnO), hemimorphite (Zn₄(SiO₇)(OH)₂H₂O), willemite (Zn₂SiO₄) and hydrozincite (ZnCO₃.2Zn(OH)₂) are the most important sources of zinc metal production after sulfides [1, 2]. Most of the zinc in the world is produced from high grade zinc sulfide ores. In recent years, the demand for zinc and zinc compounds has increased, whereas the number of high grade zinc ore stores has decreased. As a result, new sources of zinc, such as low grade ores, carbonate ores and silicate ores, are being considered, leading to an increasing focus on the processing of low grade oxide ores.

The extraction of zinc from its oxide ores can be performed using both pyrometallurgical and hydrometallurgical methods. The three main steps in the hydrometallurgical method are leaching, purification and electrolysis. Leaching processes constitute the first step of the hydrometallurgical methods and plays an important role in the extraction of metals and compounds in an economical way. The most commonly used hydrometallurgical methods for zinc production are alkaline leaching, acid leaching and ammonia leaching. Acid leaching is considered the most effective method of zinc extraction process because of its advantages, including rapid process, easy leach solution purification and high selectivity [3-5].

Leaching studies on zinc ore with sulfuric acid have been carried out by many researchers. Frenay [6] conducted leaching studies on

oxidized zinc ores using different solutions, including ammonium hydroxide, sulfuric acid, sulfurous acid, and sodium hydroxide. Caustic soda and sulfuric acid were identified as providing the best leaching results. This study highlighted that smithsonite can be completely leached, whereas hemimorphite is relatively refractory to leaching. He et al. [7] investigated the pressure leaching of high silica Pb-Zn oxide ore using air as a pressurized gas in a sulfuric acid medium. The leaching time, leaching temperature, sulfuric acid concentration, oxygen partial pressure, and solid/liquid ratio were among the parameters studied. Under optimum conditions, the study found that zinc extraction reached 96%. Moreover, the dissolution rates for Si, Pb and Fe were as low as 1%, 2%, and 6%, respectively. Pecina et al. [8] investigated the use of hydrogen peroxide as an oxidant in sulfuric acid solutions for the extraction of zinc from sphalerite concentrate. Acid and peroxide concentrations, particle size, reaction time and temperature are among the parameters studied. This study also investigated the use of complexing agents (citric acid, phosphoric acid, oxalic acid and phosphonic acid) to enhance zinc recovery in an oxidative aqueous medium. Terry and Monhemius [9] studied the acid dissolution kinetics of natural and synthetic willemites and natural hemimorphites. The parameters studied included acid type, surface area, temperature and pH. For willemite the dissolution was found to be mixed chemical/diffusion controlled and for hemimorphite the dissolution was found to be diffusion controlled.

As noted in the literature, detailed studies on the leaching of low grade zinc oxide ores are limited and therefore require more comprehensive investigations. In addition, each ore has its own chemical and mineralogical properties; therefore, the optimum leaching conditions will vary from one ore type to another. The research was specifically focused on investigating the important factors affecting sulfuric acid leaching of low grade zinc oxide ore from Niğde-Türkiye.

2. Materials and Methods

The zinc oxide ore used for the leaching experiments was supplied by a local mining company in Niğde-Türkiye. The chemical

composition of the ore was characterized by X-ray fluorescence (XRF) and is presented in Table 1.

Table 1. The chemical composition of zinc oxide ore

Component	Weight (%)
Zn	8.44
Fe	21.70
Pb	1.21
Cu	0.07
Mn	1.96
Ca	1.30
Cd	0.04
Ni	0.11
SiO ₂	28.62
S	0.08
As	1.01
K	0.29
Na	<0.10
Moisture	2.02

The X-ray diffraction (XRD) pattern of zinc oxide ore was obtained using a Rigaku DMAX IIC model X-ray diffractometer with CuK α radiation at 35 kV and 15 mV (Figure 1). As shown in Figure 1, smithsonite (ZnCO₃) and zincite (ZnO) are the main zinc oxide minerals in the sample, whereas quartz (SiO₂), goethite (FeOOH) and pyrolusite (MnO₂) are gangue minerals.

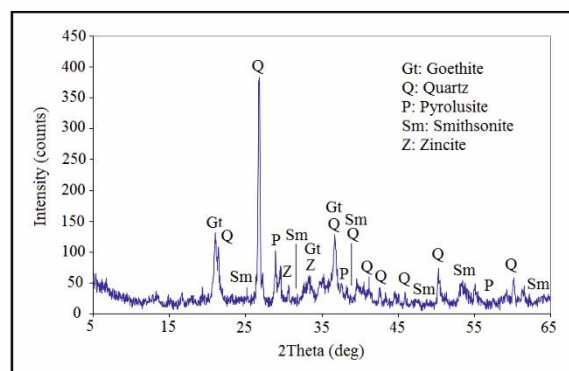


Figure 1. The XRD pattern of zinc oxide ore

Leaching tests were performed using sulfuric acid from Merck with 95-98% analytical purity. In the experiments, a 1000 mL glass beaker was used. The beaker was covered by a cap with four holes that were drilled for place the thermometer, mechanical stirrer, pH meter or back cooler and for taking samples. The experiments were

performed with 50 g of sample in a beaker placed in a thermostatically controlled water bath. Figure 2 shows the experimental setup for leaching.

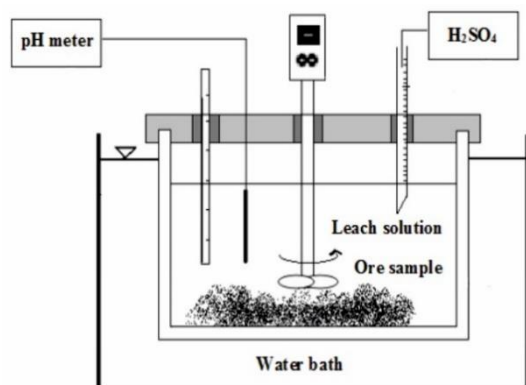


Figure 2. The experimental setup for leaching

While the method used in the leaching experiments was the same, the experiments investigated the effect of different parameters on the sulfuric acid leaching of zinc oxide ore. After the completion of each leaching experiment, the leach solution was filtered, and the solid leach residue was then washed with distilled water. The washed solid residue was dried at 105 ± 5 °C. The total dissolved weight (%) was calculated from the dried solid residue. To determine the Zn extraction (%) and Fe extraction (%), the leach solution was analyzed using Atomic Adsorption Spectrometry (AAS). The sulfuric acid consumption was determined by alkalimetric titration with NaOH.

3. Results and Discussion

3.1. Effect of leaching time

Leaching experiments were carried out in the range of 5-480 min. In the experiments, an H_2SO_4 concentration of 75 g/L, leaching temperature of 40 °C, particle size of $-82 \mu\text{m}$ and solid/liquid ratio of 1/10 were kept constant. Leaching experiments at different times are presented in Figure 3.

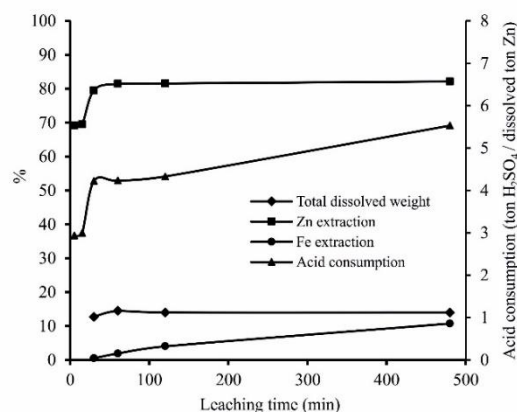


Figure 3. Effect of leaching time on the sulfuric acid leaching

As shown in Figure 3, the Zn extraction (%) increased to 81.45% with leaching times up to 60 min and remained almost constant with longer leaching times. This suggests that the majority of zinc dissolution occurs within the initial 60 min of leaching. In contrast, Fe extraction (%) increased from 0.49% after 30 min to 10.73% after 480 min of leaching. The increase in iron extraction over time indicates a progressive dissolution of iron from the ore. The iron content in the ore plays a significant role in determining zinc extraction, with higher iron content leading to lower zinc extraction.

According to Frenay [6], this is the result of smithsonite particles covered with hydroxides of iron. Simultaneously, the acid consumption (ton H_2SO_4 /dissolved ton Zn) increased with increasing leaching time. While the acid consumption at the end of 5 minutes leaching is 2.93 ton H_2SO_4 /dissolved ton Zn, it increases to 5.53 ton H_2SO_4 /dissolved ton Zn at the end of 480 minutes leaching. This indicates a relationship between leaching time and acid consumption.

From Figure 3 it can be seen that 81.45% Zn extraction, 14.46% total dissolved weight, 1.89% Fe extraction and 4.23 ton H_2SO_4 /dissolved ton Zn are achieved with the 60 min leaching time. Considering the high values of Zn extraction (%), total dissolved weight (%) and the low values of Fe extraction (%), acid consumption (ton H_2SO_4 /dissolved ton Zn), a leaching time of 60 min was considered optimal.

3.2. Effect of sulfuric acid concentration

The effect of different concentrations of sulfuric acid (25, 40, 55, 75, 100 and 125 g/L) on the leaching was studied under the following conditions: leaching time of 60 min, leaching temperature of 40 °C, particle size of -82 µm and solid/liquid ratio of 1/10. Leaching experiments with different concentrations of sulfuric acid are shown in Figure 4.

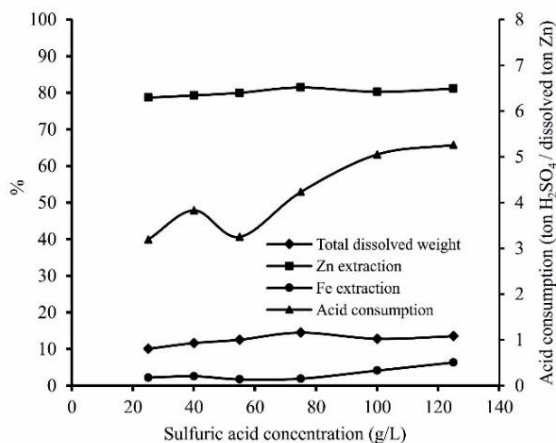


Figure 4. Effect of acid concentration on the sulfuric acid leaching

The general dissolution reactions for the main zinc oxide minerals, smithsonite (ZnCO₃) and zincite (ZnO), with sulphuric acid are given by equations (1) and (2): [4, 10-11]



Figure 4 indicates that with an increase in the sulfuric acid concentration from 25 g/L to 125 g/L, the Zn extraction (%) increased from 78.68% to 81.14%, the Fe extraction (%) increased from 2.19% to 6.30% and the total dissolved weight (%) increased from 10.04% to 13.49%. As the sulfuric acid concentration increases, the chemical reactions between zinc (Zn), iron (Fe) and sulfuric acid become more complete, resulting in higher extraction of both Zn and Fe into the leaching solution [7].

Figure 4 shows that there is a positive correlation between the sulfuric acid concentration and both the total dissolved weight (%) and Zn extraction (%). This suggests that an increase in acid

concentration increases the leaching efficiency of zinc oxide ores. The maximum values for the total dissolved weight (%) and Zn extraction (%) were obtained at a sulfuric acid concentration of 75 g/L. Above this concentration, both the values remained constant. Similar trends have been observed in previous studies by Espiari et al. [1] and Bodas [12]. Espiari et al. [1] found that zinc recovery increased up to 88% with sulfuric acid concentration up to 2 M and remained almost constant at higher acid concentrations. Bodas [12] reported that zinc extraction increased with sulfuric acid concentration up to 4.5 M and then became constant.

The maximum Zn extraction (81.45%) and total dissolved weight (14.46%) were obtained with 75 g/L of sulfuric acid. The lowest Fe extraction of 1.89% at 75 g/L sulfuric acid is desirable, as it minimizes the dissolution of iron during the leaching. This is important for maintaining the selectivity of the leaching process and avoiding contamination of the leaching solution with unwanted metals. Higher sulfuric acid concentrations can result in increased zinc extraction, but an optimum concentration needs to be identified to balance extraction efficiency and acid consumption. A sulfuric acid concentration of 75 g/L was identified as the optimum condition for achieving a balance among high Zn extraction (%), total dissolved weight (%) and low Fe extraction (%), acid consumption (ton H₂SO₄/dissolved ton Zn).

3.3. Effect of leaching temperature

Leaching experiments were carried out over a wide temperature range (25°C-90°C) to understand the effect of temperature on the leaching process. Leaching temperature experiments were performed with a leaching time of 60 min, H₂SO₄ concentration of 75 g/L, particle size of -82 µm, solid/liquid ratio of 1/10. Leaching experiments at different temperatures are shown in Figure 5.

The results from Figure 5 show a positive relationship between leaching temperature and both total dissolved weight (%) and Zn extraction (%). Increasing the leaching temperature from 25°C to 80°C resulted in a gradual increase in the total dissolved weight (4.22% to 24.68%) and Zn

extraction (76.85% to 87.95%). These results are consistent with those of Santos et al. [13], who observed a significant increase in zinc extraction from 36% to 90% when the temperature was increased from 70°C to 90°C during the leaching of zinc silicate ores.

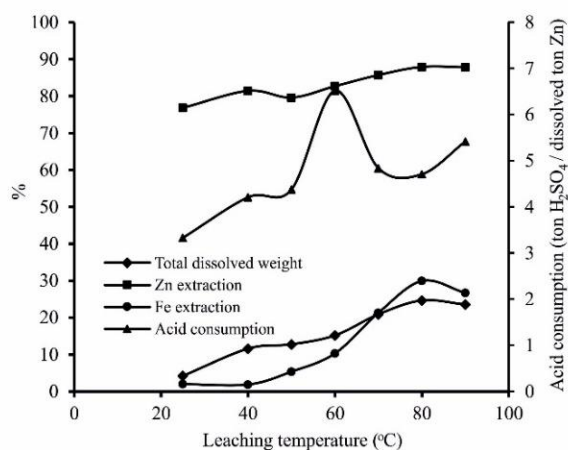


Figure 5. Effect of leaching temperature on the sulfuric acid leaching

As the leaching temperature increased from 25°C to 80°C, an increase in acid consumption was observed from 3.33 to 4.71 ton H₂SO₄/dissolved ton Zn. This indicates that too much acid is being used in the leaching process at higher temperatures. It can be seen that the leaching temperature was also effective for Fe extraction (%). At a leaching temperature of 80°C, Fe extraction reached 29.96%. Although it is known that iron dissolution affects selectivity, an optimum leaching temperature of 80 °C was chosen to increase Zn extraction, while other parameters were investigated. Figure 5 shows that at a leaching temperature of 80 °C, 24.68% total dissolved weight, 87.95% Zn extraction, 29.96% Fe extraction and 4.71 ton H₂SO₄/dissolved ton Zn acid consumption were achieved. Thus, leaching temperature of 80 °C is considered to be the optimum leaching temperature.

3.4. Effect of particle size

Four different particle sizes (-104, -82, -60 and -49 μm) were used to determine the effect of particle size on the leaching process. The leaching experiments were conducted under the conditions: leaching time of 60 min, H₂SO₄ concentration of 75 g/L, leaching temperature of

80 °C and solid/liquid ratio of 1/10. The leaching experiments with different particle sizes are shown in Figure 6.

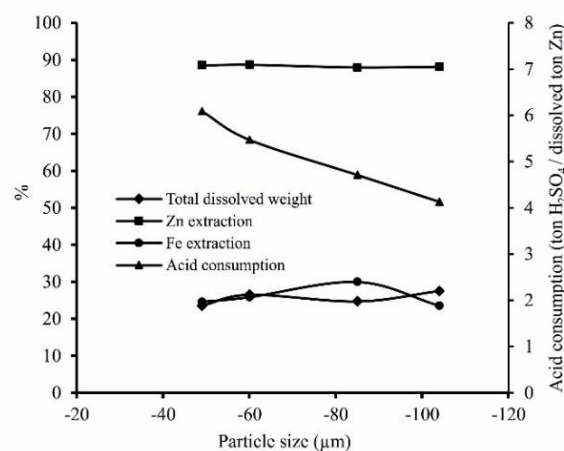


Figure 6. Effect of particle size on the sulfuric acid leaching

Figure 6 shows that decreasing the particle size had no noticeable effect on the total dissolved weight (%), Zn extraction (%), Fe extraction (%) and acid consumption (ton H₂SO₄/dissolved ton Zn). Contrary to the expectation that decreasing the particle size would positively influence the leaching process, the experimental results show that the highest total dissolved weight (26.50%) and zinc extraction (88.68%) were observed at the -60 μm particle size. This can be explained by the possibility that some other factors (surface area, agglomeration effect, and mineralogical properties) interact with the particle size to influence the leaching efficiency. An acid consumption of 5.47 ton H₂SO₄/dissolved ton Zn was achieved at this particle size. Based on these observations, a particle size of -60 μm was selected as the optimum for zinc leaching under the given conditions.

3.5. Effect of solid/liquid ratio

Four different solid/liquid ratios (1/10, 1/7.5, 1/5 and 1/4) were investigated for their effect on the leaching process. Leaching experiments were performed under conditions in which the leaching time, H₂SO₄ concentration, leaching temperature and particle size were kept constant at 60 min, 75 g/L, 80 °C and -60 μm respectively. Leaching experiments with different solid/liquid ratios are shown in Figure 7.

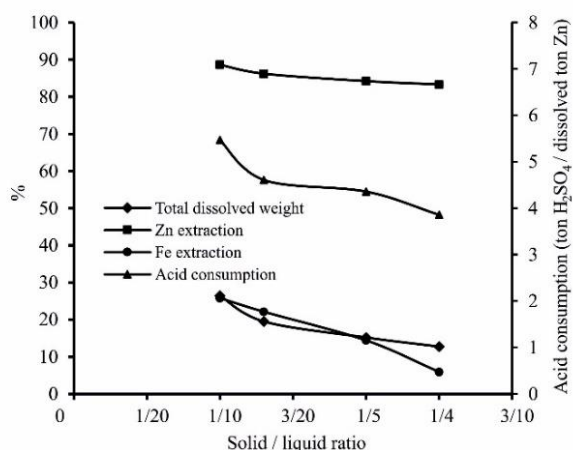


Figure 7. Effect of solid/liquid ratio on the sulfuric acid leaching

Figure 7 shows the inverse relationship between the solid/liquid ratio and total dissolved weight (%). As the solid/liquid ratio decreased from 1/4 to 1/10, the total dissolved weight (%) increased from 12.75% to 26.50%. A decrease in the solid/liquid ratio resulted in increased values of Zn extraction (%), Fe extraction (%), and acid consumption (ton H₂SO₄/ dissolved ton Zn). This indicates that a lower solid/liquid ratio results in a more efficient leaching process but requires higher acid consumption.

The experiments showed that the highest values for both the total dissolved weight (%) and Zn extraction (%) were obtained with a solid/liquid ratio of 1/10, giving 26.50% total dissolved weight and 88.68% Zn extraction. Based on these results, a solid/liquid ratio of 1/10 was chosen as optimal for the studied conditions. These results are consistent with the study by Espiari et al. [1], who reported that the leaching rate increased as the solid/liquid ratio decreased. They achieved a maximum zinc recovery of 98% at a solid/liquid ratio of 1/4.

4. Conclusion

This study investigated the extraction of zinc by sulfuric acid leaching from low grade oxidized zinc ore. Five main parameters including leaching time and temperature, acid concentration, particle size and solid/liquid ratio were optimized. The following conclusions were drawn:

(1) Smithsonite (ZnCO₃) and zincite (ZnO) were identified as the major zinc oxide minerals in the studied ore. The solubility of zinc in sulfuric acid was confirmed from these minerals.

(2) Zn and Fe extraction increased with an increase in leaching time, sulfuric acid concentration, and leaching temperature. This indicated a positive correlation between these factors and the efficiency of Zn and Fe extraction.

(3) Decreasing both the particle size and solid/liquid ratio contributed to an increase in Zn extraction (%). This suggests that finer particle sizes and lower solid/liquid ratios improve leaching efficiency.

(4) The following optimum conditions for maximum zinc extraction:
 Leaching time: 60 minutes
 Sulfuric acid concentration: 75 g/L
 Leaching temperature: 80°C
 Particle size: -60 μm
 Solid/liquid ratio: 1/10

(5) Under the optimized conditions, the study achieved maximum Zn extraction of 88.68%, with a minimum Fe extraction of 25.83% and acid consumption of 5.47 ton H₂SO₄/dissolved ton Zn. The highest total dissolved weight was obtained as 26.50%.

Article Information Form

Funding

Authors would like to thank for the financial support provided by TUBITAK (the Scientific and Technical Research Council of Turkey) for the Project no: 109M112.

Authors' Contribution

The authors contributed equally to the study.

The Declaration of Conflict of Interest/ Common Interest

No conflict of interest or common interest has been declared by the authors.

The Declaration of Ethics Committee Approval

This study does not require ethics committee permission or any special permission.

The Declaration of Research and Publication Ethics

The authors of the paper declare that they comply with the scientific, ethical and quotation rules of SAUJS in all processes of the paper and that they do not make any falsification on the data collected. In addition, they declare that Sakarya University Journal of Science and its editorial board have no responsibility for any ethical violations that may be encountered, and that this study has not been evaluated in any academic publication environment other than Sakarya University Journal of Science.

Copyright Statement

Authors own the copyright of their work published in the journal and their work is published under the CC BY-NC 4.0 license.

References

- [1] S. Espiari, F. Rashchi, S.K. Sadrnezhaad, "Hydrometallurgical treatment of tailings with high zinc content", *Hydrometallurgy*, vol. 82, pp. 54-62, 2006.
- [2] J. Deng, Q. Sun, P. Lin, G. Song, S. Wen, J. Deng and D. Wu, "Dissolution kinetics of zinc oxide ore with an organic Acid" *International Journal of Metallurgical & Materials Engineering*, vol.1: 109, 7 pages, 2015.
- [3] M. Hurşit, O. Laçın, H. Saraç, "Dissolution kinetics of smithsonite ore as an alternative zinc source with an organic leach reagent", *Journal of the Taiwan Institute of Chemical Engineers*, vol. 40, pp. 6-12, 2009.
- [4] E.A. Abdel-Aal, "Kinetics of sulfuric acid leaching of low-grade zinc silicate ore, *Hydrometallurgy*, vol. 55, pp. 247-254, 2000.
- [5] Y. Zhang, Y. Hua, X. Gao, C. Xu, J. Li, Y.Li, Q., Zhang, L. Xiong, Z. Su, M. Wang, J. Ru, "Recovery of zinc from a low-grade zinc oxide ore with high silicon by sulfuric acid curing and water leaching", *Hydrometallurgy*, vol. 166, pp. 16-21, 2016.
- [6] J. Frenay, "Leaching of oxidized zinc ore in various media", *Hydrometallurgy*, vol.15, pp. 243-253, 1985.
- [7] S. He, J. Wang, J. Yan, "Pressure leaching of high silica Pb-Zn oxide ore in sulfuric acid medium", *Hydrometallurgy*, vol. 104, no. 2, pp. 235-240, 2010.
- [8] T. Pecina, T. Franco, P. Castillo, E. Orrantia, "Leaching of a zinc concentrate in H₂SO₄ solutions containing H₂O₂ and complexing agents", *Minerals Engineering*, vol. 21, no.1, pp. 23-30, 2008.
- [9] B. Terry, A. J. Monhemius, "Acid dissolution of willemite ((Zn, Mn)₂SiO₄) and hemimorphite (Zn₄Si₂O₇(OH)₂.H₂O)", *Metallurgical Transactions B*, vol. 14B, pp. 335-346, 1983.
- [10] T. Havlik, M. Turzakova, S. Stopic, B. Friedrich, "Atmospheric leaching of EAF dust with diluted sulphuric acid", *Hydrometallurgy*, vol. 77, pp. 41-50, 2005.
- [11] H. Xu, C. Wei, C. Li, G. Fan, Z. Deng, M. Li, X. Li, "Sulfuric acid leaching of zinc silicate ore under pressure", *Hydrometallurgy*, vol. 105, pp. 186-190, 2010.
- [12] M.G. Bodas, "Hydrometallurgical treatment of zinc silicate ore from Thailand", *Hydrometallurgy*, vol. 40, pp. 37-49, 1996.
- [13] F.M. Santos, P.S. Pina, R. Porcaro, A.V. Oliveira, C.A. Silva, V.A. Leão, "The kinetics of zinc silicate leaching in sodium hydroxide", *Hydrometallurgy*, vol. 102, pp. 43-49, 2010.

Comparison of the Bactericidal Effect of the UV and Blue-Light Regions on Selected *Escherichia Coli* and *Staphylococcus Aureus* Strains

Can Saç 

Eastern Mediterranean University, Faculty of Medicine, Gazimagusa, Cypris, can.sac2006@gmail.com

ARTICLE INFO

ABSTRACT

Keywords:
Escherichia coli
Staphylococcus aureus
Blue light



Article History:
Received: 04.03.2024
Accepted: 10.09.2024
Online Available: 14.10.2024

Some Bacteria are important microorganisms that threaten human health. Especially *Escherichia coli* and *Staphylococcus aureus* can cause serious diseases in humans. Antibiotics are used to stop these infections and prevent bacteria from multiplying. However, it has been observed that these antibiotics have side effects as well as their benefits. Therefore, the resistance of these bacteria can be reduced with rays of different wavelengths. In our study, the effects of three types of light with wavelengths of 254 nm, 365 nm and 460 nm on *Escherichia coli* and *Staphylococcus aureus* bacteria were investigated. The reason we chose these rays is that two of them have short wavelengths and are harmful rays, while the other one is in the visible region and is harmless. While a significant decrease in the number of colonies was observed under the operating conditions of 254 nm and 365 nm wavelength lights falling in the UV region, no colonies were observed in the 460 nm wavelength light. In the second trial results, 44% growth was achieved at 365 nm and 56% growth was inhibited. *S. aureus* growth stopped completely at 460 nm. At 254 nm, 14% growth was achieved and 86% growth was inhibited. It was observed that there was 3% growth and 97% growth inhibition at 365 nm. As can be clearly seen from the results, no significant bacterial growth was observed at 460 nm. In our literature studies, it can be seen that no study has been done on this wavelength before.

1. Introduction

Many bacteria that can adapt to adverse conditions in nature can cause diseases in living things. Because most of the boundaries within which pathogens can multiply are in harmony with the boundaries of the living things on or within them. When maximum or minimum temperature limits are approached or exceeded, death or weakening of the effectiveness of some factors occurs, even if microorganisms grow. Virus, bacteria and fungal spores are highly resistant to environmental conditions and can survive for long periods (years) and retain their infectious abilities. With this contagious feature, they spread among living things and cause diseases. People have been searching for cures and treatments for disease-causing bacteria for

years. Many studies have been done on this subject [1-3]. The most important of these treatment methods is antibiotic treatments. However, antibiotics also have negative side effects. For this reason, different methods have been put forward to break antibiotic resistance. Some wavelengths of light can prevent bacteria from growing and multiplying. In this way, reproduction is prevented from reaching a level that could stop and cause infection.

1.1. The effects of light on bacteria

Lights of different wavelengths have long been used in microbial control because they do not require heat to kill the microorganism. The main areas of use of these microbial control lights are disinfection of air and surfaces of operating

rooms, laboratories and biological safety cabinets. In addition, they can be used in closed places such as cafeterias and hospital rooms where people are crowded together, to prevent the spread of airborne diseases by reducing the number of pathogenic microorganisms in the air [4].

This microbial property of light disrupts the structure of the bacteria and causes some changes in the bacteria. These changes can be explained as follows.

Looking at the bacterial structure, monomers (simple molecular compounds with unsaturated or double bonds) are linked to each other by phosphodiester bonds formed between 5'-phosphate groups and 3'-hydroxyl groups, forming long polymers consisting of units up to several hundred million in number. These are the bonds made by the phosphates in DNA and RNA with deoxyribose and ribose. The double bond on thymine and cytosine bases in DNA absorbs ultraviolet light. This opens the added energy bond and allows it to react with the neighbouring base.

Reactive oxygen species (ROS) include oxygen radicals (free radicals released due to single-electron reduction from oxygen), single oxygen and peroxidases. These are usually tiny molecules and highly reactive due to the presence of unpaired valence shell electrons. High amounts of ROS are known to have a lethal effect on the cell. In some diseases, tissue destruction occurs as a result of the formation of free radicals. ROS in bacteria means light induced by sensitivity to endogenous light [5].

1.2. Phototoxic effects in microorganisms are as follows:

According to the wavelength used, the light causes the ROS to be induced when it is high, while it encourages the increase of ROS in a low amount. Intense blue light (preferably around 415 nm) is better than red light to kill bacteria. High-intensity visible light kills bacteria, while light in the visible and near-infrared region enhances bacterial growth.

In a 2013 article, blue light was used for CA-MRSA (methicillin-resistant *S.aureus*) infections from mouse skin abrasions. The wavelength has been tested in the range of 405-425 nm. Trials were performed on *S.aureus* and HaCat (human keratinocytes). When 170 J/cm² blue light was given, 4,75-log₁₀ bacterial inactivation was observed in CA-MRSA and 0,29-log₁₀ bacterial inactivation was observed in HaCaT. The given light was observed in two ways, for 30 minutes and for 24 hours. Bacterial proliferation was again observed in mouse wounds receiving daylight 24 hours after blue light therapy [5].

A study on bacteria with a light source in the visible region, it was observed that blue light was more effective on bacteria than red light [6].

One study mentioned that ultraviolet rays have lethal effects on bacteria, fungi, viruses, spores and cells. It has been emphasized that UV-rays, other than lethal effects, also mutagenically acted on microbes while proteins, especially nucleic acids, easily absorbed these rays and as a result, created the formation phenomenon of bonds between thymines located side by side in DNA strands. It is stated that this situation causes protein synthesis and other mechanisms in the bacteria to be disrupted by the structure of DNA and deaths [7].

In another study, eleven types of herbal bacteria, bacterial spores and mold spores were observed to be irradiated with different UV radiation doses of a 222 nm krypton-chloride excimer lamp and a 254 nm mercury lamp under laboratory conditions. Especially, it has been determined that microbes with high UV resistance and those with more effective repair mechanisms are more ineffective with 222 nm excimer lamp. The reason for this may be that low UV fluency mainly affects radiation-sensitive microorganisms with DNA damage; however, it has been stated that protein damage mechanisms at high UV fluency (various) can be held responsible for inactivation [8]. Another study investigated the wavelength and methicillin resistance effect of *Staphylococcus aureus* (MRSA) intensity on the bactericidal effect of 405 and 470 nm light. Irradiation at both wavelengths has been reported to reduce bacterial colonies at any intensity [9].

The reason why we chose *Escherichia coli* and *Staphylococcus aureus* microorganisms in our study is that they cause many respiratory, intestinal and abdominal diseases and can be found in many environments [10-15].

The most important species in the genus *Escherichia* is *Escherichia coli*. The width of *E.coli* in the form of bacillus is higher than its length. *E. coli* was first discovered in 1885 by Theodor Escherich. Previously, these microorganisms were known as the *Bacterium coli commune* then *Escherichia coli* was named. These bacteria are the most common species that cause disease in humans and cause serious intestinal infections in humans. *E. coli* is an opportunistic pathogen for humans. *E. coli* has become the most studied model organism for understanding bacterial biology in general. *E. coli* is the most common species found in the large intestinal flora. It is also responsible for many bacterial infections. It forms urinary tract infections, intestinal infections and parenteral infections (pneumonia, meningitis, bacteremia) [16-19].

Staphylococcus aureus, one of the subjects of the study, is a bacterium that causes many infections, especially in humans. They are very common in nature because they are resistant to environmental conditions. The source of pathogenic staphylococci that infect humans is humans. These bacteria are mostly found in the nasal and throat cavities, human and animal feces, abscessed wounds and acne on the skin. They are also commonly found in food for hospital personnel and hospital settings, and in food facilities. Nasal staphylococci become dangerous by spreading around with carriers. Especially those who are carriers in the food industry and prepare food with their own hands are important sources of staphylococcal food poisoning [20, 21].

The way to destroy such bacteria is light sources. 254 nm and 365 nm light sources are light sources close to the UV region. When you look at it with the naked eye, especially when you look at 254 nm light, it may pose a health risk. However, the 460 nm visible light source does not pose a health risk. In this case, by applying it to local infection areas in the human body, the

reproductive or colony-forming effects of bacteria can be reduced.

This study aims to prevent the growth and proliferation of two different bacterial species (*Escherichia coli* and *Staphylococcus aureus*) by weakening their resistance with rays of different wavelengths. Therefore, it is thought that by reducing the risk of infection with these two bacteria that cause respiratory tract infections, people's use of medication will be minimized and the treatment process will be shortened.

2. Material and Method

2.1. Material

In this study, microorganisms of *Staphylococcus aureus* and *Escherichia coli* were used. Nutrient Broth was used as the liquid medium (growth medium). TSA (Tryptone Soy Agar) was used as a solid medium. FTS (physiological saline, 0.9 g NaCl) was used for dilutions. The light was given separately at wavelengths of 254-365-460 nm. Growth and results of microorganisms exposed to the light of different wavelengths were examined. The microorganisms we used in our project and 254-365 nm wavelength light sources were obtained from the Ege University biochemistry department and the 460 nm light source was obtained from the Nuclear Sciences Institute Thermoluminescence Laboratory at the same university. All experiments were done and evaluated in Biochemistry laboratories.

2.2. Method (preliminary trial)

S. aureus and *E. coli* strains were each inoculated into 25 mL of Nutrient Medium in 100 mL volume bottles and incubated for 24 hours at 37°C with a stirring speed of 150 rpm. After the incubation, 1000 µL of the cells produced was taken for the control group and inoculated into the empty petri dish. Then, TSA was poured on it (pour plate method) and left to freeze, stirring gently for homogeneous distribution. Frozen agar petri dishes were allowed to incubate at room temperature (25°C) for 24 h. For the sample group, 500 µL of cells were inoculated separately from each of the growth media into the tube containing 4.5 mL of FTS (physiological saline).

They formed a vortex and became homogeneous. The resulting cells were considered diluted to 10^{-1} . Then, 500 μL of these cells was taken and inoculated into the tube again with 4.5 mL of FTS. Vortex was performed. 500 μL of the resulting 10^{-2} diluted cells was taken and re-inoculated into the tube containing 4.5 mL FTS. Vortex was performed. This procedure was repeated until a 10^{-6} dilution was obtained. Then, the cast plate method was applied 3 times for 3 types of wavelengths from cells diluted 10^{-5} and 10^{-6} . As applied to the control group, 1000 μL of diluted cells were inoculated into empty petri dishes, TSA was poured on them, and the petri dishes were shaken gently to ensure homogeneous distribution of the cells in the agar. The planted agars were stored for freezing. The petri dishes were then left closed for 24 hours under light set at the specified wavelengths (Figure 1 and Figure 2).

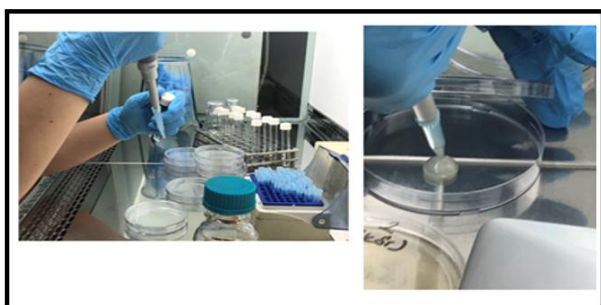


Figure 1. Taking bacteria into petri dishes

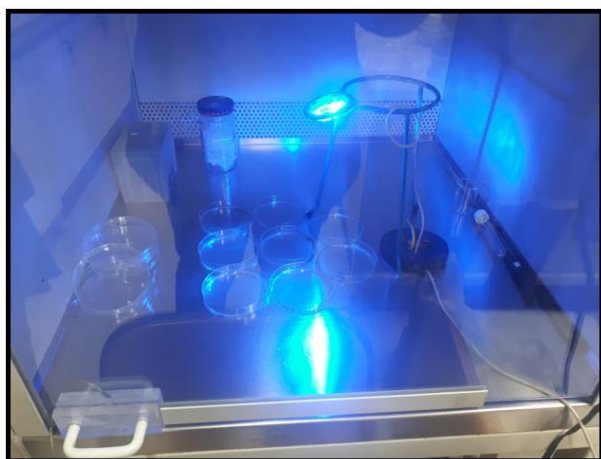


Figure 2. Blue light source with 460 nm wavelength used in experiments (petri and light distance:20cm)

S. aureus and *E. coli* strains were inoculated in 25 mL Nutrient Broth in 100 mL volumes of flasks and incubated for 24 hours at 37°C 150 rpm mixing speed. After incubation, 500 μL of

cells were inoculated into each tube containing 4.5 mL FTS (physiological saline), separately from each of the reproductive environments. By making a vortex, they became homogeneous. The diluted cells obtained continued to be diluted until their optical density (cell density-OD) was 0.5. Cells with an OD of 0.5 were considered the original cell. Then, 500 μL of these cells were taken and again inoculated into the tube with 4.5 mL FTS. Vortex was performed. The cells obtained were considered as 10^{-1} . 500 μL was taken from these cells again and again inoculated into a tube containing 4.5 mL of FTS. Vortex was performed. The cells obtained were considered as 10^{-2} . This procedure was repeated in the same manner until 10^{-6} dilution was achieved. Then, spread plate method was applied 3 times for 3 kinds of wavelengths from 10^{-4} , 10^{-5} and 10^{-6} diluted cells. 100 μL of diluted cells were previously inoculated into frozen petri dishes by pouring TSA and the cells were spread on the surface with a drigalski spatula. Petri dishes with cell transplantation were left open for 24 hours under the light set at the specified wavelengths. Without any dilution (10^{-4} , 10^{-5} , 10^{-6}) for the control group, sowing was done by spread plate method and left for 24 hours incubation at room temperature (25°C).

3. Results

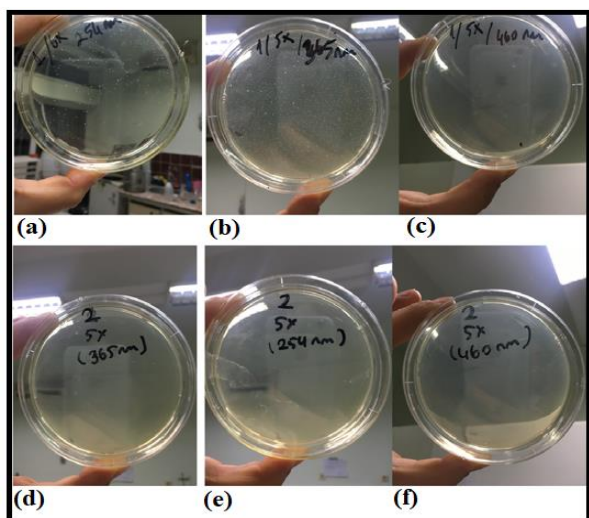
When the microorganisms were exposed UV and blue lights for 24 hours, the number of colonies decreased. However, the number of colonies was never seen in both microorganisms exposed to 460 nm light in the visible region.

3.1. Result (preliminary trial)

Decrease in the number of colonies was observed as also seen in Table 1. Colony numbers were calculated and evaluated from the number of white dots in Petri dishes (Figure3). But the effect of 460 nm wavelength blue light gave very good results in both bacteria. It completely prevented the formation of colonies and was observed to disappear.

Table 1. Colony numbers of microorganisms exposed to different wavelengths of light for 24 hours

Microorganism	Colony Number		
	254 nm	365 nm	460 nm
<i>S.aureus</i> (10^{-5})	13	3	0
<i>S.aureus</i> (10^{-6})	0	0	0
<i>E.coli</i> (10^{-5})	~210	~2560	0
<i>E.coli</i> (10^{-6})	~1840	~432	0

**Figure 3.** Bacterial colonies (a,b,c: *E.coli*; d,e,f: *S.Aureus*) seen under the influence of three different wavelengths

3.2. Results (2nd trial)

Reproduction of *E. coli* stopped completely at 254 nm (Table 2). *E. coli* generation time is 20 minutes.

Table 2. *E. coli* colonies exposed to three different wavelengths of light for 24 hours

Wavelength (<i>E.coli</i>)	10^{-4}	10^{-5}	10^{-6}
254 nm	None	None	None
365 nm	pireferasyon	60	6
460 nm	pireferasyon	117	12
Control	pireferasyon	136	14

If there were 60 growths for 136 control at 365 nm, according to the results, the number of bacteria growing was found to be 44%. The same calculation was done for 460 nm. There was

86% growth, 14% growth was prevented. Calculations were made for *S. aureus* based on the results of the first trial. *S. aureus* generation time is 30 minutes.

Table 3. *S. aureus* colonies exposed to three different wavelengths of light for 24 hours

Wavelength (<i>S. aureus</i>)	10^{-5}	10^{-6}
254	13	None
365	3	None
460	None	None

S. aureus reproduction completely stopped at 460 nm. At 254 nm, there was a 14% growth, 86% growth was prevented. There was 3% growth in 365nm, 97% growth was prevented (Table 3).

4. Conclusion and Discussion

When we look at the first trial results of the study in general, light sources with 3 different wavelengths (254 nm, 365 nm and 460 nm) were used. While a significant decrease in colony numbers was observed under the operating condition of 254 nm and 365 nm wavelength lights falling in the UV region, no colonies were observed in the 460 nm wavelength light (Table 1 and Figure 3). In the second trial results, 44% growth was achieved at 365 nm and 56% growth was inhibited. *S. aureus* growth stopped completely at 460 nm. At 254 nm, 14% growth was achieved, 86% growth was inhibited. At 365 nm there was 3% growth, 97% growth was inhibited.

As seen from the results, no significant bacterial growth was observed at 460 nm. In our literature studies, it can be seen that no study has been done at this wavelength before. In other studies, some results were obtained with visible light sources, but a decrease in colony reproduction was observed without destruction. A study stated that the effect of blue light is better than other lights [5].

Another study observed that wavelength of *Staphylococcus aureus* (MRSA) intensity and methicillin resistance irradiation at 405 and 470 nm reduced bacterial colonies at any intensity [9].

In one study, it was stated that a pressurized mercury vapor lamp was used in the treatment of the disease by destroying the DNA component of bacteria and viruses at a wavelength of 254 nm [22].

In our study, the effect of 460 nm light source on these bacteria is relatively high. In addition, the light source in the visible region does not cause much damage to normal human cells. In some cases, high-intensity visible light kills bacteria, while visible and near-infrared light increases bacterial growth.

As a result, it is important to evaluate the use of the 460 nm light source in visible areas where this type of bacteria is found, both in sterilization and in the treatment of local infections, and also in the examination and treatment of the new type of coronavirus. and the precautions to be taken.

4.1. Suggestions

For the purpose of our study, the effects of visible wavelength light on bacteria, especially *E. coli* and *S. aureus*, were examined and compared with other light sources close to UV regions. The 460 nm wavelength light source has been shown to be more effective on two types of bacteria. These two types of bacteria are extremely risky bacteria that threaten human health. Antibiotic treatment against them also negatively affects other beneficial bacteria in the body. It especially causes local throat infection. Therefore, it increases the possibility of using blue light with a wavelength of 460 nm against *S. aureus*. In the first stage of the treatment, thanks to the blue light source (460 nm) device, the reproduction of this bacterium, which first settles in the throat and mixes with the blood and causes infection, can be stopped. If the initial infection that occurs at the beginning of the human upper respiratory tract is eliminated, the treatment process will be shorter and the patient will recover more quickly. Additionally, such bacteria can cause skin infection. Especially the 460 nm wavelength light source we apply to these places can help us minimize infection. Infections in the body can then be eliminated by using low doses of antibiotics. In addition, the environments in the hospital environment can be purified from these bacteria and viruses by creating a sterile environment by using lights at these wavelengths. It is important to clean

environments where the risk of infection may occur and to prevent the spread. Evaluating and applying such alternative methods in the fight against viruses in future studies will benefit new treatment methods.

Article Information Form

Acknowledgments

The authors would like to thank Ege University Department of Biochemistry and Associate Professor Alper AKKAYA, whose laboratories we used in this study.

Funding

The author (s) has no received any financial support for the research, authorship or publication of this study.

The Declaration of Conflict of Interest/ Common Interest

No conflict of interest or common interest has been declared by the authors.

The Declaration of Ethics Committee Approval

This study does not require ethics committee permission or any special permission.

The Declaration of Research and Publication Ethics

The authors of the paper declare that they comply with the scientific, ethical and quotation rules of SAUJS in all processes of the paper and that they do not make any falsification on the data collected. In addition, they declare that Sakarya University Journal of Science and its editorial board have no responsibility for any ethical violations that may be encountered, and that this study has not been evaluated in any academic publication environment other than Sakarya University Journal of Science.

Copyright Statement

Authors own the copyright of their work published in the journal and their work is published under the CC BY-NC 4.0 license.

References

- [1] S. Singha, R. Thomas, J. N. Viswakarma, V. K. Gupta, "Foodborne illnesses of *Escherichia coli* O157 origin and its control

- measures” *Journal of Food Science and Technology*, Vol. 60, no. 4), pp. 1274-1283, 2023.
- [2] Y. Wang, K. Fu, “Genotoxins: The Mechanistic Links between *Escherichia coli* and Colorectal Cancer” *Cancers*, vol. 15(, no. 4, p. 1152, 2023.
- [3] C. dos Anjos, L. G. Leanse, M. S. Ribeiro, F. P. Sellera, M. Dropa, V. E. Arana-Chavez, N. Lincopan, M. S. Baptista, F. C. Pogliani, T. Dai, C. P. Sabino, “New Insights into the Bacterial Targets of Antimicrobial Blue Light” *Microbiology Spectrum*, Vol.11, no. 2, 2023.
- [4] N. Özkütük, *Use of Ultraviolet Lamps*, 5th National Sterilization Disinfection Congress, Antalya, Turkey, 2007.
- [5] T. Dai, A. Gupta, Y. Huang, M.E. Sherwood, C.K. Murray, T. Kiellan, and M. R. Hamblin, “Blue Light Eliminates Community-Acquired Methicillin-Resistant *Staphylococcus aureus* in Infected Mouse Skin Abrasions”, *Photomedicine and Laser Surgery*, Vol.31, p.11, 2013.
- [6] R. Lubart, A. Lipovski, Y. Nitzan, And H. A. Friedmann, “Possible Mechanism for The Bactericidal Effect of Visible Light”, *Laser Therapy*, vol. 20, no. 1, pp. 17-22, 2011.
- [7] M. Arda, *Fundamentals of Microbiology*, Second Expanded Edition. Medisan Publication Series No 46, Ankara, 2000.
- [8] M. Clauß, “Higher effectiveness of photoinactivation of bacterial spores, UV resistant vegetative bacteria and mold spores with 222 nm compared to 254 nm wavelength” *Acta Hydrochimica et Hydrobiologica*, vol. 34, pp. 525-532, 2006.
- [9] V.V. Bumah, D.S. Masson-Meyers, S.E. Cashin, C.S. Enwemeka, “Wavelength and bacterial density influence the bactericidal effect of blue light on methicillin-resistant *Staphylococcus aureus* (MRSA)”, *Photomedicine and Laser Surgery*, vol. 31, no. 11, pp. 547-553, 2013.
- [10] YQ. Li, Q. Han, JL. Feng, WL. Tian, HZ. Mo, “Antibacterial characteristics and mechanisms of 3-poly-lysine against *Escherichia coli* and *Staphylococcus aureus*”, *Food Control*, vol. 43, pp. 22-27, 2014.
- [11] Y. Zhang, X. Liu, Y. Wang, P. Jiang, SY. Quek, “Antibacterial activity and mechanism of cinnamon essential oil against *Escherichia coli* and *Staphylococcus aureus*”, *Food Control*, vol. 59, pp. 282-289, 2016.
- [12] D.A. Phoenix, Z. Sayed, S. Hussain, F. Harris, M. Wainwright, “The phototoxicity of phenothiazinium derivatives against *Escherichia coli* and *Staphylococcus aureus*”, *FEMS Immunology and Medical Microbiology*, vol. 39, pp. 17-22, 2003.
- [13] C.L. Fischer, K.S. Walters, D.R. Drake, D.R. Blanchette, D.V. Dawson, K.A. Brogden, P.W. Wertz, “Sphingoid Bases Are Taken Up by *Escherichia coli* and *Staphylococcus aureus* and Induce Ultrastructural Damage”, *Skin Pharmacol Physiol*, vol. 26, pp. 36-44, 2013.
- [14] K.J. Williams, L. J. Piddock, “Accumulation of rifampicin by *Escherichia coli* and *Staphylococcus aureus*”, *Journal of Antimicrobial Chemotherapy*, vol. 42, pp. 597-603, 1998.
- [15] J. C. Lopez-Romero, H. González-Ríos, A. Borges, M. Simões, “Antibacterial Effects and Mode of Action of Selected Essential Oils Components against *Escherichia coli* and *Staphylococcus aureus*”, *Hindawi Publishing Corporation Evidence-Based Complementary and Alternative Medicine*, vol. 2015, pp. 9, 2015.
- [16] N. Turgut, “Investigation of the Presence of *E.Coli* O157-H7 in Lettuce Served for

Consumption in Aydın Province, Adnan Menderes University Health Sciences Institute, Department of Microbiology, Doctoral Thesis, 2015.

- [17] D. Douglas Bannerman, Max J. Paape, Jai-Wei Lee, Xin Zhao, Jayne C. Hope, Pascal Rainard, “*Escherichia coli* and *Staphylococcus aureus* Elicit Differential Innate Immune Responses following Intramammary Infection”, *Clinical and Diagnostic Laboratory Immunology*, vol. 11, no. 3, pp. 463-472, 2004
- [18] F. Blanche, B. Cameron, F. X. Bernard, L. Maton, B. Manse, L. Ferrero, N. Ratet, C. Lecqo, A. Goniot, D. Bisch, J. Crouzet, “Differential Behaviors of *Staphylococcus aureus* and *Escherichia coli* Type II DNA Topoisomerases”, *Antimicrobial Agents and Chemotherapy*, vol. 40, no. 12, 2714-2720 pp. 2714–2720, 1996.
- [19] Q. L. Feng, J. Wu, G. Q. Chen, F. Z. Cui, T. N. Kim, J. O. Kim, “A mechanistic study of the antibacterial effect of silver ions on *Escherichia coli* and *Staphylococcus aureus*”, *Journal of biomedical materials research*, vol. 52, no. 4, pp. 662-668. 2000.
- [20] U. R. Pothakamury, A. Monsalve-Gonzalez, G. V. Barbosa-Cobas and B. G. Swanson, Inactivation of *Escherichia coli* and *Staphylococcus aureus* in model foods by pulsed electric field technology, *Food Research International*, vol. 28, no. 2, pp. 167-171, 1995.
- [21] A. Gulbandilar, ‘Investigation of *Staphylococcus Aureus* Carriage and Antibiotic Susceptibility in Nasal Mucosa in Kütahya Region', *Dumlupınar University Journal of Science*, no.18, pp. 1-6, 2009.
- [22] P. Boyce, *Controlling Tuberculosis Transmission with Ultraviolet Irradiation*, Lighting Research Center Publications, 2007.

An Analysis of Tiny Houses through a Viewpoint on Preferences, Satisfaction, and Expectations of Residents

Miray Gür* , Elif Çay 

Bursa Uludag University Faculty of Architecture Department of Architecture, Bursa, Türkiye, miraygur@uludag.edu.tr, elifsanturkay@gmail.com

* Corresponding author

ARTICLE INFO

ABSTRACT

Keywords:
Tiny house
User satisfaction
User preferences
Residential satisfaction
Housing satisfaction
Housing design

In recent years, there has been a significant increase in the prevalence of tiny houses, reflecting the worldwide trend of this favored living option. Scientific study on tiny houses has experienced a modest global growth in recent years, even though the notion of tiny houses has only been lately introduced to Turkish literature. Information on tiny houses is mostly available through various media channels, including television, newspapers, magazines, and social media platforms, in our country. This article seeks to examine the concept and current popularity of tiny houses, while also assessing user preferences and levels of satisfaction. User satisfaction was evaluated based on data obtained from twenty interviews conducted with owners of small-scale dwellings. The primary results suggest that individuals who exhibit a preference for residing in tiny houses have an awareness of the disparities and challenges they are likely to face. The appealing qualities of the house extends beyond its physical appearance. The mere existence of a location, regardless of its size, situated in a calm and peaceful environment, far from chaos and confusion, where individuals have a sense of belonging, is enough to satisfy their needs.

Article History:
Received: 03.04.2024
Accepted: 09.08.2024
Online Available: 14.10.2024

1. Introduction

Throughout the course of history, individuals have utilized various forms of dwellings for habitation. The Tiny House Movement has emerged as a lifestyle option for individuals that favor minimalism, cost-efficiency, and environmental sustainability when it comes to their housing preferences. The movement originated with the establishment of the Tumbleweed Tiny House company in the United States in 2002 [1], and subsequently spread to Europe and Australia in response to the economic crisis in 2008. The transmission originated in our nation subsequent to the 2019 Covid outbreak [2]. The tiny house movement is a housing trend that is popular among those who want to shift from living in metropolitan apartments. Given their affordable availability, adaptability for temporary housing requirements, and capacity to

address disasters, the concept of living in tiny houses is becoming more attractive under present conditions [3]. Small houses garnered substantial attention in the aftermath of Hurricane Katrina in the United States [4]. After the earthquake on February 6, 2023, a housing community called 'Örnek Evler' was established in Hatay to accommodate survivors. This initiative was announced through social media [5].

Despite the rise in popularity of tiny houses, scientific research on the topic has not seen a corresponding growth. In the United States and Australia, the tiny house movement lacks scholarly research [4, 6-8]. Mutter (2013) observed a scarcity of scholarly studies on tiny houses. In his study, he conducted interviews with participants to inquire about their motivations, problems, and growth potential [1]. Furthermore, it is suggested that a bigger sample

size should be used when examining the motivations for choosing to live in tiny houses [7]. Wilson and Wadham's study revealed that the growing popularity of tiny houses is a multifaceted reaction to current economic challenges faced by individuals and society as a whole, serving as both a lifestyle choice and a practical solution. The tiny house movement symbolizes a community uniting on a small scale in opposition to the larger real estate industry [9].

The majority of research on tiny dwellings pertains to legal regulations [2]. Some of the research has focused on areas such as the potential of tiny houses to meet the housing needs of the homeless, the evaluation of their environmental impact, their integration into variable contexts in terms of urban planning, and the main motivations for living in tiny houses [10, 11]. Mangold and Zschau (2019) conducted study on the factors influencing the adoption of the tiny house lifestyle. The research contends that living in a compact house is a positive lifestyle based on user interviews [8]. A different study on tiny houses focuses on those opting for a minimalist lifestyle [12].

In a study conducted by Çizmecioglu and Tanriverdi Kaya (2022), it was concluded that the main theme of international publications on tiny houses is the main motivations of the users [2]. People living in tiny houses have motivations such as living a simpler life [8], being financially secure [13], and having better sharing with close people such as family and friends [14]. There is a limited number of academic publications on tiny dwellings in our country, and scientific study on living in tiny houses is scarce. Conversely, there has been a rise in the number of enterprises specializing in designing and manufacturing tiny dwellings in recent years.

Architects and engineers specializing in tiny house design and construction assert that tiny houses are ideal for individuals seeking to circumvent financial obligations including construction expenses, building permits, land assessments, taxes, and administrative charges. Tiny dwellings are also created with customized designs simultaneously [15, 16]. In order to understand which design factors are effective in

the widespread use of tiny houses, research needs to be concentrated in this field.

This research aims to investigate the increasing demand for tiny houses and the associated lifestyle in recent years. It will focus on identifying the specific user demographics, geographic locations, factors influencing their preferences, and their levels of satisfaction. The study aims to explore the motivations behind individuals who choose to live in tiny houses and their level of contentment with this lifestyle. To achieve this goal, in-depth interviews will be conducted with consumers to gain insight into their impressions of the tiny house, variables influencing their preferences, and satisfaction levels.

2. The Emergence and Development of the Concept of the Tiny House

Providing shelter, which is a basic biological need, resulted in the development of secure enclosed spaces in a straightforward manner many years ago. The original structures constructed to offer shelter might be regarded as the fundamental basis of the tiny house concept. This section explores the notion of tiny houses, which originated in the USA as part of the "Tiny House Movement." It delves into textual sources by architects and designers considered foundational to the movement and the evolution of tiny house designs.

2.1. The tiny house movement and the global development of tiny houses

The Tiny House Movement is a developing culture embraced by individuals who choose to simplify their living, prioritize personal freedom, and make their lives easier [17]. The origins of the concept of 'Tiny House', which has become increasingly recognized by the public in recent years, date back to the 19th century romanticism of Thoreau and Emerson [18]. In the book "Walden" written by Henry David Thoreau in the 1850s, the concept of a tiny house is expressed as a self-sufficient life that makes it easier to own a house by building a tiny house [19]. Frank Lloyd Wright's book "The Natural House," published in 1950, was influential in shaping the notion and lifestyle of living in tiny houses. Frank Lloyd

Wright outlines an ideal scenario of small, one-story, cost-effective homes constructed from natural materials in what he terms the "Usonian Dream," aligning with the concept of tiny houses. Following that, the houses designed by Wright were built and gained popularity among middle-class inhabitants [20].

Le Corbusier was an architect renowned for his designs of compact dwellings. Corbusier's encounters with restricted spaces throughout his travels motivated him to integrate these small living arrangements into his architectural designs. The architect built a little house called Le Cabanon, with dimensions of 3.66 m × 3.66 m, using architectural principles derived from careful observation and experimentation [21]. Lloyd Kahn, a writer, photographer, and architect, published the book "Shelter" in 1973, followed by "Home Work: Handbuilt Shelter" in 2004, which, along with his other works, played a vital role in popularizing the tiny house movement [22].

The widespread prominence of the tiny house concept has been impacted by the 1987 book "Tiny Houses" authored by renowned architect Lester Walker. [23]. Sarah Susanka, an American individual whose spouse is also an architect, is a key figure in popularizing the modern version of the tiny house movement. Furthermore, they have resided in a compact yet highly functional dwelling that they built themselves. In 1998, Susanka wrote a book called "The Not So Big House, A Blueprint for the Way We Really Live," which specifically Explorer the concept of tiny houses [22].

In 1999, Jay Shafer, a well-known advocate of the Tiny House Movement, published his first book on the subject, titled "The Small House Book". In 2000, he established the "TumbleweedTiny House Company" to create and produce "tiny houses" [22]. The notion of tiny houses has garnered worldwide acclaim through television programs, social media videos, documentaries, and several other media outlets [3, 4].

2.2. The beginning and development of tiny houses in Türkiye

Architects and designers enthusiastically adopted the Tiny House Movement and attempted to promote it widely through the release of publications, as shown in its historical record. While Turkey has a plethora of information available on social media on tiny houses, there is a scarcity of published scholarly papers on the subject in the country.

The emergence of tiny houses in Turkey began in 2020, coinciding with the outbreak of the Covid-19 pandemic [2, 24]. However, the widespread adoption of tiny houses in Turkey did not start with architects or designers embracing this idea. Instead, it spread by the increasing number of tiny house manufacturers and the recognition of tiny houses as an alternative for individuals who were unable to relocate from their homes during the pandemic.

3. Materials and Methods

A tiny house is typically defined as a residential unit that is smaller than 37 m², although there is no universally accepted standard definition. Tiny dwellings range in size from 6 to 37 square meters [1]. Typically, these houses consist of a kitchen, living space, sleeping area, and bathroom [25]. According to Jay Shafer, a tiny house is characterized by the adequate utilization of its available space rather than its size [26].

The growing popularity of tiny houses in our country has prompted the evaluation of whether customer expectations are being satisfied by using the obtained experiences. There is a scarcity of research studies, such as surveys and interviews, on tiny houses in the literature. The purpose of this study is to cast light on the preferences and levels of satisfaction of individuals who have previously adopted this way of life. The methodology employed in this study involves conducting interviews with individuals living in tiny houses. The initial phase of the research entailed conducting a literature review pertaining to the notion of a tiny house.

The city of Bursa was selected for the case study because of the recent rise in immigration rates, challenges in locating housing due to increased population density, and the subsequent preference for tiny residences. Interviews were conducted in the Alaaddinbey Neighborhood of Nilüfer District in Bursa Province because of its close proximity to the city center and the existence of densely populated residential areas. A series of interviews were conducted with 20 individuals who own tiny houses in the area. The purpose was to assess their levels of satisfaction and determine the factors influencing their desire for these dwellings. This analysis was based on the data acquired from their responses. Based on the research results, assessments were conducted about housing preferences and utilization. The insights will also be beneficial for designers and novice users.

3.1. Reasons why people living in tiny houses in Bursa prefer this lifestyle and their satisfaction levels

A set of interview questions were formulated in response to the literature review that was essential for measuring the level of satisfaction among individuals who have lived in tiny houses. Various sources on the development of tiny houses were used to explore factors affecting satisfaction and preferences due to the limited regional research on tiny house satisfaction and the need to compare with international sources [1, 8, 11]. The survey questions in master theses and papers analyzing user satisfaction in housing were taken as references [7, 27-29]. Interview questions were prepared together with the questions that examined area-specific dynamics in the context of the analyzed researches.

The questions were formulated in a manner that allowed individuals to assess their experiences pertaining to this particular way of living. Some of the questions were closed-ended, and although options were given in these questions, the opportunity to answer freely was also provided. In the preparation of the interview form, it is aimed to reveal the profile of tiny house users and to determine some criteria that feed this profile. In this context, the questions were prepared in a way to examine the reason for the users' preference for this lifestyle, the way of use,

physical, environmental and social dimensions as well as their experiences. In some questions, more than one option could be selected. As a result of the interviews with the manufacturer companies that sell tiny houses, it was concluded that these houses are more concentrated in Nilüfer district compared to other districts. The Alaaddinbey Neighborhood in Nilüfer District was chosen as the study area because it is a neighborhood with a high density of tiny houses. The findings obtained as a result of the interviews are presented in the next section.

4. Findings and Discussion

Following a predetermined set of interview questions, we conducted interviews with residents of the Alaaddinbey Neighborhood in the Nilüfer District of Bursa Province who chose to live in tiny houses. Table 1 presents the demographic characteristics of the participants.

The findings of the study indicate that 9 of the 20 participants fall within the age range of 35 to 44 years, 5 of them are 55 years or older, and 4 of them are 45 to 54 years of age. The age group with the fewest participants is 25-34, consisting of only 2 individuals. There were 11 male participants and 9 female ones. In relation to the participants' educational attainment, it is as follows: 8 hold a bachelor's degree, 6 have completed primary school, 4 have completed secondary school, and 2 have completed postgraduate studies. 2 of the participants are unmarried, while 18 are married. Out of the participants, 10 are self-employed, 6 are retired, and 4 are employed full-time. Out of the participants, 8 individuals have a monthly household income ranging from 30,000 TL to 40,000 TL, whilst 6 participants have a monthly income below 10,000 TL. Two participants have incomes ranging from 10,000TL to 20,000TL, two participants have from 20,000TL to 30,000TL, and two participants have incomes ranging from 40,000TL to 50,000TL. As indicated in Table 1, users with diverse demographic profiles demonstrate a preference for tiny houses [4].

Table 1. Demographic information of participants

Variable	Group	n	%
Gender	Female	9	45
	Male	11	55
Age	18<		
	18-24		
	25-34	2	10
	35-44	9	45
	45-54	4	20
	55>	5	25
Education	Primary education	6	30
	High School	4	20
	University	8	40
	Postgraduate	2	10
Marital Status	Single	2	10
	Married	18	90
	Divorced		
	Widow		
Job Status	Full time	4	20
	Part-time		
	Unemployed		
	Self-employment	10	50
	Housewife		
	Student		
	Retired	6	30
Household Income	10.000TL<	6	30
	10.000TL-20.000TL	2	10
	20.000TL-30.000TL	2	10
	30.000TL-40.000TL	8	40
	40.000TL-50.000TL	2	10
	50.000TL		
	50.000TL>		

Based on the statistics, it can be concluded that the preference for tiny dwellings and this lifestyle is primarily observed among middle-aged and older individuals who have greater levels of education, are either employed or retired, and are married. The presence of low-income customers who are able to obtain tiny houses supports the finding that tiny houses can serve as an appealing and affordable dwelling option [28, 29]. Thus, it may be asserted that couples with demanding work schedules prefer for this lifestyle for the purpose of getting away their professional commitments.

Table 2. Preference reason and usage duration of tiny house

Variable	Group	n	%
Location	Close to the city center	16	80
	Near the mountain		
	Close to the Sea		
	Village Center	2	10
Reasons for choosing to live in a tiny house	Village	2	10
	Spending time in nature	20	100
	A more minimalist life	2	10
	No zoning permit required	2	10
	Economical	2	10
	Providing the possibility to move the dwelling		
	A healthy life	2	10
Frequency of use of the tiny house	Grandchildren	1	5
	Continuous	2	10
	Weekends	12	60
	Periodic	6	30
Reason for not living permanently	Distance to work		
	Not comfortable enough		
	Having another house that is lived in permanently, using this house as a secondary house for seasonal/weekend vacations	18	90
	Lack of electricity	2	10
	1 year <	9	45
	1-3 year	5	25
Time to experience the tiny house	3-5 year		
	5 year >	6	30
Time spent indoors during the day outside sleep time	1-2 hour	15	75
	2-5 hour	3	15
	5 hour >	2	10
	Full day		
Time spent in the patio or garden of the tiny house	2 hour <	3	15
	2-5 hour	11	55
	5 hour >	6	30

Table 2 presents the reasons for preferring a compact dwelling and the length of time it is used. Based on the data presented in the table, 16 participants indicated that their tiny houses were located near the city center, whereas 4 participants mentioned that their houses were located in the village. When queried about their motivations for choosing to reside in a tiny house, all respondents unanimously cited their desire to spend time in and engage with nature.

This situation supports prior research [1, 11, 14]. A more minimalist life, not requiring a zoning permit, being economical, spending time with grandchildren, and maintaining a healthy life each have a share of 2 people. Twelve of the participants stated that they live in this house on weekends, 2 live here permanently and 6 live here periodically. When those who do not live in this house permanently were asked why, 18 of the participants stated that they have another house where they live permanently and 2 of them stated that they could not stay in this house due to lack of electricity.

All the data shows that the middle and older age group prefer these houses and lifestyle for physical and mental rest. The fact that 90% of the users prefer tiny houses on weekends or periodically in the summer months supports the fact that these houses are preferred for spending time with the family in nature and resting. The fact that the tiny houses of the participants are located close to the city center plays an advantageous role in terms of transportation so that they can be used on weekends or only during certain weeks. When asked about the duration of their residence in a tiny house, 9 respondents indicated a period of less than 1 year, 5 respondents indicated a period of 1-3 years, and 6 respondents indicated a period exceeding 5 years. This scenario demonstrates the prevalence of this way of life, particularly following the outbreak of the Covid-19 pandemic and the occurrence of the earthquake tragedy in February 2023 [30].

When the time spent of the participants indoors during the day was analyzed, 15 of them stated that they spent 1-2 hours outside of sleep time. 3 of them stated between 2-5 hours and 2 of them stated more than 5 hours. As for the time spent in the patio or garden of the tiny house, 11 of the participants spent between 2-5 hours, 3 of them spent less than 2 hours and 6 of them spent more than 5 hours. The fact that the users predominantly spend time outdoors supports the reasons for tiny house preferences such as spending time in nature, experiencing the outdoors, and living a minimalist life [11]. Table 3 presents the physical characteristics of the tiny houses as reported by the participants. The number of participants who did not

participate to the design process of their tiny house is 4. Due to the vast range of difficulties such as structure material selection and furniture design in mobile houses, the production methods have also become more varied. Although there are legal restrictions on production, there are many specialized industrial production companies [31]. Several tiny house production companies in Bursa were also surveyed, and it was determined that tiny houses are often manufactured with a standardized structure. However, modifications can be made to accommodate customer preferences.

Table 3. User opinions regarding tiny house design

Variable	Group	n	%
Participation to the design of the tiny house	No participation	4	20
	Changes made regarding windows	8	40
	Changes have been made regarding furniture	12	60
	Changes have been made to the dimensions	8	40
	Changes made regarding materials	8	40
	Changes made regarding colors	8	40
	Amendment on spatial layout	6	30
	Changes made regarding flexible use		
	Amendment on the flexibility of furniture		
	Whether the tiny house has the interior organization meeting spatial needs compared to apartments with conventional plan typology	Yes, it has	11
	No, it doesn't have	9	45
Whether the interior of the tiny house) is large enough to meet your needs	Yes, it is	10	
	No, it isn't	10	50
Satisfaction with the plan of the tiny house, the layout of the spaces, and the internal volume	Yes, I am satisfied	12	60
	No, I'm not satisfied	8	40
Number of floors of the tiny house	Single storey	13	65
	Two storeys	3	15
	Mezzanine	4	20

8 of the participants made changes in furniture in line with their needs. The number of participants who made changes related to windows, dimensions of the house, materials used and colors is 8 with a rate of 40%. Another question refers to whether tiny dwellings include interior furnishings that satisfy the spatial (functional) criteria in comparison to apartments with a standard floor plan typology. Upon evaluating user opinions regarding this issue, 11 users expressed that it is sufficient, while 9 users expressed that it is not sufficient. Nevertheless, a notable circumstance is that this dwelling category is unsuitable for a permanent residence for a family of four.

Regarding the interior space of the tiny house, some users have expressed concerns about its adequacy in meeting their needs. Specifically, they have mentioned that due to having a significant number of belongings, primarily due to having small children, the tiny house does not provide sufficient storage capacity. Consequently, they find it difficult to constantly carry their belongings. Previous comments indicated that the dwelling should be larger to accommodate a large number of household members. However, it was deemed sufficient for a temporary period based on the specific characteristics of the area and time. When asked about their satisfaction regarding the design, layout, and internal space of the tiny house, the feedback indicated that it was satisfactory. This was because it was not used continuously, it met the required width standards, it created a feeling of being spacious and it effectively fulfilled its intended purpose. When the cross-sectional relationship of the tiny houses is analyzed, it is evident that 13 participants reside in single-storey houses, while 3 live in two-storey houses, and 4 participants have a mezzanine level in their dwellings asserted that waste disposal services are not provided (Table 3).

Table 4 displays the social and environmental statistics related to the participants' tiny dwellings. Upon analyzing the capacity of participants to fulfill their daily requirements while residing in tiny houses, it was found that 11 of them were able to effortlessly meet their daily needs. Eight of them have sufficient storage capacity to last them for the duration of their stay

at home, eliminating the need for additional supplies for an extended period of time. One of them experiences challenges in fulfilling their everyday need (Figures 1,2). Two participants reported that they cultivate and harvest 90% of their vegetables in their garden (Figure 3).



Figures 1-2. Interior views of a tiny house



Figure 3. An image of a tiny house garden

Tiny houses are typically situated in rural locations, which are further distant from urban areas, and characterized by a prevailing natural environment. This could potentially result in security vulnerabilities, particularly during nighttime hours. Upon analyzing the participants' attitudes of security and their need for security measures, it was found that 6 of them reported having fences surrounding their houses. Four individuals reported having security cameras, whereas seven individuals reported not experiencing any security issues. Two participants reported instances of theft during their absence from the residence, but felt secure due to the presence of their dog. The users were observed to propose their own solutions to the security concern. Additionally, these individuals asserted that waste disposal services are not provided.

Table 4. User opinions regarding socio-physical qualities

Variable	Group	n	%
Opportunity to meet daily needs while living in a tiny house	Easily welcomed	11	55
	Stored so that it will not be needed for a long time	8	40
	Changes have been made regarding furniture	12	60
Perception of safety of tiny house	No security issues	7	35
	Surrounded by fence	6	30
	There is a security camera	4	20
	Not safe enough	3	15
Visual and auditory privacy problem	There is		
	None	20	100
Living in a tiny house is suitable for families with children, 5-day routine workers, disabled people and the elderly	Suitable	12	60
	Not suitable	8	40
Electricity in the area of tiny house, GSM, internet connection, base station	There is	14	70
	None	6	30
Social relationships & neighborhood	There are no neighbors around		
	There are neighbors nearby, but not negotiated	4	20
	There are neighbors nearby and under discussion	14	70
	It's a collection of tiny houses living in a settlement	2	10
Comfort conditions of the tiny house	Getting enough daylight	18	90
	Good thermal comfort level	13	65
	Adequate ventilation	18	90
	No problem in hot water supply	8	40
	Adequate lighting	20	100
	Good auditory comfort	14	70
	Solar panels	6	30
Contribution of implementation to sustainability	Compost toilet system		
	Rainwater usage for irrigation		
	Energy with lithium batteries storage	2	10
	Natural materials in the construction of the house	15	75

This assumption was challenged based on the idea that the simultaneous existence of households in tiny houses designed in a single unit with a minimal area and living space would lead to privacy issues. Upon examining the issue of visual and aural privacy in a tiny dwelling, it becomes apparent that the participants do not have any privacy concerns. When questioned about the appropriateness of residing in a tiny house for families with children, individuals who work a 5-day schedule, individuals with disabilities, and the elderly, 12 participants affirmed its acceptability. Upon analyzing the communication infrastructure in the region, including electricity, GSM, internet connection, and base stations, it was found that these services were available in the area where 14 individuals resided.

Out of the respondents, 12 expressed pleasure with the quality of materials used in tiny houses, while 10 expressed satisfaction with the level of workmanship. Out of the total, 8 individuals express dissatisfaction with the caliber of the workforce, while 2 individuals express dissatisfaction with the caliber of the supplies. The level of satisfaction with these parameters is dependent on the firm that developed the program. User pleasure is influenced by the type and quality of materials employed by manufacturers. 6% of respondents indicated that certain areas of the house necessitate regular upkeep due to the natural deterioration of the wooden materials used in construction. Two users specifically mentioned that the kitchen requires maintenance.

When assessing neighborly interactions and frequency, 14 individuals reported having neighbors in close proximity and regularly interacting with them. Four of the participants reported that there are homes in close proximity that they may potentially have as neighbors, but they have not had any interactions with them. Two individuals indicated that they reside in a community comprised of and enjoy highly amicable relationships with their neighbors. An influential component in tiny houses determining the level satisfaction with tiny houses is its pre-use design [32].

When questioned about the satisfaction of the participants regarding the comfort conditions of their tiny houses, all of them expressed contentment with the degree of illumination. Additionally, 18 participants confirmed that they received an adequate amount of daylight and that the ventilation was satisfactory. 13% reported that the thermal comfort and auditory comfort levels were satisfactory. Out of all the participants, only 8 reported having no problems with the hot water supply. Regarding the extent to which the tiny house contributes to sustainability, 15 participants indicated that the house was constructed using natural materials (Figure 4). Out of the total, six individuals have the capability to get hot water through the utilization of solar panels, while two individuals possess the ability to store energy using lithium batteries. Regarding the adequacy of the storage space in the tiny house, two individuals expressed that it is insufficient, while two others indicated that it is small.



Figure 4. An image of a wooden tiny house bedroom

Table 5 presents the participants’ satisfaction levels with their experiences of living in a tiny house. Eleven individuals reported that they embraced this lifestyle. Out of the 5 individuals, it was reported that they were unable to adapt to the lifestyle provided by the little house. Additionally, 2 individuals expressed their inability to reside in the tiny house on a long-term basis, while another 2 individuals mentioned their reluctance to stay during the winter season. Living permanently in a tiny house presents challenges in terms of adapting routines acquired from larger houses. Living in a compact house during winter is less desirable compared to summer since the usage of the garden is limited.

Table 5. Participants’ satisfaction levels with their experiences of living in a tiny house.

Variable	Group	n	%
Belonging to tiny house life	I’m embraced it very much	11	55
	I couldn’t quite used to	5	25
	I’m having difficulty	2	10
	I guess I can’t stay forever	2	10
Positive aspects of living in a tiny house	Intertwined with nature	16	80
	Ecological life	2	10
	Calm	7	35
	Tranquility	4	20
	Being away from the city	5	25
	Healthy lifestyle	2	10
	Away from noise	3	15
	Everything is easy to access	2	10
Negative aspects of living in a tiny house	Small	2	10
	Security problem	2	10
	Energy shortage	5	25
	Transportation difficulty	6	30
	Pest problem	3	15
	None	2	10
Parts of the tiny house that you regret and want to change as you use them	None	15	75
	The solar energy system must be large	3	15
	The terrace can be covered	1	5
	Can be fireplace	1	5

When asked about the three favorable characteristics of residing in a tiny house, the predominant user replies were as follows: Embracing a symbiotic relationship with nature, leading an ecologically conscious lifestyle, enjoying peace and serenity, reducing stress levels, engaging in gardening and cultivating a connection with the earth, seeking solace away from urban environment [33], good health, cultivating fruits and vegetables through gardening, a peaceful setting away from noise, a natural surrounding, convenient access to amenities, and a spacious garden area. Additionally, it should be noted that tiny houses offer a financially efficient housing option [25].

The primary concerns expressed by users regarding the drawbacks of residing in a tiny house include limited space, absence of a security system, energy issues, water supply interruptions, pump malfunctions, electricity

shortages, transportation challenges, waste management, commuting difficulties, presence of insects and snakes, and limited access to public transportation.

When asked about the aspects of the tiny house that they feel regretful about and wish to modify when they utilize it, the user's responses are notable: A solar energy system with increased capacity, elevated floor height, a sheltered terrace, and a fireplace. The predominant user comments, when queried about additional suggestions, included the need for an expanded garden space to accommodate dense populations and the desire for a more secure atmosphere.

5. Conclusion

This study involved conducting interviews with 20 residents of tiny houses in the Alaaddinbey Neighborhood of Nilüfer District, Bursa Province. The data acquired from the interviews were analyzed to determine the level of user satisfaction. The study took into account the demographic characteristics of tiny home users, as well as the physical and environmental features of the houses. Additionally, user satisfaction was evaluated. Within the realm of literature studies, interviews were performed with individuals who reside in tiny dwellings in order to ascertain their aspirations. The lack of a satisfaction survey that examines both the factors influencing desire and the extent to which expectations are met following the experience has highlighted the need for performing such a study. The main aim of this study is to help architects, interior designers, and other professional groups engaged in the design of tiny houses to consider the expectations of tiny house users in their upcoming projects.

A significant number of individuals who prefer to live in tiny houses do not do so for an extended period, often due to their ownership of another dwelling. Generally, the selected location is situated in close proximity to the city center, ensuring convenient transportation access for the majority of participants. The majority of residents are those who feel overwhelmed by urban living but desire to spend time immersed in the natural environment. While the limited space in tiny houses presents challenges for

users, such as the inability to store all their belongings in the accustomed order and the need to adapt to a narrower living area, it is worth noting that users consciously choose these tiny houses.

This aligns with previous research and helps to mitigate any potential dissatisfaction. The primary objective of the users is to engage in outdoor activities, particularly in the gardens of their residences, as opposed to spending their time indoors. Since tiny home owners usually place their homes in large gardens, they are all capable of achieving their goal of completely immersing themselves in nature. From this context, it can be concluded that a tiny house lacking a garden is undesirable since it prevents one from enjoying the natural environment beyond the boundaries of the dwelling. The majority of individuals residing in tiny dwellings do not encounter any substantial issues regarding security.

Typically, residences are enclosed by a fence to ensure security. However, it has been found that certain residents have encountered security risks, such as theft and the presence of unfamiliar individuals in the vicinity. The residences of individuals experiencing security issues are located in suburban areas, surrounded by other residential properties. Furthermore, it has been noted that those who have robust connections with their neighbors do not encounter any security issues. When designing tiny houses to meet security issues, various solutions can be proposed using technical methods such as security cameras, alarm systems, motion sensors, and timed lighting.

Based on the observations, the overall satisfaction of young individuals with their lives vary depending on their relationship with the environment. This pertains to how individuals engage with the environmental characteristics of the region and whether they have social connections within the nearby community. Regarding the satisfaction evaluation of the younger age cohorts, there was no explicit correlation observed between the design of the tiny houses. Considering that younger age cohorts generally exhibit a proclivity for socializing with their peers, it is recommended to

build communal areas that facilitate their connection with others.

Several users claim to utilize solar panels to generate electricity for their tiny houses. Some users intend to enhance energy efficiency by gradually increasing the quantity of panels. The inference is that certain comfort circumstances are contingent upon the state of the economy. Regrettably, individuals lacking sufficient financial means are unable to afford or access solar panels at the appropriate frequency or possess them altogether. If the cost of deploying technology such as solar panels cannot be met, alternative options including electrical installations on land can be considered. In the absence of power for heating, stoves constructed with appropriate materials and insulation can function as an effective alternative.

The majority of users modified the structural characteristics or interior decorations of a prefabricated tiny house. This demonstrates the benefits of constructing tiny houses that accommodate specific and distinct needs. It is important to acknowledge that participatory design approaches can be employed in this context. Nevertheless, it appears advantageous to provide adaptable solutions that are appropriate for various user categories and varying sizes of families.

As a result, most users expect that residing in a tiny house will enable them to avoid city life and fully engage in a natural way of living. According to feedback from residents, it can be confidently stated that these expectations are not only met, but exceeded. Users face several obstacles due to factors such as limited utilization and storage capacity, constrained interior space, and security concerns. These challenges are influenced by the number of residents and the dimensions of the residences. In this minimalist lifestyle, it is clear that people who are aware of the benefits of the settlement structure are drawn to this way of living. Individuals that adopt a minimalist lifestyle, emphasize spending time in nature, demonstrate resilience in the face of moderate problems, and want to live in environmentally-friendly and sustainable environments are likely to have much higher levels of enjoyment. It is important to note that

the ideal tiny house includes a garden that is suited for leisure activities.

The design of tiny houses is a crucial component that has a favorable impact on the degree of satisfaction. The spatial layout and furniture design optimize user satisfaction by enabling diverse utilization without compromising available space. It can be argued that individuals who have a limited desire to explore outside of their comfort zone, who do not derive pleasure from being in natural environments, who feel uncomfortable in small, enclosed spaces with low ceilings, who often host guests for extended periods of time, and who have hobbies that are not suitable for a tiny house, are unlikely to find satisfaction in this lifestyle.

This research provides recommendations for addressing user satisfaction in the design phase of tiny houses by determining user preferences, developing innovative spatial solutions that meet the requirements, producing neighborhood units for security, and utilizing suitable sustainable energy alternatives. These guidelines can function as a definitive reference. Due to the limited number of participants in this study, it is essential to conduct further satisfaction surveys on residing in tiny houses in the future, particularly in areas with varied geographical and socioeconomic characteristics. Potential areas for future investigation encompass examining the satisfaction of diverse social groups residing in regions with varying attributes, as well as proposing design implications to improve residential satisfaction in tiny houses.

Article Information Form

Fundings

The author received no financial support for the research, authorship, and/or publication of this paper.

The Declaration of Conflict of Interest/ Common Interest

No conflict of interest or common interest has been declared by the author.

Author Contributions

Conceptualization, M.G. and E.Ç.; methodology, M.G. and E.Ç.; formal analysis, M.G. and E.Ç.;

investigation, M.G. and E.Ç.; resources, M.G. and E.Ç.; data curation, M.G. and E.Ç.; writing—original draft preparation, M.G. and E.Ç.; writing—review and editing, M.G. and E.Ç. All authors have read and agreed to the published version of the manuscript.

The Declaration of Ethics Committee Approval

This study does not require ethics committee permission or any special permission.

The Declaration of Research and Publication Ethics

The authors of the paper declare that they comply with the scientific, ethical and quotation rules of SAUJS in all processes of the paper and that they do not make any falsification on the data collected. In addition, they declare that Sakarya University Journal of Science and its editorial board have no responsibility for any ethical violations that may be encountered, and that this study has not been evaluated in any academic publication environment other than Sakarya University Journal of Science.

Copyright Statement

Authors own the copyright of their work published in the journal and their work is published under the CC BY-NC 4.0 license.

References

- [1] Mutter, “Growing tiny houses: Motivations and opportunities for expansion through niche markets,” IIIIEE Master thesis, 2013.
- [2] Çizmecioğlu, A. Tanrıverdi Kaya, “Küçük ev hareketi üzerine tematik bir derleme,” Mimarlık, Planlama ve Tasarım Alanında Yeni Trendler, vol. 6, pp. 7-23, 12 2022.
- [3] Wenban, “The US tiny house on wheels movement with respect to a building code and relevance to Australia,” Australian Planner, vol. 55, no. 3-4, pp. 221-225, 2018.
- [4] H. Shearer, V. Bares, R. Pieters, B. Winkle, K. Meathrel, “Planning for tiny houses,” Australian Planner, vol. 55, no. 3-4, pp. 147-156, 2018.

- [5] A. R. Akbulut, “ 'Örnek evler'de yaşam başladı” (2023, Nov 25). [Online]. Available: <https://www.hurriyet.com.tr/gundem/ornek-evlerde-yasam-basladi-42350954>.
- [6] J. Ford, L. Gomez-Lanier, “Are tiny homes here to stay? a review of literature on the tiny house movement,” Family and Consumer Sciences Research Journal, vol. 45, pp. 394-405, 6 2017.
- [7] L. M. Boeckermann, A. T. Kaczynski, S. B. King, “Dreaming big and living small: Examining motivations and satisfaction in tiny house living,” Journal of Housing and the Built Environment, vol. 34, pp. 61-71, 2019.
- [8] S. Mangold, T. Zschau, “In search of the “good life”: The appeal of the tiny house lifestyle in the USA,” Social Sciences, vol. 26, no. 8(1), 1 2019.
- [9] A. Wilson, H. Wadham, “(Tiny) spaces of hope: Reclaiming, maintaining, and reframing housing in the tiny house movement,” Environment and Planning D: Society and Space, vol. 41, no. 2, pp. 330-350, 2023.
- [10] G. Lessard, “The scaling up of the tiny house niche in Quebec—transformations and continuities in the housing regime”, Journal of Environmental Policy & Planning, vol 24, no. 6, pp. 625-639, 2022.
- [11] C. Murillo, C. Bianchi, “The experience and well-being outcomes of tiny house owners in Latin America,” Housing Studies, vol 39, no. 2, pp. 327-351, 1 2022.
- [12] M. McArthur, E. Stratford, “Housing aspirations, pathways, and provision: Contradictions and compromises in pursuit of voluntary simplicity”, Housing Studies, vol 36, no. 5, pp. 714-736, 2021.
- [13] M. Olsson, “Living Tiny - An exploratory study of the tiny house movement in Sweden,” Master thesis, Kungliga Tekniska Högskolan, Stockholm, 2020.

- [14] M. Olsson, "Living Tiny - An exploratory study of the tiny house movement in Sweden," Master thesis, Kungliga Tekniska Högskolan, Stockholm, 2020.
- [15] Z. Kahveci, (2019, Sep 7). "'Küçük ev' akımı Türkiye'de yaygınlaşıyor" [Online]. Available: <https://www.aa.com.tr/tr/yasam/kucuk-ev-akimi-turkiyede-yayginlasiyor/1575315>
- [16] G. Alagöz, (2021, April 26). "Küçük evlere büyük talep" [Online]. Available: <https://www.hurriyet.com.tr/ekonomi/kucuk-evlere-buyuk-talep-41796809>.
- [17] K. Schenk, "Flex House: Prefabricating the Tiny House Movement," Master thesis, Dept. Architecture, University of Cincinnati, Cincinnati, 2015.
- [18] A. Anson, "The World is my backyard': Romanticization, thoreauvian rhetoric, and constructive confrontation in the tiny house movement," From Sustainable to Resilient Cities: Global Concerns and Urban Efforts, vol 14, pp. 289-313, 2014.
- [19] H. Shearer, "Tiny houses: Planning for affordability and inclusion," Joint Asia-Pacific Network for Housing Research and Australasian Housing Researchers Conference, Gold Coast, Queensland, Australia, 2018.
- [20] J. K. Ochsner, "The experience of prospect and refuge: Frank Lloyd Wright's houses as holding environments," American Imago, vol 75, no. 2, pp. 179-211, 2018.
- [21] G. Berkin, "Modulor ve Le Corbusier'nin Kulübesi," İstanbul: YEM Publication, 2021.
- [22] T. M. Carlin, "Tiny homes: Improving carbon footprint and the American lifestyle on a large scale," Celebrating Scholarship & Creativity Day, no. 35, 2014.
- [23] T. Harris, "The tiny house movement: Challenging our consumer culture," Lanham, MD: Lexington Books, 2018.
- [24] Anonymous, "Tiny house sürdürülebilirlik adına kıymetli bir araç," Çelik Yapılar, no. 71, pp. 38-39, 7-8 2021.
- [25] C. Turner, "It takes a village: Designating 'tiny house' villages as transitional housing campgrounds," University of Michigan Journal of Law Reform, vol 50, no. 4, pp. 931-954, 2017.
- [26] M. E. Carras, "Tiny House, Big Impact?": An investigation into the 'rise' of the Tiny Home Lifestyle (THL) in the United States," PhD thesis, University of St Andrews, Scotland, 2019.
- [27] Ç. A. Songur, "Konut morfolojisinin kullanıcı memnuniyeti üzerindeki etkilerinin analizi," Master thesis, Istanbul Technical University, Istanbul 2001
- [28] A. Gilbert, "Housing in latin america: Revised strategies," Revista de Ingeniería, vol 35, pp. 48-50, 2011
- [29] S. McTarnaghan, C. Martin, T. Srin, "Literature review of housing in latin america and the caribbean", Research Report, The Urban Institute & Habitat for Humanity 2016 (<https://www.urban.org/sites/default/files/publication/84806/2000957-Literature-Review-of-Housing-in-Latin-America-and-the-Caribbean.pdf>) [Online], 2016.
- [30] S. McTarnaghan, C. Martin, T. Srin, "Literature review of housing in latin america and the caribbean", Research Report, The Urban Institute & Habitat for Humanity 2016 (<https://www.urban.org/sites/default/files/publication/84806/2000957-Literature-Review-of-Housing-in-Latin-America-and-the-Caribbean.pdf>) [Online], 2016.
- [31] N. S. Karaaslan, Z. Ö. Parlak Biçer, "mobil konut üretiminin mevzuat açısından değerlendirilmesi," Online Journal of Art and Design, vol 11, no. 5, pp. 527-546, 12 2023.

- [32] H. Shearer, P. Burton, “Tiny houses: Movement or moment?,” *Housing Studies*, vol 38, no. 3, pp. 360-382, 2 2021.

- [33] H. Shearer, “Tiny houses: Love, live or leave? what factors influence the decision?,” 9th State of Australian Cities National Conference, 2019.

Cost Minimization with Project Crashing: Comparison of the Traditional Solution and Genetic Algorithm Approach

Semih Çağlayan^{1*} , Sadık Yiğit² 

¹ Sakarya University of Applied Sciences, Dept. of Civil Engineering, Sakarya, Türkiye, semihcaglayan@subu.edu.tr

² Zurich University of Applied Sciences, Centre for Building Technologies and Processes, Winterthur, Switzerland, sadik.yigit@zhaw.ch

*Corresponding Author

ARTICLE INFO

ABSTRACT

Keywords:

Project crashing
Resource allocation
Project scheduling
Cost minimization
Metaheuristic algorithms
Genetic algorithm



Existence of delays and cost overruns frequently puts the project viability in jeopardy. The integrated nature of these threats brings forward project scheduling as the primary determinant of project management success. The quality of project scheduling depends highly on the way resources are assigned to activities. In the project management literature, the efficiency of resource allocation is examined closely by the phenomenon called project crashing. This study introduces traditional and genetic algorithm approaches for the project crashing events and explains their steps in achieving the most efficient resource allocation. Within this context, the project crashing event is visualized, the insights of alternative approaches are described, and their implementations are illustrated with a case study. Besides, the procedures required for adopting the genetic algorithm approach to a typical problem are expressed. The case study illustration reveals the advantages and disadvantages of the genetic algorithm approach over the traditional approach. It is observed that the genetic algorithm approach can reach the solution in a single phase while the traditional approach requires multiple phases. On the other hand, the genetic algorithm approach may not reach the optimum solution unless the toolbox options are appropriately selected. This study presents the contribution of operational research to the project management body of knowledge by demonstrating the applicability and efficiency of genetic algorithm in the project crashing events. Researchers and industry practitioners may benefit from the proposed approach by following the indicated procedures to incorporate genetic algorithm into optimization issues in different fields.

Article History:

Received: 13.04.2024

Accepted: 10.09.2024

Online Available: 14.10.2024

1. Introduction

The subject of project management has attracted the attention of practitioners and researchers from different disciplines such as management science, organization theory, operations management, and social psychology [1]. Even though many factors have been defined for the successful delivery of projects [2], it is an undeniable fact that many projects fail to perform as intended and experience delays and cost overruns [3, 4], which may put project viability at risk [5]. The integrated nature of delays and

cost overruns implies that these two phenomena should be studied together [6]. Poor scheduling, therefore, has been frequently specified as the main reason behind the project management failures [7].

Management of large-scale projects necessitates coordination of many activities with different costs and durations [8]. Achievement of project success requires organizations to efficiently assign resources to these activities. The project scheduling optimization has a wide range of applications in the fields of construction,

production planning, and manufacturing [9]. The issue lies at the heart of project management and has attracted great attention in academia [10]. Many researchers have attempted to find solutions to the issue since 1960s. The solutions have focused on creating a project schedule to minimize the project cost and duration [11].

Project crashing is a schedule compression technique that aims to minimize the total cost of the project. The technique is based on analyzing the cost and duration trade-offs to obtain the greatest compression in project schedule for the least incremental cost. The project duration is reduced by shortening the critical path, which corresponds to the longest sequence of activities. Even though shortening the critical path requires greater resource allocation to certain activities on the critical path (implying an increase in activity costs), reduction in the project duration can provide savings in penalty associated with the project delay. As long as the savings obtained outweigh the increase in activity costs, such an attempt helps the project managers decrease the total cost of the project.

Project crashing has been traditionally carried out with a multi-phase schedule compression method. In recent years, development of metaheuristic algorithms like the genetic algorithm has enabled researchers to identify the optimized solutions for such complicated issues. Several researchers have utilized metaheuristic algorithms to overcome the challenges encountered in such events [12]. This study makes a comparison between the traditional solution and genetic algorithm approach for the project crashing events. In this regard, the project crashing event is visualized; the project crashing concept is introduced; and a typical problem is represented in a table format. The steps followed by the traditional approach are presented and the procedures necessary to adopt the genetic algorithm approach are clarified. Implementation of these alternative approaches on a typical problem is illustrated with a case study. The advantages and disadvantages of genetic algorithm adoption over the traditional solution are observed.

The paper is organized as follows: Section 2 describes the genetic algorithm concept and

summarizes the fields genetic algorithm have been used for. Section 3 explains the methodology; visualization of the project crashing event, description of the alternative approaches, and illustration with a case study. The steps followed by the traditional solution and genetic algorithm approach are explained, and advantages/disadvantages are discussed in Section 4. Finally, Section 5 presents the conclusion; summary of the results, contribution to the body of knowledge, and limitations of the study.

2. Research Background

2.1. The genetic algorithm concepts

Genetic algorithm is a well-known population-based metaheuristic algorithm inspired from the biological evolution process [13]. The algorithm was proposed by John Holland in 1970s and is based on the Darwinian theory of the survival of the fittest [14]. The optimization process of genetic algorithm is illustrated in Figure 1. The process starts with randomly generating an initial population. A certain number of individuals are created, where each individual represents a solution the problem [15]. A fitness function is used to evaluate the fitness of each individual [16]. The fitness value indicates the likelihood of each individual to survive and reproduce in the new population [17].

Generation of the initial population is followed by evolution toward better solutions by means of genetic operators: selection, cross-over, and mutation [18]. The selection operator chooses the fitter individuals in the current population as parents to give birth to individuals in the new population [19]. The cross-over operator takes the chosen individuals and generates the new individuals by crossing the genes between pairs of parents [20]. The mutation operator changes the genes in the new population to increase the diversity [21]. It helps the algorithm exploit all the search space [22]. In short, the cross-over operator provides better future generations, while the mutation operator prevents the algorithm from getting stuck at local optima [23].

Generation of the new population by subjecting the current population to the genetic operators is

an iterative process. The iteration is repeated until the number of iterations equals to a predefined value for maximum generations, which implies that the termination criterion is met [24]. Satisfaction of the criterion results in

termination of the algorithm [25]. The best-so-far solution, the individual with the most satisfactory fitness value, is regarded as the optimal solution. The results obtained for the optimal solution are displayed.

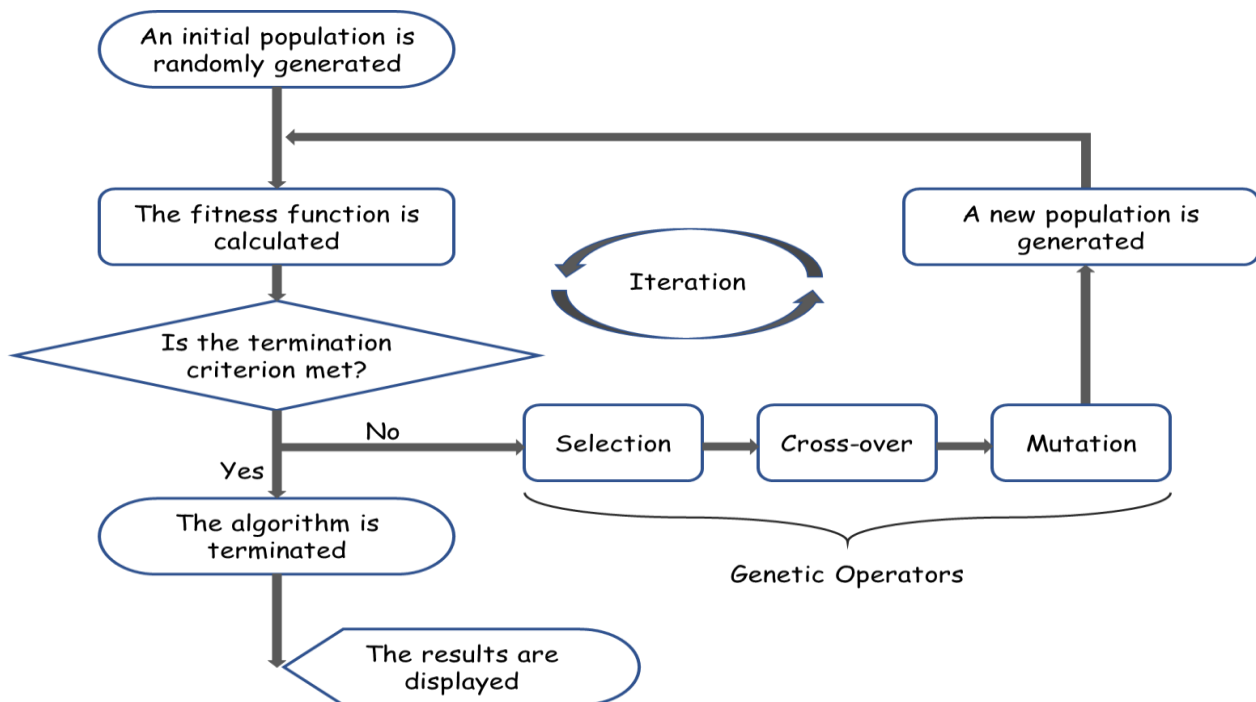


Figure 1. Genetic algorithm optimization process

2.2. Utilization of genetic algorithms for optimization

The metaheuristic algorithms, especially the genetic algorithms, have been utilized for various optimization purposes such as construction material design, energy efficiency in buildings, project layout planning, and project scheduling. A group of studies have attempted to optimize the design of construction elements. Genetic algorithms have been developed to optimize the design of multi-story composite steel frames [26], to minimize the construction cost of mass concrete [27], to produce asphalt mixtures complying with applicable specification requirements [28], to predict the adhesion strength [29], to mitigate the risk of early-age thermal cracking and delayed ettringite formation in mass concrete [30], to identify optimum parameter settings for aluminum-based hybrid metal matrix composite material [31]. Other metaheuristics-based algorithms have also been proposed for the design of cantilever retaining walls [32] and cantilever beams [33].

Another group of studies have used genetic algorithm to improve the energy efficiency in buildings. Several researchers have aimed at improving the energy efficiency through developing building retrofitting strategies [34]. Retrofitting has been done for school buildings [35], green building compliance [36], and residential buildings within a budget constraint [37]. Energy efficiency has been enhanced in another group of study with a focus on the heating energy consumption. The researchers have either developed algorithms to forecast the heating loads [38] or determined the optimum thermal design [39].

Several researchers have conducted studies for the optimization of project layout planning and logistics network design with the use of metaheuristic algorithms. Elements of the industrial production systems have been arranged in a number of studies as a part of the business operation strategy [40]. Multi-objective particle swarm optimization algorithm was proposed to minimize the construction safety risks of cranes and the total travelling distance of resources [41].

Non-dominated sorting genetic algorithm (NSGA) II was adapted to find the optimum location of facilities and transport network design to obtain sustainable supply-chain-network [42]. The link capacities and environmental protection were expressed as the problem constraints. A genetic algorithm-based model was proposed to solve the bus terminal location problem through finding efficient allocation patterns for assigning stations terminals [43]. The path planning in an unknown or partially known environment was resolved with artificial bee colony algorithm and evolutionary programming [44].

Project/program scheduling has been another application field of genetic algorithms. Algorithms have been used by several researchers for resource constraint optimization problems in construction [45, 46]. A genetic algorithm using a two-point crossover operator was proposed to a resource-constrained project scheduling problem with sequence dependent transfer times and the proposed algorithm could efficiently solve these problems [47]. A novel genetic algorithm incorporating complicated activity-dependencies for the resource leveling problem was developed by Li et al. [48]. The model could achieve near optimal solutions in fractions of a second. A NSGA-III-based algorithm was produced for a bi-objective hierarchical resource-constrained program scheduling problem [49]. The computational simulations confirmed the satisfactory performance of the model. In another study, a construction schedule was automatically generated by extracting data from a building information modeling product [50]. Behera and Sobhanayak [51] utilized genetic algorithm to optimize task scheduling in heterogeneous cloud computing environments.

Previous studies using the genetic algorithm concept for addressing certain optimization issues have mainly attempted to come up with solutions to these specific issues and have not clarified the steps that should be followed for repetition of the study in different fields. The literature obviously lacks an informative and

explanatory study that visualizes a typical mathematical optimization problem and expresses the philosophy of utilizing the genetic algorithm to solve it. The procedures necessary for genetic algorithm adaptation need to be described so that the approach can also be adjusted for optimization issues in other fields and the use of genetic algorithm can be popularized.

This study aims to fill the gap in the literature by providing a detailed description for the use of genetic algorithm in project crashing events and demonstrating its advantages and disadvantages over the traditional solution through an illustrative case study. This study goes beyond optimization of a specific project scheduling issue and explains the philosophy behind integration of genetic algorithms into the project crashing events for the purpose of cost minimization. It clarifies the steps to be followed for proper integration of genetic algorithms into optimization problems.

3. Research Methodology

The flowchart of methodology is presented in Figure 2. It is composed of three main phases, namely (i) visualization of project crashing, (ii) description of alternative approaches, and (iii) case study illustration.

In the first phase, the project crashing event is introduced and visually represented. Categorization of the project cost is clarified, the project crashing concept is explained, and a typical problem is represented. The second phase presents the philosophy behind the traditional and proposed genetic algorithm approaches. It elaborates on the steps followed by the traditional and proposed genetic algorithm approaches to optimize resource allocation with the project crashing. The iterative process of the traditional approach is introduced and the requirements for adopting the genetic algorithm are expressed. The third phase involves implementation of the steps followed by these approaches on a case study.

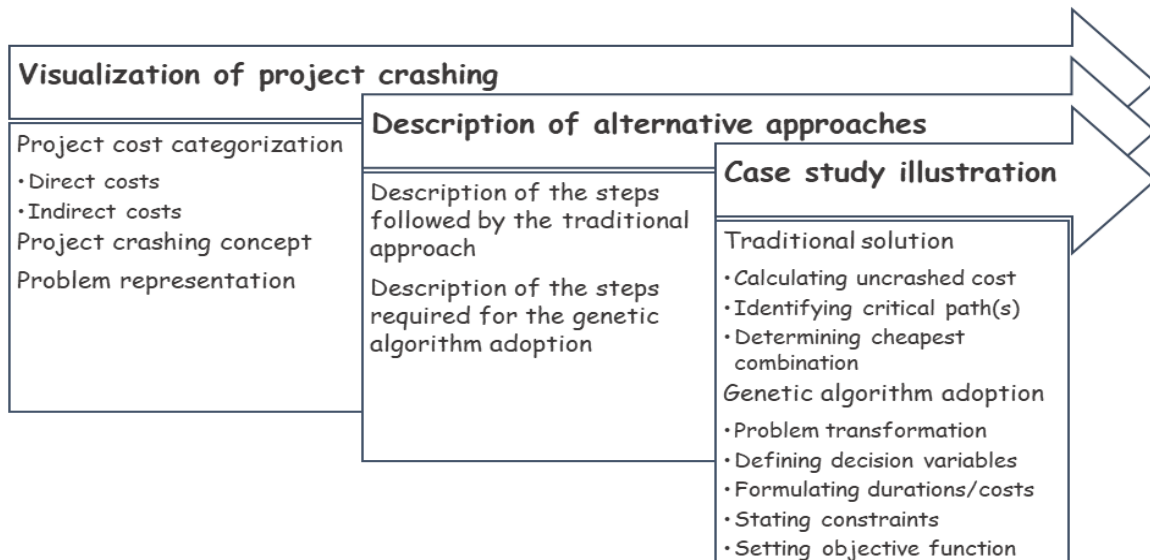


Figure 2. Flowchart of the methodology

3.1. Visualizing the project crashing events

The project cost is categorized into two different costs, namely the direct and indirect costs. The direct costs represent the costs directly attributable to the product. These may include the cost of raw materials, labor, and equipment costs. In project crashing events, the individual cost of each activity is evaluated under this category. In other words, the sum of the activity costs equals the direct costs. The indirect costs extend beyond the expenses realized in creating the product. General administration, supplies, and building rental costs can be given as the examples of indirect costs. Indirect costs are assumed to be linearly related to the project duration in the project crashing events.

Project crashing is a technique used to speed up the timeline of a project by providing more resources to certain activities in the critical path. More resources can be provided to the activities by assigning additional personnel or paying a premium. Shortening the project duration through allocating greater resources increases the direct cost. However, the indirect cost is decreased as it is directly associated with the duration of the project. Project crashing aims to shorten the project while keeping the project cost at a minimum. Determining the minimum project cost via the project crashing technique can be achieved through the traditional approach or the proposed genetic algorithm approach. These approaches follow different steps to calculate the optimum duration and cost of the project.

A typical project crashing problem is represented in Table 1. The first two columns show the list of activities and the relations between them. The third column indicates the normal duration (the duration when no crashing occurs) of each activity. The crushed duration stands for the duration of each activity after all the possible crashes are applied. Thus, the difference between the normal and crashed duration implies the number of crashes applicable to the corresponding activity.

To illustrate, if the difference is equal to two, the activity cannot be crashed more than two times (the duration cannot be decreased by more than two days). The remaining columns are the normal costs and the cost of each crash. The direct cost of the project is equal to the sum of the normal costs and costs of the crashes realized. The indirect cost is obtained by multiplying the overhead cost by the project duration determined by the critical path method (CPM).

3.2. Alternative approaches for project crashing

The steps followed by the two alternative approaches to minimize cost with project crashing are presented in Figure 3. In the traditional approach, it is firstly assumed that all the activities are realized in their normal durations/costs and the project duration/cost is calculated accordingly. CPM is used to calculate the project duration and identify the critical

Table 1. Representation of a typical project crashing problem

Activity	Predecessor	Normal Duration (days)	Crashed Duration (days)	Normal Cost (\$)	Cost of Crashes (\$)		
					1 st Crash	2 nd Crash	3 rd Crash
A
B
C
D
⋮	⋮	⋮	⋮	⋮	⋮	⋮	⋮

*Overhead cost: ... \$/day

path(s). Acquisition of saving in indirect costs requires the project duration to be decreased by one unit. Therefore, the cheapest combination of activities is determined such that crashing these activities can satisfy the specified condition.

Shortening the project duration by one unit requires crashing all the critical paths. It is also necessary to explain the difference between crashing an activity and crashing a critical path. While the former implies decreasing the duration of the activity by one unit, the latter means crashing at least one of the activities in the corresponding path. The cost of crashing the selected activities is compared with the saving obtained from indirect costs. If the saving exceeds the cost of crashing; the selected activities are crashed, the new project duration and cost are calculated, and the process is repeated. Otherwise, the current project duration and cost are regarded as the optimum.

The proposed genetic algorithm approach follows totally different steps. Implementation of the proposed genetic algorithm approach requires transformation of the problem (Table 2). The duration/cost alternatives are presented for each activity rather than expressing the costs of crashes. Such a transformation is required for the formulations to be described in the following steps. A decision variable is defined for each activity as the number of times the corresponding activity is crashed. Afterwards, the duration and cost of each activity is expressed as a function of the decision variable. The number of times each activity can be crashed becomes the constraints

for the decision variables. The objective function is defined as the minimization of the project cost. The project cost is formulated such that it becomes a function of the decision variables.

3.3. Case study illustration

The steps followed by two different approaches for the project crashing events are illustrated in a case study. A typical project crashing problem is presented in Table 3. The problem includes a total of 12 activities. The relations between the activities are given in the second column. A finish-to-start relationship exists between them. The normal and crashed duration of each activity are shown in the third and fourth columns.

For activity 1, the normal and crashed durations are 8 and 5 days, respectively. It is implied that the activity has the potential to be crashed for three days (8 days – 5 days). The fifth column shows the cost of the activity when it is completed in its normal duration. The last three columns show the cost of crashes. It is realized that the cost of crashing increases in each additional crash.

3.3.1. The traditional approach

The first step in the traditional approach is to calculate the project cost based on the normal durations and costs of activities. As already mentioned, the project cost is composed of the direct and indirect costs. The direct cost is calculated by summing up the costs stated in the fifth column of Table 3, which is determined as

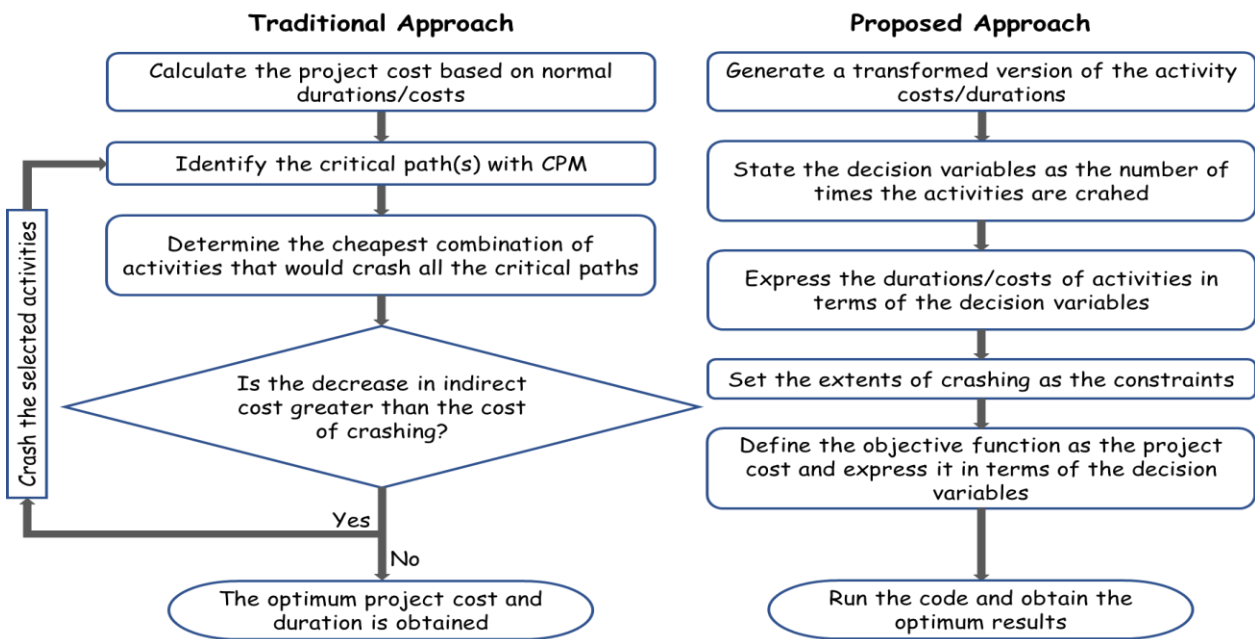


Figure 3. Steps followed by alternative approaches for project crashing events

Table 2. Representation of the transformed version of the problem

Activity	Predecessor	Normal Duration / Cost (days / \$)	1 st crash Duration / Cost (days / \$)	2 nd crash Duration / Cost (days / \$)	3 rd crash Duration / Cost (days / \$)
A / / / / ...
B / / / / ...
C / / / / ...
D / / / / ...
⋮	⋮	⋮	⋮	⋮	⋮

*Overhead cost: ... \$/day

\$23750. The indirect cost is calculated by multiplying the overhead cost by the project duration determined according to the CPM (Figure 4). The project duration and cost are identified as 21 days and \$25850 (direct and indirect costs), respectively. The critical path is Activity 3 - Activity 6 - Activity 9 - Activity 10. The situation before crashing is summarized as:

- Duration: 21 days
- Cost: $23750 + 21 * 100 = \$25850$
- Critical path(s):
 - Act. 3 – Act. 6 – Act. 9 – Act. 10

Completing the project one day earlier provides a \$100 saving in indirect cost. Reducing the project duration by one day requires all the critical paths to be crashed. Therefore, the cheapest combination of activities crashing all the critical paths is determined and compared with the saving in indirect cost. It is noticed that

crashing Activity 9 by 1 day is cheapest way to crash the identified critical path and it is less than the saving realized (\$20 vs \$100).

The activity is crashed, the resultant project duration and cost are calculated, and the new critical paths are determined (Figure 5). The situation after the first crash is summarized as:

- 1st crash: Crash Activity 9 by 1 day
- Resultant duration: 20 days
- Resultant cost: $2585 + 20 - 100 = \$25770$
- Resultant critical path(s):
 - Act. 3 – Act. 6 – Act. 9 – Act. 10
 - Act. 1 – Act. 4 – Act. 8

Two critical paths are identified at the end of the first crash. The cheapest combination of the activities that can crash these critical paths are determined as Activity 1 and Activity 3.

Table 3. Information about the activity costs/durations

Activity	Predecessor	Normal Duration (days)	Crashed Duration (days)	Normal Cost (\$)	Cost of Crashes (\$)		
					1 st Crash	2 nd Crash	3 rd Crash
1	-	8	5	2500	20	25	35
2	-	6	4	1200	30	45	-
3	-	7	5	1450	30	35	-
4	1, 2, 3	6	4	1350	30	30	-
5	1, 2, 3	4	2	1250	20	30	-
6	2, 3	5	3	2300	40	55	-
7	3	4	2	2000	40	45	-
8	4, 5	6	5	2750	40	-	-
9	6, 7	5	2	1800	20	35	50
10	4, 5, 9	4	2	850	45	55	-
11	7	8	5	3800	50	50	50
12	3	10	7	2500	15	20	25

*Overhead cost: ... \$/day

Crashing these activities costs \$50 (\$20+\$30), which is less than the additional saving to be realized. These activities are crashed and project duration is decreased by one day (Figure 6). The situation after the second crash is summarized as:

- 2nd crash: Crash Activity 1 and Activity 3 by 1 day
- Resultant duration: 19 days
- Resultant cost: $25770 + 20 + 30 - 100 = \25720
- Resultant critical path(s):
 - Act. 3 – Act. 6 – Act. 9 – Act. 10
 - Act. 1 – Act. 4 – Act. 8
 - Act. 2 – Act. 6 – Act. 9 – Act. 10

Realization of the second crash leads to an additional critical path. The number of critical paths is increased to three. The cheapest combination to crash these paths is determined as Activity 1 and Activity 9. It should be noted that Activity 1 and Activity 9 are already crashed for one day in the second and first crashes, respectively. Thus, the cost of crashing becomes \$25 for Activity 1 and \$35 for Activity 9. It is realized that these three critical paths can be crashed simultaneously by crashing two activities because Activity 9 is the mutual activity in the first and third critical paths. As the cost of crashing (\$25+\$35) is less than the additional saving, the activities are crashed (Figure 7). The situation after the third crash is:

- 3rd crash: crash Activity 1 and Activity 9 by 1 day
- Resultant duration: 18 days
- Resultant cost: $25720 + 25 + 35 - 100 = \25680
- Resultant critical path(s):
 - Act. 3 – Act. 6 – Act. 9 – Act. 10
 - Act. 1 – Act. 4 – Act. 8
 - Act. 2 – Act. 6 – Act. 9 – Act. 10
 - Act. 3 – Act. 4 – Act. 8
 - Act. 3 – Act. 7 – Act. 11

Two additional critical paths occur after the third crash, resulting in a total of five critical paths. The cheapest way to crash these critical paths is to crash Activity 2, Activity 3, and Activity 4. Activity 3 is already crashed for one day in the second crash, so the crashing cost becomes \$35 for Activity 3. The cost of crashing (\$30+\$35+\$30) is still less than the potential saving in indirect costs. Thus, the fourth crash is also realized (Figure 8). The situation after the fourth crash is summarized as:

- 4th crash: crash Activity 2, Activity 3, and Activity 4 by 1 day
- Resultant duration: 17 days
- Resultant cost: $25680 + 30 + 35 + 30 - 100 = \25675
- Resultant critical path(s):
 - Act. 3 – Act. 6 – Act. 9 – Act. 10

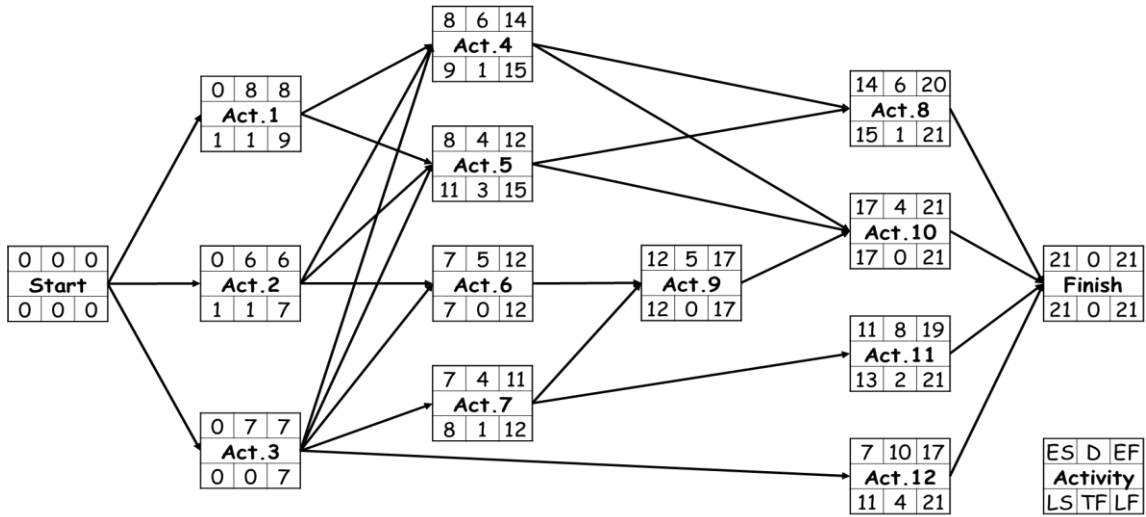


Figure 4. CPM analysis before crashing

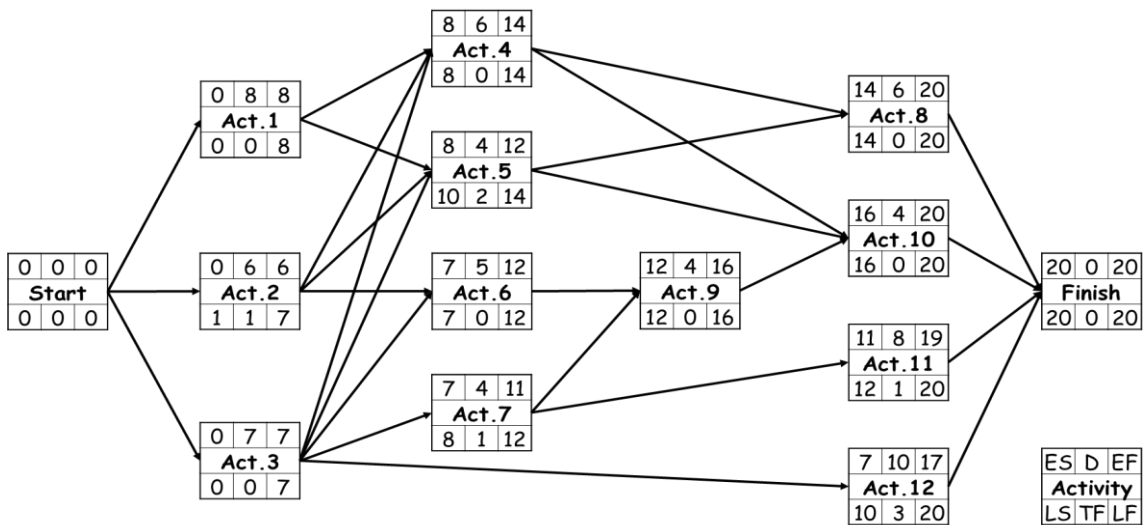


Figure 5. CPM analysis after 1st crash

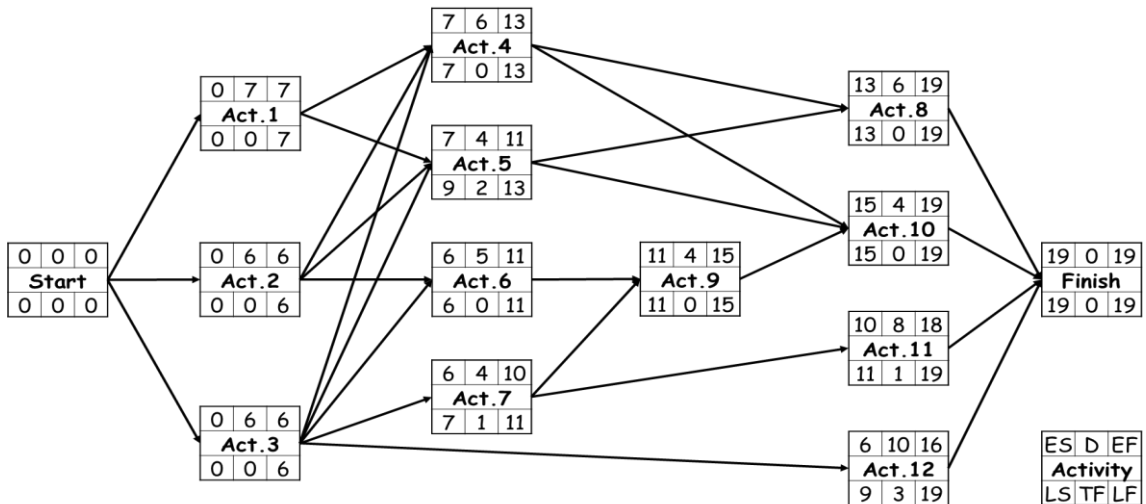


Figure 6. CPM analysis after 2nd crash

- Act. 1 – Act. 4 – Act. 8
- Act. 2 – Act. 6 – Act. 9 – Act. 10
- Act. 3 – Act. 7 – Act. 11

Four critical paths are identified after the fourth crash. The cheapest way to decrease project duration by one day is to crash Activity 4, Activity 6, and Activity 7. The cost of crashing

(\$30+\$40+\$40) exceeds the potential saving in indirect costs. It implies that crashing these activities results in an increase in total project cost. Therefore, the process is terminated and the current situation is described as the optimum. The optimum project duration and project cost are obtained as 17 days and \$25675. The optimum situation is achieved by crashing Activity 1 by 2 days, Activity 2 by 1 day, Activity 3 by 2 days, Activity 4 by 1 day, and Activity 9 by 2 days. The other activities are realized in their normal durations and costs.

3.3.2. The genetic algorithm approach

The proposed genetic algorithm approach follows entirely different steps to optimize project crashing events. Adaptation of the genetic algorithm approach principally requires transformation of the problem. After the original problem is transformed, necessary coding is done in a programming platform that supports the genetic algorithm optimization. MATLAB has been preferred as a commercial programming platform. Definition of the decision variables, formulation of the durations/costs, statement of the constraints, and the expression of the objective function are explained to demonstrate the use of the genetic algorithm concept for the optimization of project crashing events.

Transforming the problem

A typical project crashing problem is most of the time presented as shown in Table 3. The normal duration/cost of each activity is given and costs of the crashes are indicated if available. The genetic algorithm approach requires a clear presentation of the alternatives for each activity. The cost and duration of an activity after each crash should be presented as a package. In this context, the presentation of the problem is transformed (Table 4). The alternatives for each activity are clearly observed in the transformed version. The number of alternatives for the activities ranges between two and four. Multiplication of the number of alternatives results in more than one million solutions. To be more precise, the genetic algorithm is expected to find the optimal solution among 1,119,744 solutions.

Defining the decision variables

The way the decision variables are defined is one of the most critical part of the genetic algorithm approach. The decision variable should be defined such that all the other variables and the objective function can be expressed as a function of the decision variable. For this purpose, the decision variable is defined as:

$$x_i = \text{Number of times Activity } i \text{ is crashed} \\ x_i \in \mathbb{Z}^n$$

The decision variable is an integer that shows the number of times the corresponding activity is crashed. Thus, with this approach, the project crashing problem is transformed into a selection of how many times each activity should be crashed. The other variables that are to be expressed as a function of the decision variables are defined as follows:

$$d_i = \text{Duration of Activity } i \\ c_i = \text{Cost of Activity } i \\ ES_i = \text{Early start time of Activity } i \\ EF_i = \text{Early finish time of Activity } i$$

Formulating the durations/costs

It is already mentioned that the other variables and the objective function must be expressed as a function of the decision variables. The duration and cost of each activity are formulated as follows:

$$d_1 \text{ and } c_1 \\ = \begin{cases} d_1 = 8 \text{ days and } c_1 = \$2500, & \text{for } x_1 = 0 \\ d_1 = 7 \text{ days and } c_1 = \$2520, & \text{for } x_1 = 1 \\ d_1 = 6 \text{ days and } c_1 = \$2545, & \text{for } x_1 = 2 \\ d_1 = 5 \text{ days and } c_1 = \$2580, & \text{for } x_1 = 3 \end{cases}$$

$$d_2 \text{ and } c_2 \\ = \begin{cases} d_2 = 6 \text{ days and } c_2 = \$1200, & \text{for } x_2 = 0 \\ d_2 = 5 \text{ days and } c_2 = \$1230, & \text{for } x_2 = 1 \\ d_2 = 4 \text{ days and } c_2 = \$1275, & \text{for } x_2 = 2 \end{cases}$$

$$d_3 \text{ and } c_3 \\ = \begin{cases} d_3 = 7 \text{ days and } c_3 = \$1450, & \text{for } x_3 = 0 \\ d_3 = 6 \text{ days and } c_3 = \$1480, & \text{for } x_3 = 1 \\ d_3 = 5 \text{ days and } c_3 = \$1515, & \text{for } x_3 = 2 \end{cases}$$

$$d_4 \text{ and } c_4 \\ = \begin{cases} d_4 = 6 \text{ days and } c_4 = \$1350, & \text{for } x_4 = 0 \\ d_4 = 5 \text{ days and } c_4 = \$1380, & \text{for } x_4 = 1 \\ d_4 = 4 \text{ days and } c_4 = \$1410, & \text{for } x_4 = 2 \end{cases}$$

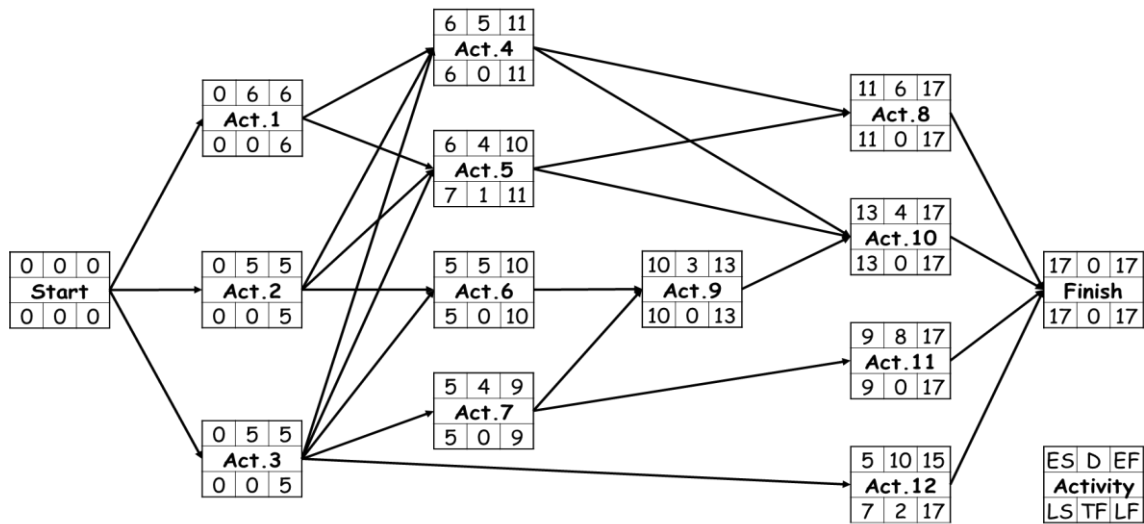


Figure 8. CPM analysis after 4th crash

Table 4. Transformed version of the activity costs/durations

Activity	Predecessor	Normal Duration / Cost (days / \$)	1 st crash Duration / Cost (days / \$)	2 nd crash Duration / Cost (days / \$)	3 rd crash Duration / Cost (days / \$)
1	-	8 / 2500	7 / 2520	6 / 2545	5 / 2580
2	-	6 / 1200	5 / 1230	4 / 1275	-
3	-	7 / 1450	6 / 1480	5 / 1515	-
4	1, 2, 3	6 / 1350	5 / 1380	4 / 1410	-
5	1, 2, 3	4 / 1250	3 / 1270	2 / 1300	-
6	2, 3	5 / 2300	4 / 2340	3 / 2395	-
7	3	4 / 2000	3 / 2040	2 / 2085	-
8	4, 5	6 / 2750	5 / 2790	-	-
9	6, 7	5 / 1800	4 / 1820	3 / 1855	2 / 1905
10	4, 5, 9	4 / 850	3 / 895	2 / 950	-
11	7	8 / 3800	7 / 3850	6 / 3900	5 / 3950
12	3	10 / 2500	9 / 2515	8 / 2535	7 / 2560

*Overhead cost: 100 \$/day

Setting the objective function

The final step of the genetic algorithm approach is to define and express the objective function. The aim of the project crashing event is to minimize the project cost ($C_{Project}$). As already mentioned, the project cost is equal to the sum of the direct and indirect costs. The direct costs are calculated by summing the individual cost of each activity ($c_1 + c_2 + c_3 \dots + c_{12}$). The indirect costs are calculated by multiplying the overhead cost (100 \$/day) by the project duration ($d_{Project}$). The objective function is formulated as follows:

$$C_{Project} = c_1 + c_2 + c_3 + c_4 + c_5 + c_6 + c_7 + c_8 + c_9 + c_{10} + c_{11} + c_{12} + 100 * d_{Project}$$

In this equation, the individual cost of each activity is a function of the decision variables and

the overhead cost is 100 \$/day. The project duration should also be expressed as a function of the decision variables. The project duration is calculated according to CPM as in the traditional approach. However, rather than calculating the project duration after each crash, the relations between the activities are formulated for once. The early start (ES) and early finish (EF) times of each activity are expressed as a function of the activity durations (d_i), which are already stated as a function of the decision variables (x_i). The project duration is equal to the EF of the last activity (Finish). The late start (LS) and late finish (LF) times of the activities are not formulated because there is no need to identify the total float (TF) times and the critical path(s) in the genetic algorithm approach. In other words, calculation of the project duration is sufficient. The project duration is formulated as follows:

$$\begin{aligned}
ES_{Start} &= 0 \\
EF_{Start} &= 0 \\
EF_i &= ES_i + d_i, \quad \text{for } i = 1, 2, 3, \dots, 12 \\
ES_1 &= EF_{Start} \\
ES_2 &= EF_{Start} \\
ES_3 &= EF_{Start} \\
ES_4 &= \max(EF_1, EF_2, EF_3) \\
ES_5 &= \max(EF_1, EF_2, EF_3) \\
ES_6 &= \max(EF_2, EF_3) \\
ES_7 &= EF_3 \\
ES_8 &= \max(EF_4, EF_5) \\
ES_9 &= \max(EF_6, EF_7) \\
ES_{10} &= \max(EF_4, EF_5, EF_9) \\
ES_{11} &= EF_7 \\
ES_{12} &= EF_3 \\
ES_{Finish} &= \max(EF_8, EF_{10}, EF_{11}, EF_{12}) \\
EF_{Finish} &= ES_{Finish} \\
d_{Project} &= EF_{Finish}
\end{aligned}$$

4. Research Results and Discussion

The steps indicated for adopting the genetic algorithm approach is coded in MATLAB and the results are obtained. The genetic algorithm toolbox options, which are essential for the optimization process are presented in Table 5. It should be noted that the options are highly dependent on experience and trial and error [52]. Arbitrarily estimated options may lead to convergence to a local optimum [53]. If the population size and maximum generations are insufficiently estimated, the algorithm may end up with a misleading solution. However, overestimation of these toolbox options can lead to an inefficient and time-consuming algorithm.

Table 5. Genetic algorithm options

Option	Description	Value
Population size	Number of individuals in the population	150
Selection	Selection of individuals for the next generation	Stochastic uniform
Maximum generations	Maximum number of iterations	100
Elitism	How many individuals in the current generation are guaranteed to survive	0.12 * 100
Tolerance function	Whether the average relative change in the best fitness function value is less than or equal to Funtool	10 ⁻⁸
Cross-over function	The function that the algorithm uses to create cross-over members	Constraint dependent
Cross-over fraction	The fraction of the population created by the cross-over function	0.8
Mutation function	The function that produces mutation children	Constraint dependent

The genetic algorithm iterations are shown in Figure 9. It is noticed that the best members of the population do not show noticeable improvement after the 40th generation. It can be explained by the fact that the algorithm developed for the project crashing problem reaches nearly optimum values in 40 generations and stays there. Nevertheless, in an attempt to make sure that the optimum solution is obtained, the maximum number of iterations is selected as 100 (much greater than 40) as shown in Table 5. As the average change in the penalty fitness is lower than the tolerance function (10⁻⁸), the process stops nearly at the 80th generation.

The values of the decision variables for the optimum solution are shown in Table 6. The optimum solution requires that Activity 1, Activity 2, Activity 3, Activity 4, and Activity 9 are crashed for 2, 1, 2, 1, and 2 times,

respectively. Such a situation implies that greater resources are assigned to these activities. The other activities are realized in their normal durations and costs. The optimum cost of the project is determined as \$25675. The solution is exactly the same as the solution in the traditional approach.

The solution of the project crashing problem is presented with two different approaches, namely the traditional approach and the proposed genetic algorithm approach. These two approaches arrive at the same solution by following entirely different steps. The traditional approach follows an iterative process that requires drawing the network diagram, identifying the critical path(s), and detecting the cheapest combination of activities to reduce the project duration by one day. These operations need to be realized before

each crash, which results in a multi-phase process.

The most challenging part of the traditional approach is the selection of cheapest combination of activities to crash. This part might be relatively easy in the first crashes as the network diagram results in a reasonable number of critical paths. However, as the process continues, the number of critical paths is increased and the selection becomes complicated. The critical paths and the number of crashing options before each crash are

summarized in Table 7. It is seen that the number of critical paths is less than three before the first and second crashes. However, it is increased up to five in the following crashes. The activities in the critical paths are the candidates for selection. Each activity can either be “crashed” or “not crashed”. Thus, there are 24, 27, 28, 210, and 210 options before the first, second, third, fourth, and fifth crashes, respectively. It is necessary to select the cheapest option (among more than a thousand options before the fourth and fifth crashes) that can crash all the critical paths.

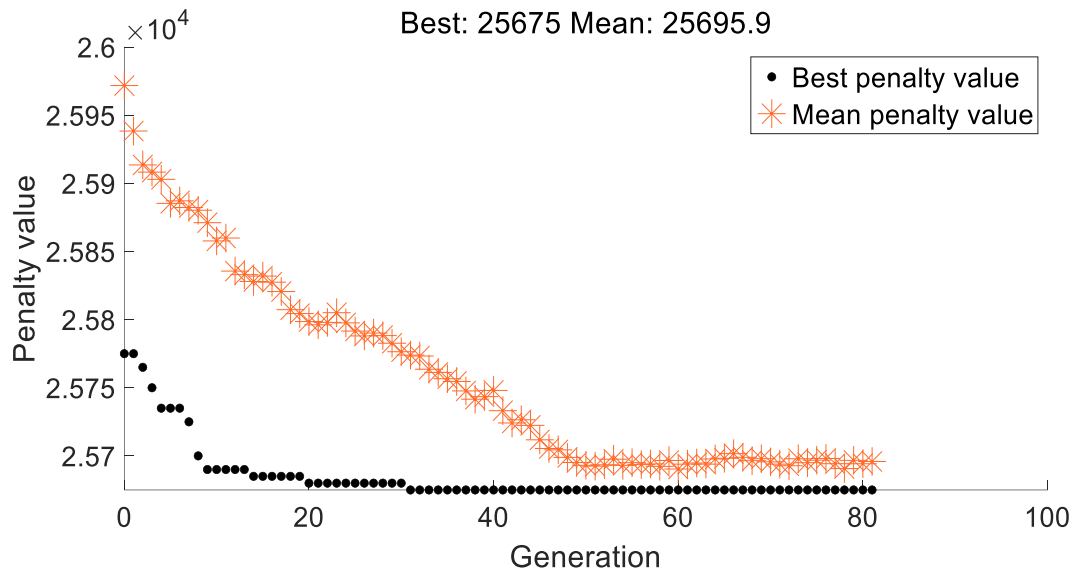


Figure 9. Genetic algorithm iterations

Table 6. The values of the decision variables at optimality

#	x_1	x_2	x_3	x_4	x_5	x_6	x_7	x_8	x_9	x_{10}	x_{11}	x_{12}
Result	2	1	2	1	0	0	0	0	2	0	0	0

Table 7. Number of crashing options in the traditional approach

Crash No	Critical Path(s)	Activities Concerned	# of Options
1	3 – 6 – 9 – 10	3, 6, 9, 10	16
2	3 – 6 – 9 – 10 1 – 4 – 8	1, 3, 4, 6, 8, 9, 10	128
3	3 – 6 – 9 – 10 1 – 4 – 8 2 – 6 – 9 – 10	1, 2, 3, 4, 6, 8, 9, 10	256
4	3 – 6 – 9 – 10 1 – 4 – 8 2 – 6 – 9 – 10 3 – 4 – 8 3 – 7 – 11	1, 2, 3, 4, 6, 7, 8, 9, 10, 11	1024
5	3 – 6 – 9 – 10 1 – 4 – 8 2 – 6 – 9 – 10 3 – 7 – 11	1, 2, 3, 4, 6, 7, 8, 9, 10, 11	1024

5. Conclusion

Project managers quite often suffer from delays and cost overruns in consequence of poor project scheduling. An efficient resource allocation process is essential for achieving the project success. It is a complicated process valid for many industries including construction and manufacturing. Numerous studies have been conducted in an attempt to create schedules minimizing the cost and duration. This study has proposed a genetic algorithm approach to achieve the most efficient resource allocation and minimize the total cost of the project with project crashing. The project crashing event has been visualized, alternative approaches have been described, and their implementations have been illustrated with a case study.

The results show that the same solution can be obtained with both approaches that follow entirely different steps. The main advantage of the genetic algorithm approach is that the solution is obtained in a single phase. Once the problem is appropriately transformed, decision variables are defined, and objective function is expressed in terms of the decision variables; the optimum solution can be easily obtained. The traditional approach is a multi-phase crashing process where a number of operations should be realized at each phase. On the other hand, it should be noted that the genetic algorithm approach may not reach optimum solution if the toolbox options are not appropriately selected. Selection of inappropriate toolbox options may lead to identification of the local optimum rather than the global optimum.

This study contributes to the body of knowledge by describing the philosophy behind the use of a genetic algorithm for cost minimization, demonstrating its applicability to the project crashing events, expressing the procedures required for its adaptation, and indicating the advantages and disadvantages compared to the traditional approach. It goes beyond optimizing a single phenomenon in the field of project management and enters into the spirit of integrating a genetic algorithm into any optimization event. It expresses how the problem should be handled, and data should be transformed to enable proper execution of the

optimization process with genetic algorithm. The proposed approach is intended to encourage project managers to create effective schedules and allocate resources efficiently in their projects by means of such contemporary algorithms. The genetic algorithm adaptation procedures are expected to promote research focusing on the integration of metaheuristic approaches into optimization events in various fields.

The main limitation of the study is that both the traditional and proposed genetic algorithm approaches assume deterministic activity durations and costs. In practice, projects may involve uncertainty in these parameters [54]. The results at optimality might be subjected to variations as these parameters are subjected to changes. Nevertheless, it must be noted that the project crashing events are most of the time expressed in this format in the project management literature and potential solutions are developed accordingly. In addition, the steps followed in these approaches have been illustrated with a theoretical case rather than a real case. Illustration with a real case can be more influential and preferred in further studies. Further studies may also concentrate on the integration of the other metaheuristic algorithms (ant colony optimization, simulated annealing, particle swarm optimization, etc.) into various optimization events in different fields through following the steps expressed for the adaptation.

Article Information Form

Funding

The author(s) have not received any financial support for the research, authorship, or publication of this study.

Authors' Contribution

The authors contributed equally to the study.

The Declaration of Conflict of Interest/ Common Interest

No conflict of interest or common interest has been declared by the authors.

The Declaration of Ethics Committee Approval

This study does not require ethics committee permission or any special permission.

The Declaration of Research and Publication Ethics

The authors of the paper declare that they comply with the scientific, ethical and quotation rules of SAUJS in all processes of the paper and that they do not make any falsification on the data collected. In addition, they declare that Sakarya University Journal of Science and its editorial board have no responsibility for any ethical violations that may be encountered, and that this study has not been evaluated in any academic publication environment other than Sakarya University Journal of Science.

Copyright Statement

Authors own the copyright of their work published in the journal and their work is published under the CC BY-NC 4.0 license.

References

- [1] H. L. Chen, "Performance measurement and the prediction of capital project failure," *International Journal of Project Management*, vol. 33, no. 6, pp. 1393-1404, 2015.
- [2] E. Durna, B. Ozorhon, S. Caglayan, "Identifying critical success factors of public private partnership projects in Türkiye," *Sakarya University Journal of Science*, vol. 28, no. 1, pp. 30-50, 2024.
- [3] T. Huo, H. Ren, W. Cai, G. Q. Shen, B. Liu, M. Zhu, H. Wu, "Measurement and dependence analysis of cost overruns in megatransport infrastructure projects: Case study in Hong Kong," *Journal of Construction Engineering and Management*, vol. 144, no. 3, pp. 05018001, 2018.
- [4] P. Ballesteros-Perez, E. Sanz-Ablanedo, R. Soetanto, M. C. González-Cruz, G. D. Larsen, A. Cerezo-Narváez, "Duration and cost variability of construction activities: An empirical study," *Journal of Construction Engineering and Management*, vol. 146, no. 1, pp. 04019093, 2020.
- [5] C. Callegari, A. Szklo, R. Schaeffer, "Cost overruns and delays in energy megaprojects: How big is big enough?" *Energy Policy*, vol. 114, pp. 211-220, 2018.
- [6] G. Heravi, M. Mohammadian, "Investigating cost overruns and delay in urban construction projects in Iran," *International Journal of Construction Management*, vol. 21, no. 9, pp. 958-968, 2021.
- [7] S. Durdyev, "Review of construction journals on causes of project cost overruns," *Engineering, Construction and Architectural Management*, vol. 28, no. 4, pp. 1241-1260, 2020.
- [8] S. Zareei, "Project scheduling for constructing biogas plant using critical path method," *Renewable and Sustainable Energy Reviews*, vol. 81, pp. 756-759, 2018.
- [9] H. F. Rahman, R. K. Chakraborty, M. J. Ryan, "Memetic algorithm for solving resource constrained project scheduling problems," *Automation in Construction*, vol. 111, pp. 103052, 2020.
- [10] R. Pellerin, N. Perrier, F. Berthaut, "A survey of hybrid metaheuristics for the resource-constrained project scheduling problem," *European Journal of Operational Research*, vol. 280, no. 2, pp. 395-416, 2020.
- [11] M. Á. Vega-Velázquez, A. García-Nájera, H. Cervantes, "A survey on the software project scheduling problem," *International Journal of Production Economics*, vol. 202, pp. 145-161, 2018.
- [12] E. Osaba, E. Villar-Rodríguez, J. Del Ser, A. J. Nebro, D. Molina, A. LaTorre, P. N. Suganthan, C. A. C. Coello, F. Herrera, "A tutorial on the design, experimentation and application of metaheuristic algorithms to real-world optimization problems," *Swarm and Evolutionary Computation*, vol. 64, pp. 100888, 2021.

- [13] S. Katoch, S. S. Chauhan, V. Kumar, "A review on genetic algorithm: past, present, and future," *Multimedia Tools and Applications*, vol. 80, no. 5, pp. 8091-8126, 2021.
- [14] Y. Fang, S. T. Ng, "Genetic algorithm for determining the construction logistics of precast components," *Engineering, Construction and Architectural Management*, vol. 26, no. 10, pp. 2289-2306, 2019.
- [15] K. Kim, J. Walewski, Y. K. Cho, "Multiobjective construction schedule optimization using modified niched pareto genetic algorithm," *Journal of Management in Engineering*, vol. 32, no. 2, pp. 04015038, 2016.
- [16] S. Mirjalili, J. S. Dong, A. S. Sadiq, H. Faris, "Genetic algorithm: Theory, literature review, and application in image reconstruction," *Nature-Inspired Optimizers*, pp. 69-85, 2020.
- [17] M. S. El-Abbasy, A. Elazouni, T. Zayed, "MOSCOPEA: Multi-objective construction scheduling optimization using elitist non-dominated sorting genetic algorithm," *Automation in Construction*, vol. 71, pp. 153-170, 2016.
- [18] S. Sabharwal, P. Bansal, N. Mittal, S. Malik, "Construction of mixed covering arrays for pair-wise testing using probabilistic approach in genetic algorithm," *Arabian Journal for Science and Engineering*, vol. 41, no. 8, pp. 2821-2835, 2016.
- [19] A. Elkelesh, M. Ebada, S. Cammerer, S. ten Brink, "Decoder-tailored polar code design using the genetic algorithm," *IEEE Transactions on Communications*, vol. 67, no. 7, pp. 4521-4534, 2019.
- [20] Z. Tong, "A genetic algorithm approach to optimizing the distribution of buildings in urban green space," *Automation in Construction*, vol. 72, pp. 46-51, 2016.
- [21] S. M. Lim, A. B. M. Sultan, M. N. Sulaiman, A. Mustapha, K. Y. Leong, "Crossover and mutation operators of genetic algorithms," *International Journal of Machine Learning and Computing*, vol. 7, no. 1, pp. 9-12, 2017.
- [22] Z. Shen, A. Hassani, Q. Shi, "Multi-objective time-cost optimization using Cobb-Douglas production function and hybrid genetic algorithm," *Journal of Civil Engineering and Management*, vol. 22, no. 2, pp. 187-198, 2016.
- [23] M. Mangal, J. C. Cheng, "Automated optimization of steel reinforcement in RC building frames using building information modeling and hybrid genetic algorithm," *Automation in Construction*, vol. 90, pp. 39-57, 2018.
- [24] S. RazaviAlavi, S. AbouRizk, "Genetic algorithm-simulation framework for decision making in construction site layout planning," *Journal of Construction Engineering and Management*, vol. 143, no. 1, pp. 04016084, 2017.
- [25] L. Zhang, T. N. Wong, "An object-coding genetic algorithm for integrated process planning and scheduling," *European Journal of Operational Research*, vol. 244, no. 2, pp. 434-444, 2015.
- [26] M. Artar, A. Daloglu, "The optimization of multi-storey composite steel frames with genetic algorithm including dynamic constraints," *Technical Journal*, vol. 26, no. 2, pp. 7077-7098, 2015.
- [27] M. Rita, E. Fairbairn, F. Ribeiro, H. Andrade, H. Barbosa, "Optimization of mass concrete construction using a twofold parallel genetic algorithm," *Applied Sciences*, vol. 8, no. 3, pp. 399, 2018.
- [28] H. Sebaaly, S. Varma, J. W. Maina, "Optimizing asphalt mix design process using artificial neural network and genetic algorithm," *Construction and Building Materials*, vol. 168, pp. 660-670, 2018.

- [29] E. Hazir, T. Ozcan, K. H. Koç, "Prediction of adhesion strength using extreme learning machine and support vector regression optimized with genetic algorithm," *Arabian Journal for Science and Engineering*, vol. 45, pp. 6985-7004, 2020.
- [30] A. A. Chiniforush, M. Gharehchaei, A. A. Nezhad, A. Castel, F. Moghaddam, L. Keyte, D. Hocking, S. Foster, "Minimising risk of early-age thermal cracking and delayed ettringite formation in concrete—A hybrid numerical simulation and genetic algorithm mix optimisation approach," *Construction and Building Materials*, vol. 299, pp. 124280, 2021.
- [31] A. Kumar, N. Grover, A. Manna, R. Kumar, J. S. Chohan, S. Singh, S. Singh, C. I. Pruncu, "Multi-objective optimization of WEDM of aluminum hybrid composites using AHP and genetic algorithm," *Arabian Journal for Science and Engineering*, vol. 47, no. 7, pp. 8031-8043, 2022.
- [32] E. Uray, O. Tan, S. Carbas, I. H. Erkan, "Metaheuristics-based pre-design guide for cantilever retaining walls," *Technical Journal*, vol. 32, no. 4, pp. 10967-10993, 2021.
- [33] A. M. Rayeni, H. G. Arab, M. R. Ghasemi, "An effective improved multi-objective evolutionary algorithm (IMOEA) for solving constraint civil engineering optimization problems," *Technical Journal*, vol. 32, no. 2, pp. 10645-10674, 2021.
- [34] I. Costa-Carrapiço, R. Raslan, J. N. González, "A systematic review of genetic algorithm-based multi-objective optimisation for building retrofitting strategies towards energy efficiency," *Energy and Buildings*, vol. 210, pp. 109690, 2020.
- [35] Q. Li, L. Zhang, L. Zhang, X. Wu, "Optimizing energy efficiency and thermal comfort in building green retrofit," *Energy*, vol. 237, pp. 121509, 2021.
- [36] Y. Fan, X. Xia, "Energy-efficiency building retrofit planning for green building compliance," *Building and Environment*, vol. 136, pp. 312-321, 2018.
- [37] Y. He, N. Liao, J. Bi, L. Guo, "Investment decision-making optimization of energy efficiency retrofit measures in multiple buildings under financing budgetary restraint," *Journal of Cleaner Production*, vol. 215, pp. 1078-1094, 2019.
- [38] L. T. Le, H. Nguyen, J. Dou, J. Zhou, "A comparative study of PSO-ANN, GA-ANN, ICA-ANN, and ABC-ANN in estimating the heating load of buildings' energy efficiency for smart city planning," *Applied Sciences*, vol. 9, no. 13, pp. 2630, 2019.
- [39] S. N. Al-Saadi, K. S. Al-Jabri, "Optimization of envelope design for housing in hot climates using a genetic algorithm (GA) computational approach," *Journal of Building Engineering*, vol. 32, pp. 101712, 2020.
- [40] P. Pérez-Gosende, J. Mula, M. Díaz-Madroño, "Facility layout planning. An extended literature review," *International Journal of Production Research*, vol. 59, no. 12, pp. 3777-3816, 2021.
- [41] M. Oral, S. Bazaati, S. Aydinli, E. Oral, "Construction site layout planning: Application of multi-objective particle swarm optimization," *Technical Journal*, vol. 29, no. 6, pp. 8691-8713, 2018.
- [42] M. A. Brahami, M. Dahane, M. Souier, "Sustainable capacitated facility location/network design problem: a Non-dominated Sorting Genetic Algorithm based multiobjective approach," *Annals of Operations Research*, vol. 311, pp. 821-852, 2020.
- [43] A. Taghavi, R. Ghanbari, K. Ghorbani-Moghadam, A. Davoodi, A. Emrouznejad,

- “A genetic algorithm for solving bus terminal location problem using data envelopment analysis with multi-objective programming,” *Annals of Operations Research*, vol. 309, pp. 259-276, 2022.
- [44] S. Kumar, A. Sikander, “Optimum mobile robot path planning using improved artificial bee colony algorithm and evolutionary programming,” *Arabian Journal for Science and Engineering*, vol. 47, no. 3, pp. 3519-3539, 2022.
- [45] A. Mahdavian, A. Shojaei, “Hybrid genetic algorithm and constraint-based simulation framework for building construction project planning and control,” *Journal of Construction Engineering and Management*, vol. 146, no. 12, pp. 04020140, 2020.
- [46] J. Liu, Y. Liu, Y. Shi, J. Li, “Solving resource-constrained project scheduling problem via genetic algorithm,” *Journal of Computing in Civil Engineering*, vol. 34, no. 2, pp. 04019055, 2020.
- [47] R. L. Kadri, F. F. Boctor, “An efficient genetic algorithm to solve the resource-constrained project scheduling problem with transfer times: The single mode case,” *European Journal of Operational Research*, vol. 265, no. 2, pp. 454-462, 2018.
- [48] H. Li, L. Xiong, Y. Liu, H. Li, “An effective genetic algorithm for the resource levelling problem with generalised precedence relations,” *International Journal of Production Research*, vol. 56, no. 5, pp. 2054-2075, 2018.
- [49] W. Peng, J. Zhang, L. Chen, “A bi-objective hierarchical program scheduling problem and its solution based on NSGA-III,” *Annals of Operations Research*, vol. 308, no. 1, pp. 389-414, 2022.
- [50] Z. Wu, G. Ma, “Automatic generation of BIM-based construction schedule: Combining an ontology constraint rule and a genetic algorithm,” *Engineering, Construction and Architectural Management*, vol. 30, no. 10, pp. 5253-5279, 2023.
- [51] I. Behera, S. Sobhanayak, “Task scheduling optimization in heterogeneous cloud computing environments: A hybrid GA-GWO approach,” *Journal of Parallel and Distributed Computing*, vol. 183, pp. 104766, 2024.
- [52] S. Caglayan, S. Yigit, B. Ozorhon, G. Ozcan-Deniz, “A genetic algorithm-based envelope design optimisation for residential buildings,” *Proceedings of the Institution of Civil Engineers - Engineering Sustainability*, vol. 173, no. 6, pp. 280-290, 2020.
- [53] H. G. Lee, C. Y. Yi, D. E. Lee, D. Arditi, “An advanced stochastic time-cost tradeoff analysis based on a CPM-guided genetic algorithm,” *Computer-Aided Civil and Infrastructure Engineering*, vol. 30, no. 10, pp. 824-842, 2015.
- [54] S. Tao, C. Wu, Z. Sheng, X. Wang, “Stochastic project scheduling with hierarchical alternatives,” *Applied Mathematical Modelling*, vol. 58, pp. 181-202, 2018.

Additions to the Knowledge of the Flat Wasps Fauna of Türkiye (Hymenoptera, Bethyidae)

İlyas Can^{1*}, Serdar Tezcan², Jeroen de Rond³

¹ Tokat Gaziosmanpaşa University, Faculty of Arts and Science, Department of Biology, Tokat, Türkiye, ilyascan41@gmail.com

² Ege University, Faculty of Agriculture, Department of Plant Protection, İzmir, Türkiye, serdar.tezcan@gmail.com

³ Wederiklaan 10, 8245 JB, Lelystad, Netherlands, jeroen@naturalmedia.nl

*Corresponding Author

ARTICLE INFO

ABSTRACT

Keywords:

Türkiye

Bethylus

Cephalonomia

Goniozus

New record

Article History:

Received: 15.04.2024

Accepted: 02.08.2024

Online Available: 14.10.2024

To detect the natural enemies of *Scolytus rugulosus* (Muller, 1818) (Coleoptera: Curculionidae: Scolytinae), which is harmful to cherry trees, parasitoid wasp specimens were collected during field studies in the Kemalpaşa district of İzmir, Türkiye, between 1993 and 1995. This study evaluated 89 bethylid specimens collected in field studies. The wasps were collected by beating branches of cherry trees and reared on *S. rugulosus* larvae. All collected specimens were identified, and as a result, two previously unreported Bethyidae species, *Bethylus mandibularis* (Kieffer, 1904) and *Goniozus claripennis* (Förster, 1851) (Hymenoptera: Bethyidae), were recorded from Türkiye. The newly recorded species are briefly described and illustrated. Additional records are provided for *Cephalonomia hypobori* Kieffer, 1919, already reported from Türkiye. The number of species now known from the country has increased from 14 to 16, belonging to 14 genera and four subfamilies.

1. Introduction

The family Bethyidae (flat wasps) is a moderately large group of about 3000 known species [1, 2]. Members of this family are recognized mainly as gregarious ectoparasitoids developing on larvae of Coleoptera and Lepidoptera. Some members of the family Bethyidae are of interest as potential biological pest control agents [3].

Published records of Bethyidae from Türkiye are relatively scarce and only limited faunistic studies have been conducted on this group of insects by local and foreign researchers in this country [4–12]. Most recently, *Cephalonomia hypobori* Kieffer, 1919 was reported for the first time from Türkiye by Tezcan et al. [2]. The updated list of species of the flat wasp fauna, which reaches 14 species, was also presented in that study.

This study aims to identify the Bethyidae species collected during the research to determine the natural enemies of *Scolytus rugulosus* in the sweet cherry orchards of İzmir (Kemalpaşa district). As a result, two additional species, *Bethylus mandibularis* (Kieffer, 1904) and *Goniozus claripennis* (Foerster, 1851), were reported for the first time from Türkiye. The newly recorded species are briefly described and illustrated. In addition, new data about the previously known *Cephalonomia hypobori* was also shared.

2. Materials and Methods

The material was obtained from sweet cherry orchards in İzmir (Kemalpaşa), Western Türkiye, by beating and rearing in 1992-1995. Branches of trees infested by *S. rugulosus* were cut off, the tips were painted with paraffin wax to reduce drying, and the parasitoids were reared in cages

under lab conditions. At the same time, they were also reared under natural conditions in cages on the branches of the trees [13–15]. The material was preserved and stored in the Entomology Research Laboratory, Department of Biology, Tokat Gaziosmanpaşa University (Tokat, Turkey). While the second author carried out field studies and specimen collection, species identifications were made by the other two authors. The photographs of the specimens were taken using a Leica M205C stereomicroscope controlled by the Leica Application Suite 3 software.

3. Results

Bethylus mandibularis (Kieffer, 1904), *Goniozus claripennis* (Förster, 1851), and *Cephalonomia hypobori* Kieffer, 1919 were identified in this study, and the first two species were new records for the Turkish Bethylidae fauna. All newly recorded species belonged to the subfamily Bethylinae.

Subfamily Bethylinae

Genus *Bethylus* Latreille, 1802

Bethylus mandibularis (Kieffer, 1904) (Figures 1a-e)

Material examined (1 ♀): İzmir (Kemalpaşa), Central province, 02.VII.1995, beating from branches of *Prunus avium*, 1 ♀, leg. S. Tezcan, det. İ. Can and J. de Rond, 2024.

Global distribution: Iran, Italy, Spain, Scotland (doubtful record) [6, 16, 17].

Remarks: This species is reported from Türkiye for the first time in this article.

Brief description: Female. Body length 3.6 mm (Fig. 1a). Body mostly black, metasoma reddish brown. Antenna yellow to brown (Fig. 1c). Legs castaneous, tarsi reddish. Forewing hyaline tinged with yellow (Fig. 1e); veins and pterostigma castaneous. Head coriaceous with sparse punctures (Fig. 1d). The dorsal part of pronotal area and mesoscutum coriaceous with shallow punctures (Fig. 1b). Metapostnotal disc rugulose, median ridge elevated and shiny; lateral marginal carina incomplete, absent near

transverse anterior carina of metapectal-propodeal disc. Metasomal terga shiny with shallow tiny punctures.

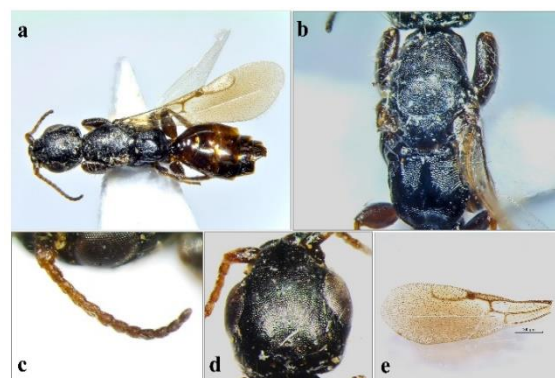


Figure 1. *Bethylus mandibularis* ♀; a) lateral habitus; b) mesosoma, dorsal view; c) antenna; d) head, dorsal view; e) forewing.

Genus *Goniozus* Förster, 1856

Goniozus claripennis (Förster, 1851) (Figures 2a-d)

Material examined (1 ♀): İzmir (Kemalpaşa), Central province, 23.VIII.1993, beating from branches of *Prunus avium*, 1 ♀, leg. S. Tezcan, det. İ. Can and J. de Rond, 2024.

Global distribution: Belgium, Czech Republic, Germany, France, Hungary, Iran, Italy, Norway, Russia, Slovakia, United Kingdom [18].

Remark: The species is reported from Türkiye for the first time in this article.

Brief description: Female. Body length: 3.9 mm (Fig. 2a). Body black; legs with coxa and femur testaceous, other segments yellow; antenna uniformly yellow except for the brownish scape; mandible brownish yellow, basal, dorsal, and ventral margins brownish; wings hyaline, pterostigma and prostigma testaceous, costa and subcosta light brown, other veins unpigmented. Basal part of metasoma testaceous. Head longer than wide; frons and vertex coriaceous with scattered shallow punctures (Fig. 2b). Clypeal carina strong and arcuate in profile. The dorsal part of the pronotum coriaceous with scattered shallow punctures, as in the head. Mesoscutum and scutellum shiny with sparse punctures. The median basal triangle of the metapectal propodeal disc smooth and polished, extended to the centre of the disc, connected to the posterior

transverse carina by a longitudinal carina; other parts of the disc and posterior declivity microreticulate (Fig. 2c). Forewing without areolet; Rs+M slightly curved at the apex (Fig. 2d).

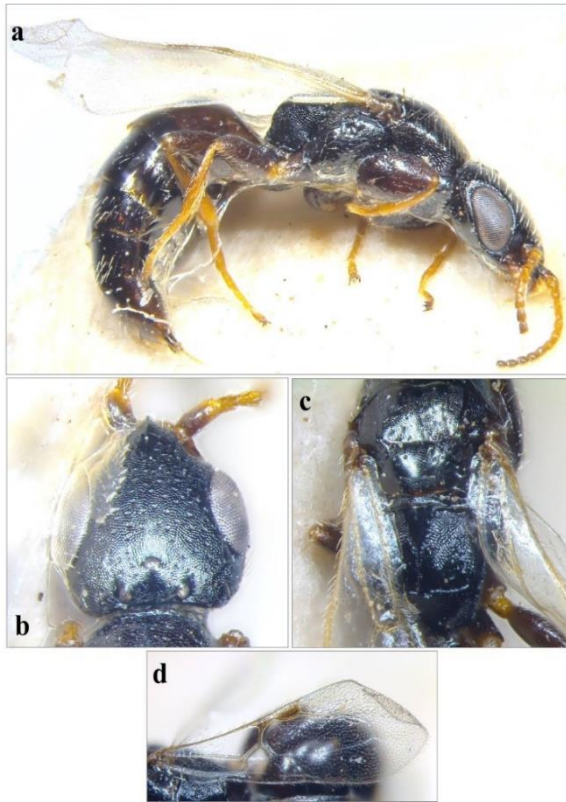


Figure 2. *Goniozus claripennis* ♀; a) lateral habitus; b) head, dorsal view; c) mesosoma, dorsal view; d) forewing.

Subfamily Scleroderminae

Genus *Cephalonomia* Westwood, 1833

Cephalonomia hypobori Kieffer, 1919 (Figures 3a-3b)

Material examined (83 ♀♀, 4 ♂♂): İzmir (Kemalpaşa), Central province, October 1992 / November 1992 reared from larvae of *Scolytus rugulosus*, 22 ♀♀, 2 ♂♂; 18.01.1993, reared from larvae of *S. rugulosus*, 1 ♀; 21.01.1993, reared from larvae of *S. rugulosus* in branches of *Prunus avium*, 1 ♀; 03.06.1993, reared from larvae of *S. rugulosus* in branches of *P. avium*, 23 ♀♀; 08.06.1993, beating from branches of *P. avium*, infested with *S. rugulosus*, 2 ♀♀; 02.07.1995, beating from branches of *P. avium*, 1 ♀; 27.07.1995, beating from branches of *P. avium*, 3 ♀♀, 3 ♂♂; **Ören**, 15.01.1993, reared from larvae of *S. rugulosus*, 1 ♀; 03.05.1993,

beating from branches of *P. avium*, infested with *S. rugulosus*, 1 ♀; 28.05.1993, reared from larvae of *S. rugulosus*, 1 ♀; 08.11.1993, reared from larvae of *S. rugulosus*, 3 ♀♀; 02.09.1994, reared from larvae of *S. rugulosus*, 1 ♀; **Sütçüler**, 11.03.1993, reared from larvae of *S. rugulosus*, 2 ♀♀; 14.06.1993, beating, from branches of *P. avium*, infested with *S. rugulosus*, 1 ♀; 08.11.1993, reared from larvae of *S. rugulosus*, 1 ♀; **Kuyucak**, 06.05.1993, reared from larvae of *S. rugulosus* in cages on the branches of *P. avium* under natural conditions, 1 ♀; 13.05.1993, reared from larvae of *S. rugulosus*, 2 ♀♀; 17.05.1993, reared from larvae of *S. rugulosus* in branches of *P. avium*, 1 ♀; 14.06.1993, beating, from branches of *P. avium*, infested with *S. rugulosus*, 3 ♀♀; 08.11.1993, reared from larvae of *S. rugulosus* in branches of *P. avium*, 1 ♀; 25.07.1994, beating, from branches of *P. avium*, infested with *S. rugulosus*, 1 ♀; 21.10.1994, beating, from branches of *P. avium*, infested with *S. rugulosus*, 2 ♀♀; **Bağyurdu**, 22.01.1993, reared from larvae of *S. rugulosus*, 4 ♀♀; 23.01.1993, reared from larvae of *S. rugulosus* in branches of *P. avium*, 2 ♀♀; **Örnekköy**, 09.09.1994, beating, from branches of *P. avium*, infested with *S. rugulosus*, 1 ♀ leg. S. Tezcan, det. J. de Rond, 2024.

Global distribution: Czech Republic, France, Iran, Israel, Italy, Morocco, Tunisia, Türkiye [2, 18].

4. Discussion

In the study carried out to determine the parasitoids that are the natural enemies of *Scolytus rugulosus*, which damages the cherry orchards in İzmir, three species belonging to the Bethylinidae family were identified: *Bethylus mandibularis*, *Cephalonomia hypobori* and *Goniozus claripennis*. *B. mandibularis* and *G. claripennis* are new records for the Turkish fauna.

It is known that species of *Bethylus* and *Goniozus* prefer various lepidopteran larvae as hosts [1]. Therefore, they are unrelated to *Scolytus rugulosus* and were caught incidentally in this study. These two species are probably parasitoids of the lepidopteran larvae found in the cherry orchards in Kemalpaşa. As a result of the studies

carried out in cherry orchards in Türkiye, it has been reported that there are 140 species/subspecies belonging to 21 families of Lepidoptera [19]. In previous studies conducted in cherry orchards in Manisa (Sultanyayla), a *Goniozus* species was reared from the larvae of *Archips rosana* (Linnaeus, 1758). However, the author was not able to identify it at the species level [f20].

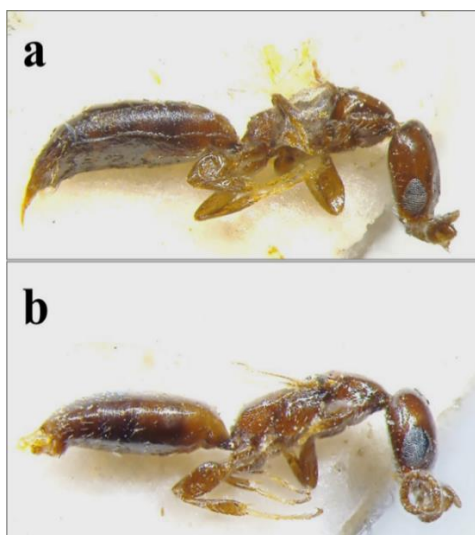


Figure 3. *Cephalonomia hypobori* a) female, lateral habitus; b) male, lateral habitus.

C. hypobori is a parasitoid of many larvae of Scolytinae species that manifest themselves as agricultural pests. The presence of this bethylid species in Türkiye has only recently been detected [2]. In this study, many specimens of this species were obtained by beating from branches and reared from larvae. Considering the large number of specimens of *C. hypobori*, it can be said that this species is a control agent that has significant potential to affect the population development of *S. rugulosus* in the study area. Nearly 30 years have passed since the field studies were carried out in this research. So, future studies should evaluate the extent to which this flat wasp is effective against *S. rugulosus* in the area.

Most Bethyridae species in Türkiye are often challenging to collect in the field because their habits are poorly known. It is evaluated that many potential discoveries regarding this poorly studied family can be made in Türkiye. In conclusion, we hope that future studies will provide more biological information, such as the species' host, distribution, and occurrence, and

use it as a reference in understanding the habits of these species.

Article Information Form

Acknowledgments

The authors would like to express their gratitude to Dr. H. S. Civelek and Ş. Karaman for field work and rearing. Research Fund of the Rectorate of Ege University for financial support of the project.

Funding

This study was supported by the Research Fund of the Rectorate of Ege University.

Authors' Contribution

The authors contributed equally to the study.

The Declaration of Conflict of Interest/ Common Interest

No conflict of interest or common interest has been declared by the authors.

The Declaration of Ethics Committee Approval

This study does not require ethics committee permission or any special permission.

The Declaration of Research and Publication Ethics

The authors of the paper declare that they comply with the scientific, ethical and quotation rules of SAUJS in all processes of the paper and that they do not make any falsification on the data collected. In addition, they declare that Sakarya University Journal of Science and its editorial board have no responsibility for any ethical violations that may be encountered, and that this study has not been evaluated in any academic publication environment other than Sakarya University Journal of Science.

Copyright Statement

Authors own the copyright of their work published in the journal and their work is published under the CC BY-NC 4.0 license.

References

- [1] C. O. Azevedo, I. D. C. C. Alencar, M. S. Ramos, D. N. Barbosa, W. D. Colombo, J. M. R. Vargas, J. Lim, "Global guide of the

- flat wasps (Hymenoptera, Bethylidae)". *Zootaxa*, vol. 4489, no. 1, pp. 1–294, 2018.
- [2] S. Tezcan, J. de Rond, H. S. Civelek, "Notes on the *Cephalonomia* (Hymenoptera: Bethylidae) species in sweet cherry orchards of Western Turkey". *Munis Entomology & Zoology*, vol. 19, no. 1, pp. 439-442, 2024.
- [3] S. Malabusini, I. C. W. Hardy, C. Jucker, G. Guanzani, S. Savoldelli, D. Lupi, "Reproductive performance effects of rearing the quasi-social parasitoid, *Sclerodermus brevicornis* (Hymenoptera: Bethylidae), on a factitious host". *Journal of Insect Science*, vol. 23, no. 5, pp. 1-9, 2023.
- [4] J. J. Kieffer, "Description de nouveaux hymenopteres". *Societe Scientifique de Bruxelles Annales*, vol. 30, pp. 136–140, 1906.
- [5] H. Ertürk, "Batı Anadolu incirlerinde zarar yapan Lepidopter'lerden Phycitidae familyası türleri ve bunlardan İncir kurdu (*Ephestia cautella* Walk.)'ın biyolojisi, zarar şekli ve mücadele imkanları üzerinde araştırmalar". Gıda-Tarım Bakanlığı, Bornova Zirai Mücadele Enstitüsü Yayını, No: 9, pp. 1-118, 1963.
- [6] G. Gordh, L. Móczár, "A catalog of the world Bethylidae (Hymenoptera: Aculeata)". *Memoirs of the American Entomological Institute*, vol. 46, pp. 1-364, 1990.
- [7] C. Öncüer, "A Catalogue of the Parasites and Predators of Insect Pests of Turkey". Ege Üniversitesi Ziraat Fakültesi Yayınları, İzmir, pp. 1-354, 1991.
- [8] Q. Argaman, "Generic synopsis of Mesitinae Kieffer, 1914 (Hymenoptera: Bethylidae)". *Entomofauna*, vol. 24, pp. 61–95, 2003.
- [9] I. K. Fadeev, "Review of the genera *Pristocera* Klug and *Pristepyris* Kieffer (Hymenoptera: Bethylidae, Pristocerinae) of Russia and adjacent territories". *Zootaxa*, vol. 4965, no. 3, pp. 461–482, 2021.
- [10] M. Doğanlar, B. Laz, "Notes on the parasitoid community of Bethylidae and Chalcidoidea (Hymenoptera) reared from *Gundelia tournefortii* L. (Asterales: Asteraceae) in Kahramanmaraş, Turkey". *Munis Entomology & Zoology*, vol. 17, no. 2, pp. 1104-1111, 2022.
- [11] İ. Can, "The Turkish Bethylidae (Hymenoptera, Chrysidoidea) fauna, with the new records of Epyrinae and Scleroderminae". *Zootaxa*, vol. 5169, no. 5, pp. 447-456, 2022.
- [12] İ. Can, "New findings of the family Bethylidae (Hymenoptera) from Türkiye". *Journal of Insect Biodiversity and Systematics*, vol. 9, no. 3, pp. 473-482, 2023.
- [13] S. Tezcan, H. S. Civelek, "Investigations on the distribution, damage, biology and natural enemies of Cherry bark beetle, *Scolytus rugulosus* Ratzeburg (Coleoptera: Scolytidae) in Kemalpaşa (Izmir) district, Turkey". Unpublished project report supported by the Research Fund of Ege University, 1994.
- [14] S. Tezcan, H. S. Civelek, "Investigations on the biology and damage of *Scolytus rugulosus* (Müller, 1818) (Coleoptera: Scolytidae) in cherry orchards of Kemalpaşa (Izmir) district (Turkey)" in III. Entomoloji Kongresi, Ankara, Turkey, Ankara Üniversitesi Basımevi, 1996, pp. 135-142.
- [15] S. Tezcan, H. S. Civelek, "Investigations on the determination of the natural enemies of *Scolytus rugulosus* (Müller) (Coleoptera: Scolytidae) in cherry orchards of Kemalpaşa (İzmir) district (Turkey)" in IV. Biyolojik Mücadele Kongresi, Adana, Turkey, 1999, pp. 333-340.
- [16] M. Kiany, F. Ehteshami, K. Minaei, J. de Rond, "Four new records for flat wasps

from Iran (Hymenoptera: Bethylidae” in Proceedings of the 4th National Conference on Environmental Sciences, Agriculture and Natural Resources; Hamadan, Iran, 2020.

- [17] N. S. Gadallah, M. Terayama, H. Ghahari, “An annotated catalogue of the Bethylidae (Hymenoptera: Chrysidoidea) of the Middle East, with special reference to the Iranian fauna.” *Oriental Insects*, vol. 58, no. 2, pp. 309-391, 2024.
- [18] H. Barahoei, N. Khajeh, C. O. Azevedo, M. Olmi, E. Rakhshani, “A review of Chrysidoidea (Hymenoptera, Aculeata), excluding Chrysididae of Iran.” *Journal of Insect Biodiversity and Systematics*, vol. 8, no. 4, pp. 617–645, 2022.
- [19] S. Tezcan, N. Gülperçin, “An evaluation on insect fauna of cherry agroecosystems of Turkey. Part III: Insecta: Neuroptera, Raphidioptera, Lepidoptera, Diptera, Hymenoptera.” *Munis Entomology & Zoology*, vol. 19, no. 1, pp. 461-508, 2024.
- [20] O. Ulu, “İzmir ve Manisa illeri çevresi taş çekirdekli meyve ağaçlarında zarar yapan *Archips* (= *Cacoecia* spp.) (Lepidoptera: Tortricidae) türleri, tanımları, konukçuları, yayılışları ve kısa biyolojileri üzerinde araştırmalar.” *Zirai Mücadele ve Zirai Karantina Genel Müdürlüğü, Bornova Bölge Zirai Mücadele Araştırma Enstitüsü Müdürlüğü Araştırma Eserleri, Seri No: 45, 165 pp., 1983.*

Eco-Friendly Green Synthesis of Zinc Oxide Nano/Microparticles Using Aqueous Leaf Extract of *Polygonum cognatum* Meisn. Plant

Erdem Akça 

Sivas Cumhuriyet University, Department of Metallurgical and Materials Engineering, Faculty of Engineering, Sivas, Türkiye, erdemakca@cumhuriyet.edu.tr

ARTICLE INFO

ABSTRACT

Keywords:

Green synthesis
Polygonum cognatum Meisn
Zinc oxide
Powder characterization
Nanoparticles



Article History:

Received: 04.05.2024
Accepted: 06.08.2024
Online Available: 14.10.2024

The environmentally friendly plant-based green synthesis approach provides a fabulous opportunity to produce versatile zinc oxide powders with multifarious morphology and/or size. In this study, it was mainly aimed at using *Polygonum cognatum* Meisn. extract to synthesize zinc oxide powder via a simple green synthesis route. For this purpose, zinc nitrate solution was mixed with an aqueous extract of fresh *Polygonum cognatum* Meisn. plant leaves to obtain a zinc-based precursor, and then zinc oxide powder was synthesized by means of calcination conducted at 400°C for 2 hours in air. Phase, spectroscopic, and microstructural analysis techniques, as well as Rietveld refinement method and Williamson-Hall analysis, were performed to investigate the powder characteristics. It was found that the synthesized high-purity zinc oxide powder had a hexagonal wurtzite crystal structure. Zinc oxide powder was observed to have a particularly large amount of nano-sized equiaxed particles (~25 nm in average diameter) together with micron-sized hourglass-like particles consisting of two hexagonal prisms (each <1 µm in height). All in all, the main implication of our research is that the *Polygonum cognatum* Meisn. plant can be potentially used as a biomass source for the green synthesis of zinc oxide nano/microparticles.

1. Introduction

Zinc oxide (ZnO) is an important inorganic material with multifunctional characteristics due to its unusual physical, chemical, or biological properties [1–3]. Therefore, it is unsurprising that ZnO attracts great attention in technological areas and scientific studies. In the global market, ZnO-based products are mainly demanded by various industries, ranging from rubber, ceramic, and paint manufacturing to agricultural, food, pharmaceutical, electronics [4–6]. It stands out that the scientific community has made tremendous efforts to improve the properties and performance of zinc oxide-based compounds, particularly in powdery forms. Nano- and micrometer-sized zinc oxide particles have been synthesized through chemical, physical, and biological processing approaches [4, 6–8].

Green synthesis routes, one of the most creative bottom-up synthesis methods, distinguish themselves from the others due to their straightforward implementation, cost-effectiveness, eco-friendliness, and safety characteristics. The green synthesis procedure is considered a cleaner, more reliable, and more sustainable technique since it mainly requires biomass resources, non-toxic solvents and results in negligible waste and pollutant formation [2, 6, 9–11].

Biogenic compounds are usually derived from the most abundant life forms, i.e., plants, bacteria, algae, fungi, etc., by simple extraction methods. Especially, plant-based phytochemicals with chemical functional groups are widely used for reducing, stabilizing, and/or capping agents for metallic ions in the solvents. There are innumerable scientific studies in the

literature related to laboratory-scale processing, characterizations, and applications of the green synthesis of zinc oxide particles [11–27].

Polygonum cognatum Meisn., colloquially known as "Madımak", belongs to the Polygonaceae family, which is a perennial plant that grows naturally in various regions of Anatolia in Türkiye at altitudes ranging from 720 to 3000 meters. The shoots and leaves of this plant are usually consumed as meals in Central Anatolian cuisine, as well as used for some traditional medicinal purposes [28–37]. *Polygonum cognatum* Meisn. contains phytochemical compounds, i.e., phenolics, vitamins, flavonoids, and carotenoids together with some macro- and micro-nutrients [28, 29, 31–38]. Moreover, previous studies have shown the presence of antioxidant, antimicrobial, cytotoxic, or antiproliferative activities in extracts derived from this plant [28, 31, 35, 36, 38–40]. Recently, many scientists have shown great interest in the *Polygonum cognatum* spices for research and development activities in the fields of medicine, pharmacy, agriculture, biology, chemistry, biochemistry, etc.

Polygonum cognatum plant extract possesses potential phytochemicals that can be used for green synthesis; however, there are few papers related to the biosynthesis of nano-sized particles using *Polygonum cognatum* plant extract in the literature. It was reported that metallic nanoparticles of copper, iron, or silver (ranging from 20 to 100 nm) were synthesized through extracts derived from *Polygonum cognatum* plant [41–43]. In addition, magnetite-reduced graphene oxide particles prepared using the aqueous extract of *Polygonum cognatum* as a stabilizing and reducing agent [44]. To the best of our knowledge, there is a gap in the literature about the green synthesis of metal oxide particles by using *Polygonum cognatum* spices. We believe that the *Polygonum cognatum* Meisn. plant could be a promising natural resource for green chemistry processing of metal oxide particles due to its bioactive components.

The main motivation of this study is to demonstrate the green synthesis of ZnO particles

by using the *Polygonum cognatum* Meisn. plant. For this purpose, the aqueous extract was first obtained from the fresh leaves of the *Polygonum cognatum* Meisn. plant collected in Sivas Province, Türkiye. Next, the reaction between zinc nitrate hexahydrate and plant extract solutions yielded the precursor. Finally, zinc oxide was synthesized via solid-state calcination of the precursor, and XRD, SEM/EDS, STEM analyses, as well as spectroscopic characterizations (FT-IR, UV-Vis, and Raman spectroscopy) were carried out.

2. Materials and Methods

Zinc nitrate hexahydrate ($\text{Zn}(\text{NO}_3)_2 \cdot 6\text{H}_2\text{O}$) ($\geq 98\%$, Tekkim) was the sole chemical raw material as a zinc source used as received without further purification in this study. Figure 1 shows the steps of the green synthesis for zinc oxide in detail.

In the first step, fresh *Polygonum cognatum* Meisn. plant collected in rural areas of Sivas Province (Türkiye) was purchased from the domestic market hall located in the downtown. The plant was kept in tap water in the deep, transparent container for a while. Thereby, it was easy to remove dirt and unwanted foreign substances since those had sunk to the bottom. Following that, we repeatedly washed the plant leaves, which had separated from the stem, in distilled water.

In the second step, 40 grams of fresh leaves were soaked in 400 ml of distilled water in a 600 ml beaker and mixed for 2 hours on a hot plate at 75°C with continuous stirring. The beaker was covered by PVC cling film to minimize evaporation during the process. Also, the constant temperature was maintained by using an external thermocouple attached to the magnetic stirrer. The mixture, which turned into a brownish-green color, was left for a while in the laboratory to cool down naturally to room temperature. The extract solution was filtered through Whatman filter paper (No. 1) and centrifuged at 15,000 rpm for 3 min. Subsequently, it was stored in the refrigerator until the next use.



Figure 1. Detailed processing steps for the green synthesis of zinc oxide particles

In the third step, 50 ml of the extract solution poured into a 250 ml beaker on a hot plate was heated up with continuous stirring at 400 rpm until temperature reached 60°C. Then, 50 ml of 1 M zinc nitrate hexahydrate solution was gradually dripped into the heated extract solution. During this process, the formation of suspended gel-like small particles in the mixture, which was probably due to the reaction between zinc ions and bioactive compounds, could be immediately observed. The mixture with 50:50 (% v/v) in a covered beaker was stirred at 300 rpm at 60°C for 3 h.

Subsequently, the temperature of the hot plate was increased above 100°C to evaporate the excess water in the heated mixture. Also, a fan was placed on the beaker after removing the PVC cling film. Meanwhile, the mixture turned into a viscous fluid with a brownish-orange color during the 7-hour heating procedure. 75 ml of distilled water was poured into the viscous fluid and then sonicated for 15 min. It was transferred into the polypropylene measuring cylinder to ensure the spontaneous sinking of the precipitate to the bottom. The supernatant was removed for each step before refreshing the water. Thereby, the precipitate was rinsed with distilled water several times to remove any unwanted excess. Eventually, dried participate was put in the porcelain crucible and calcined at 400°C for 2 h with 5°C/min heating and cooling rates in air.

The phase formation of the powder was checked by an X-ray diffractometer (XRD) (Rigaku Miniflex600, Japan) using $\text{CuK}\alpha$ radiation. Rietveld refinement for the XRD data of ZnO powder was carried out using MAUD software (Materials Analysis Using Diffraction, Version 2.9993) [45]. Microstrain (ϵ) and crystallite size (D) were determined by using Williamson-Hall analysis [46]. The microstructure and elemental analysis of powder were examined by a field emission scanning electron microscopy (SEM) equipped with an energy dispersive spectroscopy (EDS) detector and a STEM detector (TESCAN MIRA3 XMU). Attenuated total reflection Fourier-transform infrared (ATR-FTIR) spectrum was recorded in the range of 4000–400 cm^{-1} (Bruker, Tensor II). A UV–Vis diffuse reflectance spectroscopy (Thermo Scientific Evolution 201) was used to determine the band gap of ZnO in the wavelength range of 200–800 nm. The Raman spectrum of calcined powder was measured directly by using Raman spectroscopy with a 532 nm laser (Jasco NRS4500 confocal Raman microspectroscopy) performed between 95 and 875 cm^{-1} .

3. Results and Discussion

Figure 2 shows the X-ray diffraction patterns of green synthesized powder zinc oxide calcined at 400°C for 2 h. The peaks observed at $2\theta = 31.76^\circ$ (100), 34.42° (002), 36.26° (101), 47.54° (102), 56.58° (110), 62.84° (103), 66.36° (200), 67.97° (112), 69.08° (201), 72.58° (004), and 76.92°

(202) nicely correspond to the characteristic peaks of zincite crystal (JCPDS card # 36-1451). In addition, Rietveld analysis was performed to determine the crystal structure of synthesized ZnO particles based on the Crystallographic Information File (CIF) of the zincite mineral (card no. 2300450) obtained from Crystallography Open Database [47]. During the refinement process, all indexed peaks were used, excluding the $K\beta$ peak (at $2\theta \sim 28^\circ$) arose from the instrumental setup. The experimental diffraction data (Y_{obs}), the calculated diffraction data (Y_{cal}), and their difference ($Y_{\text{obs}} - Y_{\text{cal}}$) were demonstrated in Figure 2, as well as the peak positions of zincite (vertical blue lines).

The Rietveld refinement output of R_b (%) = 6.83, R_{wp} (%) = 7.65, R_{exp} (%) = 3.41, and $\chi^2 = 2.24$ obviously indicated that the calculated data was in good agreement with the observed ones. In other words, the XRD pattern revealed that the peaks match well with the zincite ZnO. Besides, the lattice parameters such as unit cell lengths, angles, and volume for synthesized particles were computed as $a=b= 3.2508 \text{ \AA} \pm 7.59\text{E-}5$, $c= 5.2074 \text{ \AA} \pm 1.37\text{E-}4$ ($c/a= 1.60188$), $\alpha=\beta= 90^\circ$, $\gamma= 120^\circ$, and $V= 47.656 \text{ \AA}^3$. It means that the green synthesized zinc oxide particles clearly possess a hexagonal wurtzite-type crystalline structure.

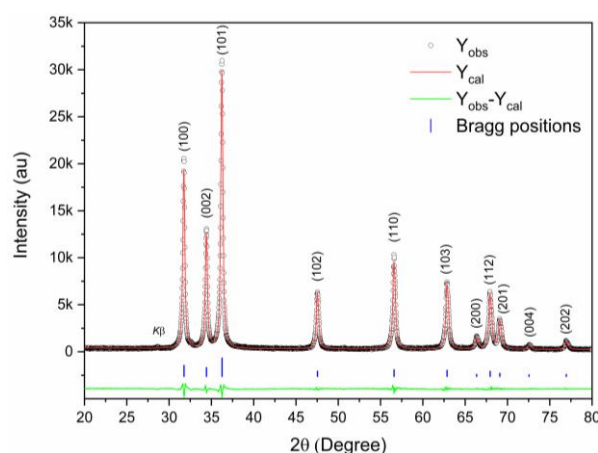


Figure 2. X-ray diffraction patterns of green synthesized calcined zinc oxide powder and Rietveld refinement result

Meanwhile, bond length (L) between Zn and O was calculated as 1.9783 \AA by using lattice parameters based on the equation (1) [48].

$$L = \sqrt{\left(\frac{a^2}{3} + c^2 \left(\frac{1-2u}{2}\right)^2\right)} \quad (1)$$

where both a and c are unit cell lengths, u is the positional parameter ($u = [1/4 + 1/3 (a/c)^2]$). On the other hand, Williamson-Hall analysis was carried out based on the equation (2) to determine the lattice strain and crystallite size of green synthesized zinc oxide powder [46].

$$\beta_{hkl} \cos \theta = \frac{K\lambda}{D} + 4\epsilon \sin \theta \quad (2)$$

where β_{hkl} is the peak broadening, K is the shape factor (0.94), λ is the wavelength of $\text{CuK}\alpha$ radiation (1.5406 \AA), D is crystallite size, and ϵ is the lattice microstrain. β_{hkl} values were

obtained from the full width of half maximum (FWHM) of each XRD peak estimated by using the Voigt model. Figure 3 depicts the Williamson-Hall plot together with linear regression results for green synthesized zinc oxide powder. The crystallite size (D) and microstrain (ϵ) values, which are obtained by the intercept on the y-axis and the slope of linear fit line, respectively, are 48 nm and 0.00133 for calcined zinc oxide powder.

Powder characteristics could differ based on the processing conditions, raw materials, ingredients, etc. For example, the crystallite size and microstrain values for ZnO powders synthesized via similar green routes by using various plant-based extracts and calcined at 400°C were reported to be $D = 4.5\text{-}17.8 \text{ nm}$ and $\epsilon = 0.0065\text{-}0.0078$ in a previous work [49], whereas another study reported $D \approx 35 \text{ nm}$ and $\epsilon = 0.000346$ [50].

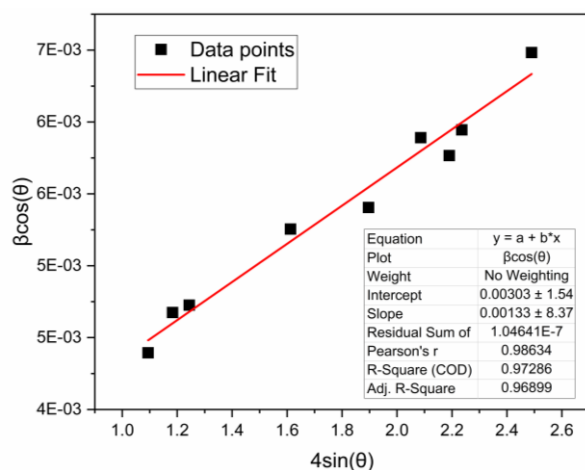


Figure 3. Williamson-Hall plot of green synthesized zinc oxide powder

FTIR spectroscopy is a practical tool for analyzing the functional groups of materials. Figure 4 depicts the room-temperature ATR-FTIR spectrum of the green synthesized ZnO particles taken in the range between 400 and 4000 cm^{-1} . All prominent absorption peaks at

479, 552, 705, 1055, 1396, 1624, 2097, 2343, and 3382 cm^{-1} were marked in the FTIR spectrum. The absorption peaks observed at 479, 552, and 705 cm^{-1} highly likely belong to zinc oxide with a hexagonal wurtzite structure. The absorption bands around 400-700 cm^{-1} were reported to be

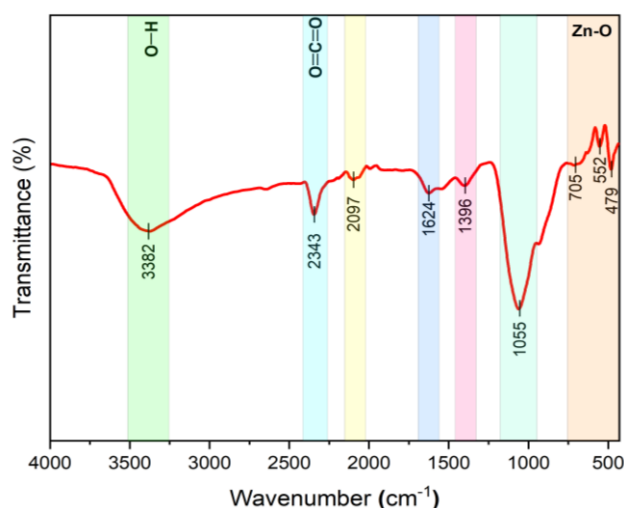


Figure 4. ATR-FTIR spectrum of green synthesized zinc oxide particles

associated with the Zn–O stretching in the zinc oxide lattice in previous works [20, 22, 49–55]. Especially, the strong peak at 479 cm^{-1} that appeared in the FTIR spectrum was very close to the ones stated as the characteristic absorption peak for ZnO. On the other hand, the explicit peaks at ~ 2343 and 3382 cm^{-1} were undoubtedly corresponding to the characteristic O–H stretching and O=C=O stretching arising from atmospheric moisture and carbon dioxide, respectively [14, 20, 55]. In addition, there were some divergent evaluations about the other absorption bands between ~ 1000 and 3000 cm^{-1} could belong to various functional groups of organic compounds with stretching or bending

vibrations, i.e. C=C, C=O, C–N, C–H, etc [14, 20, 49, 51, 53]. Meanwhile, it was also possible that some residual matters, resulting from organic extracts used for the green synthesis of zinc oxide, remained in the structure due to the low heat treatment procedure [20, 22, 50, 55].

Raman spectroscopy is one of the most useful characterization techniques that provides insight into the chemical fingerprints of various materials. Figure 5 shows the room-temperature Raman spectrum of the green synthesized ZnO particles taken in the spectral range between 95 and 875 cm^{-1} . All distinguishable peaks at 100, 118, 165, 263, 334, 380, 410, 438, 579, 685, and

812 cm^{-1} were marked in the Raman spectrum. The optical phonons (Γ_{opt}) at the center of the Brillouin zone can be described as $\Gamma_{\text{opt}} = A_1 + E_1 + 2E_2 + 2B_1$ for the crystalline zinc oxide with a

hexagonal wurtzite structure, which is a member of the $P6_3mc$ space group. The Raman active polar modes of A_1 and E_1 split into the vibration modes of transverse optical (TO) and longitudinal

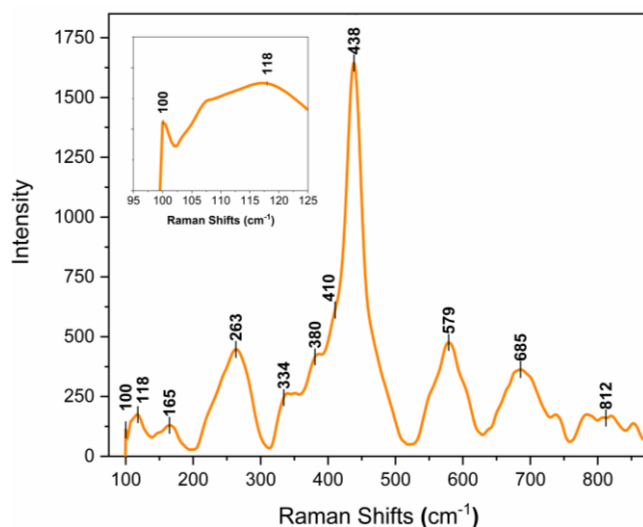


Figure 5. Room-temperature Raman spectrum of green synthesized zinc oxide particles

optical (LO), whereas E_2 modes (E_2^{low} and E_2^{high}) are Raman active but exhibiting a non-polar nature. On the other hand, the B_1 modes are silent, in other words, Raman inactive [56]. The peaks at 100 cm^{-1} and 438 cm^{-1} are the characteristic phonon modes belonging to ZnO, designated as E_2^{low} and E_2^{high} , respectively [56, 57]. The vibration of zinc atoms results in low-frequency phonon mode (E_2^{low}), whereas high-frequency phonon mode (E_2^{high}) is associated with the vibration of oxygen atoms. On the other hand, the sharp intense peak observed at 438 cm^{-1} is an obvious indication of the hexagonal wurtzite structure of zinc oxide [58–60].

Meanwhile, the peaks at 118 cm^{-1} and 165 cm^{-1} could arise from E_2^{low} asymmetric tail ($E_2^{\text{low, tail}}$) modes [57]. The peaks located at 334 cm^{-1} and 410 cm^{-1} are related to the $E_2^{\text{high}}-E_2^{\text{low}}$ and $E_1(TO)$, respectively [56]. As for the Raman active polar of A_1 , the peaks at 380 cm^{-1} and 579 cm^{-1} highly likely correspond to $A_1(TO)$ and $A_1(LO)$ modes, respectively [56, 57]. The peaks at 263 and 812 cm^{-1} could be associated with the B_1 silent modes. Those modes were reported as B_1^{low} at 261 cm^{-1} and $B_1^{\text{low}}+B_1^{\text{high}}$ at 810 cm^{-1} [61], which were predicted by the calculations for wurtzite-type zinc oxide in earlier works. The silent peaks seen in the Raman spectrum of zinc oxide could be activated due to the lattice disorder or defects triggered by impurities,

dopants, secondary phases, or processing conditions [56, 58, 61].

The activation of the Raman inactive B_1 silent modes was believed to be linked to probable minor amounts of elements resulting from raw materials and/or plant extract used for green synthesized zinc oxide. On the one hand, we assumed that the peak at 685 cm^{-1} was a combination of several peaks nearby. According to peak-fit analysis (not shown here), there were highly likely two separated multiphonon peaks at 674 and 700 cm^{-1} , which was in good agreement with the literature results [56, 57].

Figure 6 shows the UV-Vis spectrum of synthesized zinc oxide powder in the range between 200 and 800 nm, together with the Tauc plot. There is an obvious absorption peak appeared at 375 nm, which is within the UVA region, in the UV-Vis spectrum of the powder. The absorption peak values were reported to be typically between 367 and 393 nm for various zinc oxide powders synthesized by means of the plant-based green chemistry route [14, 27, 49, 50, 53].

The absorption peak at 375 nm was close to the characteristic peak for ZnO with a hexagonal wurtzite crystal structure. In some cases, a red-shift or blue-shift of the absorption peak for ZnO

in the UV-Vis spectrum could be observed due to the processing parameters (i.e., impurities, doping, concentration, calcination temperature, etc.) [14, 49, 50]. The Tauc plot (see inset in Figure 6.) was used to ascertain the optical band gap energy (E_g) of synthesized zinc oxide

powder. The plot of energy vs $(\alpha h\nu)^2$, in other words, the Tauc plot, was obtained based on the equation (3) [62].

$$(\alpha h\nu)^{1/\gamma} = A(h\nu - E_g) \quad (3)$$

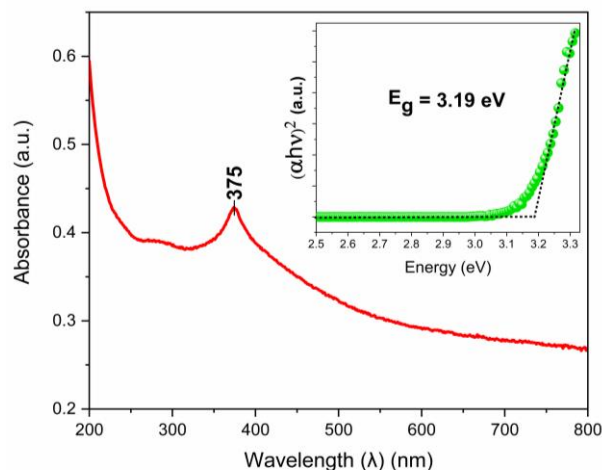


Figure 6. UV-Vis spectrum of the zinc oxide powder and the Tauc plot

where α is the energy-dependent absorption coefficient, h is the Planck's constant, ν is the photon's frequency, A is energy-independent constant, E_g is the optical band gap energy, and γ is the coefficient related to the nature of the electron transition and corresponds to $1/2$ or 2 for direct and indirect allowed transition band gaps, respectively. The direct E_g was represented by the intersection of the x -axis of the Tauc plot, which was determined with the help of the extrapolation of linear fitting, where an abrupt increase in the values of $(\alpha h\nu)^2$. The direct E_g of synthesized zinc oxide powder was estimated at 3.19 eV. It is known that the direct E_g is approximately 3.37 eV for zincite mineral with a hexagonal wurtzite crystal structure [4, 21]. In addition, it is seen that direct bandgap values between 3 and 3.37 eV to have been reported for pure zinc oxide powder produced by various green synthesis methods in the literature [14, 20, 49, 63].

Figure 7 demonstrates the SEM micrographs and EDS analyses of calcined powder. The low-magnification image in Figure 7a represents the general view of agglomerated calcined powder. There are three distinct types of particle shapes, such as nano-sized round-like, micron-sized hourglass-like, and sub-micron plate-like shown in Figure 7b-d. Plenty of nano-sized round-like

particles stand out as well as a considerable amount of micron-sized hourglass-like particles and few amounts of sub-micron plate-like particles. It is highly likely that several bioactive phytochemical compounds, especially phenolics, vitamins, flavonoids, or carotenoids in the *Polygonum cognatum* Meisn. extract, act as reducing, stabilizing, and/or capping agents for Zn^{2+} metallic ions in the solution. During the green synthesis procedure, disassociated Zn^{2+} ions from zinc nitrate solution were probably attached to functional groups of biogenic compounds in the extract due to interaction between them; therefore, the nucleation arose in the early stages of the process. Then, particle growth occurred as a result of the Ostwald ripening mechanism, and thereby a zinc-based intermediate complex precipitated [2, 9, 10, 12, 13, 21].

Besides, a calcination procedure (200 - 900°C , most preferably about 400°C) is usually required to transform an intermediate compound consisting of the coalescence of very small precursors into crystalline pure zinc oxide nano- or micro-particles [2, 16, 20, 50]. During the solid-state calcination step, smaller particles are basically consumed by bigger ones thanks to the Ostwald ripening mechanism. Particularly, the agglomeration tendency of nano-sized particles

with higher surface energy is supposed to have been responsible for the formation of bigger, micron-sized hexagonal columnar particles via the heat treatment process.

The exiting of small precipitates on the hexagonal columnar particles seen in Figure 7c was considered as the evidence of the aforesaid growth mechanism. Meanwhile, hexagonal

prism-shaped zinc oxide particles essentially resembled hourglass-like morphology (max. ~ 2 μm in height). Similar micron-sized zinc oxide particles were reported to be synthesized by various methods [64–68], i.e. chemical bath deposition, hydrothermal, sol-gel, combined ultrasonic/microwave irradiation, etc. Indeed, the hourglass-like morphology consisted of two

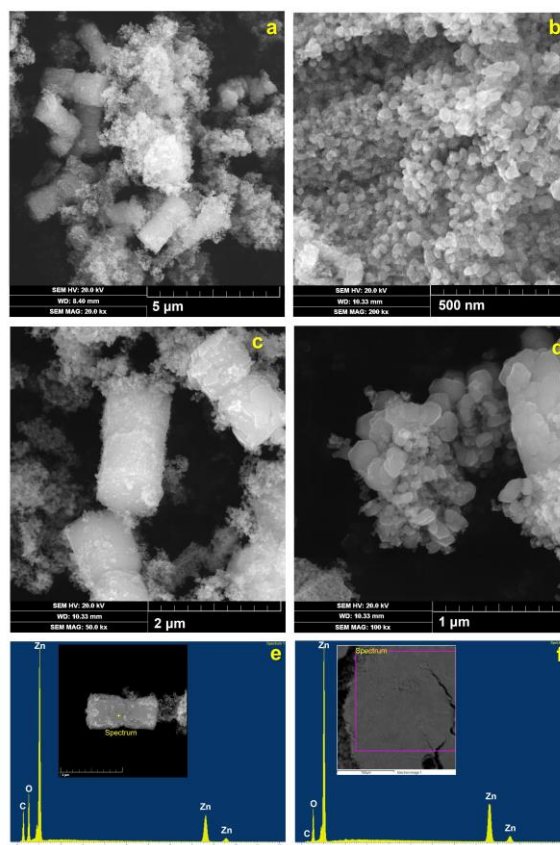


Figure 7. SEM micrographs and EDS analyses of green synthesized ZnO particles. General view of agglomerated calcined powder (a), nano-sized round-like particles (b), micron-sized hourglass-like particles (c), sub-micron plate-like particles (d), EDS spectrum of hourglass-like particle (e), and EDS spectrum of synthesized zinc oxide powder (f)

identical hexagonal prisms, that is, dimer structure.

Each ZnO microcrystal with a hexagonal prism shape typically possesses two polar planes: (0001) at the top and (000 $\bar{1}$) at the down of the wurtzite unit cell. Previous studies highlighted the effects of the Ostwald ripening phenomenon, van der Waals interaction, and/or electrostatic interactions on the nucleation, the aggregation of small particles, and the formation of hexagonal dimer structures of ZnO [65, 66, 68]. It was believed similar mechanism(s) resulted in the formation of small-sized truncated hexagonal prisms with approximately 800 ± 100 nm in

height and 500 ± 50 nm in side-length of base in the first stages of the process. It was highly likely that the final hourglass-like dimer structure emerged when two hexagonal prisms joined each other by virtue of the coupling of their (0001) planes [65, 66, 68].

EDS analysis clearly indicated that the presence of zinc and oxygen atoms for the individual hourglass-like particle shown in Figure 7e. According to the ESD analysis taken from the larger area of the suppressed powder shown in Figure 7f, atomic ratios were found to be 44.59% of Zn, 54.50% of O, 0.53% of P, 0.22% of S, and 0.13% of Cl, except for C from conductive

carbon tape. Note that characteristic peaks of negligible amounts of minor elements cannot be well distinguishable compared to the main elements (Zn and O) in the EDS spectrum in Figure 7f. Some residual elements were known to remain in the green synthesized zinc oxide by using the plant extract after even high-temperature calcination ($\geq 400^\circ\text{C}$) [14, 50].

For instance, *Polygonum cognatum* Meisn. plant extract was reported to involve some elements such as P, S, Cl, N, etc. in previous works [31, 69]. Also, residual elements could be attributed to the used zinc nitrate hexahydrate raw material with $\geq 98\%$ purity, which was used in this study. Regardless of the origin of residuals, the existence of minor elements was believed to be associated with their energetic stability at the calcination temperature of 400°C . This temperature was very close to the most preferred ones for synthesized zinc oxide powders in the literature. Actually, the aim of the calcination is to ensure the formation of a crystalline phase together with the decomposition and/or burnout of residual matters come from the plant extract. Maybe a higher calcination temperature is useful in terms of being free from residuals; however, the risk of the exaggerated particle growth and the deterioration of morphology should be taken into account at the same time. Given that the overall phase characteristics of green synthesized

zinc oxide in our study were in good agreement with those reported in the literature, the calcination temperature of about 400°C was believed to be reasonable.

Figure 8 depicts the STEM images of nanoparticles separated from synthesized zinc oxide powder, particle size distribution, and the Tyndall effect of colloidal suspension. Figure 8a-b shows STEM images of nanoparticles isolated from synthesized zinc oxide powder by simple procedure. Briefly, a small amount of ZnO powder was added to distilled water and subjected to ultrasonic energy, then kept stationary. It was observed that the larger particles settled down immediately owing to the gravitational force, while nanoparticles suspended in the distilled water exhibited colloidal dispersion behavior. The isolated nanoparticles stand out as having a virtually equiaxed particle shape together with 24.8 nm of mean particle size, as seen in Figure 8c. In addition, the Tyndall effect was conspicuously observed for nanoparticles suspended in the distilled water that exhibited colloidal dispersion behavior because the light beam from the laser source dramatically scattered due to the strong interaction with the suspended nanoparticles (see Figure 8d). On the contrary, the light was invisible in distilled water because it directly passed through without any interaction.

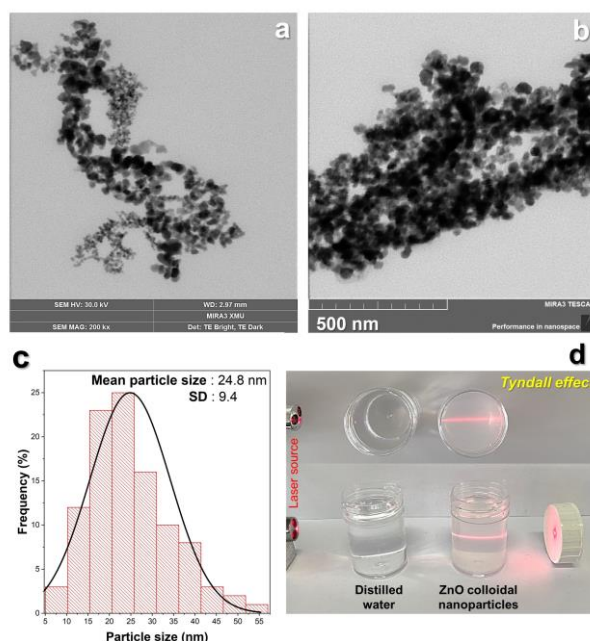


Figure 8. STEM image of nanoparticles (a-b), particle size distribution (c), the Tyndall effect of colloidal zinc oxide particles (d).

Indeed, the number, morphology, size, and purity of the particles strongly depend on the process parameters of the green synthesis procedure, especially the type of plant species and their ingredients, the concentration of the raw material and extract, the pH of the solutions, reaction time and temperature, calcination temperature, etc. In this study, we essentially focused on the specific process parameters to find out whether or not the *Polygonum cognatum* Meisn. could be a promising plant in terms of the green synthesis of zinc oxide. In the light of these results, particle characteristics, especially size and morphology, of zinc oxide particles can be tailored for various applications by using *Polygonum cognatum* Meisn. extract thanks to future systematic studies.

4. Conclusion

The aim of the current study is to reveal the potential of using *Polygonum cognatum* Meisn. plant extract in the green synthesis of zinc oxide powder. Zinc oxide powder was synthesized via the calcination at 400°C for 2 hours of the precursor, which was obtained by mixing zinc nitrate solution and *Polygonum cognatum* Meisn. aqueous leaf extract with the specific process conditions. X-ray diffraction, spectroscopic, and microstructural analysis techniques were used for the powder characterizations.

The results obviously demonstrated that the synthesized powder was pure zinc oxide with a hexagonal wurtzite crystal structure ($a=b=3.2508 \text{ \AA}$, $c=5.2074 \text{ \AA}$, $\alpha=\beta=90^\circ$, and $\gamma=120^\circ$). The crystallite size and microstrain values were estimated at 48 nm and 0.00133, respectively. The direct allowed E_g was calculated as 3.19 eV based on the absorption peak observed at 375 nm in the UV-Vis spectrum of zinc oxide powder. It was found that equiaxed nanoparticles with a mean particle size of ~25 nm were accompanied by hourglass-like microparticles, which consisted of two hexagonal prisms with a height of <1 μm each. In conclusion, the main implication of this study is that the *Polygonum cognatum* Meisn. plant extract can be a promising biomass source to tailor the green synthesis of zinc oxide nano/microparticles with various morphologies, which can be used for numerous technological applications.

Article Information Form

Funding

The author has not received any financial support for the research, authorship, or publication of this study.

The Declaration of Conflict of Interest/ Common Interest

No conflict of interest or common interest has been declared by the authors.

The Declaration of Ethics Committee Approval

This study does not require ethics committee permission or any special permission.

The Declaration of Research and Publication Ethics

The authors of the paper declare that they comply with the scientific, ethical and quotation rules of SAUJS in all processes of the paper and that they do not make any falsification on the data collected. In addition, they declare that Sakarya University Journal of Science and its editorial board have no responsibility for any ethical violations that may be encountered, and that this study has not been evaluated in any academic publication environment other than Sakarya University Journal of Science.

Copyright Statement

Authors own the copyright of their work published in the journal and their work is published under the CC BY-NC 4.0 license.

References

- [1] A. Czyżowska, A. Barbasz, "A review: zinc oxide nanoparticles – friends or enemies?," *International Journal of Environmental Health*, vol. 32, no. 4, pp. 885–901, 2022.
- [2] S. Zeghoud, H. Hemmami, B. Ben Seghir, I. Ben Amor, I. Kouadri, A. Rebiai, M. Messaoudi, S. Ahmed, P. Pohl, J. Simal-Gandara, "A review on biogenic green synthesis of ZnO nanoparticles by plant biomass and their applications," *Materials Today Communications*, vol. 33, Dec. 2022, Art. no. 104747.

- [3] C. B. Ong, L. Y. Ng, A. W. Mohammad, "A review of ZnO nanoparticles as solar photocatalysts: Synthesis, mechanisms and applications," *Renewable and Sustainable Energy Reviews*, vol. 81, pp. 536–551, Jan. 2018.
- [4] A. Kołodziejczak-Radzimska, T. Jesionowski, "Zinc Oxide—from synthesis to application: A review," *Materials*, vol. 7, no. 4, pp. 2833–2881, Apr. 2014.
- [5] P. Sharma, M. R. Hasan, N. K. Mehto, Deepak, A. Bishoyi, J. Narang, "92 years of zinc oxide: has been studied by the scientific community since the 1930s- An overview," *Sensors International*, vol. 3, Jan. 2022, Art. no. 100182.
- [6] S. Raha, Md. Ahmaruzzaman, "ZnO nanostructured materials and their potential applications: progress, challenges and perspectives," *Nanoscale Advances*, vol. 4, no. 8, pp. 1868–1925, 2022.
- [7] G. Dutta, A. Sugumaran, "Bioengineered zinc oxide nanoparticles: Chemical, green, biological fabrication methods and its potential biomedical applications," *Journal of Drug Delivery Science and Technology*, vol. 66, Dec. 2021, Art. no. 102853.
- [8] K. Bachhav, A. S. Garde, "Versatile synthesis of zinc oxide nanoparticles via chemical route: A review," *Materials Today: Proceedings*, Aug. 2023.
- [9] D.-M. Radulescu, V.-A. Surdu, A. Ficai, D. Ficai, A.-M. Grumezescu, E. Andronescu, "Green synthesis of metal and metal oxide nanoparticles: A review of the principles and biomedical applications," *International Journal of Molecular Sciences*, vol. 24, no. 20, 2023, Art. no. 15397.
- [10] J. Singh, T. Dutta, K.-H. Kim, M. Rawat, P. Samddar, P. Kumar, "'Green' synthesis of metals and their oxide nanoparticles: applications for environmental remediation," *Journal of Nanobiotechnology*, vol. 16, no. 1, 2018, Art. no. 84.
- [11] H. Al Jabri, M. H. Saleem, M. Rizwan, I. Hussain, K. Usman, M. Alsafran, "Zinc Oxide nanoparticles and their biosynthesis: Overview," *Life*, vol. 12, no. 4, Apr. 2022, Art. no. 594.
- [12] J. Xu, Y. Huang, S. Zhu, N. Abbas, X. Jing, L. Zhang, "A review of the green synthesis of ZnO nanoparticles using plant extracts and their prospects for application in antibacterial textiles," *Journal of Engineered Fibers and Fabrics*, vol. 16, 2021, Art. no. 15589250211046242.
- [13] A. Kavitha, A. Doss, R. P. Praveen Pole, T. P. K. Pushpa Rani, R. Prasad, S. Satheesh, "A mini review on plant-mediated zinc oxide nanoparticles and their antibacterial potency," *Biocatalysis and Agricultural Biotechnology*, vol. 48, Mar. 2023, Art. no. 102654.
- [14] A. G. Kaningini, S. Azizi, N. Sintwa, K. Mokalane, K. C. Mohale, F. N. Mudau, M. Maaaza, "Effect of optimized precursor concentration, temperature, and doping on optical properties of ZnO nanoparticles synthesized via a green route using bush tea (*Athrixia phylicoides* DC.) leaf extracts," *ACS Omega*, vol. 7, no. 36, pp. 31658–31666, Sep. 2022.
- [15] V. Batra, I. Kaur, D. Pathania, Sonu, V. Chaudhary, "Efficient dye degradation strategies using green synthesized ZnO-based nanoplatforms: A review," *Applied Surface Science Advances*, vol. 11, Oct. 2022, Art. no. 100314.
- [16] G. T. Tran, N. T. H. Nguyen, N. T. T. Nguyen, T. T. T. Nguyen, D. T. C. Nguyen, T. V. Tran, "Formation, properties and applications of microalgae-based ZnO nanoparticles: A review," *Journal of Environmental Chemical Engineering*, vol. 11, no. 5, Oct. 2023, Art. no. 110939.
- [17] M. Naseer, U. Aslam, B. Khalid, B. Chen, "Green route to synthesize zinc oxide nanoparticles using leaf extracts of *Cassia fistula* and *Melia azadarach* and their

- antibacterial potential,” *Scientific Reports*, vol. 10, no. 1, 2020, Art. no. 9055.
- [18] S. Faisal, H. Jan, S. A. Shah, S. Shah, A. Khan, M. T. Akbar, M. Rizwan, F. Jan, Wajidullah, N. Akhtar, A. Khattak, S. Syed, “Green synthesis of zinc oxide (ZnO) nanoparticles using aqueous fruit extracts of *Myristica fragrans*: Their characterizations and biological and environmental Applications,” *ACS Omega*, vol. 6, no. 14, pp. 9709–9722, Apr. 2021.
- [19] B. Naiel, M. Fawzy, M. W. A. Halmy, A. E. D. Mahmoud, “Green synthesis of zinc oxide nanoparticles using Sea Lavender (*Limonium pruinatum* L. Chaz.) extract: characterization, evaluation of anti-skin cancer, antimicrobial and antioxidant potentials,” *Scientific Reports*, vol. 12, no. 1, 2022, Art. no. 20370.
- [20] T. U. Doan Thi, T. T. Nguyen, Y. D. Thi, K. H. Ta Thi, B. T. Phan, K. N. Pham, “Green synthesis of ZnO nanoparticles using orange fruit peel extract for antibacterial activities,” *RSC Advances*, vol. 10, no. 40, pp. 23899–23907, 2020.
- [21] J. Ali, S. Bibi, W. B. Jatoy, M. Tuzen, M. A. Jakhani, X. Feng, T. A. Saleh, “Green synthesized zinc oxide nanostructures and their applications in dye-sensitized solar cells and photocatalysis: A review,” *Materials Today Communications*, vol. 36, Aug. 2023, Art. no. 106840.
- [22] R. Álvarez-Chimal, V. I. García-Pérez, M. A. Álvarez-Pérez, R. Tavera-Hernández, L. Reyes-Carmona, M. Martínez-Hernández, J. Á. Arenas-Alatorre, “Influence of the particle size on the antibacterial activity of green synthesized zinc oxide nanoparticles using *Dysphania ambrosioides* extract, supported by molecular docking analysis,” *Arabian Journal of Chemistry*, vol. 15, no. 6, Jun. 2022, Art. no. 103804.
- [23] C. Vivek, B. Balraj, S. Thangavel, “Structural, optical and electrical behavior of ZnO@Ag core-shell nanocomposite synthesized via novel plasmon-green mediated approach,” *Journal of Materials Science: Materials in Electronics*, vol. 30, no. 12, pp. 11220–11230, 2019.
- [24] H. Mirzaei, M. Darroudi, “Zinc oxide nanoparticles: Biological synthesis and biomedical applications,” *Ceramics International*, vol. 43, no. 1, pp. 907–914, Jan. 2017.
- [25] H. Mohd Yusof, N. Abdul Rahman, R. Mohamad, U. H. Zaidan, A. A. Samsudin, “Biosynthesis of zinc oxide nanoparticles by cell-biomass and supernatant of *Lactobacillus plantarum* TA4 and its antibacterial and biocompatibility properties,” *Scientific Reports*, vol. 10, no. 1, 2020, Art. no. 19996.
- [26] S. W. Balogun, O. O. James, Y. K. Sanusi, O. H. Olayinka, “Green synthesis and characterization of zinc oxide nanoparticles using bashful (*Mimosa pudica*), leaf extract: a precursor for organic electronics applications,” *SN Applied Sciences*, vol. 2, no. 3, 2020., Art. no. 504.
- [27] A. S. Abdelbaky, A. M. H. A. Mohamed, M. Sharaky, N. A. Mohamed, Y. M. Diab, “Green approach for the synthesis of ZnO nanoparticles using *Cymbopogon citratus* aqueous leaf extract: characterization and evaluation of their biological activities,” *Chemical and Biological Technologies in Agriculture*, vol. 10, no. 1, 2023, Art. no. p. 63.
- [28] A. Yıldırım, A. Mavi, A. A. Kara, “Antioxidant and antimicrobial activities of *Polygonum cognatum* Meissn extracts,” *Journal of the Science of Food and Agriculture*, vol. 83, no. 1, pp. 64–69, Jan. 2003.
- [29] F. Demirgöl, M. Divriklioğlu-Kundak, O. Sağdıç, “Bioactive properties, antibacterial activity, and color features of *Polygonum cognatum*: The effects of frozen storage and cooking process,” *Food Science and*

- Technology, vol. 42, Jul. 2022, Art. no. e00322.
- [30] Ö. Ergen Akçin, Y. Akçin, M. K. Akbulut, “The ethnobotanical and anatomical properties of *Polygonum cognatum* Meissn. (Polygonaceae),” *Biological Diversity and Conservation*, vol. 7, no. 2, pp. 117–121, 2014.
- [31] H. Saraç, T. Daştan, A. Demirbaş, S. Durna Daştan, T. Karaköy, H. Durukan, “Nutrient composition and in vitro anti-carcinogenic activity of knotweed (*Polygonum cognatum* Meissn.) plant extracts,” (in Turkish), *Ziraat Fakültesi Dergisi*, pp. 340–347, 2018.
- [32] H. İ. Ulusoy, H. Acıdereli, U. Tutar, “Optimization of extraction parameters for fat soluble vitamins and major element analysis in *Polygonum cognatum* Meissn plant (Madımak),” *Journal of the Turkish Chemical Society Section A: Chemistry*, vol. 4, no. 1, pp. 165–178, 2017.
- [33] A. Gümüştü, S. Dinç, M. Kara, M. Akkuş, G. Gümüştü, “Phenolic compounds of natural knotweed (*Polygonum cognatum* Meissn.) populations from Turkey,” *International Journal of Plant Based Pharmaceuticals*, vol. 2, no. 1, pp. 37–41, 2022.
- [34] S. Ulusoy, S. Erdoğan, M. G. Karaaslan, B. Ateş, H. İ. Ulusoy, S. Erdemoğlu, “Optimization of extraction parameters for folic acid and antioxidant compounds from an edible plant (*Polygonum Cognatum* Meissn) using pressurized liquid extraction (PLE) system,” *Cumhuriyet Science Journal*, vol. 39, no. 4, pp. 1069–1080, 2018.
- [35] R. Akpınar, G. Yıldırım Baştemur, B. Bıçak, N. O. Sanlı, E. Mertoğlu Kamalı, M. Pekmez, S. Kecel Gündüz, S. Perçin Özkorucuklu, “Phytochemical profiling, in vitro biological activities, and in silico (molecular docking and absorption, distribution, metabolism, excretion, toxicity) studies of *Polygonum cognatum* Meissn,” *Journal of Separation Science*, vol. 47, no. 1, 2024, Art. no. 2300750.
- [36] S. Pekdemir, M. Çiftci, M. Karatepe, “Determination of in vitro biological activities and some phytochemical components of *Polygonum cognatum* Meissn (Madımak) plant grown in Elazığ,” (in Turkish), *Avrupa Bilim ve Teknoloji Dergisi*, no. 18, pp. 368–378, 2020.
- [37] M. Bayram, S. Topuz, “Optimization of phenolic compound extraction using response surface method from Madımak (*Polygonum cognatum* Meissn.),” (in Turkish), *Gıda*, vol. 48, no. 1, pp. 118–129, 2023.
- [38] N. Eruygur, E. Ucar, M. Ataş, M. Ergul, M. Ergul, F. Sozmen, “Determination of biological activity of *Tragopogon porrifolius* and *Polygonum cognatum* consumed intensively by people in Sivas,” *Toxicology Reports*, vol. 7, pp. 59–66, Jan. 2020.
- [39] Ö. Çevik, A. Şener, Z. Özdemir Kumral, Ş. Çetinel, A. Altıntaş, R. Oba, B. Yeğen, A. Yarat, “Protective and therapeutic effects of *Polygonum cognatum* Meissn aqueous extract in experimental colitis,” *Marmara Pharmaceutical Journal*, vol. 18, no. 3, pp. 126–134, 2014.
- [40] S. Gözcü, R. A. Uğan, H. Özbek, B. Gündoğdu, Z. Güvenalp, “Evaluation of antidiabetic and antioxidant effects of *Polygonum cognatum* Meissn. and phytochemical analysis of effective extracts,” *Biomedical Chromatography*, vol. 38, no. 3, 2024, Art. no. e5809.
- [41] N. Gürsoy, S. Elagöz, E. Gölge, “Investigation of antimicrobial effects of silver nanoparticles (AgNPs) synthesized on *Polygonum cognatum* Meissn. and fungus environment,” (in Turkish), *Türk Tarım ve Doğa Bilimleri Dergisi*, vol. 7, no. 1, pp. 221–230, 2020.
- [42] M. Yılmaz, A. Yılmaz, A. Karaman, F. Aysin, O. Aksakal, “Monitoring

- chemically and green-synthesized silver nanoparticles in maize seedlings via surface-enhanced Raman spectroscopy (SERS) and their phytotoxicity evaluation,” *Talanta*, vol. 225, 2021, Art. no. 121952.
- [43] Ö. Kaplan, N. Gökşen Tosun, “Biosynthesis of iron, copper and silver nanoparticles using *Polygonum Cognatum* and *Tragopogon Porrifolius* extracts and evaluation of their antimicrobial potentials,” *Düzce University Journal of Science and Technology*, vol. 11, no. 4, pp. 2155–2167, 2023.
- [44] H. Meskher, S. B. Belhaouari, K. Deshmukh, C. M. Hussain, F. Sharifianjazi, “A magnetite composite of molecularly imprinted polymer and reduced graphene oxide for sensitive and selective electrochemical detection of catechol in water and milk samples: an artificial neural network (ANN) application,” *Journal of The Electrochemical Society*, vol. 170, no. 4, Apr. 2023, Art. no. 047502.
- [45] L. Lutterotti, “Total pattern fitting for the combined size–strain–stress–texture determination in thin film diffraction,” *Nuclear Instruments and Methods in Physics Research Section B: Beam Interactions with Materials and Atoms*, vol. 268, no. 3, pp. 334–340, 2010.
- [46] V. D. Mote, Y. Purushotham, B. N. Dole, “Williamson-Hall analysis in estimation of lattice strain in nanometer-sized ZnO particles,” *Journal of Theoretical and Applied Physics*, vol. 6, no. 1, 2012, Art. no. 6.
- [47] S. Gražulis, D. Chateigner, R. T. Downs, A. F. T. Yokochi, M. Quirós, L. Lutterotti, E. Manakova, J. Butkus, P. Moeck, A. Le Bail, “Crystallography Open Database – an open-access collection of crystal structures,” *Journal of Applied Crystallography*, vol. 42, no. 4, pp. 726–729, Aug. 2009.
- [48] S. Mansy, H. Musleh, S. Shaat, J. Asad, N. AlDahoudi, “Computational and experimental study of wurtzite phase ZnO nanoparticles,” *Materials Today Communications*, vol. 35, 2023, Art. no. 105688.
- [49] J. Vera, W. Herrera, E. Hermosilla, M. Díaz, J. Parada, A. B. Seabra, G. Tortella, H. Pesenti, G. Ciudad, O. Rubilar, “Antioxidant activity as an indicator of the efficiency of plant extract-mediated synthesis of zinc oxide nanoparticles,” *Antioxidants*, vol. 12, no. 4, 2023, Art. no. 784.
- [50] Q. P. Pham, Q. N. Le Nguyen, N. H. Nguyen, U. T. T. Doan, T. D. T. Ung, V. C. Tran, T. B. Phan, A. T. T. Pham, N. K. Pham, “Calcination-dependent microstructural and optical characteristics of eco-friendly synthesized ZnO nanoparticles and their implementation in analog memristor application,” *Ceramics International*, vol. 49, no. 12, pp. 20742–20755, 2023.
- [51] H. Naseer, T. Iqbal, “Green synthesis of silver-doped zinc oxide nanoparticles for investigation of their photocatalytic activity and shelf life applications,” *Biomass Conversion and Biorefinery*, 2023.
- [52] K. Dulta, G. Koşarsoy Ağçeli, P. Chauhan, R. Jasrotia, P. K. Chauhan, “A novel approach of synthesis zinc oxide nanoparticles by *Bergenia ciliata* Rhizome extract: Antibacterial and anticancer potential,” *Journal of Inorganic and Organometallic Polymers and Materials*, vol. 31, no. 1, pp. 180–190, 2021.
- [53] M. Jarvin, S. A. Kumar, D. R. Rosaline, E. L. Foletto, G. L. Dotto, S. S. R. Inbanathan, “Remarkable sunlight-driven photocatalytic performance of Ag-doped ZnO nanoparticles prepared by green synthesis for degradation of emerging pollutants in water,” *Environmental Science and Pollution Research*, vol. 29, no. 38, pp. 57330–57344, 2022.

- [54] A. Jayachandran, A. T.R., A. S. Nair, "Green synthesis and characterization of zinc oxide nanoparticles using *Cayratia pedata* leaf extract," *Biochemistry and Biophysics Reports*, vol. 26, 2021, Art. no. 100995.
- [55] A. Sangeetha, S. Jaya Seeli, K. P. Bhuvana, M. A. Kader, S. K. Nayak, "Correlation between calcination temperature and optical parameter of zinc oxide (ZnO) nanoparticles," *Journal of Sol-Gel Science and Technology*, vol. 91, no. 2, pp. 261–272, 2019.
- [56] R. Cuscó, E. Alarcón-Lladó, J. Ibáñez, L. Artús, J. Jiménez, B. Wang, M. J. Callahan, "Temperature dependence of Raman scattering in ZnO," *Physical Review B*, vol. 75, no. 16, Apr. 2007, Art. no. 165202.
- [57] S. Knust, L. Ruhm, A. Kuhlmann, D. Meinderink, J. Bürger, J. K. N. Lindner, M. T. de los Arcos de Pedro, G. Grundmeier, "In situ backside Raman spectroscopy of zinc oxide nanorods in an atmospheric-pressure dielectric barrier discharge plasma," *Journal of Raman Spectroscopy*, vol. 52, no. 7, pp. 1237–1245, Jul. 2021.
- [58] A. K. Rana, Y. Kumar, P. Rajput, S. N. Jha, D. Bhattacharyya, P. M. Shirage, "Search for origin of room temperature ferromagnetism properties in Ni-doped ZnO nanostructure," *ACS Applied Materials & Interfaces*, vol. 9, no. 8, pp. 7691–7700, Mar. 2017.
- [59] D. Kumar, M. K. Singh, M. S. Mehata, "Exploration of grown cobalt-doped zinc oxide nanoparticles and photodegradation of industrial dye," *Materials Research Bulletin*, vol. 150, Jun. 2022, Art. no. 111795.
- [60] R. D. Chandra, L. Veena, K. G. Gopchandran, "Suppression of visible emission in low-temperature synthesized cobalt-doped ZnO nanoparticles and their photosensing applications," *Inorganic Chemistry*, vol. 62, no. 29, pp. 11360–11371, Jul. 2023.
- [61] F. J. Manjón, B. Marí, J. Serrano, A. H. Romero, "Silent Raman modes in zinc oxide and related nitrides," *Journal of Applied Physics*, vol. 97, no. 5, Feb. 2005, Art. no. 053516.
- [62] P. Makuła, M. Pacia, W. Macyk, "How to correctly determine the band gap energy of modified semiconductor photocatalysts based on UV–Vis spectra," *The Journal of Physical Chemistry Letters*, vol. 9, no. 23, pp. 6814–6817, Dec. 2018.
- [63] N. Rana, S. Chand, A. K. Gathania, "Green synthesis of zinc oxide nano-sized spherical particles using *Terminalia chebula* fruits extract for their photocatalytic applications," *International Nano Letters*, vol. 6, no. 2, pp. 91–98, 2016.
- [64] G. Tang, S. Tian, Z. Zhou, Y. Wen, A. Pang, Y. Zhang, D. Zeng, H. Li, B. Shan, C. Xie, "ZnO micro/nanocrystals with tunable exposed (0001) facets for enhanced catalytic activity on the thermal decomposition of ammonium perchlorate," *The Journal of Physical Chemistry C*, vol. 118, no. 22, pp. 11833–11841, Jun. 2014.
- [65] X. Meng, L. Jiang, W. Wang, Z. Zhang, "Enhanced photocatalytic activity of BiOBr/ZnO heterojunction semiconductors prepared by facile hydrothermal method," *International Journal of Photoenergy*, vol. 2015, 2015, Art. no. 747024.
- [66] K. X. Yao, R. Sinclair, H. C. Zeng, "Symmetric linear assembly of hourglass-like ZnO nanostructures," *The Journal of Physical Chemistry C*, vol. 111, no. 5, pp. 2032–2039, Feb. 2007.
- [67] J. M. Hancock, W. M. Rankin, B. Woolsey, R. S. Turley, R. G. Harrison, "Controlled formation of ZnO hexagonal prisms using ethanalamines and water," *Journal of Sol-*

Gel Science and Technology, vol. 84, no. 1, pp. 214–221, 2017.

- [68] D. Li, J. Wang, X. Wu, C. Feng, X. Li, “Ultraviolet-assisted synthesis of hourglass-like ZnO microstructure through an ultrasonic and microwave combined technology,” *Ultrasonics Sonochemistry*, vol. 20, no. 1, pp. 133–136, 2013.
- [69] M. Turan, S. Kordali, H. Zengin, A. Dursun, Y. Sezen, “Macro and micro mineral content of some wild edible leaves consumed in Eastern Anatolia,” *Acta Agriculturae Scandinavica, Section B — Soil & Plant Science*, vol. 53, no. 3, pp. 129–137, Jan. 2003.

Role of Mechanical Activation in Enhancing Li and Co Recovery from Spent Li-ion Batteries through Citric Acid Leaching

Hasan Algül* , Figen Algül 

¹ Sakarya University, Faculty of Engineering, Department of Metallurgical and Materials Science, Sakarya, Türkiye, halgul@sakarya.edu.tr, figenozboz@gmail.com

*Corresponding Author

ARTICLE INFO

ABSTRACT

Keywords:

Battery recycling
Citric acid leaching
Li and co extraction
Mechanical activation rotation speed
Mechanical activation time

This study investigates the effect of mechanical activation parameters such as mechanical activation rotation speed (0-550 rpm), mechanical activation time (15-75 min), and solid/ball ratio (1/20-1/50) on the leaching efficiencies in the recycling of lithium-ion batteries. In addition to mechanical activation, the study explores the use of organic acids, specifically citric acid, as leaching agents to enhance metal recovery. A green and innovative recycling process is developed, focusing on optimal conditions of 15 minutes activation time, 450 rpm rotational speed, and a 1/20 solid/ball ratio. The synergistic effect of mechanical activation and organic acid leaching is examined to optimize the process for sustainability and efficiency in recovering valuable metals from lithium-ion batteries. Results indicate that these parameters significantly influence leaching efficiencies, with the highest yields achieved under the identified conditions. This research contributes to advancing sustainable practices in battery recycling by integrating mechanical activation and organic acid leaching as effective and environmentally friendly approaches. The findings highlight the potential of these methods in advancing green technology and materials science, paving the way for more efficient and eco-friendly battery recycling processes.

Article History:

Received: 28.06.2024

Accepted: 02.09.2024

Online Available: 14.10.2024

1. Introduction

With the increasing use of lithium-ion batteries in portable devices and particularly in automobiles, the demand for sustainable battery components and resources is growing daily. Considering the energy demands in the battery sector, the energy demand, which was 102 GW-hours in 2017, is projected to reach 709 GW-hours by 2026 [1]. Additionally, to reduce carbon dioxide emissions, the sales of electric cars, which were 2 million in 2018, are expected to reach approximately 11 million by 2025 [2].

However, with the anticipated increase in the supply of lithium-ion batteries, while carbon dioxide emissions are reduced, another adverse

effect is looming for the planet. London-based Circular Energy Storage (CES) estimates that China alone produced half a million tons of lithium-ion battery waste by 2020, and this number is expected to reach two million tons annually by 2030 when considering global consumption. Certain materials found in lithium-ion battery waste, such as heavy metals and toxic electrolytes, pose specific threats to ecosystems and human health. Approximately 1,100 tons of the 4,000 tons of lithium-ion battery waste consist of heavy metals, and over 200 tons are toxic electrolytes [1]. Therefore, if lithium battery waste is disposed of through methods other than recycling, it will lead to numerous adverse effects. For instance, if disposed of through solid waste landfilling, the dissolution of

toxic heavy metals into groundwater could cause severe environmental pollution. Similarly, if lithium-ion battery waste is incinerated as general solid waste, it will produce significant amounts of toxic gases, such as hydrogen fluoride (HF), polluting the atmosphere.

Therefore, it is crucial to process waste lithium-ion batteries in the least harmful way to humans and nature. Furthermore, an average waste lithium-ion battery contains 5-20% Co, 5-7% Li, 5-10% Ni, 5-10% Cu, other metals like Al and Fe, 15% organic compounds, and 7% plastics [3]. The significant number of valuable metals in waste lithium-ion batteries, often exceeding the content found in some natural ores, provides substantial economic value [3]. Thus, the primary goal of recycling waste lithium-ion batteries is to reduce or eliminate potential environmental impacts; the secondary goal is to ensure an industrially sustainable and improvable lithium-ion battery industry through the recovery of valuable metals.

Therefore, recycling waste lithium-ion batteries not only complies with environmental requirements but also serves as an alternative source for conserving valuable metals. A lithium-ion battery typically consists of an anode, cathode, binder, electrolyte solution, separator, current collectors, and plastic and metallic outer layers. Besides carbon, other materials like SiO_x , silicon, and $\text{Li}_4\text{Ti}_5\text{O}_{12}$ can be used as anodes, but natural graphite is preferred due to its low cost, high efficiency, and high capacity [4, 5]. The binder, which usually is polyvinylidene difluoride (PVDF), ensures the adhesion of the anode and cathode materials onto copper and aluminum foils [6]. The separator is a microporous film usually made from polymers such as polyethylene (PE) and polypropylene (PP) [7]. The electrolytes used in lithium-ion batteries include LiPF_6 , LiBF_4 , LiCF_3SO_3 , or $\text{Li}(\text{SO}_2\text{CF}_3)_2$.

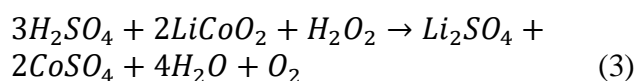
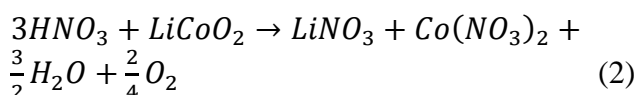
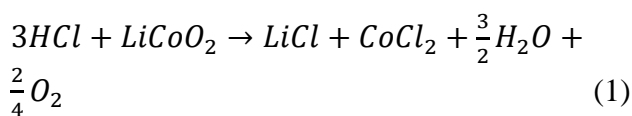
The cathode materials in lithium-ion batteries are primarily lithium intercalation oxides such as LiNiO_2 , LiMn_2O_4 , LiFePO_4 , $\text{LiNi}_x\text{Co}_y\text{Mn}_{1-x-y}\text{O}_2$, with LiCoO_2 being the most used [8, 9].

Today, three main techniques are employed for recycling lithium-ion batteries: pyrometallurgy,

bio metallurgy, and hydrometallurgy [10]. The pyrometallurgical method does not require pre-processing as organic solvents, plastic coatings, and connectors decompose and burn at the high temperatures applied in this process. The high temperature and capacity used allow for the recycling of large quantities of lithium-ion batteries. However, the disadvantages of the pyrometallurgical method include the emission of hazardous gases such as HF, high investment costs, high energy consumption, and the loss of some metals like lithium and manganese in the slag. The bio metallurgical method, which uses microorganisms for leaching, is less costly and requires less industrial equipment.

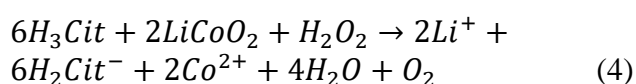
However, due to slower leaching kinetics and efficiencies, it requires much more time for recycling. Hydrometallurgical processes can be faster, provide higher purity, consume less energy, and result in lower gas emissions. Due to the disadvantages of pyrometallurgy and bio metallurgy, hydrometallurgical processes are more commonly used for recycling lithium-ion batteries [11, 12]. Leaching reagents are primarily inorganic acids, organic acids, and alkaline solutions. Inorganic acids like HCl, HNO_3 , and H_2SO_4 have been extensively studied in the recycling processes of lithium-ion batteries.

One of the most valuable components within a lithium-ion battery is the cathode material LiCoO_2 . The leaching (selective dissolution) reactions of LiCoO_2 with HCl, HNO_3 , and H_2SO_4 are as follows [13–15]:



In the absence of a reductant, the leaching efficiency of cobalt is higher with HCl compared to HNO_3 and H_2SO_4 , due to higher reduction potential of HCl. However, as shown in Reaction (3), the addition of H_2O_2 or similar agents can

facilitate the reduction of Co^{3+} when the cathode material is subjected to leaching with H_2SO_4 [16–19]. The leaching process of metals with inorganic acids can be successfully carried out with high efficiency. However, inorganic acids produce environmentally harmful components such as acidic wastewater, Cl_2 , SO_2 , NO_x , and other harmful gases [20]. Therefore, eco-friendly organic acids such as ascorbic acid, citric acid, oxalic acid, formic acid, acetic acid, and tartaric acid are used as leaching agents for metal recovery from waste lithium-ion batteries [21]. In this study, the leaching reaction of the cathode material LiCoO_2 with citric acid, which will be used, is provided in Reaction (4) [22].



Mechanical activation, used prior to leaching, is a widely applied scientific discipline with applications in metal production processes, reaction control in chemical technologies, and more. Heinicke describes this application as “Mechanochemistry, a branch of chemistry that deals with chemical and physical transformations of materials induced by mechanical energy” [23]. Mechanical activation is defined as a process that increases the reactivity of an otherwise unreactive solid, enhancing the dissolution of minerals.

The primary reasons for this enhancement include morphological irregularities, amorphization of mineral particles, the emergence of crystal areas conducive to preferential dissolution, and surface oxidation of minerals during prolonged grinding [24]. An additional fundamental advantage of mechanical activation is its ability to extract low-content, highly dispersed multi-source metal elements from electronic waste with complex compositions and sensitive structures. In the cathode material, cobalt generally exists in the Co^{3+} oxidation state. However, it has been reported that Co^{2+} is more easily soluble in aqueous solutions at room temperature compared to Co^{3+} [25].

Despite numerous reports on the recycling of spent Li-ion batteries, to the best of our knowledge, there have been no systematic

investigations into the effects of the mechanical activation process and its parameters on recycling using organic acids such as citric acid. In this study, the effects of mechanical activation parameters on the process of recovering valuable metals, lithium and cobalt, from waste lithium-ion batteries using an environmentally friendly method of organic acid leaching were investigated, with an emphasis on minimizing the use of toxic substances.

2. General Methods

All experiments utilized powders derived from spent lithium-based waste batteries. To fully understand the components of a cylindrical Li-ion battery extracted from a laptop battery, a spent Li-ion battery based on LiCoO_2 (LCO) was manually disassembled (Figure 1).

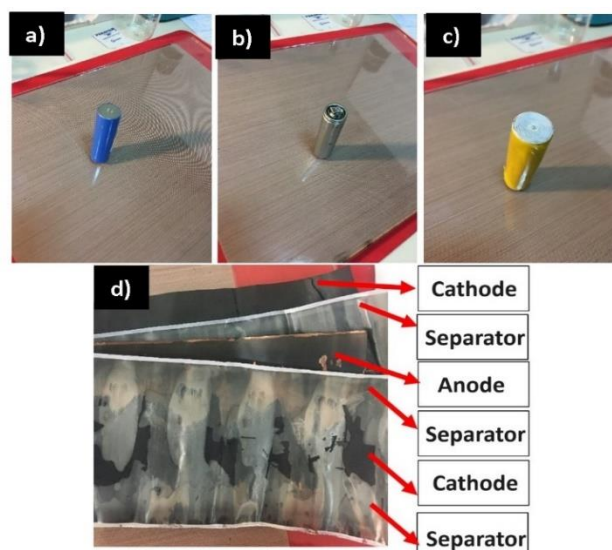


Figure 1. Manual disassembly of waste lithium-ion batteries: a) outer plastic layer, b) metal casing, c) inner plastic layer, and d) internal components of the battery

Prior to all experiments, the waste powders (comprising graphite, LCO, activated carbon, electrolyte, and PVDF) were initially homogenized in a ball mill using a stainless-steel ball-to-waste powder mass ratio of 1:20 at a mixing speed of 300 rpm for 12 hours. A primary powder blend (mixture) was obtained for use in all experiments. To better understand the metallic content of the waste powders and to remove the binder (PVDF) and carbon-based materials (graphite and carbon black) from the samples, a calcination process was conducted at 700 °C for 3 hours.

To analyze the Li and Co content after calcination, the powders were subjected to dissolution in aqua regia (1/3 nitric acid and 2/3 hydrochloric acid) for 24 hours. Subsequently, the Li and Co contents by weight were determined using inductively coupled plasma-optical emission spectrometry (ICP-OES). After the calcination process, it was determined through ICP-OES analysis that the calcined LCO powders contain 5% Li and 31.3% Co. To understand the effects of mechanical activation, a planetary ball mill from Fritch was utilized.

The samples (calcined LCO powders) were subjected to dry mechanical activation in a container made of WC using WC balls with a diameter of 10 mm.

For the identification of compounds in the powders, X-ray diffraction analysis (XRD) was performed using a Rigaku d/MAX 2000 model instrument with CuK α radiation in the range of 10-90°. Morphological analyses before and after calcination were obtained using a Jeol JSM-6060 LV model scanning electron microscope (SEM). To observe the effects of mechanical activation, experiments were conducted at different planetary mill rotation speeds (0, 300, 350, 400, 450, 500, and 550 rpm), various mechanical activation times (15, 30, 45, and 60 minutes), and different sample/WC ball weight ratios (1/20, 1/30, 1/40, and 1/50).

Table 1. Parameters of leaching processes of calcined LCO powders with citric acid leaching agent

	Mechanical Activation Parameters		Leaching Parameters
Mechanical Activation Rotation Speed	0 rpm	Mechanical activation time:	1 M citric acid
	300 rpm	15 min.	30 min. leaching time
	350 rpm	Solid/WC ball ratio: 1/20	1/80 solid/citric acid ratio
	400 rpm		50 °C
	450 rpm		
	500 rpm 550 rpm		
Mechanical Activation Time	15 min.	Mechanical activation	1 M citric acid
	30 min.	rotation speed: 450 rpm	30 min. leaching time
	45 min.	Solid/WC ball ratio: 1/20	1/80 solid/citric acid ratio
	60 min.		50 °C
	75 min.		
Mechanical Activation Solid/WC Ball Ratio	1/20	Mechanical activation time:	1 M citric acid
	1/30	15 min.	30 min. leaching time
	1/40	Mechanical activation	1/80 solid/citric acid ratio
	1/50	rotation speed: 450 rpm	50 °C

The mechanically activated calcined LCO sample powders were then subjected to leaching in a 1 M citric acid solution for 30 minutes at a leaching temperature of 50 °C, with a solid-to-citric acid ratio of 1/80 (mechanically activated calcined LCO powder to citric acid). All leaching experiments were conducted in a glass reactor using a thermostat-controlled magnetic stirrer to maintain the reaction temperature within ± 1.0 °C. A water-cooled reflux condenser was used to prevent vapor loss at high temperatures. The stirring speed was kept constant at 300 rpm for

all leaching processes. Table 1 lists all mechanical activation and leaching conditions. After the leaching process, the leach solution was separated from the solid phase using filtration. The factors influencing the recovery of Li and Co from spent powders were investigated under various experimental conditions: (i) mechanical activation rotation speed, (ii) mechanical activation time and (iii) mechanical activation solid/WC ball ratio. The metal contents in the leaching solutions were determined using Atomic Absorption Spectroscopy (AAS) for each

experiment. The recovery efficiency was calculated according to the following equation:

$$E_{Li,Co}(\%) = \frac{C \times V}{P \times M} \times 100$$

where C is the concentration of Li and Co in the leaching solution (g/L), V is the volume of the leaching solution (L), P is the percentage of Li and Co in spent LiBs (%), and M is the amount of the leached solid (g).

3. Results and Discussion

The leaching behavior of waste Li-ion active material during the leaching process is influenced by various mechanical activation parameters. It has been observed that increasing the mechanical activation time, rotational speed, and ball-to-powder mass ratio enhances the leaching efficiencies of cobalt and lithium [26]. Moreover, the leaching efficiencies of metals exhibit a linear relationship with the surface area of the existing structure [27]. The mechanical activation process alters the leaching behavior of valuable metals, resulting in higher leaching efficiencies compared to non-activated samples [28].

The improved leaching efficiency is associated with reduced particle size, increased specific surface area, and the disrupted crystal structure of the activated samples [29]. Mechanical activation also leads to changes in the physicochemical properties of LCO powders, such as reduced particle size, increased specific surface area, and the formation of mesoporous structures. Figure 2 presents the XRD patterns of calcined LCO powders subjected to mechanical activation at different rotational speeds, with a 1/20 solid/WC ball ratio, and a mechanical activation processing time of 15 minutes.

In Figure 2, it is observed that the mechanical activation processes do not result in significant amorphization or reorientation of the crystal structure within short durations such as 15 minutes. However, at rotational speeds of 400 and particularly 450 rpm, changes in the structures of LiCoO₂ and Co₃O₄ peaks are evident. At lower rotational speeds, as seen in the enlarged graph on the right side of Figure 2, the two peaks at 37° and 37.5° 2θ merge into a single

peak. During mechanical activation at 450 rpm, it is observed that the Co₃O₄ structure formed after calcination transforms into the LiCoO₂ structure, reducing or eliminating the amount of Co₃O₄ in the structure.

It is understood that during mechanical activation at 450 rpm, the Co₃O₄ and LiO₂ present in the structure transform into LiCoO₂ due to the high temperatures generated by solid-phase micro-region collisions. Studies in the literature on the production of LiCoO₂ through mechanical activation using LiO₂ and Co₃O₄ starting materials support this claim [26, 27]. During the leaching process, the dissolution of LiCoO₂ and Co₃O₄ involves different chemical mechanisms. For LiCoO₂, the leaching mechanism is controlled by surface chemical reactions [30]. The leaching of cobalt from LiCoO₂ is influenced by the disintegration of the crystal structure and diffusion, whereas the leaching mechanism for Co₃O₄ is significantly affected by the concentration and type of acid used as well as solvent effects [31].

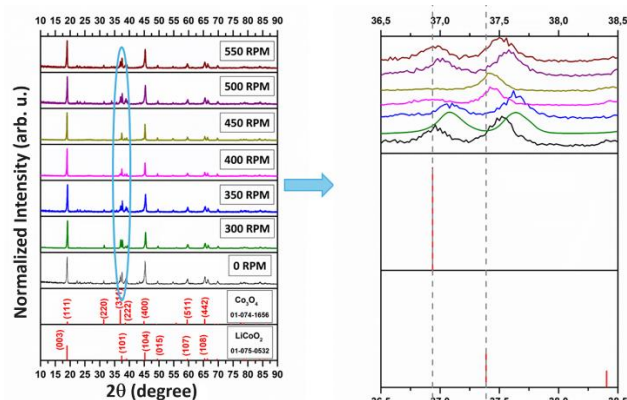


Figure 2. XRD patterns of calcined LCO powders at different mechanical activation rotation speed

SEM images are presented in Figure 3 to examine the impact of different mechanical activation speeds on the morphology of waste calcined LCO powders.

In Figure 3a, it is evident that the morphology of the original, non-activated calcined sample shows agglomeration of the powders during calcination. This agglomeration occurs due to chemical changes and attractive forces between the particles during the calcination process. In Figure 3b, at a mechanical activation speed of 300 rpm, partial liberation of the grains is

observed, although the grains are still coarse, indicating that low-scale mill rotations promote and facilitate agglomeration. However, after this stage, the bonds between particles begin to loosen, resulting in a more liberated structure.

This is evident in Figure 3c, where increasing the mechanical activation speed to 450 rpm leads to further liberation and a reduction in grain size. This can be attributed to the particles being subjected to more energy with the increased mill rotation speed of the WC balls, leading to a more loosened structure. However, with the increase in mechanical activation speed, the heating effect caused by collisions and friction between the balls and grains also increases. As shown in the SEM image in Figure 3d, this results in localized sintering and an increase in particle size. The temperatures, which can reach thousands of degrees on a micro scale, cause partial melting, sintering at the contact points of the particles, and an increase in particle size.

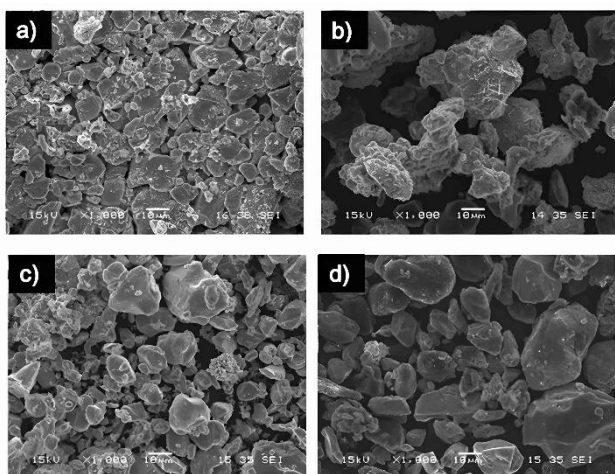


Figure 3. a) Calcined LCO powder (0 rpm) and LCO powders mechanically activated at different rotation speeds b) 300, c) 450, and d) 550 rpm

Figure 4 illustrates the relationship between mechanical activation rotation speed and the leaching efficiencies of Li and Co metals in waste calcined LCO powders.

The fixed parameters used in the leaching processes from which the data in Figure 4 were obtained are provided in Table 1. For the non-mechanically activated sample at 0 rpm, the leaching efficiency was found to be approximately 45% for Li and 10% for Co. With increasing mill speed and mechanical activation,

defects are introduced in the internal structure, enhancing the recoveries of Li and Co. The maximum leaching efficiencies were achieved at 450 rpm, with yields of 87.20% for Li and 24.85% for Co.

However, when the rotational speed of mechanical activation was increased to 500 rpm, significant decreases in leaching efficiencies were observed. This is likely due to the agglomeration of grains at speeds above 500 rpm (as seen in Figure 3d), which reduces the available surface area for leaching. Guan et al. observed the same phenomenon and found that the leaching efficiency significantly increased with the rise in mechanical activation rotation speed. This improvement is attributed to the enhanced kinetic energy transferred to the samples due to the series of collisions among the balls [32]. Additionally, as seen in the XRD patterns in Figure 2, the formation of the LiCoO_2 structure through the reaction of Co_3O_4 with LiO_2 may contribute to the reduced leaching efficiency due to the increased difficulty in dissolving this complex structure. While Co extraction increases with the mill rotation speed similar to Li, no significant increase in Co extraction was observed, which is related to changes in the crystal structure [33].

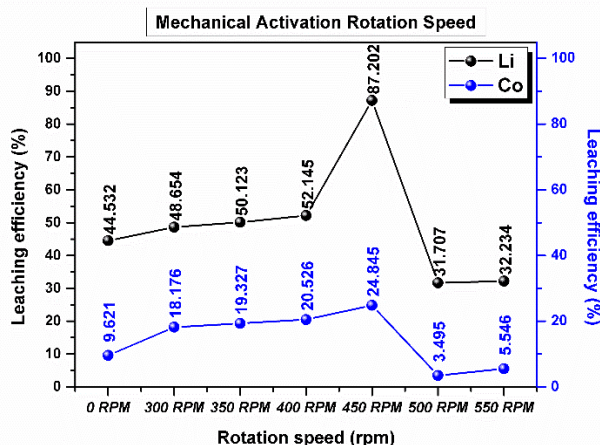


Figure 4. Leaching efficiencies of Li and Co obtained from the leaching process of waste calcined LCO powders subjected to mechanical activation at different rotational speeds

Figure 5 shows the leaching efficiencies of Li and Co obtained from the samples mechanically activated for times ranging from 15 to 75 minutes under the parameters provided in Table 1.

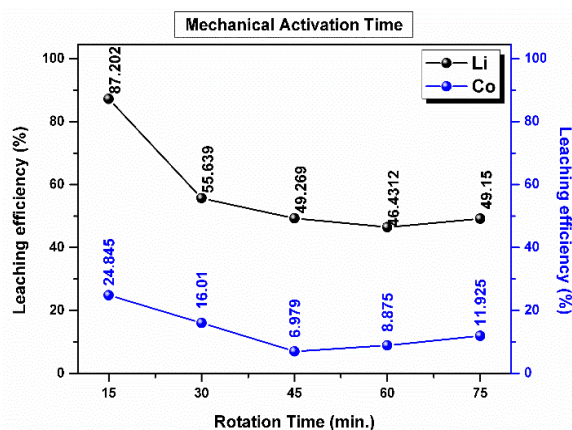


Figure 5. Leaching efficiencies of Li and Co obtained from the leaching process of waste calcined LCO powders subjected to mechanical activation at different activation times

As seen in Figure 5, when the mechanical activation time is increased from 15 minutes to 75 minutes, the extraction efficiencies of Co and Li decrease from 25% to 12% and from 87% to 49%, respectively. The obtained results indicate that mechanical activation time and the rotational speed of the planetary mill are critical factors for the recovery of Co and Li from recycled LIBs. Extending the activation duration beyond 15 minutes leads to a significant increase in the tendency for sintering events, due to local temperature rises, which in turn reduces leaching efficiency. Additionally, the literature explains that the agglomeration caused by cold welding of particles during mechanical activation contributes to this phenomenon [34]. It is clearly observed that excessively long mechanical activation times result in increased particle sizes and reduced surface areas, which decrease the extraction efficiencies of Co and Li.

Figure 6 shows the leaching efficiencies of Li and Co obtained from the leaching process at different solid/WC ball ratios under the fixed leaching parameters provided in Table 1.

As seen in Figure 6, as the solid/WC ball ratio decreases from 1/20 to 1/50, the leaching efficiencies for both Li and Co decrease.

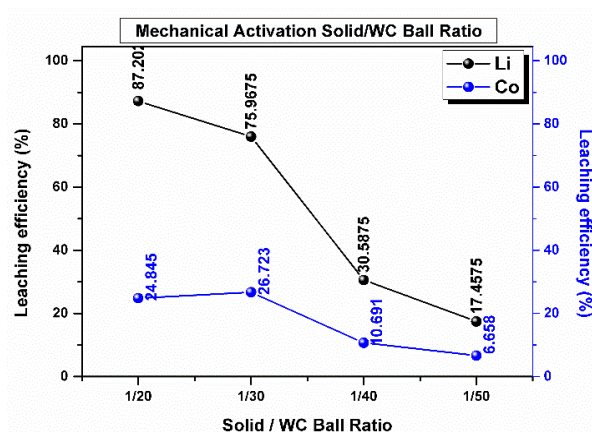


Figure 6. Leaching efficiencies of Li and Co obtained from the leaching process of waste calcined LCO powders subjected to activation at different waste calcined LCO/WC ball ratios

This is attributed to the limited high-speed collisions of the mechanical activation balls with the samples during the mechanical activation process (due to increased ball numbers per unit volume, which reduces collision intervals and strength) and the larger contact area of the grinding balls [33]. An inappropriate solid/WC ratio results in both a waste of mechanical energy and reduced leaching efficiencies of the metals.

4. Conclusion

It has been understood that low-speed and short-time mechanical activation positively contributes to the recovery of Li and Co from waste batteries, while high-speed and long-duration mechanical activation has adverse effects. It has been observed that even with a low concentration of 1 M citric acid in the leaching process, Li can be extracted at levels of approximately 87% and Co at approximately 25%. The conditions with a solid/WC ball ratio of 1/20 have emerged as the ratio at which the highest leaching efficiency is obtained.

Article Information Form

Acknowledgments

We would like to thank Exitcom A.Ş. for providing us with the waste batteries used in this study.

Funding

This work is supported by Sakarya University Science Research Projects Coordinators under contract number SAU BAP 2022-6-23-63.

Authors' Contribution

The authors contributed equally to the study.

The Declaration of Conflict of Interest/ Common Interest

No conflict of interest or common interest has been declared by the authors.

The Declaration of Ethics Committee Approval

This study does not require ethics committee permission or any special permission.

The Declaration of Research and Publication Ethics

The authors of the paper declare that they comply with the scientific, ethical and quotation rules of SAUJS in all processes of the paper and that they do not make any falsification on the data collected. In addition, they declare that Sakarya University Journal of Science and its editorial board have no responsibility for any ethical violations that may be encountered, and that this study has not been evaluated in any academic publication environment other than Sakarya University Journal of Science.

Copyright Statement

Authors own the copyright of their work published in the journal and their work is published under the CC BY-NC 4.0 license.

References

- [1] D. J. Garole, R. Hossain, V. J. Garole, V. Sahajwalla, J. Nerkar, D. P. Dubal, "Recycle, Recover and Repurpose Strategy of Spent Li-ion Batteries and Catalysts: Current Status and Future Opportunities," *ChemSusChem*, vol. 13, pp. 3079-3100, 2020.
- [2] G. Harper, R. Sommerville, E. Kendrick, L. Driscoll, P. Slater, R. Stolkin, A. Walton, P. Christensen, O. Heidrich, S. Lambert, A. Abbott, K. Ryder, L. Gaines, P. Anderson, "Recycling lithium-ion batteries from electric vehicles," *Nature*, vol. 575, pp. 75-86, 2019.
- [3] Y. Miao, L. Liu, Y. Zhang, Q. Tan, J. Li, "An overview of global power lithium-ion batteries and associated critical metal recycling," *Journal of Hazardous Materials*, vol. 425, pp. 1279001-14, 2022.
- [4] M. Jiao, Y. Wang, C. Ye, C. Wang, W. Zhang, C. Liang, "High-capacity SiO_x (0<x≤2) as promising anode materials for next-generation lithium-ion batteries," *Journal of Alloys and Compounds*, vol. 482, pp.155774 1-21, 2020.
- [5] X. Zhang, S. Han, P. Xiao, C. Fan, W. Zhang, "Thermal reduction of graphene oxide mixed with hard carbon and their high performance as lithium ion battery anode," *Carbon*, vol. 100, pp. 600-607, 2016.
- [6] S. L. Chou, Y. Pan, J. Z. Wang, H. K. Liu, S. X. Dou, "Small things make a big difference: Binder effects on the performance of Li and Na batteries," *Physical Chemistry Chemical Physics*, vol. 16, pp. 20347-20359, 2014.
- [7] E. Asadi Dalini, G. Karimi, S. Zandevakili, M. Goodarzi, "A Review on Environmental, Economic and Hydrometallurgical Processes of Recycling Spent Lithium-ion Batteries," *Mineral Processing and Extractive Metallurgy Review*, vol. 42, no. 7, pp. 451-472, 2020.
- [8] Y. Yang, G. Huang, S. Xu, Y. He, X. Liu, "Thermal treatment process for the recovery of valuable metals from spent lithium-ion batteries," *Hydrometallurgy*, vol. 165, pp. 390-396, 2016.
- [9] R. Golmohammadzadeh, F. Rashchi, E. Vahidi, "Recovery of lithium and cobalt from spent lithium-ion batteries using organic acids: Process optimization and kinetic aspects," *Waste Management*, vol. 64, pp. 244-254, 2017.
- [10] G. Mishra, R. Jha, A. Meshram, K. K. Singh, "A review on recycling of lithium-ion batteries to recover critical metals," *Journal of Environmental Chemical Engineering*, vol. 10 (6), pp. 108534 1-15, 2022.

- [11] M. Joulié, E. Billy, R. Laucournet, D. Meyer, "Current collectors as reducing agent to dissolve active materials of positive electrodes from Li-ion battery wastes," *Hydrometallurgy*, vol. 169, pp. 426-432, 2017.
- [12] W. Gao, C. Liu, H. Cao, X. Zheng, X. Lin, H. Wang, Y. Zhang, Z. Sun, "Comprehensive evaluation on effective leaching of critical metals from spent lithium-ion batteries," *Waste Management*, vol. 75, pp.477-485, 2018.
- [13] R. C. Wang, Y. C. Lin, S. H. Wu, "A novel recovery process of metal values from the cathode active materials of the lithium-ion secondary batteries," *Hydrometallurgy*, vol. 99, pp. 194-201, 2009.
- [14] L. Li, R. Chen, F. Sun, F. Wu, J. Liu, "Preparation of LiCoO_2 films from spent lithium-ion batteries by a combined recycling process," *Hydrometallurgy*, vol. 108, pp. 220-225, 2011.
- [15] D. A. Ferreira, L. M. Z. Prados, D. Majuste, M. B. Mansur, "Hydrometallurgical separation of aluminium, cobalt, copper and lithium from spent Li-ion batteries," *Journal of Power Sources*, vol. 187, pp. 238-246, 2009.
- [16] E. Gratz, Q. Sa, D. Apelian, Y. Wang, "A closed loop process for recycling spent lithium ion batteries," *Journal of Power Sources*, vol. 262, pp. 255-262, 2014.
- [17] Y. Guo, F. Li, H. Zhu, G. Li, J. Huang, W. He, "Leaching lithium from the anode electrode materials of spent lithium-ion batteries by hydrochloric acid (HCl)," *Waste Management*, vol. 51, pp. 227-233, 2016.)
- [18] L. Li, W. Qu, X. Zhang, J. Lu, R. Chen, F. Wu, K. Amine, "Succinic acid-based leaching system: A sustainable process for recovery of valuable metals from spent Li-ion batteries," *Journal of Power Sources*, vol. 282, pp. 544-551, 2015.
- [19] Q. Sa, E. Gratz, M. He, W. Lu, D. Apelian, Y. Wang, "Synthesis of high performance $\text{LiNi}_{1/3}\text{Mn}_{1/3}\text{Co}_{1/3}\text{O}_2$ from lithium ion battery recovery stream," *Journal of Power Sources*, vol. 282, pp. 140-154, 2015.
- [20] L. Yao, Y. Feng, G. Xi, "A new method for the synthesis of $\text{LiNi}_{1/3}\text{Co}_{1/3}\text{Mn}_{1/3}\text{O}_2$ from waste lithium ion batteries," *RSC Advances*, vol. 5, pp. 44107-44114, 2015.
- [21] X. Zheng, Z. Zhu, X. Lin, Y. Zhang, Y. He, H. Cao, Z. Sun, "A Mini-Review on Metal Recycling from Spent Lithium Ion Batteries," *Engineering*, vol. 4, pp. 361-370, 2018.
- [22] L. Li, J. Ge, F. Wu, R. Chen, S. Chen, B. Wu, "Recovery of cobalt and lithium from spent lithium ion batteries using organic citric acid as leachant," *Journal of Hazardous Materials*, vol. 176, pp. 288-293, 2010.
- [23] P. Balaz, "Mechanical activation in hydrometallurgy," *International Journal of Mineral Processing*, vol. 72, pp. 341-354, 2003.
- [24] D. Tromans, J. A. Meech, "Enhanced Dissolution of Minerals: Stored Energy," *Amorphism and Mechanical Activation*, vol. 14, no. 7, 1359-1377, 2001.
- [25] X. Zeng, J. Li, N. Singh, "Recycling of spent lithium-ion battery: A critical review," *Critical Reviews in Environmental Science and Technology*, vol. 44, pp. 1129-1165, 2014.
- [26] J. Guan, H. Xiao, X. Lou, Y. Guo, X. Luo, Y. Li, C. Yan, X. Yan, G. Gao, H. Yuan, J. Dai, R. Su, W. Gu, Z. Guo, "Enhanced Hydrometallurgical Recovery of Valuable Metals from Spent Lithium-ion Batteries by Mechanical Activation Process," *ES Energy & Environment*, vol. 1, pp. 80-88, 2018.
- [27] S. Zhang, C. Zhang, X. Zhang, E. Ma, "A mechanochemical method for one-step leaching of metals from spent LIBs,"

- Waste Management, vol. 161, pp. 245-253, 2023.
- [28] Y. Yang, X. Zheng, H. Cao, C. Zhao, X. Lin, P. Ning, Y. Zhang, W. Jin, Z. Sun, "A Closed-Loop Process for Selective Metal Recovery from Spent Lithium Iron Phosphate Batteries through Mechanochemical Activation," *ACS Sustainable Chemistry & Engineering*, vol. 5, pp. 9972-9980, 2017.
- [29] B. Musariri, G. Akdogan, C. Dorfling, S. Bradshaw, "Evaluating organic acids as alternative leaching reagents for metal recovery from lithium ion batteries," *Minerals Engineering*, vol. 137, pp. 108-117, 2019.
- [30] M. Wang, Q. Tan, J. Li, "Unveiling the Role and Mechanism of Mechanochemical Activation on Lithium Cobalt Oxide Powders from Spent Lithium-Ion Batteries," *Environmental Science and Technology*, vol. 52, pp. 13136-13143, 2018.
- [31] N. V. Kosova, V. F. Anufrienko, T. V. Larina, A. Rougier, L. Aymard, J. M. Tarascon, "Disordering and electronic state of cobalt ions in mechanochemically synthesized LiCoO_2 ," *Journal of Solid State Chemistry*, vol. 165, pp. 56-64, 2002.
- [32] J. Guan, H. Xiao, X. Lou, Y. Guo, X. Luo, Y. Li, C. Yan, X. Yan, G. Gao, H. Yuan, J. Dai, R. Su, W. Gu, Z. Guo, "Enhanced Hydrometallurgical Recovery of Valuable Metals from Spent Lithium-ion Batteries by Mechanical Activation Process," *ES Energy & Environment*, vol. 1, 80-88, 2018.
- [33] J. Guan, Y. Li, Y. Guo, R. Su, G. Gao, H. Song, H. Yuan, B. Liang, Z. Guo, "Mechanochemical Process Enhanced Cobalt and Lithium Recycling from Wasted Lithium-Ion Batteries," *ACS Sustainable Chemistry & Engineering*, vol. 5, pp. 1026-1032, 2017.
- [34] L. Li, J. Ge, R. Chen, F. Wu, S. Chen, X. Zhang, "Environmental friendly leaching reagent for cobalt and lithium recovery from spent lithium-ion batteries," *Waste Management*, vol. 30, pp. 2615-2621, 2010.

Ultraviolet Protection and Antibacterial Properties of Polylactic Acid Nonwoven Fabrics Coated with Water-Borne Polyurethane/Zinc Oxide Composite Coatings

Gülçin Baysal 

Eskisehir Technical University, Research-Development, Technology Management and Innovation Unit, Eskisehir, Türkiye, g_baysal@eskisehir.edu.tr

ARTICLE INFO

ABSTRACT

Keywords:

Zinc oxide
Water-borne polyurethane
Nonwoven fabric
Composite coating



Article History:

Received: 16.10.2023
Accepted: 20.09.2024
Online Available: 18.10.2024

This study aimed to create thermally curable, water-borne polyurethane/zinc oxide (WPU/ZnO) composite coating pastes with varying ZnO concentrations. ZnO nanoparticles were synthesized using a wet chemical process, and the resulting WPU/ZnO coating pastes were applied to PLA nonwoven fabrics (NWFs). In characterization studies, differential scanning calorimetry (DSC), scanning electron microscopy (SEM), Fourier transform-infrared (FTIR) spectroscopy, and X-ray diffraction (XRD) analyses were conducted. Ultraviolet (UV) protection and antibacterial activity of fabrics were investigated. With WPU/ZnO composite coatings, the UV protection properties of the coated fabrics were enhanced compared to the uncoated fabric. The highest UPF value of 53.57 was obtained with the fabric coated with the formulation containing a ZnO concentration of 10%. This fabric also demonstrated more effective antibacterial activity against both *S. aureus* and *E. coli* bacteria. Inhibition zone diameters against *E. coli* and *S. aureus* bacteria were measured as 15.5 ± 0.70 mm and 18.25 ± 0.35 mm, respectively. The results of this study illustrate that functional composite coatings for bio-based NWF structures hold great promise for producing effective UV protective and antibacterial materials, potentially setting the stage for future applications.

1. Introduction

Nanotechnology is an precise arrangement of atoms and molecules to fabricate functional materials, devices, and systems on a nanometer scale, generally spanning from about 0.1 to 100 nanometers. This level of control leads to the development of structures with outstanding properties. Nanomaterials possess distinctive optical, mechanical, catalytic, and biological properties. These characteristics have gained the interest of researchers in the textile industry, rapidly increasing the exploration of nanotechnology in this domain. Textiles are a prime application area for nanotechnology due to the potential to enhance functional properties. Metallic nanoparticles (NPs) are extensively studied for their integration into textiles, improving properties like water and soil resistance, wrinkle resistance, antimicrobial

action, antistatic properties, UV protection, and flame resistance [1, 2].

Metal oxide particles are used in textiles especially for their antibacterial properties. There are different incorporating approaches of them onto textiles. The effectiveness of antimicrobial action on textiles depends on factors such as the type, nature, concentration, and application method of the antimicrobial agent [1]. The researches suggests that metal NPs hold promise for creating antimicrobial fabrics. However, despite their remarkable efficacy against microorganisms, the industry's utilization of silver and gold nanoparticles as antibacterial agents is restricted due to their high cost. In contrast, metal oxide NPs such as ZnO, copper oxide (CuO), and magnesium oxide (MgO) are now commonly used in the textile industry to produce functional textiles [2].

Inorganic nanometal oxides like ZnO, titanium dioxide, and MgO are safe for both humans and animals. Among these oxides, ZnO has captured attention in textile research because of its affordability, easy accessibility, and distinctive chemical and physical attributes. Nano ZnO finds applications in various technologies such as photocatalysis, solar cells, sensors, displays, anti-reflection coatings, sunscreens, UV absorbers, piezoelectric devices, and more [2]. ZnO is bio-safe, biocompatible, and applicable in biomedical uses. These unique features position ZnO as a highly significant nanomaterial for future research and applications [3].

ZnO is recognized as safe by the United States Federal Drug Administration [4]. Therefore, ZnO nanoparticles function as essential ingredients for cosmetics, polymers, food packaging, medicine, and more, contributing a range of versatile functional properties. Recent years functional textile fabrics have been advancing with the integration of nano ZnO, offering safeguard against harmful UV rays and aiding in the prevention of sunburn, skin cancer, and allergies resulting from excessive UV exposure [2].

ZnO NPs are applied to textiles using methods like composite spinning or finishing approaches [5]. ZnO-functionalized textiles can be created through methods like dip-coating, sol-gel, padding, electro deposition, and chemical bath deposition. These techniques deposit nano- and micro-sized ZnO onto textiles using prepared suspensions or in situ synthesis [4]. Various polymers, like polyurethane (PU), poly(vinylidenechloride) and polyethylene are used to laminate or coat textiles. PU coating stands out for its multifunctionality, offering precise mechanical, physical, biological, and chemical properties, as well as excellent flexibility and thermophysiological comfort. [6]. Recently, eco-friendly water-borne polyurethane (WPU) dispersions, have become popular. Incorporating nanofillers or biopolymers into polymer matrix improves its thermophysical and mechanical properties and offers extra functional advantages to the coated surfaces [7-11].

The global monthly consumption and disposal of medical products, driven by COVID-19 and similar illnesses, reaches 130 billion items. These

disposable products, typically made from polyester, polyethylene, and polypropylene, degrade slowly and harm the environment. Switching to eco-friendly, biodegradable materials is essential. PLA, a biodegradable polymer, is emerging as a viable alternative. It is affordable, widely available, and used in various industries, making it a valuable option for improving disposable medical textiles like masks, covers, and aprons [12]. In the current literature, synthetic nonwovens are predominantly used, with cotton fabrics being less common, for creating functional surfaces with ZnO. In one study, Nikiforov et al., employed a three-step atmospheric pressure plasma process to create polyethylene terephthalate (PET) NWFs with three types of NPs: AgNP, CuNP, and ZnONP. All nano fabrics exhibited strong antimicrobial effects on *E. coli* and *S. aureus*. Notably, CuNPs were nearly as effective as AgNPs, while ZnONPs showed lower efficiency against *S. aureus* [13].

Ramamurthy et al., reported PP hydroentangled NWF's antimicrobial properties. They initially etched the NWFs using RF plasma. Following this, they applied nano-scale coatings of ZnO and CuO using KrF excimer-based PLD. The team then conducted morphological and antimicrobial analyses to comprehend the antibacterial mechanism of the coated fabrics. These coatings exhibited enhanced activity against the gram-positive *S. aureus* compared to the gram-negative *E. Coli* [14].

In another study, polyacrylonitrile and poly(vinylidene fluoride) (PVDF) based nanofibrous nonwoven were created through electrospinning by Dong et al. In order to introduce antibacterial properties, ZnO NPs were covalently bonded to the PVDF nanofibers. The obtained nonwoven structure demonstrated effective antibacterial function and maintained good anti-wash properties [15]. Ferreira et al., investigated the properties of PP NWF, focusing on structure, physicochemical aspects, and comfort. They functionalized intermediate layer fabrics with ZnO NPs at 0.3% and 1.2% by using electrospinning, dip-pad-dry, and exhaustion methods. The samples were tested for antimicrobial properties. A three-layered structure was then assembled and thermoformed

into facemasks, which were evaluated for antimicrobial effectiveness, filtration efficiency, and breathability [16]. Tania and Ali investigated the impact of nano ZnO coatings on cotton fabric and obtained results were compared to uncoated fabric. ZnO nanoparticles were applied with and without an acrylic binder using a mechanical thermo-fixation technique.

Antimicrobial activity, UV protection, crease resistance, and mechanical properties like tensile strength, tearing strength, bending length, and frictional resistance were assessed. The findings indicated that the binder significantly affects nanoparticle deposition and enhances both functional and mechanical properties, with the binder-coated fabric demonstrating superior performance against microorganisms [17]. Zhang et al., used a simple ion exchange method to create ZnO nanoparticle-coated calcium alginate NWF. They immersed alginate NWF in $Zn(NO_3)_2$ solution for ion exchange, followed by amino hyperbranched solutions to prepare ZnO NPs. The results showed a consistent, high-density ZnO NP coating on the alginate NWF [18]. Deng et al., used magnetron sputter coating to deposit Al-doped ZnO (AZO) films on PET spunbonded nonwovens, and the AZO films showed enhanced UV absorption properties [19].

Adding antimicrobial features to protective gear can greatly reduce pathogen contamination and help mitigate healthcare-associated infections. In a study, PP NWF, commonly used in personal hygiene products and hospital protective gear, was surface-modified using corona treatment. Dyne liquid assessed the surface polarity, showing increased polarization. The polarized PP NWF was then coated with ZnO antiviral agents via a spray method, using a polyurethane solution as an adhesive. The study focused on the antiviral and antibacterial activities of the coated fabric against MS2 bacteriophage, *S. aureus*, and *Klebsiella pneumoniae*. The polyurethane binder minimized antiviral coating leaching, and the fabric achieved a 99.90% reduction in microorganisms after 24 hours [20]. Uğur et al., prepared multilayer nanocomposite films with ZnO nanoparticles on cationized woven cotton fabrics using a layer-by-layer molecular self-assembly method. Cotton fabrics were pretreated with 2,3-epoxypropyltrimethylammonium

chloride (EP3MAC) to impart a cationic surface charge. These films showed excellent antimicrobial activity against *Staphylococcus aureus* and improved UV protection for the fabrics [21].

Recently, there has been an increasing attention in research focused on developing biodegradable medical textiles to enhance sustainability. In this context, it is crucial to functionalize textile surfaces made from natural and biodegradable materials using environmentally friendly materials and cost effective methods to explore their potential use in medical textiles. In recent years, PLA based nonwoven substrates have gained attention to develop functional textile surfaces. In the literature, Zhang et al., prepared PLA/ZnO/additives non-woven slices by melt blending method. These fabrics showed good hydrophobicity and antibacterial properties [22].

In previous studies, functional properties of PLA fabrics were examined by applying lignin/WPU composite coatings using both unmodified lignin [8] and modified lignin biopolymers [9], as well as lignin/ZnO/WPU-based composite coating formulations combining lignin biopolymer with ZnO metal oxide [10]. In previous study, lignin/ZnO/WPU coatings on PLA nonwoven fabrics enhanced antibacterial properties, tensile strength, abrasion resistance, and UV protection and presented potential of this study for medical textiles applications. UV absorption ability of lignin biopolymer provided excellent UV protection to PLA fabrics. Color properties, air and water vapor permeability performances and surface wettability measurements of coated PLA fabrics were also examined [10].

However, no research exists on ZnO/WPU coatings for biodegradable PLA fabrics, especially in terms of UV transmittance and antibacterial features. This study focuses solely on the effect of ZnO concentration in WPU-based coatings on PLA fabric, in terms of UV transmittance and antibacterial properties. Coating formulations with four different ZnO concentrations, combined with a WPU binder, were applied to PLA spunlace NWFs using a film applicator and then thermally cured. Also, the prepared WPU/ZnO coating formulations were applied to glass plates as thin films and then

thermally cured. The synthesized ZnO particles obtained through a homogeneous phase reaction between zinc nitrate hexahydrate and sodium hydroxide were characterized by SEM and XRD. The chemical and thermal properties of thermally cured pure WPU and WPU/ZnO films were characterized by FTIR and DSC. The uniformity of ZnO distribution across the ZnO/WPU films and coated fabrics was examined by SEM.

2. Experimental

2.1. Materials

In this study, as a base material PLA spunlace fabric with fabric weight of 50 g/m² (Mogul Tekstil, Türkiye) was used. The list of materials used for preparing WPU/ZnO formulations was given in Table 1.

Table 1. Materials used in water-borne coating paste formulations

Materials	
PLA spunlace nonwoven (fabric weight of 50 g/m ²)	Mogul Tekstil, Türkiye
Aliphatic polyether anionic waterborne polyurethane dispersion, 60% solid content	Witcobond® 358-90, Lanxess, Germany
Zinc nitrate hexahydrate (Zn(NO ₃) ₂ ·6H ₂ O, 98%),	Merck, Germany
Sodium hydroxide	Merck, Germany
Crosslinker	Trixene® Aqua BI 201, Lanxess, Germany
Wetting agent	NC WET 1200, NC İstanbul Kimyevi Ürünler, Türkiye
Thickener	Pigmacolor Pigmapol PF, Kemiteks, Türkiye
Defoamer	Pigmacolor HC, Kemiteks, Türkiye
Ammonium hydroxide solution	NH ₄ OH, Kimetsan, Türkiye
Distilled water	

2.2. Methods

2.2.1. Preparation and application of WPU/ZnO coatings on NWFs

WPU/ZnO composite formulations (Table 2) were created with varying ZnO concentrations, following methods from previous studies [8-10]. For ZnO nanopowder synthesis, zinc nitrate hexahydrate (Zn(NO₃)₂·6H₂O) and NaOH (~20 wt.%) were used. First, 10 grams of Zn(NO₃)₂·6H₂O and 20 grams of NaOH were dissolved separately in 500 mL of deionized water. The NaOH solution was mixed with the Zn(NO₃)₂ solution and heated to 85°C, stirred at 750 rpm for 4 hours, then cooled.

The pH was adjusted to 7.5 using 20 wt% H₂SO₄, and the mixture was kept at 40°C for 2 hours before being filtered and rinsed with deionized water to collect the ZnO powder. ZnO, in the proportions specified in Table 2, was combined with 50 mL of deionized water. The ZnO dispersion and the blocked isocyanate crosslinker were then added to the binder-water mixture and mixed at 1500 rpm for 30 minutes using a mechanical stirrer (Weightlab WF-OD20).

Following this, additives such as thickener, wetting agent, defoamer, and NH₄OH solution, as detailed in Table 2, were incorporated, and the mixture was stirred for an additional 30 minutes. The pH and viscosity measurements of coating pastes and applications on PLA nonwoven were made as described in previous studies [9, 10].

2.2.2. FTIR and SEM analysis

The thermally cured WPU/ZnO films underwent chemical analysis through FTIR spectroscopy (VERTEX 70v, Bruker, Germany), equipped with a universal ATR attachment and diamond crystal. The measurements were taken across a wavelength range of 400 to 4000 cm⁻¹, with a scan resolution of 4 cm⁻¹. SEM analysis was performed on ZnO powder, WPU-X, WPU/ZnO films, and fabric samples utilizing a FE-SEM instrument (Hitachi Regulus 8230) at an operating voltage of 10.0 kV. To enhance the electrical conductivity of the samples (both films and fabrics) before the analysis, a thin gold layer was applied to the surfaces using a Leica EM ACE600 coating system, with deposition rates between 0 to 10 nm/min.

2.2.3. DSC and XRD analysis

Thermal analysis of cured films was conducted using differential scanning calorimetry (DSC; Q20, TA Instruments). The device was set to heat from 25°C to 500°C at a rate of 10°C/min for

both heating and cooling. The crystal structures and phases of ZnO powder were analyzed using XRD. The samples were ground to ~63 µm, dried at ~105±5°C for 4 hours, and then measured with an XRD device (Rigaku Miniflex 600) over a 2θ range of 5°-70°.

Table 2. Coating paste formulations

Formulation	DI Water (%)	WPU (%)	ZnO (%)	Crosslinker (%)	Thickener (%)	Wetting agent (%)	Defoamer (%)	NH ₄ OH solution (%)
WPU-X	18.61	75	0	2	2.63	0.75	0.46	0.55
WPU/ZnO-1%	18.61	75	1	2	2.63	0.75	0.46	0.55
WPU/ZnO-3%	18.61	75	3	2	2.63	0.75	0.46	0.55
WPU/ZnO-5%	18.61	75	5	2	2.63	0.75	0.46	0.55
WPU/ZnO-10%	18.61	75	10	2	2.63	0.75	0.46	0.55

2.2.4. UV-VIS measurements

Fabric samples (2 x 2 cm²) were scanned over a wavelength range of 200 to 800 nm using a UV-VIS-NIR spectrometer (Shimadzu UV-3600 Plus) according to AATCC TM183 and UV protection levels were determined following ASTM D6603 [23].

2.2.5. Antibacterial activity

The antibacterial effectiveness of WPU/ZnO coated fabrics, influenced by different ZnO concentrations, was assessed against gram-positive and gram-negative bacteria. This test was made using the agar disc diffusion method, following the PN-EN ISO 20645:2006 standard for determining antibacterial activity in textile fabrics [24]. *E. coli* and *S. aureus* bacterial solutions with a density equivalent to the 0.5 McFarland standard were prepared. After spreading 100 µL of these bacterial solutions onto Mueller-Hinton agar, the coated fabrics were placed in the environment and incubated at 35 °C for 24 hours. The inhibition zone results formed after 24 hours were measured.

3. Results and Discussion

3.1. FTIR analysis results

The thermally cured pure WPU (WPU-X) film and WPU/ZnO composite coating films were analyzed by FTIR spectroscopy and composite films' FTIR spectra was given in Figure 1. FTIR spectra of the film prepared with WPU-X

formulation showed the characteristic peaks of pure WPU [8-11].

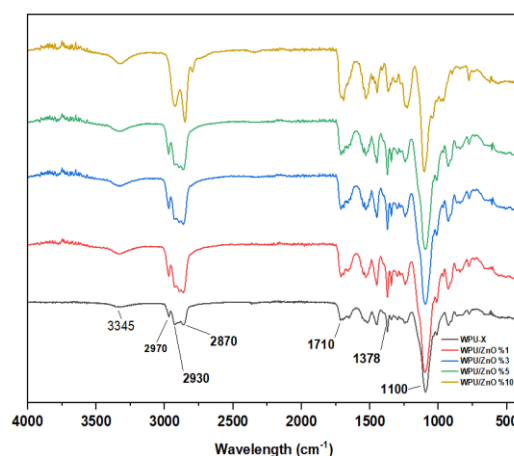


Figure 1. Fourier transform-infrared spectra of thermally cured films

The absorption peak observed at 3345 cm⁻¹ was attributed to stretching vibrations caused by the -O-H- groups, and its intensity showed a notable increase with higher concentrations of ZnO. The absorption peaks at 2930 cm⁻¹ and 2870 cm⁻¹ were linked to asymmetric and symmetric -CH₂ groups. With the increase in ZnO concentration, the peak at the wavelength of 2930 was disappeared and the density of peaks occurred at 2970 cm⁻¹ and 2870 cm⁻¹ increased. The intensity of these peaks demonstrated an increase in correlation with higher concentrations of ZnO. The spectral bands ranging from 1460 to 1378 cm⁻¹ reveal various modes of -CH₃ and -CH₂ vibrations. At the wavelength of 1100 cm⁻¹, the band is attributed to the deformation of O-C=O stretching vibration in the rigid urethane group, while at the wavelength of 778 cm⁻¹, the band is

associated with the out-of-plane bending of the ester group. The absorption band density observed at the wavelength of 1710 cm^{-1} , intensifying with higher ZnO concentration, was attributed to the presence of free and hydrogen-bonded $\text{C}=\text{O}$ groups [25].

The absorption peak in the $\text{C}=\text{O}$ region exhibited an increase across all ZnO concentration levels. Nonetheless, the increase in absorption peaks for samples exceeding the amount of 5% ZnO showed a minor increment compared to those below 5%. The increase in the density of absorption peaks occurred at 3345 cm^{-1} implies that ZnO was incorporated into the PU matrix, thereby contributing to the disturbance of phase separation. The interaction between WPU and the surface hydroxyl groups on the ZnO particles emerged as the catalyst for disrupting the phase within the WPU matrix. The WPU/ZnO composite films exhibited a reduction in the formation of hard phases compared to the neat WPU film. This phenomenon arises from the interaction between WPU and the surface

hydroxyl groups of ZnO-NPs, where each nanoparticle serves as a cross-linker, constraining the mobility of the polymer chains and consequently restricting and decreasing phase formation [26].

3.2. DSC analysis results

Thermal properties of WPU/ZnO films were investigated by DSC analysis. The results of DSC analysis results were given in Table 3. According to the results obtained, as the ZnO concentration increased in WPU/ZnO films, T_g and T_m values increased. WPU/ZnO films exhibited enhanced T_g and T_m values (T_g : $323.53\text{ }^\circ\text{C}$ and T_m : $386.02\text{ }^\circ\text{C}$) compared to those of the WPU-X film analyzed in previous studies [8, 10]. The highest T_g and T_m values were obtained with the formulation including 10% ZnO nano powder. The rise in the T_g value due to decreased mobility of polymer chains, was attributed to a robust interaction between WPU polymer and ZnO particles [27].

Table 3. Thermal analysis results of composite films

Sample	T_g ($^\circ\text{C}$)	ΔH_m (J/g)	T_m ($^\circ\text{C}$)	ΔH_m (J/g)
WPU/ZnO 1%	343.51	30.57	412.63	56.57
WPU/ZnO 3%	344.71	48.22	413.51	65.08
WPU/ZnO 5%	348.43	48.50	414.09	63.05
WPU/ZnO 10%	371.42	110.0	452.74	65.73

3.3. XRD analysis results

XRD analysis was used to investigate the crystal structure of the synthesized ZnO nanopowder (Figure 2). The parameters of the synthesized ZnO, obtained from X-ray diffraction patterns, were provided in Table 4. The XRD patterns of the synthesized ZnO nanopowder closely obtained those of pure ZnO nanopowder [10]. Nine distinct peaks were observed at specific

angles: 31.72, 34.37, 36.21, 48.07, 57.19, 63.61, 67.10, 68.72, and 69.85. These angles correspond to crystal planes of (100), (002), (101), (102), (110), (103), (200), (112), and (201). Notably, the intensity of the (101) peak is significantly higher than others, indicating it as the preferred growth plane for the samples. The average size of nanocrystalline (Table 4) was determined using the Debye-Scherrer formula [28].

Table 4. Parameters obtained from x-ray diffraction patterns

Sample	hkl	2Θ	Fwhm (deg)	Crystallite size (nm)
ZnO	100	31.88	0.371	22.2
ZnO	002	34.52	0.298	27.9
ZnO	101	36.36	0.411	20.3

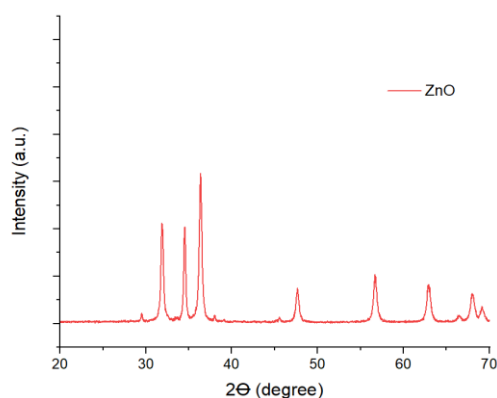


Figure 2. X-ray diffraction pattern of the synthesized ZnO nano powder

3.4. SEM analysis results

The analysis of the synthesized ZnO nano powder, WPU/ZnO composite film and coated PLA nonwoven fabric surface was performed by SEM (Figure 3). The presence of ZnO incorporated into the fabric structure was determined by SEM-EDX. The SEM analysis of composite film (Figure 3 (b)) showed that the ZnO particles (white regions) homogeneously distributed into the polymeric matrix including 10 wt.% of ZnO.

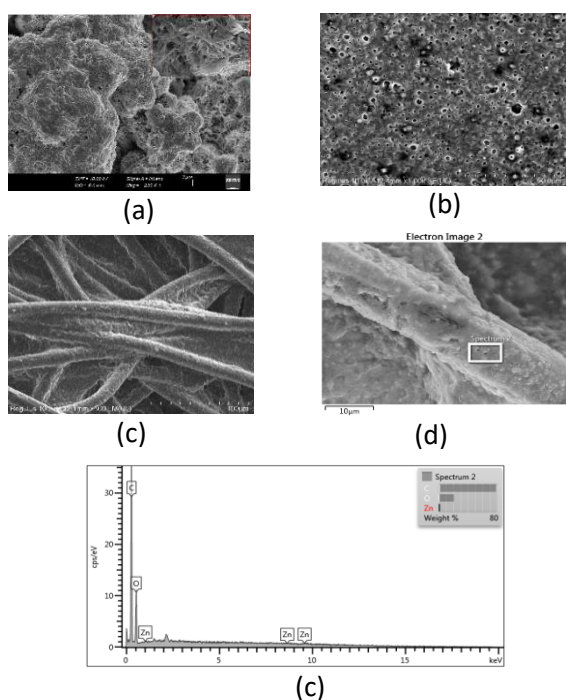


Figure 3. Scanning electron microscopy images of (a) zinc oxide nano powder, (b) thermally cured ZnO/WPU film (c) coated fabric surface (d) fiber surface image and (e) energy-dispersive x-ray spectrum of the coated fabric

It was observed that the WPU/ZnO coating paste coated on the fabric surface filled the gaps between the fibers of the fabric and the ZnO particles create a rough structure on the fiber surface. This indicated that the ZnO-NPs were evenly distributed in the WPU matrix and there is a good compatibility between them [24]. This aggregation may be attributed to the formation of interaction between ZnO particles and water molecules. SEM analysis demonstrated satisfactory filler homogeneity within the polymer matrix. However, notable agglomeration points were observed, particularly in regions with the high concentration of ZnO particles (Figure 3 (c) and Figure 3(d)) [25]. The presence of ZnO nanoparticles included in the fabric structure was confirmed by SEM EDX analysis (Figure 3 (e)).

3.5. UV-VIS measurement results

Table 5 presents the UV protection levels of coated fabrics, denoted by the transmittance values within the 200–800 nm wavelength range. The UV transmittance through the fabric plays a crucial role determining the UPF values of fabrics [28]. The UV transmittance values of the fabrics coated with WPU/ZnO coatings showed improvement compared to the uncoated PLA fabric and the PLA fabrics coated with ZnO-free coating paste (WPU-X), whose UV transmittance values were examined in previous studies [9, 10]. This reduction in UV transmittance signifies enhanced UV blockage, preventing the UV rays from passing through the fabric surface [29]. The highest UPF value of 53.57 was obtained with the formulation of WPU/ZnO-10%. A higher UPF value indicates better protection against UV radiation [28].

3.6. Antibacterial activity results

In the antibacterial activity measurements, this analysis was performed using the agar disc diffusion method. After analysis, inhibition zones were measured, and the numerical results and photographic images were given in Table 6 and Figure 4, respectively.

Table 5. Ultraviolet protection factors and transmission values of coated NWFs

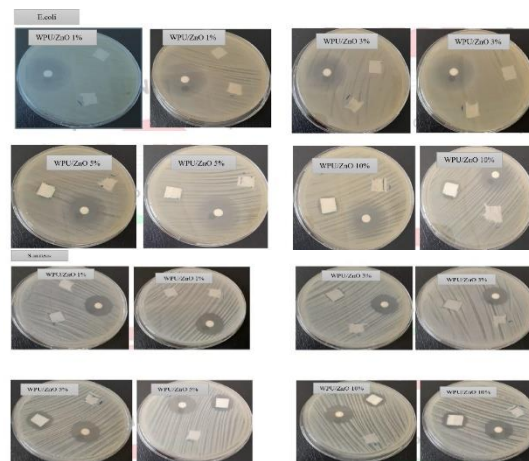
Sample	T(UVB) %	T(UVA) %	UPF	Blocking (UVA)	Blocking (UVB)	Protection Grade
WPU/ZnO-1%	18.52	20.22	5.14	79.78	81.48	-
WPU/ZnO-3%	8.41	10.03	8.28	89.97	91.59	-
WPU/ZnO-5%	4.49	7.56	20.80	92.44	95.51	Good
WPU/ZnO-10%	3.96	7.11	53.57	92.89	96.04	Very Good

It was determined that the fabrics coated with formulations containing 1% and 3% ZnO have no antibacterial activity against *E. coli* and *S. aureus* bacteria. While the fabric coated with the formulation containing 5% ZnO has no resistance to *E. coli*, resistance was obtained against *S. aureus* bacteria. The diameter of the inhibition zone was measured as 17.75 ± 0.35 mm. Inhibition zone diameters against *E. coli* and *S. aureus* bacteria were measured as 15.5 ± 0.70 mm and 18.25 ± 0.35 mm, respectively in the fabric coated with the formulation including 10% ZnO. Due to bacterial attack degradation of various polymer materials poses a common issue.

Table 6. Inhibition zone measurements of coated fabrics against to bacteria

Sample	<i>E. coli</i> (ATCC 25922) inhibition zone (mm)	<i>S. aureus</i> (ATCC 25923) inhibition zone (mm)
Uncoated fabric	-	-
WPU/ZnO %1	-	-
WPU/ZnO %3	-	-
WPU/ZnO %5	-	17.75 ± 0.35
WPU/ZnO %10	15.5 ± 0.70	18.25 ± 0.35
Positive control streptomycin	19	21

When exposed to suitable environment, bacteria can proliferate on the material's surface, rendering it significantly compromised for use. Addressing this issue involves employing various strategies to shield the material from bacterial attacks. A particularly effective approach is augmenting antibacterial capabilities through the incorporation of metal oxide nanoparticles, specifically tailored for the material. Utilizing ZnO in PU/ZnO nanocomposites has proven beneficial in enhancing antibacterial properties. Typically, pristine PU materials exhibit negligible antibacterial properties. However, the incorporation of ZnO into the PU matrix leads to a substantial enhancement of antibacterial attributes [30].

**Figure 4.** Antibacterial activities of uncoated and coated spunlace fabrics against bacteria

Smaller ZnO nanoparticles can penetrate bacterial membranes due to their large surface area, enhancing their antibacterial effectiveness. A significant difference in antibacterial activity was observed between *S. aureus* and *E. coli*, with *S. aureus* showing better susceptibility. The antibacterial efficacy increased with higher concentrations of ZnO NPs, as shown in Figure 4, which depicts a larger inhibition zone for both *E. coli* and *S. aureus* with higher ZnO NP concentrations. The antimicrobial effects of ZnO NPs are primarily due to their disruption of bacterial and fungal cell membranes, likely through the generation of reactive oxygen species such as superoxide anions, hydroxyl radicals, and hydroxyl ions [26].

4. Conclusion

In this study, ZnO nanoparticles were synthesized using wet chemical methods. WPU/ZnO composite coatings were prepared and applied to PLA spunlace NWFs using a film applicator. The functional properties of the coated and thermally cured fabrics were assessed for UV protection and antibacterial activity. FTIR analysis revealed that increasing ZnO concentration enhanced the absorption peaks

related to C=O groups in the WPU/ZnO composite films. XRD analysis confirmed the successful synthesis of ZnO nanopowder by verifying its crystal structure. In the SEM analysis, surface analyzes of coated and cured films and fabrics showed that ZnO-NPs were evenly distributed in the WPU matrix and there was good compatibility between them. DSC analysis of cured composite films showed that with the increase in ZnO concentration a decrease occurred in the mobility of polymer chains due to a strong interaction between WPU polymer and ZnO particles and T_g and T_m values improved.

Higher UV protection properties were obtained with the fabrics coated with the formulation including having higher ZnO concentration. The highest UPF value of 53.57 was obtained with the fabric coated with the formulation of WPU/ZnO-10%. This result was attributed to UV absorption properties of ZnO nanoparticles. In the antibacterial activity analysis, the more effective antibacterial activity was obtained with the fabric coated with the WPU/ZnO 10% formulation having higher ZnO concentration. The results of this study revealed that biodegradable sustainable functional NWFs with UV protection effect and antibacterial activity can be developed with composite coatings including WPU and ZnO nanoparticles.

The findings demonstrated that employing binders to immobilize nanoparticles within NWF structures could offer a promising pathway for creating highly efficient antibacterial materials, paving the way for future applications. The primary advantages of utilizing WPU/ZnO composite materials lie in their biocompatibility and potential antibacterial properties, making them highly suitable for both medical applications and particularly for their UV protection attributes they may be suitable for everyday use. The main uses of PLA NWFs coated with WPU/ZnO composite coatings may be medical textiles applications such as hospital bedding, gloves, surgical drapes.

Article Information Form

Acknowledgments

The author expresses gratitude to the East Anatolia High Technology Application and

Research Center at Atatürk University for the UV-VIS, FTIR, and SEM measurements, the Central Research Laboratory at Amasya University for the antibacterial activity and DSC analysis, the Ceramic Research Center at Eskişehir Technical University for XRD analysis, and the Central Research Laboratory Application and Research Center at Eskişehir Osmangazi University for SEM measurements.

Funding

The author is grateful for the financial support (project number 122M737) from The Scientific and Technological Research Council of Türkiye (TÜBİTAK).

Authors' Contribution

The author is responsible for the design, implementation, analysis of the results, and writing of this study.

The Declaration of Conflict of Interest/ Common Interest

No conflict of interest or common interest has been declared by the author.

The Declaration of Ethics Committee Approval

This study does not require ethics committee permission or any special permission.

The Declaration of Research and Publication Ethics

The author of the paper declares that they comply with the scientific, ethical and quotation rules of SAUJS in all processes of the paper and that she does not make any falsification on the data collected. In addition, she declares that Sakarya University Journal of Science and its editorial board have no responsibility for any ethical violations that may be encountered, and that this study has not been evaluated in any academic publication environment other than Sakarya University Journal of Science.

Copyright Statement

Authors own the copyright of their work published in the journal and their work is published under the CC BY-NC 4.0 license.

References

- [1] E. O. Ogunsona, R. Muthuraj, E. Ojogbo, O. Valerio, T. H. Mekonnen, "Engineered nanomaterials for antimicrobial applications: A review," *Applied Materials Today*, vol. 18, p. 100473, 2020.
- [2] I. S. Tania, M. Ali, M. Akter, "Fabrication, characterization, and utilization of ZnO nanoparticles for stain release, bacterial resistance, and UV protection on cotton fabric," *Journal of Engineered Fibers and Fabrics*, vol. 17, 2022.
- [3] S. Kathirvelu, L. D'Souza, B. Dhurai, "UV protection finishing of textiles using ZnO nanoparticles," *Indian Journal of Fibre & Textile Research*, vol. 34, no. 3, pp. 267–273, 2009.
- [4] A. Verbič, M. Gorjanc, B. Simončič, "Zinc oxide for functional textile coatings: Recent advances," *Coatings*, vol. 9, no. 9, pp. 17–23, 2019.
- [5] G. Zhang, Y. Liu, H. Morikawa, Y. Chen, "Application of ZnO nanoparticles to enhance the antimicrobial activity and ultraviolet protective property of bamboo pulp fabric," *Cellulose*, vol. 20, no. 4, pp. 1877–1884, 2013.
- [6] P. Sikdar, S. Islam, A. Dhar, G. Bhat, D. Hinchliffe, B. Condon, "Barrier and mechanical properties of water-based polyurethane-coated hydroentangled cotton nonwovens," *Journal of Coatings Technology and Research*, vol. 19, no. 4, pp. 1255–1267, 2022.
- [7] Y. Zhang, T.-T. Li, C.-W. Lou, J.-H. Lin, "Facile method for tent fabrics with eco-friendly/durable properties using waterborne polyurethane/lignin: Preparation and evaluation," *Journal of Industrial Textiles*, vol. 51, no. 3, pp. 4149S–4166S, Jun. 2022.
- [8] G. Baysal, "Investigation of barrier effectiveness and comfort properties of biodegradable PLA nonwoven fabrics coated with unmodified lignin/water-borne polyurethane composite coatings," *Hittite Journal of Science and Engineering*, vol. 11, no. 2, pp. 77–88, Jun. 2024.
- [9] G. Baysal, "Mechanical and UV protection performances of polylactic acid spunlace nonwoven fabrics coated by eco-friendly lignin/water-borne polyurethane composite coatings," *Journal of The Textile Institute*, vol. 0, no. 0, pp. 1–13, 2023.
- [10] G. Baysal, "Sustainable polylactic acid spunlace nonwoven fabrics with lignin/zinc oxide/water-based polyurethane composite coatings," *International Journal of Biological Macromolecules*, vol. 254, no. P1, p. 127678, 2024.
- [11] G. Baysal, "Effect of lignin / water-borne polyurethane composite coatings on tensile strength and UV protection properties of PET/PA6 bicomponent nonwoven fabrics," *Pamukkale University Journal of Engineering Sciences*, 2024.
- [12] X. Liu, D. Jiang, Y. Qin, Z. Zhang, M. Yuan, "ZnO-PLLA/PLLA preparation and application in air filtration by electrospinning technology," *Polymers (Basel)*, vol. 15, no. 8, pp. 1–12, 2023.
- [13] A. Y. Nikiforov, X. Deng, I. Onyshchenko, D. Vujosevic, V. Vuksanovic, U. Cvelbar, N. De Geyter, R. Morent, C. Leys, "Atmospheric pressure plasma deposition of antimicrobial coatings on non-woven textiles," *The European Physical Journal Applied Physics*, vol. 75, no. 2, pp. 1–6, 2016.
- [14] P. Ramamurthy, K. P. Chellamani, B. Dhurai, S. P. Thankarajan, B. Subramanian, E. Santhini, "Antimicrobial characteristics of pulsed laser deposited metal oxides on polypropylene hydroentangled nonwovens for medical textiles," *Fibres & Textiles in Eastern Europe*, vol. 25, no. 2, pp. 112–119, 2017.

- [15] Y. Dong, N. L. Thomas, X. Lu, "Electrospun dual-layer mats with covalently bonded ZnO nanoparticles for moisture wicking and antibacterial textiles," *Materials & Design.*, vol. 134, pp. 54–63, 2017.
- [16] T. Ferreira, A. C. Vale, A. C. Pinto, R. V. Costa, V. Pais, D. Sousa, F. Gomez, G. Pinto, J. G. Dias, I. P. Moreira, C. Mota, J. Bessa, J. C. Antunes, M. Henriques, F. Cunha, R. Fangueiro, "Comparison of zinc oxide nanoparticle integration into non-woven fabrics using different functionalisation methods for prospective application as active facemasks," *Polymers (Basel).*, vol. 15, no. 17, pp. 1–21, 2023.
- [17] I. S. Tania, M. Ali, "Effect of the coating of zinc oxide (ZnO) nanoparticles with binder on the functional and mechanical properties of cotton fabric," *Materials Today: Proceedings*, vol. 38, pp. 2607–2611, 2020.
- [18] G. Zhang, Y. Xiao, J. Yan, W. Zhang, "Fabrication of ZnO nanoparticle-coated calcium alginate nonwoven fabric by ion exchange method based on amino hyperbranched polymer," *Materials Letters*, vol. 270, no. 3, p. 127624, 2020.
- [19] B. Deng, Q. Wei, W. Gao, "Physical properties of Al-doped ZnO films deposited on nonwoven substrates by radio frequency magnetron sputtering," *Journal of Coatings Technology and Research*, vol. 5, no. 3, pp. 393–397, 2008.
- [20] G. Deshmukh, "ZnO coated nonwoven polypropylene fabric with antibacterial and antiviral function for medical applications," 2022 International Conference on Emerging Trends in Engineering and Medical Sciences ICETEMS 2022, pp. 395–400, 2022.
- [21] Ş. S. Uğur, M. Sarişik, A. H. Aktaş, M. Ç. Uçar, E. Erden, "Modifying of cotton fabric surface with Nano-ZnO multilayer films by Layer-by-Layer deposition method," *Nanoscale Research Letters*, vol. 5, no. 7, pp. 1204–1210, 2010.
- [22] R. Zhang, L. Tang, X. Ji, Y. Su, N. Xu, Y. Feng, L. Pan, "Continuous preparation and antibacterial mechanisms of biodegradable polylactic acid/nano-zinc oxide/additives antibacterial non-wovens," *International Journal of Biological Macromolecules*, vol. 269, Part 2, 132188, Jan. 2024.
- [23] K. A. V. Prilla, J. M. Jacinto, L. J. O. Ricardo, J. T. S. Box, A. B. C. Lim, E. F. Francisco, G. I. N. De Vera, J. A. T. Yaya, V. V. M. Natividad, E. N. Awi, R. Encina, "Flame retardant and UV-protective cotton fabrics functionalized with copper (II) oxide nanoparticles," *Antorcha*, vol. 7, no. 2, pp. 11–16, 2021.
- [24] M. H. Kudzin, Z. Mrozińska, "Biofunctionalization of textile materials. 2. antimicrobial modification of poly(lactide) (PLA) nonwoven fabrics by fosfomicin," *Polymers (Basel).*, vol. 12, no. 4, p. 768, Apr. 2020.
- [25] S. Vlad, C. Ciobanu, R. V Gradinaru, L. M. Gradinaru, A. Nistor, "Antibacterial evaluation of some polyurethane membranes modified by zinc oxide nanoparticles," *Digest Journal of Nanomaterials and Biostructures*, vol. 6, no. 3, pp. 921–930, 2011.
- [26] T. S. Velayutham, W. H. Abd Majid, W. C. Gan, A. Khorsand Zak, S. N. Gan, "Theoretical and experimental approach on dielectric properties of ZnO nanoparticles and polyurethane/ZnO nanocomposites," *Journal of Applied Physics*, vol. 112, no. 5, 2012.
- [27] R. R. Soares, C. Carone, S. Einloft, R. Ligabue, W. F. Monteiro, "Synthesis and characterization of waterborne polyurethane/ZnO composites," *Polymer Bulletin*, vol. 71, no. 4, pp. 829–838, 2014.
- [28] A. Belay, M. Mekuria, G. Adam, "Incorporation of zinc oxide nanoparticles in cotton textiles for ultraviolet light

protection and antibacterial activities,” *Nanomaterials and Nanotechnology*, vol. 10, pp. 1–8, 2020.

- [29] I. S. Tania, M. Ali, M. Akter, “Fabrication, characterization, and utilization of ZnO nanoparticles for stain release, bacterial resistance, and UV protection on cotton fabric,” *Journal of Engineered Fibers and Fabric*, vol. 17, pp. 1–11, Jan. 2022.
- [30] M. M. Rahman, “Polyurethane/zinc oxide (PU/ZnO) composite-synthesis, protective property and application,” *Polymers (Basel)*, vol. 12, no. 7, 2020.

Improved Singlet Oxygen Production of Zinc Phthalocyanine Bearing Pyridine-4-Thiol Groups Using Sonochemistry and Comparison with Photochemistry

Öznur Dülger Kutlu 

Yıldız Technical University, Faculty of Arts and Science, Department of Chemistry, İstanbul, Türkiye, ozdulger@yildiz.edu.tr

ARTICLE INFO

Keywords:

Sensitizer
Zinc phthalocyanine
Sonophotodynamic therapy
Photodynamic therapy



Article History:

Received: 15.11.2023
Accepted: 26.09.2024
Online Available: 18.10.2024

ABSTRACT

The interest in research to enhance the ability of sensitizers to generate singlet oxygen using light and/or ultrasound in cancer treatment has increased significantly in recent years, and studies have attracted considerable interest. In addition, phthalocyanines (Pcs) have become increasingly important as sensitizers in photodynamic therapy (PDT) (stimulation source: light) and/or sonodynamic therapy (SDT) (stimulation source: light and ultrasound). Sonophotodynamic therapy (SPDT), a new technique that gives more effective results than PDT, is now gaining in importance. Although there are published articles on SPDT studies, studies in this field are limited. In this context, we synthesized a zinc(II) phthalocyanine molecule bearing 4-(pyridine-4-ylthio) substituents to determine its potential as a sensitizer in SPDT applications as well as PDT applications, and the structure of the synthesized complex was illuminated using FTIR, ¹H-NMR, UV-Vis, and MS spectroscopic techniques. When light and ultrasound were combined, the calculated $\Phi\Delta$ value for zinc (II) phthalocyanine (3) increased to greater than 1, even though it was 0.76 after light excitation. When evaluating the two methods, it was observed that singlet oxygen production was greatly enhanced by the SPDT method. In this way, the research will add to the enhancement of knowledge on the subject of the SPDT method's enhancement of singlet oxygen generation.

1. Introduction

Cancer is a complex disease that requires careful consideration of treatment options. Chemotherapy, radiotherapy, and immunotherapy available for cancer, as various traditional treatment methods have been developed and studied to determine their effectiveness in combating different types of cancer. These methods often do not provide sufficient benefit due to the invasive and damaging nature of cancer cells. The most difficult process in cancer treatment is the harm to both healthy and malignant cells during the treatment phase. To overcome this issue, researchers have turned to two new therapy approaches in recent years: PDT and SDT, which are novel, non-invasive, and regionally selective

treatment methods that could be used to treat cancer [1, 2].

PDT and SDT are based on the principle that when a sensitizer is irradiated with a stimulant, it excites the sensitizer and generates reactive oxygen species (ROS). Ultimately, this cause irreversible damage to tumour cells [3]. The difference between these two methods is the energy source used to activate the sensitizer. PDT uses a specific wavelength of light to stimulate the sensitizer that accumulates in the tumour cells, while SDT uses ultrasound at low intensity and frequency [4-6]. The limited light and low penetration into the tumor tissue is an important disadvantage of PDT in comparison to SDT [7]. For this reason, SPDT method, which combines the effects of PDT and SDT approaches, has been developed as an alternative application. When

ultrasound and light are combined to stimulate the sensitizer, SPDT provides a more effective treatment method [8-11].

Over the last four decades, Pcs have been presented as highly promising photosensitizers due to their ability to absorb red light in the therapeutic window (650 nm–900 nm), high efficiency in generating reactive oxygen.

Over the last four decades, Pcs have been presented as highly promising photosensitizers due to their ability to absorb red light in the therapeutic window (650 nm–900 nm), high efficiency in generating reactive oxygen species, low dark toxicity, and low skin photosensitivity [12-15]. However, the application of Pcs as SDT sonosensitizers has been little studied [16-19].

The Pcs with different central metal ions and functional groups have different structural and physicochemical properties. Zinc(II) phthalocyanine complexes have a high singlet oxygen production capacity, which leads to their usage as photosensitizers in PDT [20, 21]. One of the most critical properties of the photosensitizer for PDT therapies is its solubility without any aggregation [21].

Pyridine and pyridine derivatives are pharmacophores with a prototypical π -axis heterocyclic structure, which is preferred in medical chemistry, exhibiting both substrate and reactive different chemistries [22]. Pyridine derivatives are one of the most important heterocyclic compounds due to their wide range of biological activities, such as anticancer [23], antiviral [24], anticonvulsant [25], and antidiabetic [26]. Zinc(II) phthalocyanines, which are functionalized with pyridine derivatives, have been proposed as effective photosensitizers due to their high degree of water solubility and their ability to generate high levels of singlet oxygen [3, 27, 28].

In this study, the tetra-pyridine derivative-substituted zinc(II) phthalocyanine complex was prepared, followed by photophysicochemical and sono-photochemical measurements. The primary objective of this study is to achieve an efficient increase in singlet oxygen production. Because of this, the singlet oxygen quantum

yield of the studied complex was determined with light and/or ultrasound as the source of stimulating the photosensitizer and the results were compared.

2. Experimental

2.1. Materials and equipments

The chemicals, materials and equipment utilized are given as 'supporting information'.

2.2. Synthesis of compounds

2.2.1. 4-(pyridine-4-ylthio) phthalonitrile (2a)

4-nitrophthalonitrile (2.76 g, 16 mmol) (**1**) and pyridine-4-thiol (1.55 g, 16 mmol) (**2**) were dissolved in DMF (15 mL) and stirred at room temperature for 30 minutes. The powdered K_2CO_3 (8 g, 58 mmol) was added in pieces for 2 hours and then mixed at room temperature for 96 hours. When the mixing time is complete, the reaction mixture is poured into 100 ml of ice water and mixed for 30 minutes. The resulting precipitate was filtered and washed thoroughly with water until the wash water was neutral. After drying in a vacuum oven, compound **1** was crystallized in an ethyl alcohol solvent.

The resultant cream-colored compound was then purified via column chromatography using chloroform:methanol (10:1) solvent systems.

Yield: 3.094 g (%87.5). $C_{13}H_7N_3S$
 1H NMR (500 MHz, DMSO- d_6), (δ : ppm): 8.61 (d, 2H, ArH), 8.35 (s, 1H, ArH), 8.22 (d, 1H, ArH), 7.97 (d, 1H, ArH), 7.42 (d, 2H, ArH). FT-IR (ATR, cm^{-1}): 3089 (Ar., C-H), 2234 ($C\equiv N$), 1011-1067 (C-S-C), 705. MS (MALDI-TOF): m/z = Calc.237.28; Found: 237.020 [M] $^+$.

2.2.2. Tetrakis[4-(pyridine-4-ylthio)] phthalocyaninato zinc(II) (3)

A mix of 4-(pyridine-4-ylthio)phthalonitrile (**2a**) (0.28 mmol, 0.066 g), DBU (0.50 mmol, 0.3 mL), and anhydrous zinc(II) acetate ($Zn(OAc)_2$) (0.28 mmol, 0.66 g) in n-pentanol (3 mL) underwent stirring at 140°C in an argon atmosphere for 18 hours. After the stirring time was completed, the mixture was cooled to room temperature, and the reaction mixture was

gradually added to n-hexane and precipitated. The resulting precipitate was collected by centrifugation and washed sequentially with n-hexane, methanol, and ethanol. The impure green precipitate was purified by column chromatography using a mixture of THF and CHCl_3 as eluent (1:10).

Yield: 0.035 g (50%). $\text{C}_{58}\text{H}_{28}\text{N}_{12}\text{S}_4\text{Zn}$

^1H NMR (500 MHz, DMSO-d_6), (δ : ppm): 8.53-8.39 (m, 8H, ArH), 7.89-7.68 (m, 8H, ArH), 7.54-7.38 (b, 4H, ArH), 7.29-7.08 (m, 8H, ArH). FT-IR (ATR, cm^{-1}): 3089 (Ar., C-H), 1648 (C=N), 1298 (C-S-C). MS (MALDI-TOF): m/z = Calc.1014.170; Found: 1014.953 [M] $^+$.

2.3. Photophysicochemical studies

In order to investigate the aggregation behavior and photophysicochemical properties of complex **3**, all test solutions were prepared in DMSO used as a drug delivery vehicle for various human and animal diseases [29]. In photophysical studies, the fluorescence property of the substance was investigated, and the fluorescence quantum yield (Φ_F) was calculated. In photochemical studies, the singlet oxygen generation potential and resistance to photodegradation were investigated, and singlet oxygen quantum yields (Φ_Δ) and photodegradation quantum yield (Φ_d) were calculated. The photophysical and photochemical properties of the synthesized complex were investigated using the methods and related formulas given in the 'Supporting Information'.

3. Result and Discussion

3.1. Synthesis and characterization

Compounds **2a** and **3** have been previously published in another article [27]. In this study, compound **2a** was synthesized according to the procedure in this article, and compound **3** was synthesized in a different solvent medium. Figure 1 summarizes the synthesis pathway of compounds **2a** and **3**. The synthesis of tetra-substituted phthalocyanine **3** was conventionally carried out by cyclotramerization of 4-(pyridin-4-ylthio)-substituted phthalonitrile (**2a**) in the presence of K_2CO_3 , $\text{Zn}(\text{OAc})_2$, and DBU as catalysts. The chemical structures of synthesized

compounds were certified by various spectroscopic techniques. The predicted structure of compounds **2a** and **3** is in agreement with their spectral information. The spectral data of compounds **2a** and **3** are presented in the 'Supporting Information'.

In the FT-IR spectrum of **2a** (Figure S1), at 3063.90 and 2234 cm^{-1} peaks belong to the aromatic C-H and characteristic $\text{C}\equiv\text{N}$ vibrations corresponding to, respectively.

After the conversion of **2a** to **3** by the cyclotramerization reaction, the characteristic C-N of 2234 cm^{-1} of **2a** has disappeared in the FT-IR spectrum of **3** (Figure S1), which is an indication of the formation of metalloftalocyanine. Characteristic vibrations corresponding to the C-S-C group were observed in 698 cm^{-1} (for **3**). The structure of the **2a** ve **3** compounds was confirmed by the detection of the molecules in their own regions of the protons belonging to the structures in the ^1H NMR spectrum. In the ^1H NMR spectra of **2a** (Figure S2), the aromatic protons were observed within the resonance region of 7.61–8.42 ppm. In the ^1H NMR spectra of complex **3** (Figure S3), the phthalocyanine ring protons appeared as unresolved multiplets in the range of 9.50–7.00 ppm.

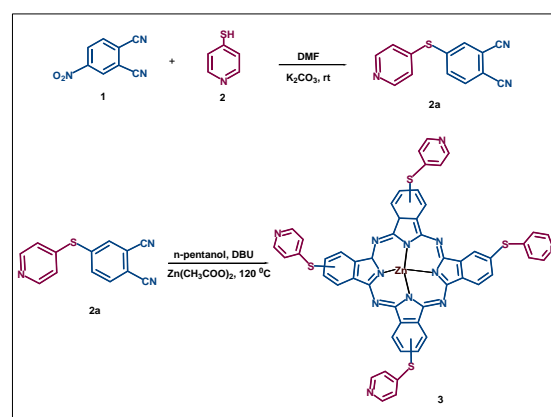


Figure 1. The synthesis procedure for compounds **2a** and **3**.

In the Mass spectra, molecular ion peaks of the compounds **2a** and **3** show m/z peak at 237.020 [M] $^+$ (Figure S4) and 1014.953 [M] $^+$ (Figure S5), respectively. The results of mass spectrometry approved the desired structure for the compounds.

3.2. The ground state electronic absorption spectra and aggregation studies

The chemical and electronic properties of the Pc ring rely on the 18π electron system. In Pcs' absorption spectra, a single absorption band (Q band) of the metal phthalocyanine with D_{4h} symmetry is generally observed around 650-750 nm, and in addition, a less intense absorption band called Soret band (B band) is observed around 300-400 nm [30]. The Q band's position and intensity prove important in determining the application of Pc derivatives. The spectral properties are mainly influenced by the central metal ion, aggregation, π -conjugation, molecular symmetry and substituents.

The electronic spectrum of compound **3** displayed identifying absorption bands at 685 nm and 320–370 nm within the Q-band and B-band regions. These regions are typical for metallophthalocyanines present in DMSO (Table 1) [30]. In Table 1, it is evident that the addition of 4-(pyridine-4-ylthio) groups to the zinc(II) phthalocyanine framework resulted in a 13 nm red-shifted absorption within DMSO in comparison to standard **ZnPc** ($\lambda_{\max} = 672$ nm) [31]). The aggregation results from high concentrations of compounds or the use of polar solvents. Increasing the rate of phthalocyanine compound forming aggregates in solution reduces its photosensitizing effectiveness; Therefore, aggregation study is important before a molecule can be recommended as a usable photosensitizer in PDT applications. [31].

To determine the aggregation tendency of **3**, its solutions at different concentrations (1×10^{-5} to 5×10^{-5}) were prepared in DMSO, and its absorption spectra (Figure 2) were monitored using a UV-Vis spectrophotometer. As seen in Figure 2, complex **3** did not form aggregates in DMSO and conformed to the Lambert-Beer law. Thus, complex **3** is a potential photosensitizer for PDT applications as it does not aggregate in the studied solvent environment.

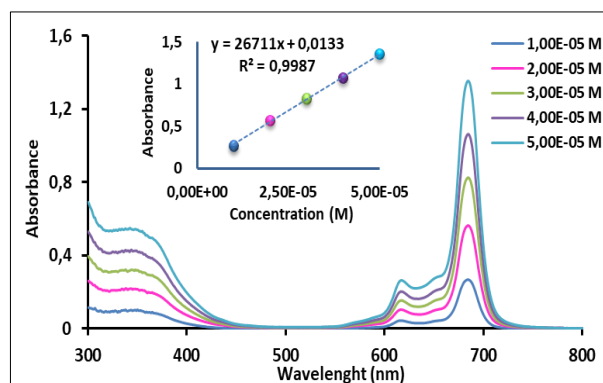


Figure 2. Aggregation properties of complex **3** in DMSO (Inset: Absorbances versus)

3.3. Photophysical studies

3.3.1. Fluorescence quantum yield (Φ_F)

One important parameter in assessing the suitability of a molecule as a photosensitizer for PDT applications is to ascertain its fluorescence properties. The fluorescence characteristics of such molecules are critical for the photosensitizer's traceability within biological systems. Therefore, the solution of complex **3** (solvent: DMSO) was stimulated at 617 nm, and the fluorescence behavior was studied. Emission bands at 698 nm (Figure 3) were observed, and Φ_F value was calculated 0.15 (Table 1). The fluorescence quantum yield of complex **3** in DMSO shows a lower value than that of unsubstituted **ZnPc** ($\Phi_F=0.20$) [31]. The data supports that complex **3** facilitates intersystem crossing (ISC) to a greater extent than unsubstituted-**ZnPc**, hence increases singlet oxygen production while reducing fluorescence efficiency [6].

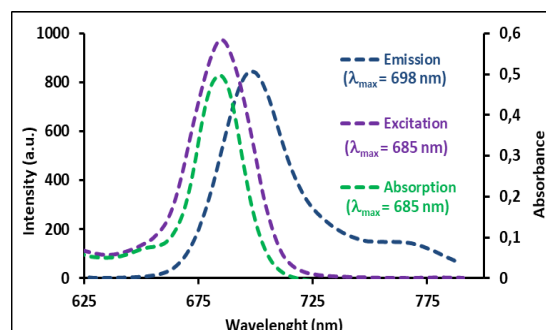


Figure 3. Absorption, excitation and emission spectra of complex **3** in DMSO

Table 1. Spectral and photophysical features of **3** in DMSO.

λ_{Abs} (nm)	$\log \epsilon$	λ_{Em} (nm)	Δ_{Stokes} (nm)	Φ_{F}
685	4.42	698	13	0.15

3.4. Photochemical studies

3.4.1. Singlet oxygen quantum yield (Φ_{Δ})

Singlet oxygen ($^1\text{O}_2$), which is one of the three components of PDT, has a direct relationship with cancer cell death. Hence, the efficiency of PDT is directly linked to the sensitizer responsible for $^1\text{O}_2$ production. The Φ_{Δ} is defined as the ratio of the number of $^1\text{O}_2$ molecules produced to the number of photons absorbed by the sensitizer. This quantity is used to determine the $^1\text{O}_2$ production capacity of the photosensitizer to be used in PDT applications for effective treatment.

Although singlet oxygen production is associated with the sensitizer, the stimulation method is also significant. Singlet oxygen production has been noted to increase significantly, particularly when using the method, combining ultrasound and light (SPDT) as the sensitizer activation technique [12].

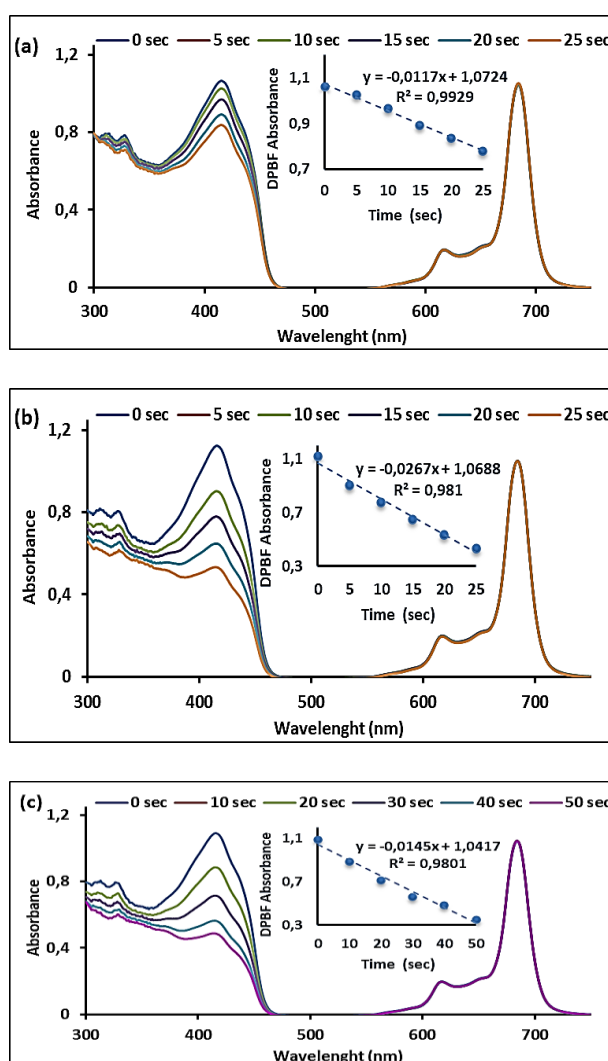
Two different methods were utilized to investigate the effect of the stimulating method on the production of singlet oxygen in complex **3**, namely photodynamic and sonophotodynamic techniques. Using 1,3-diphenylisobenzofuran (DPBF) as the chemical singlet oxygen quencher and unsubstituted zinc phthalocyanine as the standard, the Φ_{Δ} of complex **3** was computed for both applications.

To evaluate the potential of sensitizers, in PDT, solutions containing **3** and DPBF were exposed to light (intensity of 1.15×10^{15} photons $\text{s}^{-1} \text{cm}^{-2}$) every 5 seconds; In SPDT, the solutions were excited with 5 seconds of ultrasound (35 kHz) following 5 seconds of light irradiation, and the change in the absorbance of quencher at 417 nm was monitored using UV-Vis spectrophotometry. All Φ_{Δ} values are listed in Table 2 and all relevant spectra are shown in Figure 4. In addition, the study seen no change in absorption band intensities during photochemical

and sonophotochemical measurements, indicating that **3** did not degrade during singlet oxygen studies. Molecular stability may potentially be affected by light and ultrasound. Figure 3 demonstrates that the Q-band intensity of molecule **3** remained consistent throughout the photochemical and sonophotochemical investigations, indicating that the compound is stable to light and/or ultrasound [32].

Table 2. Photochemical and Sonophotochemical parameters of **3** in DMSO.

Method	Φ_{Δ}	Φ_{d}
Photochemical	0.76	7.02×10^{-4}
Sonophotochemical	1.14	

**Figure 4.** Absorption spectral changes in DMSO during the determination of singlet oxygen quantum yields for complex **3** using sonochemical (a), photochemical (b), and sono-photochemical (c) methods. (Appendix: DPBF absorbance versus time plots).

As a result of photochemical measurements using only light source excitation, the Φ_{Δ} value of complex **3** in DMSO was calculated as 0.76. When this value was compared to unsubstituted **ZnPc** ($\Phi_{\Delta} = 0.67$ in DMSO), it was observed that substituent molecules increased the singlet oxygen yield [33]. In particular, phthalocyanine molecules carrying pyridine derivative groups were theoretically found to contribute positively to singlet oxygen production in PDT [28, 29]. As a result of sonophotochemical measurements using ultrasound and light source excitation, the Φ_{Δ} value of complex **3** in DMSO was found to be greater than 1.

The singlet oxygen production obtained by the sonophotochemical method was also found to be compatible with the photochemical method. According to the results obtained from the aforementioned methods, it has been determined that simultaneous excitation of complex **3** by the synergistic effect of light and ultrasound provides singlet oxygen production much more efficiently. In this way, it has been theoretically demonstrated that the synergistic effect of PDT and SDT on phthalocyanine molecules contributes positively to singlet oxygen production [11, 34].

3.4.2. Photodegradation quantum yield (Φ_d)

One of the important properties of a photosensitizer suitable for use in photodynamic therapy is its resistance to photodegradation caused by UV radiation. Photodegradation studies as well as singlet oxygen quantum yields are used to determine the photochemical properties of Pcs. In order to determine the stability of metallophthalocyanine **3** was exposed to light (intensity of 4.92×10^{15} photons $s^{-1} cm^{-2}$) every 60 seconds the changes in the intensity of the characteristic bands were monitored by measurements (Figure 5) by taking UV-Vis spectra and the Φ_d value calculated. The Φ_d value depends on the structure of the molecule, the type of solvent and light [28].

The photodegradation quantum yield (Φ_d) value for the complex is shown in Table 2 and is of the order of 10^{-4} . Stable **ZnPc** molecules have values as low as 10^{-6} , while unstable molecules have values in the order of 10^{-3} [28]. This

indicates that the molecule is moderately stable in solvent used. In agreement with this, it was found that the addition of a pyridine derivative molecule to the standard zinc phthalocyanine ring increases the degradation resistance of the molecule against light exposure. The synthesised compound was found to be more stable than standard **ZnPc** (0.26×10^{-4} [28]) in DMSO.

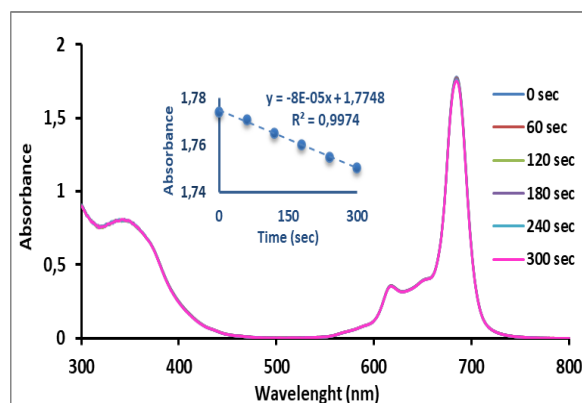


Figure 5. Representative absorption spectral changes during photodegradation studies in DMSO (Appendix: plot of complex **3** absorbances versus time).

4. Conclusion

The nature of the sensitizer and the methods of irradiating the sensitizer are important factors in singlet oxygen production. In PDT and SPDT studies, the use of a highly efficient singlet oxygen-producing sensitizer is very important. In this study, the Φ_{Δ} of sensitizer was compared by applying different methods with irradiation sources: photodynamic and sonophotodynamic methods. When the singlet oxygen quantum yields were examined, the Φ_{Δ} value in the sonophotochemical study reached 1.14, with a 50 % increase when compared to the Φ_{Δ} value ($\Phi_{\Delta} = 0.76$) in the photochemical study. In addition, the molecule's stability under light exposure and high singlet oxygen production make it an ideal sensitizing agent for PDT and SPDT applications. Based on these results, it can be concluded that the synthesized pyridine-derived substituted zinc phthalocyanine molecule is a remarkably promising potential candidate as a sono-photosensitizer for malignant tumor elimination.

Article Information Form

Acknowledgments

Thanks to Prof. Dr. Ali Erdoğan from Yıldız Technical University for his contributions.

Funding

This study was supported by Yıldız Technical University, Scientific Research Projects Coordination Unit (Project No: FKD-2021-4759).

The Declaration of Conflict of Interest/ Common Interest

No conflict of interest or common interest has been declared by the authors.

The Declaration of Ethics Committee Approval

This study does not require ethics committee permission or any special permission.

The Declaration of Research and Publication Ethics

The authors of the paper declare that they comply with the scientific, ethical and quotation rules of SAUJS in all processes of the paper and that they do not make any falsification on the data collected. In addition, they declare that Sakarya University Journal of Science and its editorial board have no responsibility for any ethical violations that may be encountered, and that this study has not been evaluated in any academic publication environment other than Sakarya University Journal of Science.

Copyright Statement

The author owns the copyright of work published in the journal, which is published under the CC BY-NC 4.0 license.

References

- [1] P. Yan, L. H. Liu, P. Wang, "Sonodynamic Therapy (SDT) for Cancer Treatment: Advanced Sensitizers by Ultrasound Activation to Injury Tumor," *ACS Appl Bio Mater*, vol. 3, no. 6, pp. 3456–3475, 2020.
- [2] I. P. F. Nunes, P. J. L. Crueira, F. J. P. Sampaio, S. C. P. S. de Oliveira, J. M. Azevedo, C. L. O. Santos, L. G. P. Soares, I. D. W. Samuel, S. Persheyev, P. F. de Almeida, A. L. B. Pinheiro, "Evaluation of dual application of photodynamic therapy-PDT in *Candida albicans*," *Photodiagnosis and Photodynamic Therapy*, vol. 42, 2023.
- [3] Ö. D. Kutlu, A. Erdoğan, P. Şen, S. Z. Yıldız, "Peripherally tetra-Schiff base substituted metal-free and zinc (II) phthalocyanine, its water-soluble derivative: Synthesis, characterization, photo-physicochemical, aggregation properties and DNA/BSA binding activity," *Journal of Molecular Structure*, vol. 1284, p. 135375, 2023.
- [4] N. Kocağa, Ö. D. Kutlu, A. Erdoğan, "New peripherally substituted lutetium mono and bis phthalocyanines: Synthesis and comparative photophysical and photochemical properties," *Journal of Porphyrins and Phthalocyanines*, vol. 23, no. 11n12, pp. 1099-1409, 2019.
- [5] C. C. Karanlık, G. Y. Atmaca, A. Erdoğan, "Comparison of singlet oxygen production of ethyl vanillin substituted silicon phthalocyanine using sonophotodynamic and photodynamic methods," *Journal of Molecular Structure*, vol. 1274, p. 134498, 2023.
- [6] C. McEwan, H. Nesbitt, D. Nicholas, O. N. Kavanagh, K. McKenna, P. Loan, I. G. Jack, A. P. McHale, J. F. Callan, "Comparing the efficacy of photodynamic and sonodynamic therapy in non-melanoma and melanoma skin cancer," *Bioorganic & Medicinal Chemistry*, vol. 24, no. 13, pp. 3023–3028, 2016.
- [7] N. Nomikou, K. Curtis, C. McEwan, B. M. G O'Hagan, B. Callan, J. F. Callan, A. P. McHale, "A versatile, stimulus-responsive nanoparticle-based platform for use in both sonodynamic and photodynamic cancer therapy," *Acta Biomaterialia*, vol. 49, pp. 414–421, 2017.
- [8] M. Aksel, O. Bozkurt-Girit, M. D. Bilgin, "Pheophorbide a-mediated sonodynamic, photodynamic and sonophotodynamic therapies against prostate cancer,"

- Photodiagnosis and Photodynamic Therapy, vol. 31, p. 101909, 2020.
- [9] M. Aksel, Ö. Kesmez, A. Yavaş, M. D. Bilgin, "Titaniumdioxide mediated sonophotodynamic therapy against prostate cancer," *Journal of Photochemistry and Photobiology B: Biology*, vol. 225, p. 112333, 2021.
- [10] L. C. Nene, A. Magadla, T. Nyokong, "Enhanced mitochondria destruction on MCF-7 and HeLa cell lines in vitro using triphenyl-phosphonium-labelled phthalocyanines in ultrasound-assisted photodynamic therapy activity," *Journal of Photochemistry and Photobiology B: Biology*, vol. 235, p. 112553, 2022.
- [11] L. C. Nene, T. Nyokong, "Photo-sonodynamic combination activity of cationic morpholino-phthalocyanines conjugated to nitrogen and nitrogen-sulfur doped graphene quantum dots against MCF-7 breast cancer cell line in vitro," *Photodiagnosis and Photodynamic Therapy*, vol. 36, p. 102573, 2021.
- [12] K. Plaetzer, B. Krammer, J. Berlanda, F. Berr, T. Kiesslich, "Photophysics and photochemistry of photodynamic therapy: fundamental aspects," *Lasers in Medical Science*, vol. 24, no. 2, pp. 259–268, Mar. 2009.
- [13] J. P. Celli, B. Q. Spring, I. Rizvi, C. L. Evans, K. S. Samkoe, S. Verma, B. W. Pogue, T. Hasan, "Imaging and Photodynamic Therapy: Mechanisms, Monitoring, and Optimization," *Chemical Reviews*, vol. 110, no. 5, pp. 2795–2838, May 2010.
- [14] J. F. Lovell, T. W. B. Liu, J. Chen, G. Zheng, "Activatable Photosensitizers for Imaging and Therapy," *Chemical Reviews*, vol. 110, no. 5, pp. 2839–2857, May 2010.
- [15] W. M. Sharman, C. M. Allen, J. E. van Lier, "Photodynamic therapeutics: basic principles and clinical applications," *Drug Discovery Today*, vol. 4, no. 11, pp. 507–517, 1999.
- [16] H. Kolarova, K. Tomankova, R. Bajgar, P. Kolar, R. Kubinek, "Photodynamic and Sonodynamic Treatment by Phthalocyanine on Cancer Cell Lines," *Ultrasound in Medicine & Biology*, vol. 35, no. 8, pp. 1397–1404, 2009.
- [17] F. Ayaz, D. Yetkin, A. Yüzer, K. Demircioğlu, M. Ince, "Non-canonical anti-cancer, anti-metastatic, anti-angiogenic and immunomodulatory PDT potentials of water soluble phthalocyanine derivatives with imidazole groups and their intracellular mechanism of action," *Photodiagnosis and Photodynamic Therapy*, vol. 39, p. 103035, 2022.
- [18] J. Wang, M. Xu, M. Chen, Z. Jiang, G. Chen, "Study on sonodynamic activity of metallophthalocyanine sonosensitizers based on the sonochemiluminescence of MCLA," *Ultrasonics Sonochemistry*, vol. 19, no. 2, pp. 237–242, 2012.
- [19] H.-N. Xu, H.-J. Chen, B.-Y. Zheng, Y.-Q. Zheng, M.-R. Ke, J.-D. Huang, "Preparation and sonodynamic activities of water-soluble tetra- α -(3-carboxyphenoxy) zinc(II) phthalocyanine and its bovine serum albumin conjugate," *Ultrasonics Sonochemistry*, vol. 22, pp. 125–131, 2015.
- [20] J. D. Spikes, "Phthalocyanines As Photosensitizers In Biological Systems And For The Photodynamic Therapy Of Tumors," *Photochemistry and Photobiology*, vol. 43, no. 6, pp. 691–699, 1986.
- [21] D. Li, Q. Y. Hu, X. Z. Wang, X. Li, J. Q. Hu, B. Y. Zheng, M. R. Ke, J. D. Huang, "A non-aggregated silicon(IV) phthalocyanine-lactose conjugate for photodynamic therapy," *Bioorganic & Medicinal Chemistry Letters*, vol. 30, no. 12, p. 127164, 2020.
- [22] P. E. Alford, "Six-Membered Ring Systems: Pyridines and Benzo Derivatives," 30, G.W. Gribble, J. A. Joule, Elsevier Inc 2011, pp. 349–391.

- [23] A. M. Rolim Bernardino, L. C. da Silva Pinheiro, C. R. Rodrigues, N. I. Loureiro, H. C. Castro, A. Lanfredi-Rangel, J. Sabatini-Lopes, J. C. Borges, J. M. Carvalho, G. A. Romeiro, V. F. Ferreira, C. P. P. I. Frugulhetti, M. A. Vannier-Santos, "Design, synthesis, SAR, and biological evaluation of new 4-(phenylamino)thieno[2,3-b]pyridine derivatives," *Bioorganic & Medicinal Chemistry*, vol. 14, no. 16, pp. 5765–5770, 2006.
- [24] M. Vrábel, M. Hocek, L. Havran, M. Fojta, I. Votruba, B. Klepetářová, R. Pohl, L. Rulíšek, L. Zendlová, P. Hobza, I. Shih, E. Mabery, R. Mackman, "Purines Bearing Phenanthroline or Bipyridine Ligands and Their RuII Complexes in Position 8 as Model Compounds for Electrochemical DNA Labeling – Synthesis, Crystal Structure, Electrochemistry, Quantum Chemical Calculations, Cytostatic and Antiviral Activ," *European Journal of Inorganic Chemistry*, vol. 2007, no. 12, pp. 1752–1769, Apr. 2007.
- [25] E. G. Paronikyan, A. S. Noravyan, I. A. Dzhagatspanyan, I. M. Nazaryan, R. G. Paronikyan, "Synthesis and anticonvulsant activity of isothiazolo[5,4-b]pyrano(thiopyrano)[4,3-d]pyridine and isothiazolo[4,5-b]-2,7-naphthyridine derivatives," *Pharmaceutical Chemistry Journal*, vol. 36, no. 9, pp. 465–467, 2002.
- [26] V. R. Firke, S. D., Firake, B. M., Chaudhari, R. Y., Patil, "Synthetic and pharmacological evaluation of some pyridine containing thiazolidinones," *Asian Journal of Research in Chemistry*, vol. 2, no. 2, pp. 157–161, 2009.
- [27] J. B. Pereira, E. F. Carvalho, M. A. Faustino, R. Fernandes, M. G. Neves, J. A. Cavaleiro, N. C. Gomes, A. Cunha, A. Almeida, J. P. Tomé, "Phthalocyanine Thio-Pyridinium Derivatives as Antibacterial Photosensitizers," *Photochemistry and Photobiology*, vol. 88, no. 3, pp. 537–547, 2012.
- [28] T. Keleş, B. Barut, A. Özel, Z. Biyiklioglu, "Synthesis of water soluble silicon phthalocyanine, naphthalocyanine bearing pyridine groups and investigation of their DNA interaction, topoisomerase inhibition, cytotoxic effects and cell cycle arrest properties," *Dyes and Pigments*, vol. 164, pp. 372–383, May 2019.
- [29] B. X. Hoang, B. O. Han, W. H. Fang, H. D. Tran, C. Hoang, D. G. Shaw, T. Q. Nguyen, "The Rationality of Implementation of Dimethyl Sulfoxide as Differentiation-inducing Agent in Cancer Therapy," *Cancer Diagnosis & Prognosis*, vol. 3, no. 1, pp. 1–8, Dec. 2022.
- [30] C. C. Lever, A. B. P., Leznoff, *Phthalocyanines: Properties and Applications*, First Edit. New York: VCH Publications, New York., 1996.
- [31] A. Ogunsipe, D. Maree, T. Nyokong, "Solvent effects on the photochemical and fluorescence properties of zinc phthalocyanine derivatives," *Journal of Molecular Structure*, vol. 650, no. 1–3, pp. 131–140, 2003.
- [32] C. C. Karanlık, G. Y. Atmaca, A. Erdoğan, "Improved singlet oxygen yields of new palladium phthalocyanines using sonochemistry and comparisons with photochemistry," *Polyhedron*, vol. 206, p. 115351, 2021.
- [33] A. Ogunsipe, T. Nyokong, "Effects of substituents and solvents on the photochemical properties of zinc phthalocyanine complexes and their protonated derivatives," *Journal of Molecular Structure*, vol. 689, no. 1–2, pp. 89–97, 2004.
- [34] C. C. Karanlık, G. Y. Atmaca, A. Erdoğan, "Improved singlet oxygen yields of few palladium phthalocyanines using sonochemistry and comparisons with photochemistry," *Polyhedron*, vol. 206, p. 115351, 2021.

Analysis of Electrochemical Deposition of Polyaniline and Polyaniline Composites in Sodium Tungstate and Sodium Molybdate Solutions

Asuman Ünal 

Cankiri Karatekin University, Faculty of Science, Department of Chemistry, Çankırı, Türkiye, asumanunal@karatekin.edu.tr

ARTICLE INFO

ABSTRACT

Keywords:

Polyaniline
 $\text{Na}_2\text{WO}_4 \cdot 2\text{H}_2\text{O}$
 $\text{Na}_2\text{MoO}_4 \cdot 2\text{H}_2\text{O}$
Electrochemical deposition
Polymer composites

Article History:

Received: 11.06.2024
Accepted: 17.09.2024
Online Available: 18.10.2024

Although polyaniline has a high electroactivity in environments below pH 5, it loses its electroactivity in neutral and basic environments. In addition, polyaniline film does not give physically stable film when it becomes thick. For these reasons, polyaniline has been synthesized in the presence of other monomers or inorganic/organic species, leading to the obtaining of composite polymers with some new electrochemical and physical properties. In this study, novel composite polymer films of polyaniline were synthesized electrochemically in the presence of different concentrations of $\text{Na}_2\text{MoO}_4 \cdot 2\text{H}_2\text{O}$ and $\text{Na}_2\text{WO}_4 \cdot 2\text{H}_2\text{O}$, and these composite polymer films were examined in monomer-free solutions for electrochemical investigation. As a result, the cathodic charge of polyaniline increased from 0.25 mC to 1.50 mC in the presence of 0.05 M $\text{Na}_2\text{MoO}_4 \cdot 2\text{H}_2\text{O}$. Also, the polyaniline/ WO_3 composite achieved a charge transfer of 0.42 mC in the presence of 0.25 M $\text{NiSO}_4 \cdot 2\text{H}_2\text{O}$, 0.05 M $\text{NiCl}_2 \cdot 6\text{H}_2\text{O}$, Na_2WO_4 , $\text{Na}_2\text{MoO}_4 \cdot 2\text{H}_2\text{O}$, 0.4 M $\text{Na}_3\text{C}_6\text{H}_5\text{O}_7 \cdot 2\text{H}_2\text{O}$ and 0.05 $\text{Na}_2\text{WO}_4 \cdot 2\text{H}_2\text{O}$ as a metal source. These prove the better charge transfer during the redox reaction of the polyaniline composite film.

1. Introduction

Studies on the synthesis, characterization and applications of conductive polymers are still being studied extensively due to their high conductivity and cost-effectiveness [1-3]. Moreover, this interest in conductive polymers has increased with the discovery of polymer composites (or polymer hybrids) because these compounds provide new application areas for polymers by revealing new and improved chemical and physical properties. A wide range of studies have been conducted with composite films in energy storage device, biosensors, and corrosion protection [4-7]. These studies also prove that composites are generally better than their components in terms of electrochemical and physical aspects [3].

Polyaniline is the most preferred conductive polymer due to its high electroactivity, its

remarkable stability and processibility in exposure to air and moisture, for both conducting and as well, as insulating forms [8-11]. It also provides a good network for the distribution of other species (monomer, organic, or inorganic). In other words, its easy integration with other species makes polyaniline advantageous for the synthesis of polymer composites [12-16].

Polyaniline can be prepared by chemical or electrochemical techniques [8-9, 17] but cannot be prepared or even used without acid. The pH of the medium must be above 5, otherwise polyaniline will not be synthesized and cannot exhibit electroactive behavior [3, 18]. This is an important limitation of polyaniline. It is possible to eliminate this problem with polyaniline composite syntheses. According to some studies, polyaniline composites show new electrochemical properties and can also show electroactivity at high pH values [19-22]. Hao *et*

al. reported that polyaniline/boron-doped graphene exhibits a dramatic increase in electrochemical specific capacitance in an alkaline medium [13]. Another study reports that a polyaniline-based nickel molybdate composite could be used as a cation exchanger by the sol-gel method [23].

According to the literature, tungstate and molybdate can be promising alternatives for energy storage devices [24-26]. A few studies have explored their polymer composites but often do not provide detailed explanations of their effects on polymer matrices [27-30]. This study aims to understand these effects and describe the resulting film properties.

In this work, the electrochemical deposition of polyaniline was studied in the different ratios of $\text{Na}_2\text{MoO}_4 \cdot 2\text{H}_2\text{O}$ and $\text{Na}_2\text{WO}_4 \cdot 2\text{H}_2\text{O}$ under optimal conditions with or without the presence of nickel sulfate, nickel chloride and sodium citrate (as complexing agent). The resultant polymer composites were examined in terms of electrochemical properties by cyclic voltammetry.

2. Experimental Work

2.1. Chemicals and reagents

Aniline and HCl were purchased from Sigma Aldrich. Reagents for the synthesis of polyaniline composites including $\text{Na}_2\text{MoO}_4 \cdot 2\text{H}_2\text{O}$ and $\text{Na}_2\text{WO}_4 \cdot 2\text{H}_2\text{O}$ were purchased from Carla Erba while nickel sulfate $\text{NiSO}_4 \cdot 6\text{H}_2\text{O}$, nickel chloride $\text{NiCl}_2 \cdot 6\text{H}_2\text{O}$ and sodium citrate ($\text{Na}_3\text{C}_6\text{H}_5\text{O}_7$) were purchased from Sigma Aldrich.

2.2. Instrumentation

Gamry Instruments Interface – 1000E was used to conduct cyclic voltammetry experiments. Electrochemical experiments of electrode materials were carried out using a three-electrode system, in which a glassy carbon electrode was the working electrode (0.018 cm^2), platinum flag as counter electrode (0.25 cm^2) and Ag/AgCl electrode was preferred as reference electrode.

2.3. Synthesis of polymer composites

Polyaniline and polyaniline composite polymers were deposited on the working electrode (glassy carbon electrode) by electrochemical method. Electrochemical deposition of polyaniline was performed from a solution containing 0.1 M aniline monomer and 0.1 M HCl solutions at 10 mVs^{-1} for several cycles. Electrochemical deposition of polyaniline composite polymer films was obtained from 0.1 M aniline and 0.1 M HCl and different ratios of $\text{Na}_2\text{MoO}_4 \cdot 2\text{H}_2\text{O}$ (or $\text{Na}_2\text{WO}_4 \cdot 2\text{H}_2\text{O}$) at 10 mVs^{-1} . The obtained polyaniline polymer film and polyaniline composite films were examined by cyclic voltammetry in 1 M monomer-free HCl solutions at 50 mVs^{-1} for several cycles. At this stage, the reason for choosing a solution containing 1 M HCl that polyaniline-based films show high electroactivity when acidity increases. In this way, the electroactivity of the resulting film can be tested easily.

On the other hand, the reason for using 0.1 M HCl during the electrochemical deposition of the polyaniline is the tendency of inorganic species to precipitate in the presence of 1 M HCl. Using 0.1 M HCl prevented this the film during deposition. If the test solution is in 1 M HCl, polyaniline composite films in which inorganic species have already been incorporated can be easily tested. Similarly, polyaniline composites were obtained from $\text{Na}_2\text{MoO}_4 \cdot 2\text{H}_2\text{O}$ and $\text{Na}_2\text{WO}_4 \cdot 2\text{H}_2\text{O}$ in the presence of nickel sulfate, nickel chloride and sodium citrate to make nickel/Mo and nickel/W alloy in polymer matrices. For this, the solution containing 0.25 M $\text{NiSO}_4 \cdot 2\text{H}_2\text{O}$, 0.05 M $\text{NiCl}_2 \cdot 6\text{H}_2\text{O}$, Na_2WO_4 , $\text{Na}_2\text{MoO}_4 \cdot 2\text{H}_2\text{O}$ as metal sources (with 0.05 M W and/or 0.05 M Mo) and 0.4 M $\text{Na}_3\text{C}_6\text{H}_5\text{O}_7 \cdot 2\text{H}_2\text{O}$ as complexing agent was prepared.

3. Results and Discussions

3.1. Electrochemical deposition of polyaniline and its electrochemical properties

Initially, monomer solutions of aniline were prepared in the presence of $\text{Na}_2\text{MoO}_4 \cdot 2\text{H}_2\text{O}$ and $\text{Na}_2\text{WO}_4 \cdot 2\text{H}_2\text{O}$, but since $\text{Na}_2\text{WO}_4 \cdot 2\text{H}_2\text{O}$ was insoluble in hydrochloric acid according to

Equation 1 and it gives a tungstic acid, which is amorphous yellow powder. Therefore, the synthesis and electrochemical properties of polyaniline/ MoO_4 were only discussed in the first part of the study. The other part of the study is related to the synthesis of both $\text{Na}_2\text{MoO}_4 \cdot 2\text{H}_2\text{O}$ and $\text{Na}_2\text{WO}_4 \cdot 2\text{H}_2\text{O}$ polymer composite films in a solution consisting of nickel sulfate, nickel chloride and sodium citrate.

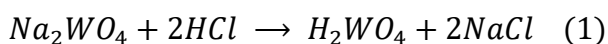


Figure 1 shows the electrochemical deposition of polyaniline from a solution containing 0.1 M aniline and 0.1 M HCl at 10 mVs^{-1} . The current of the anodic and cathodic peaks increases with continuing cycling, and three redox peaks were observed throughout the redox reaction, with an irreversible peak at 0.80 V. While the anodic peaks occur at 0.25 V, 0.50 V and 0.75 V, the cathodic peaks occur around 0.1 V, 0.45 V and 0.70 V, and these are consistent with the literature [31-33]. The first redox pair of polyaniline can corresponds to the transformations between leucoemeraldine state and emeraldine states of polyaniline and the second pair of redox peaks is attributed to the transformation between emeraldine state and pernigraniline states [31]. When it was cycled in monomer-free 1 M HCl solution, as shown in Figure 1b, the next peaks at 0.25 V and 0.63 V are more prominent, unlike the growth voltammogram. The anodic charge and cathodic charge passing during the redox reaction are determined as 0.25 mC and 0.25 mC.

As seen in Figure 1, electrochemical deposition of polyaniline is carried out in 0.1 M HCl, and it is reported in the literature that more concentrated acids contribute to the formation of electroactive polyaniline. On the other hand, electrochemical deposition of polyaniline can be implemented at lower acid concentrations, which facilitates the integration of other species into polymer matrices. Therefore, the synthesis of polyaniline composite polymer films was carried out in 0.1 M HCl under identical conditions.

Figure 2a and Figure 3a reveal the electrochemical precipitation of polyaniline into the composite polymer film from a solution containing 0.1 M aniline, 0.1 M HCl, and 0.05 M

$0.1 \text{ M Na}_2\text{MoO}_4 \cdot 2\text{H}_2\text{O}$ at 10 mVs^{-1} for 20 cycles. As seen in Figure 2a and Figure 3a, the excessive increase in the amount of $\text{Na}_2\text{MoO}_4 \cdot 2\text{H}_2\text{O}$ resulted in the formation of a graph that gave only two specific redox pairs. In other words, the other redox pairs seen in Figure 2a have disappeared. However, when the current of the redox peaks in Figure 2a and Figure 3a is compared, it is seen that the current of the peaks in Figure 3a also becomes lower. This can be explained as the addition of $\text{Na}_2\text{MoO}_4 \cdot 2\text{H}_2\text{O}$ in high amounts blocks some electroactive sites in the polymer matrices.

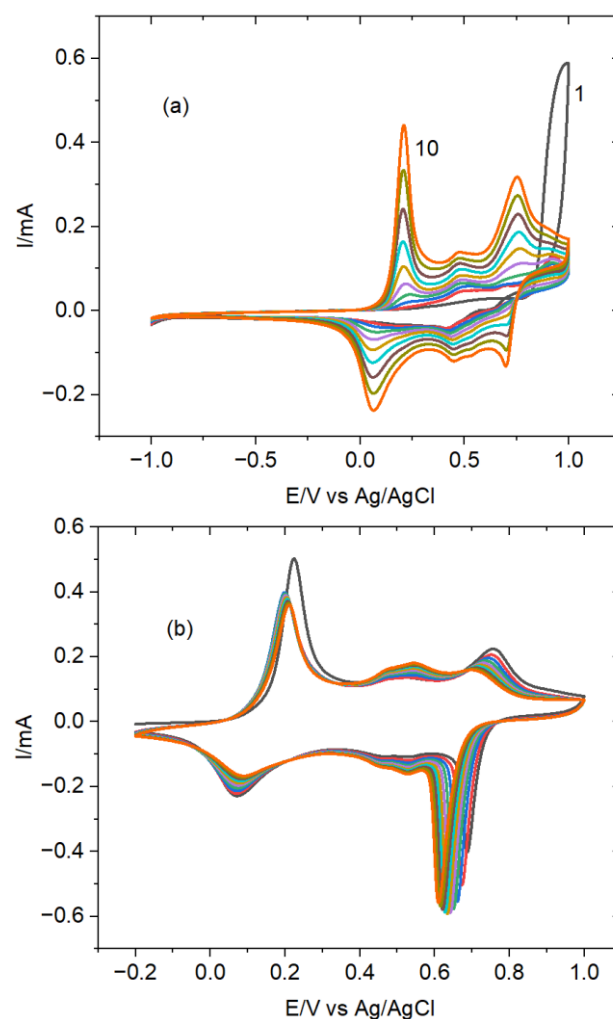


Figure 1. (a) Electrochemical deposition of polyaniline from 0.1 M aniline and 0.1 M HCl at 10 mVs^{-1} over 10 cycles (b) Cycling of polyaniline film in 1 M HCl monomer free solution

Additionally, a closer look at Figure 2a shows that the current is 0.25 mA for the 10th scan, which is higher than the current of the 10th peak of polyaniline obtained from 0.1 M HCl. This also proves that a low amount of $\text{Na}_2\text{MoO}_4 \cdot 2\text{H}_2\text{O}$

contributes the stability and electroactivity while giving reversible redox reactions.

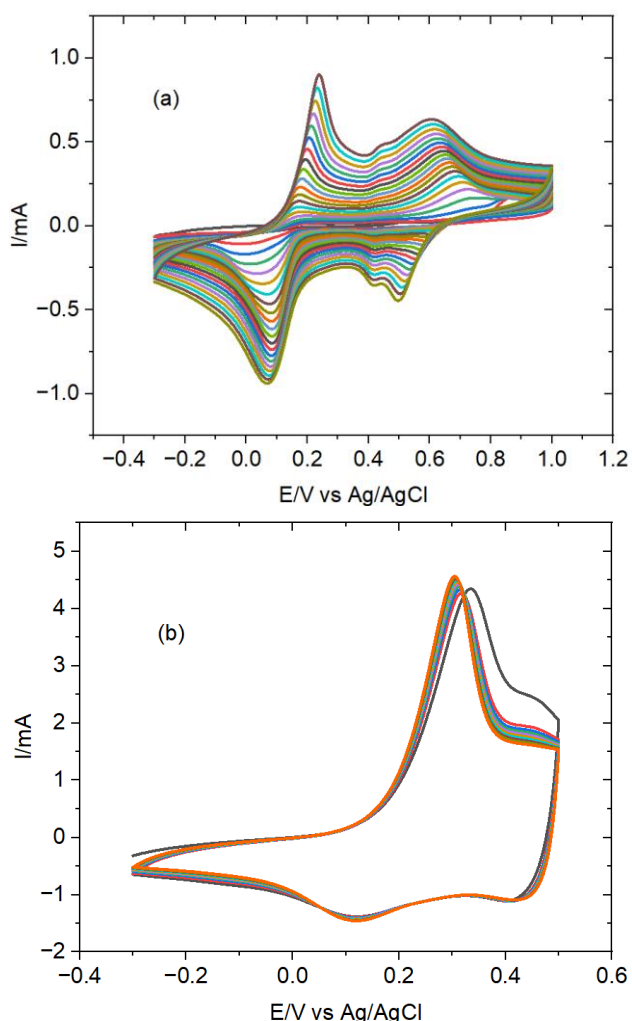


Figure 2. (a) Electrochemical deposition of polyaniline from 0.1 M aniline and 0.1 M HCl in the presence of 0.05 M $\text{Na}_2\text{MoO}_4 \cdot 2\text{H}_2\text{O}$ at 10 mVs^{-1} over 20 cycles (b) Cycling of polyaniline/ $\text{Na}_2\text{MoO}_4 \cdot 2\text{H}_2\text{O}$ in 1 M HCl at 50 mVs^{-1}

The electroactivity of these polyaniline composite polymer films was examined at 50 mVs^{-1} in monomer-free 1 M HCl solutions and their cyclic voltammograms are given in Figure 2b and Figure 3b.

As seen in the Figures 2b and 3b, polyaniline/ MoO_4 (0.05 M) shows high electroactivity with stable cycling. On the other hand, polyaniline/ MoO_4 (0.1 M) started to give peaks at lower currents (0.15 mA) as the cycle continued to increase, indicating the unstable behavior of the film. The anodic load in Figure 2b and Figure 3b was determined as **1.57 mC** and **1.50 mC**, and the cathodic load was determined as **0.18 mC** and **0.20 mC**. As a result, it can be

said that the optimum amount of $\text{Na}_2\text{MoO}_4 \cdot 2\text{H}_2\text{O}$ in the polymer matrices increases the electroactivity, while its excess amount blocks the electroactive regions of the polyaniline film.

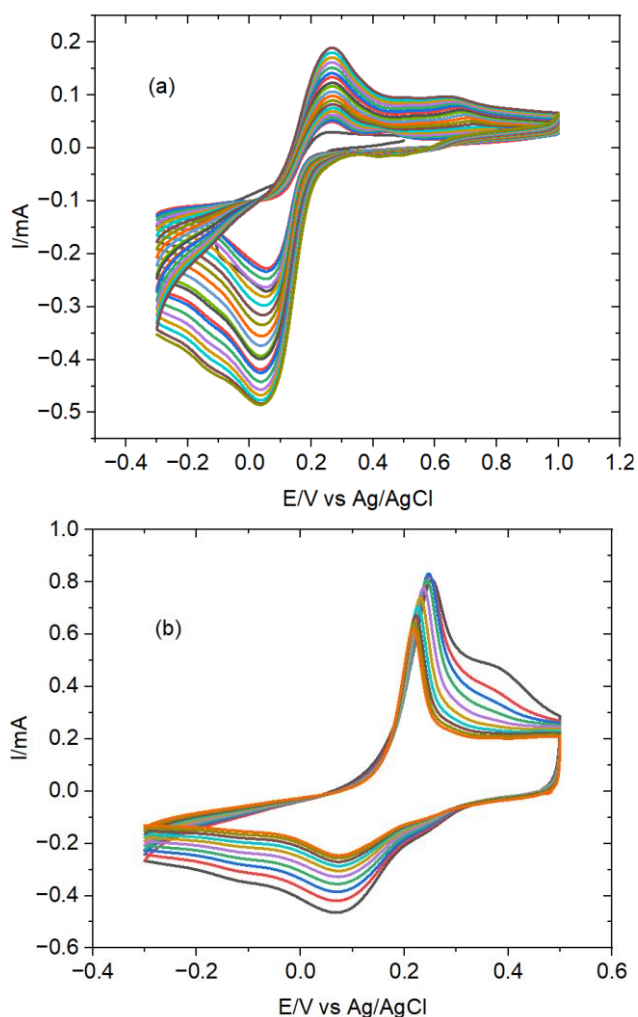


Figure 3. (a) Electrochemical deposition of polyaniline from 0.1 M aniline and 0.1 M HCl in the presence of 0.1 M $\text{Na}_2\text{MoO}_4 \cdot 2\text{H}_2\text{O}$ at 10 mVs^{-1} over 20 cycles (b) Cycling of polyaniline/ $\text{Na}_2\text{MoO}_4 \cdot 2\text{H}_2\text{O}$ in 1 M HCl at 50 mVs^{-1}

Electrochemical deposition of $\text{Na}_2\text{MoO}_4 \cdot 2\text{H}_2\text{O}$ and $\text{Na}_2\text{WO}_4 \cdot 2\text{H}_2\text{O}$ was also carried out from 0.1 M aniline and 0.1 M HCl in the existence of 0.25 M $\text{NiSO}_4 \cdot 2\text{H}_2\text{O}$, 0.05 M $\text{NiCl}_2 \cdot 6\text{H}_2\text{O}$, Na_2WO_4 , $\text{Na}_2\text{MoO}_4 \cdot 2\text{H}_2\text{O}$ as metal sources (with 0.05 M W and/or Mo) and 0.4 M $\text{Na}_3\text{C}_6\text{H}_5\text{O}_7 \cdot 2\text{H}_2\text{O}$ as previously mentioned. Figure 4 shows this electrochemical deposition of polyaniline without $\text{Na}_2\text{MoO}_4 \cdot 2\text{H}_2\text{O}$ and $\text{Na}_2\text{WO}_4 \cdot 2\text{H}_2\text{O}$ [34]. Sodium citrate forms stable complexes for electroplating metal or alloys such as NiMoW [34].

The cyclic voltammogram of this polyaniline is quite different from the pure polyaniline film, which has given three anodic peaks and three cathodic peaks (see Figure 1). Here, a broad anodic peak and two cathodic peaks were observed. Additionally, the current of an anodic peak is 0.07 mA, which is quite low compared to the peak current values of pure polyaniline. This solution appears to result in the synthesis of low electroactive polyaniline. On the other hand, when the resulting film is cycled in a monomer-free 1 HCl solution, it gives a voltammogram similar to the pure polyaniline voltammogram (Figure 1b) with low electroactivity. The anodic and cathodic loads determined from cyclic voltammograms are 0.18 mC and 0.17 mC.

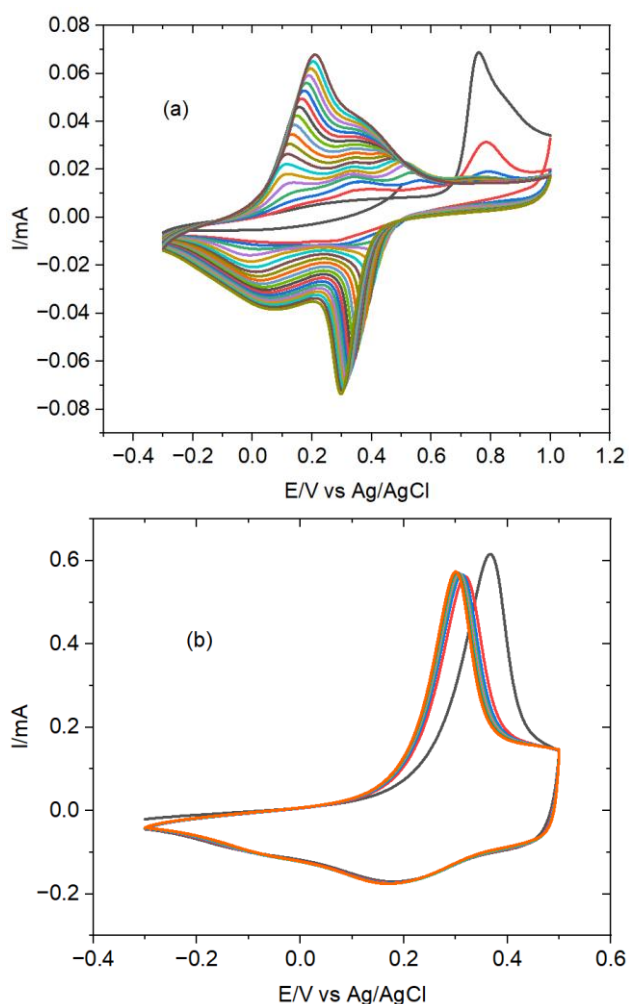


Figure 4. (a) Electrochemical deposition of polyaniline from 0.1 M aniline and 0.1 M HCl in the presence of 0.25 M $\text{NiSO}_4 \cdot 6\text{H}_2\text{O}$, 0.05 M $\text{NiCl}_2 \cdot 6\text{H}_2\text{O}$ and 0.4 M $\text{Na}_3\text{C}_6\text{H}_5\text{O}_7$ at 10 mVs^{-1} (b) Cycling of polyaniline composite polymer film in 1 M HCl monomer free solution

Figure 5 presents the electrochemical co-deposition of polyaniline in the presence of $\text{Na}_2\text{MoO}_4 \cdot 2\text{H}_2\text{O}$ and $\text{Na}_2\text{WO}_4 \cdot 2\text{H}_2\text{O}$ in addition to $\text{NiSO}_4 \cdot 6\text{H}_2\text{O}$, $\text{NiCl}_2 \cdot 6\text{H}_2\text{O}$ and $\text{Na}_3\text{C}_6\text{H}_5\text{O}_7$. The participation of $\text{Na}_2\text{MoO}_4 \cdot 2\text{H}_2\text{O}$ and $\text{Na}_2\text{WO}_4 \cdot 2\text{H}_2\text{O}$ did not affect the electroactive properties of polyaniline much, and the anodic and cathodic charge transfer was found to be lower, at 0.15 mC and 0.14 mC. Afterward, $\text{Na}_2\text{MoO}_4 \cdot 2\text{H}_2\text{O}$ and $\text{Na}_2\text{WO}_4 \cdot 2\text{H}_2\text{O}$ were added into the solution separately and the polymer composites were obtained under identical conditions.

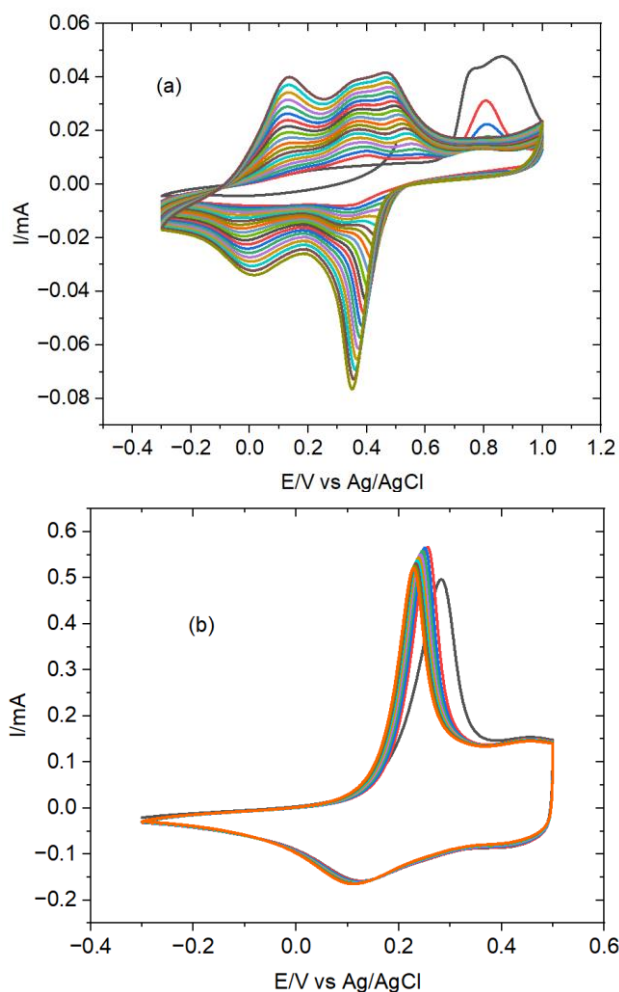


Figure 5. (a) Electrochemical deposition of polyaniline from 0.1 M aniline and 0.1 M HCl in the presence of 0.25 M $\text{NiSO}_4 \cdot 6\text{H}_2\text{O}$, 0.05 M $\text{NiCl}_2 \cdot 6\text{H}_2\text{O}$ and 0.4 M $\text{Na}_3\text{C}_6\text{H}_5\text{O}_7$ with 0.05 M $\text{Na}_2\text{MoO}_4 \cdot 2\text{H}_2\text{O}$ and 0.05 M $\text{Na}_2\text{WO}_4 \cdot 2\text{H}_2\text{O}$ at 10 mVs^{-1} (b) Cycling of polyaniline composite polymer film in 1 M HCl monomer free solution

Figure 6 shows the electrochemical deposition of polyaniline/ WO_4 in the presence of $\text{NiSO}_4 \cdot 6\text{H}_2\text{O}$, $\text{NiCl}_2 \cdot 6\text{H}_2\text{O}$ and $\text{Na}_3\text{C}_6\text{H}_5\text{O}_7$. The first thing worth noting is that the peak current is increased

by the addition of $\text{Na}_2\text{WO}_4 \cdot 2\text{H}_2\text{O}$ without changing the voltammogram of pure polyaniline. On the other hand, the incorporation of $\text{Na}_2\text{WO}_4 \cdot 2\text{H}_2\text{O}$ electroactive properties of the resulting film because its current is still between 0.04 mA and 0.06 mA. This suggests that $\text{Na}_2\text{WO}_4 \cdot 2\text{H}_2\text{O}$ contributes to the increase of electroactive sites in polymer matrices.

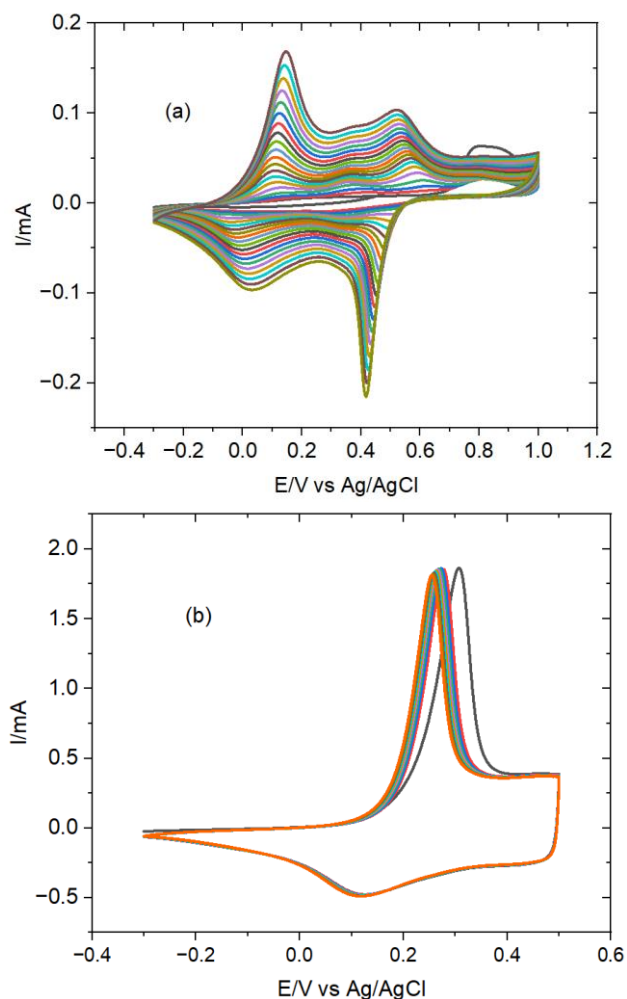


Figure 6. (a) Electrochemical deposition of polyaniline from 0.1 M aniline and 0.1 M HCl in the presence of 0.25 M $\text{NiSO}_4 \cdot 6\text{H}_2\text{O}$, 0.05 M $\text{NiCl}_2 \cdot 6\text{H}_2\text{O}$ and 0.4 M $\text{Na}_3\text{C}_6\text{H}_5\text{O}_7$ with 0.05 M $\text{Na}_2\text{WO}_4 \cdot 2\text{H}_2\text{O}$ at 10 mVs^{-1} (b) Cycling of polyaniline composite polymer film in 1 M HCl monomer free solution

Figure 7 displays the electrochemical deposition of polyaniline/ MoO_4 in the presence of $\text{NiSO}_4 \cdot 6\text{H}_2\text{O}$, $\text{NiCl}_2 \cdot 6\text{H}_2\text{O}$ and $\text{Na}_3\text{C}_6\text{H}_5\text{O}_7$. The addition of $\text{Na}_2\text{MoO}_4 \cdot 2\text{H}_2\text{O}$ affects the size of the anodic peaks without significantly impacting the cathodic peaks. The current values are lower compared to the growth of polyaniline/ WO_4 , as seen in Figure 6. The characterization of the resulting film also supports that polyaniline/ WO_4

is more electroactive than the polyaniline/ MoO_4 composite film. The anodic peak and cathodic peak charge for polyaniline/ WO_4 were found to be 0.43 mC and 0.42 mC, while polyaniline/ MoO_4 was 0.20 mC and 0.18 mC.

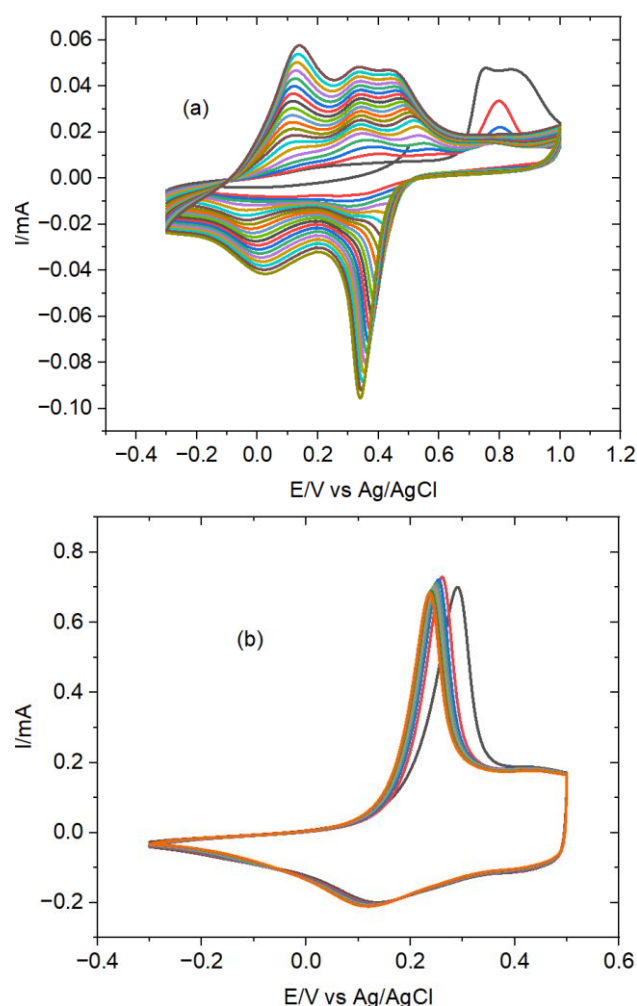


Figure 7. (a) Electrochemical deposition of polyaniline from 0.1 M aniline and 0.1 M HCl in the presence of 0.25 M $\text{NiSO}_4 \cdot 6\text{H}_2\text{O}$, 0.05 M $\text{NiCl}_2 \cdot 6\text{H}_2\text{O}$ and 0.4 M $\text{Na}_3\text{C}_6\text{H}_5\text{O}_7$ with 0.05 M $\text{Na}_2\text{MoO}_4 \cdot 2\text{H}_2\text{O}$ at 10 mVs^{-1} (b) Cycling of polyaniline composite polymer film in 1 M HCl monomer free solution

4. Conclusion

In the current study, the electrochemical deposition of polyaniline with $\text{Na}_2\text{MoO}_4 \cdot 2\text{H}_2\text{O}$ and $\text{Na}_2\text{WO}_4 \cdot 2\text{H}_2\text{O}$ in the presence or absence of $\text{NiSO}_4 \cdot 6\text{H}_2\text{O}$, $\text{NiCl}_2 \cdot 6\text{H}_2\text{O}$ and $\text{Na}_3\text{C}_6\text{H}_5\text{O}_7$ was investigated. The fact that the cathodic charge of polyaniline/ MoO_4 composites increased from 0.25 mC to 1.50 mC shows that $\text{Na}_2\text{MoO}_4 \cdot 2\text{H}_2\text{O}$ improves the properties of pure polyaniline. Polyaniline/ MoO_4 composite also shows a

charge value of 0.18 mC when synthesized in the presence of 0.1 aniline monomers, 0.1 M HCl and NiSO₄·6H₂O, NiCl₂·6H₂O and Na₃C₆H₅O₇. This shows that MoO₄ does not have a significant effect on this solution. On the other hand, polyaniline/WO₄ composites show that 0.42 mC cathodic load passes after reduction. This proves that WO₄²⁻ doping into polyaniline matrices increases the electroactive sites of polyaniline, enabling fast, reversible redox reactions. Well distribution of WO₄²⁻ in polymer matrices can be used to increase the synergic effect between two components with other techniques such as spin coating and can be examined for energy storage devices in further studies.

According to the literature, the chemical synthesis of polyaniline with zinc tungstate and copper tungstate demonstrates that a PANI/CuWO₄ modified electrode can selectively detect quercetin [29], while PANI/ZnWO₄ enhances conductivity [28]. Additionally, the electrosynthesis of PANI/MoO₄ in oxalic acid on steel reveals the corrosion protection properties of polyaniline [27]. In light of these, the reversible behavior of PANI/WO₄ and PANI/WO₄ suggests its potential use in chemical and biosensors.

Article Information Form

Acknowledgments

The author are thankful to Prof. Dr. Abdullah Yıldız and Yıldız Research Group for useful discussions and providing support.

Funding

The author (s) has no received any financial support for the research, authorship or publication of this study.

The Declaration of Conflict of Interest/ Common Interest

No conflict of interest or common interest has been declared by the authors.

The Declaration of Ethics Committee Approval

This study does not require ethics committee permission or any special permission.

The Declaration of Research and Publication Ethics

The authors of the paper declare that they comply with the scientific, ethical and quotation rules of SAUJS in all processes of the paper and that they do not make any falsification on the data collected. In addition, they declare that Sakarya University Journal of Science and its editorial board have no responsibility for any ethical violations that may be encountered, and that this study has not been evaluated in any academic publication environment other than Sakarya University Journal of Science.

Copyright Statement

Authors own the copyright of their work published in the journal and their work is published under the CC BY-NC 4.0 license.

References

- [1] G. Inzelt, "Conducting polymers: past, present, future," *Journal of Electrochemical Science and Engineering*, vol. 8, no. 1, 2018.
- [2] S. A. Campbell, Y. Li, S. Breakspear, F. C. Walsh, J. R. Smith, "Conducting polymer coatings in electrochemical technology Part 1 – Synthesis and fundamental aspects," *Transactions of the IMF*, vol. 85, no. 5, pp. 237-244, 2007.
- [3] M. H. Naveen, N. G. Gurudatt, Y. B. Shim, "Applications of conducting polymer composites to electrochemical sensors: A review," *Applied Materials Today*, vol. 9, pp. 419-433, 2017.
- [4] P. C. de León, S. A. Campbell, J. R. Smith, F. C. Walsh, "Conducting polymer coatings in electrochemical technology Part 2 – Application areas," *Transactions of the IMF*, vol. 86, no. 1, pp. 34-40, 2008.
- [5] M. Gerard, A. Chaubey, B. D. Malhotra, "Application of conducting polymers to biosensors," *Biosensors and Bioelectronics*, vol. 17, no. 5, pp. 345-359, 2002.

- [6] T. K. Das, S. Prusty, "Review on Conducting Polymers and Their Applications," *Polymer - Plastics Technology and Engineering*, vol. 51, no. 14, pp. 1487-1500, 2012.
- [7] R. Tucceri, "Practical Applications of Poly(o-aminophenol) film electrodes," *The Open Physical Chemistry Journal*, vol. 4, pp. 45-61, 2010.
- [8] A. A. Syed, M. K. Dinesan, "Review: Polyaniline-A novel polymeric material," *Talanta*, vol. 38, no. 8, pp. 815-837, 1991.
- [9] Y. Wei, W. W. Focke, G. E. Wnek, A. Ray, A. G. MacDiarmid, "Synthesis and electrochemistry of alkyl ring-substituted polyanilines," *The Journal of Physical Chemistry*, vol. 93, no. 1, pp. 495-499, 1989.
- [10] D. D. Borole, U. R. Kapadi, P. P. Mahulikar, D. G. Hundiwale, "Electrochemical behaviour of polyaniline, poly(o-toluidine) and their copolymer in organic sulphonic acids," *Materials Letters*, vol. 58, no. 29, pp. 3816-3822, 2004.
- [11] G. Dwivedi, G. Munjal, A. N. Bhaskarwar, A. Chaudhary, "Dye-sensitized solar cells with polyaniline: A review," *Inorganic Chemistry Communications*, vol. 135, pp. 109087, 2022.
- [12] B. Wessling, "New insight into organic metal polyaniline morphology and structure," *Polymers*, vol. 2, no. 4, pp. 786-798, 2010.
- [13] Q. Hao, X. Xia, W. Lei, W. Wang, J. Qiu, "Facile synthesis of sandwich-like polyaniline/boron-doped graphene nano hybrid for supercapacitors," *Carbon*, vol. 81, no. 1, pp. 552-563, 2015.
- [14] P. Gajendran, R. Saraswathi, "Polyaniline-carbon nanotube composites," *Pure and Applied Chemistry*, vol. 80, no. 11, pp. 2377-2395, 2008.
- [15] W. Feng, X. D. Bai, Y. Q. Lian, J. Liang, X. G. Wang, K. Yoshino, "Well-aligned polyaniline/carbon-nanotube composite films grown by in-situ aniline polymerization," *Carbon*, vol. 41, no. 8, pp. 1551-1557, 2003.
- [16] J.-E. Park, S.-G. Park, A. Koukitu, O. Hatozaki, N. Oyama, "Electrochemical Behavior of the Polyaniline-Organosulfur Composite Film Containing Ag Nanoparticles," *Journal of The Electrochemical Society*, vol. 150, no. 7, 2003.
- [17] A. F. Diaz, J. A. Logan, "Electroactive polyaniline films," *Journal of Electroanalytical Chemistry and Interfacial Electrochemistry*, vol. 111, no. 1, pp. 111-114, 1980.
- [18] Q. Yang, Y. Zhang, H. Li, Y. Zhang, M. Liu, J. Luo, L. Tan, H. Tang, S. Yao, "Electrochemical copolymerization study of o-toluidine and o-aminophenol by the simultaneous EQCM and in situ FTIR spectroelectrochemistry," *Talanta*, vol. 81, no. 1-2, pp. 664-672, 2010.
- [19] A. Unal, A. Robert Hillman, K. S. Ryder, S. Cihangir, "Electrogravimetric analysis of poly(aniline-co-o-toluidine) copolymer films in the presence of fluoride ions," *Journal of Electroanalytical Chemistry*, vol. 895, pp. 115519, 2021.
- [20] A. Unal, A. R. Hillman, K. S. Ryder, S. Cihangir, "Highly Efficient Defluoridation of Water through Reusable poly(aniline-co-o-aminophenol) Copolymer Modified Electrode Using Electrochemical Quartz Crystal Microbalance," *Journal of The Electrochemical Society*, vol. 168, no. 2, pp. 022502, 2021.
- [21] R. Gangopadhyay, A. De, "Conducting polymer nanocomposites: A brief

- overview,” *Chemistry of Materials*, vol. 12, no. 3, pp. 608-622, 2000.
- [22] A. Malinauskas, J. Malinauskiene, A. Ramanavičius, “Conducting polymer-based nanostructured materials: Electrochemical aspects,” *Nanotechnology*, vol. 16, no. 10, pp. 51-62, 2005.
- [23] M. A. Khan, U. Ishrat, A. M. Dar, A. Ahmad, “Structural, electrical, optical and analytical applications of newly synthesized polyaniline based nickel molybdate composite,” *Journal of Alloys and Compounds*, vol. 636, pp. 124-130, 2015.
- [24] S. Emin, C. Altinkaya, A. Semerci, H. Okuyucu, A. Yildiz, P. Stefanov, “Tungsten carbide electrocatalysts prepared from metallic tungsten nanoparticles for efficient hydrogen evolution,” *Applied Catalysis B: Environmental*, vol. 236, pp. 147-153, 2018.
- [25] D. Szymanska, I. A. Rutkowska, L. Adamczyk, S. Zoladek, P. J. Kulesza, “Effective charge propagation and storage in hybrid films of tungsten oxide and poly(3,4-ethylenedioxythiophene),” *Journal of Solid State Electrochemistry*, vol. 14, pp. 2049-2056, 2010.
- [26] T. He, W. Zhang, P. Manasa, F. Ran, “Quantum dots of molybdenum nitride embedded in continuously distributed polyaniline as novel electrode material for supercapacitor,” *Journal of Alloys and Compounds*, vol. 812, pp. 152138, 2020.
- [27] V. Karpakam, K. Kamaraj, S. Sathiyarayanan, G. Venkatachari, and S. Ramu, “Electrosynthesis of polyaniline-molybdate coating on steel and its corrosion protection performance,” *Electrochim Acta*, vol. 56, no. 5, pp. 2165-2173, 2011.
- [28] T. Machappa, S. Badrunnisa, M. V. N. A. Prasad, “Conducting polyaniline doped with zinc tungstate matrix film as gas sensing composite,” *Materials Today: Proceedings*, vol. 49, no. 5, pp. 1899-1904, 2022.
- [29] S. S. K. Ponnaiah, P. Periakaruppan, “A glassy carbon electrode modified with a copper tungstate and polyaniline nanocomposite for voltammetric determination of quercetin,” *Microchimica Acta*, vol. 185, no. 11, pp. 524, 2018.
- [30] M. Sabouri, T. Shahrabi, M. G. Hosseini, “Improving corrosion protection performance of polypyrrole coating by tungstate ion dopants,” *Russian Journal of Electrochemistry*, vol. 43, no. 12, pp. 1390-1397, 2007.
- [31] J. Chu, D. Lu, B. Wu, X. Wang, M. Gong, R. Zhang, S. Xiong, “Synthesis and electrochromic properties of conducting polymers: Polyaniline directly grown on fluorine-doped tin oxide substrate via hydrothermal techniques,” *Solar Energy Materials and Solar Cells*, vol. 177, pp. 70-74, 2018.
- [32] M. A. Mohamoud, A. R. Hillman, “The effect of anion identity on the viscoelastic properties of polyaniline films during electrochemical film deposition and redox cycling,” *Electrochimica Acta*, vol. 53, no. 3, pp. 1206-1216, 2007.
- [33] A. R. Hillman, M. A. Mohamoud, “Ion, solvent and polymer dynamics in polyaniline conducting polymer films,” *Electrochimica Acta*, vol. 51, no. 27, pp. 6018-6024, 2006.
- [34] M. Allam, M. Benaicha, A. Dakhouche, “Electrodeposition and characterization of NiMoW alloy as electrode material for hydrogen evolution in alkaline water electrolysis,” *International Journal of Hydrogen Energy*, vol. 43, no. 6, pp. 3394-3405, 2018.

Comparison of *MCM6* rs4988235 Polymorphism Allele and Genotype Frequencies in Professional Football Players and a Sedentary Control Group

Beste Tacal Aslan¹ , Tolga Polat¹ , Özlem Özge Yılmaz^{1*} , Aleyna Tanrıverdi Muhan² , Rukiye Ziya² , Korkut Ulucan¹ 

¹ Marmara University, Faculty of Dentistry, Department of Medical Biology and Genetics, İstanbul, Türkiye, btacal@gmail.com, tolga.polat@marmara.edu.tr, ozlem.ozge@marmara.edu.tr, korkutulucan@hotmail.com

² Marmara University, Institute of Health Sciences, Department of Basic Medical Sciences, İstanbul, Türkiye, aleynantanriverdimbg@gmail.com, rukiyeziyaa@gmail.com

*Corresponding Author

ARTICLE INFO

ABSTRACT

Keywords:

MCM6

Lactose

SNP

Football

Genetic



Article History:

Received: 13.06.2024

Accepted: 03.10.2024

Online Available: 18.10.2024

This study investigated the minichromosome maintenance 6 (*MCM6*) rs4988235 polymorphism in professional football players, comparing genotype and allele frequencies with a sedentary control group. The control group comprised 64 participants with no history of athletic activity, while the athlete group included 20 football players. DNA extraction from blood samples was performed using a PureLink DNA isolation kit, following the manufacturer's instructions. Real-Time PCR was employed to analyze the *MCM6* rs4988235 polymorphism in the isolated DNA. Statistical analysis of the acquired data was conducted using chi-square analysis via IBM SPSS 21.0 software (IBM Statistical Package for Social Sciences Corp., Armonk, NY, USA). A p-value less than 0.05 was considered statistically significant. The CC genotype was absent in all football players. Conversely, CT (10%) and TT (90%) genotypes were identified in 2 and 18 individuals, respectively. In the control group, the distribution of genotypes was as follows: CC (0%), CT (17, 26.6%), and TT (47, 73.4%). The C allele frequency was 5% (2 individuals) in football players and 13.28% (17 individuals) in the control group. The T allele frequency was 95% (38 individuals) in football players and 86.72% (111 individuals) in the control group. No statistically significant differences were observed between the football players and the control group regarding genotype ($p = 0.122$) or allele frequencies ($p = 0.149$).

1. Introduction

Lactose is a disaccharide, a molecule formed by the combination of glucose and galactose. Lactose occurs naturally in mammalian milk and is the main carbohydrate component of milk. In the small intestine, it is hydrolyzed by the enzyme lactase into glucose and galactose monosaccharides and absorbed into the bloodstream (Ingram, et al, 2009). Lactose intolerance is a pathophysiological condition that occurs when lactose cannot be digested or absorbed due to a lack of β -galactosidase enzyme

in the jejunum. This condition affects the majority of the elderly population [1].

Lactase deficiency stands as a prevalent autosomal recessive ailment characterized by a diminished activity of lactase fluorohydrolase, a pivotal enzyme responsible for lactose hydrolysis within the small intestine. In the absence of adequate enzymatic function, lactose, a disaccharide, remains unabsorbed, traversing undigested into the colon where it becomes subject to bacterial fermentation. Consequently, individuals afflicted by this condition encounter a spectrum of gastrointestinal symptoms

including discomfort and bloating. Commonly denoted as lactose intolerance, this physiological incapacity to effectively metabolize lactose underscores the intricate interplay between genetic predisposition and biochemical mechanisms governing human digestive processes [2].

Within the global demographic structure, approximately 70% of the human population is characterized by a primary deficiency of the enzyme lactase. This prevalence rate varies in correlation with the diversity of ethnological origins and can be interpreted as a result of genetic selection due to the prevalence of dairy-based foods in the diet. Especially in communities where pastoralist cultures predominate and dairy products play a central role in the diet, as in the septentrional regions of Europe, the prevalence of primary lactase deficiency is remarkably low at two percent. According to findings in the anthropological literature, populations with a high prevalence of lactose malabsorption among adults are usually communities with agricultural and hunting traditions, which historically introduced milk consumption at a late stage and/or preferred fermented dairy products with reduced lactose content [3-6].

The Lactase gene (*LCT*, 2q21-22) encodes the lactase enzyme expressed in the intestine [7]. There are many single nucleotide polymorphisms (SNPs) associated with lactose intolerance and they occur at different frequencies in different populations [8]. A group from Finland described two polymorphisms in introns 9 and 13 of the minichromosome maintenance 6 (*MCM6*) gene [9]. One of these, -13910T (rs4988235), was the first allele identified to be associated with lactase digestive capacity [10]. SNPs known as -13910C/T or rs4988235 are located in intron 13. The single nucleotide polymorphism at position -13910 of the *LCT* gene (rs4988235) has been shown to regulate lactase expression. In addition, the T variant has been associated with an increased transcription of the LCT protein [11].

Individuals harboring at least one copy of the -13910T variant allele are deemed genetically endowed with lactase persistence, thereby retaining the ability to efficiently metabolize

lactose into adulthood. This genetic predisposition confers a distinct advantage over counterparts possessing the CC genotype, characterized by markedly diminished lactase activity. Consequently, those with the -13910T variant exhibit a heightened capacity for lactose tolerance, facilitating enhanced digestion and assimilation of lactose-containing foods, in stark contrast to individuals lacking this genetic variant [12, 13].

Athletic performance is considered to be a combination of many factors. Nutrition and diet programs of athletes are one of the main factors affecting athletic performance [14]. Determination of polymorphisms affecting athletic performance among football players can play an active role in changing and regulating the nutritional habits of football players. In our study, we aimed to examine the genotype and allelic distributions of *MCM6* rs4988235 polymorphism in football players and the relationship between the distribution and the positions of the athletes.

2. General Methods

2.1. Study group

20 football players of Turkish origin from Maltepespor football club in the age range of 17-33 years, who were active and regularly training, participated in the study. In the same age range, 64 sedentary individuals were included in the study for genotype and allele analysis. The training program of the football players was reported as a minimum of 4 days (40-120 min) and one match per week. The study protocol was approved by the Üsküdar University Ethics Committee (61351342/ŞUBAT 2024-79) and was prepared in accordance with the guidelines of the Helsinki Declaration-2 (2015).

Consent Form The athletes were invited to participate in the study as part of an independent research conducted by Marmara University Faculty of Dentistry, Department of Medical Biology and Genetics. After the athletes were informed about the study and their questions were answered, the consent forms were mutually signed, first by the athletes. DNA Isolation DNA isolation was completed from peripheral blood

samples using PureLink DNA isolation kit (Invitrogen, Van Allen Way Carlsbad, CA, USA) according to the manufacturer's procedures. The DNA samples obtained were stored at -20°C until the analysis process of the relevant genes was completed.

2.2. Genotyping

Genotyping of the Minichromosome maintenance 6 (*MCM6*) rs4988235 polymorphism was performed using Taqman Genotyping Assays (Applied Biosystems Foster City, CA, USA) using Real-Time PCR device (StepOne Plus, USA) from the isolated DNA material. Genotyping procedures were completed by real-time PCR with Taq-Man probe method using 5 µL master mix, 3.75 µL H₂O, 0.25 µL assay and 1 µL (10 ng) DNA for a total of 10 µL.

2.3. Statistical analysis

Statistical analyses of the obtained data were performed with chi-square analysis using IBM SPSS 21.0 (IBM Statistical Package for Social Sciences Corp., Armonk, NY, USA). $p < 0.05$ was considered statistically significant.

3. Results and Discussion

When the genotypes were analyzed, it was found that 2 players had CT (10%) and 18 players had TT (90%) genotypes, and no player had CC genotype. C allele was found to be 2 (5%) and T allele was found to be 38 (95%) in football players. No individual in the control group was found to have CC genotype, 17 individuals were found to have CT (26.6%) and 47 individuals were found to have TT (73.4%) genotypes. In allelic distribution, C allele was found in 17 (13.28%) and T allele in 111 (86.72%) individuals. Statistically significant differences were not found between the two groups in terms of genotype ($p = 0.122$) and allelic distribution ($p = 0.149$) (Table 1).

Table 1. *MCM6* rs4988235 genotype and allelic distribution comparison

<i>MCM6</i> rs4988235	Genotype Distribution			P	Allelic Distribution		P
	TT	CT	CC		C	T	
Athlete (n=20)	18	2	-	0.122	2	38	0.149
%	%90	%10	-		%5	%95	
Control (n=64)	47	17	-		17	111	
%	%73.4	%26.6	-		%13.28	%86.72	

Chi-Square Test; $p < 0.05$

The table shows *MCM6* rs4988235 genotype distribution and allele frequency. This gene is associated with lactose intolerance. It can be interpreted that those with TT genotype are lactose tolerant, those with CT genotype are partially tolerant and those with CC genotype are prone to intolerance.

According to the table, 18 of the 20 people in the football player group had TT genotype and 2 had CT genotype. In other words, lactose tolerance is very high in this group. In the control group, 47 of 64 people had TT and 17 had CT genotype. In other words, lactose tolerance is also high in this group, but lower than in the football player group.

The difference between genotype distribution and allele frequency is not statistically significant. P values are greater than 0.05. This means that there is no significant difference in *MCM6* rs4988235 genotype and allele frequency between football players and control groups.

Table 2 includes the physical characteristics and genotypes of football players in different positions, such as age, height, weight and Body Mass Index (BMI).

According to these data, it can be said that the team is generally young and has a physically fit structure. BMI values are generally in a healthy range. In terms of genotype, it appears that only two players have the 'TC' genotype and the others have the 'TT' genotype.

In addition to environmental factors such as nutrition, genetic predispositions play an important role in the development of athletes [15]. Since an individual's dietary and supplementation strategies can significantly affect their physical performance, personalized nutrition aims to optimize health, body composition and exercise performance by targeting dietary recommendations in sport populations according to the individual's genetic profile [16]. In lactose-sensitive individuals, lactose digestion can cause many abnormal symptoms. In this case, a hydrogen test or invasive biopsy sample is taken to make a diagnosis. Genetic testing can provide highly

sensitive lactose intolerance results noninvasively [17].

Raz et al. [18] conducted a study in the Israeli population with 439 participants. The results showed a significant association between *LCT* rs4988235 (-13910C/T) ethnicity and genotype. The prevalence of the CC (*LCT* rs4988235) genotype associated with adult hypolactasia was 97%, 93%, 83% and 82% among Bedouin Arabs and Iraqi, Ashkenazi and Moroccan Jews, respectively. A significant correlation was found in determining the genotype prevalence in Jews and it was recommended to adjust dietary recommendations accordingly.

Table 2. Position, age, height, weight, body mass index (BMI) and genotype distribution of football players

Footballers	Location	Age	Length (cm)	Weight (kg)	BMI (kg/m) ²	Genotype
1	Goalkeeper	19	193	81	21,7	TT
2	Right Back	22	178	73	23	TT
3	Right Back	32	164	60	22,3	TT
4	Left Back	32	171	73	25	TT
5	Left Back	20	174	69	22,8	TT
6	Center Back	21	186	79	22,8	TT
7	Center Back	21	186	82	23,7	TT
8	DM	21	182	77	23,2	TT
9	DM	21	185	78	22,8	TT
10	DM	22	185	73	21,3	TT
11	CM	25	171	70	23,9	TT
12	CM	20	175	72	23,5	TT
13	CM	21	176	65	21	TT
14	CM	21	180	74	22,8	TT
15	Right Wing	27	180	73	22,5	TT
16	Right Wing	20	174	72	23,8	TT
17	Left Wing	20	180	73	22,5	CT
18	Left Wing	21	179	74	23,1	CT
19	Center Forward	21	186	82	23,7	TT
20	Center Forward	17	187	80	22,9	TT
		Age $\bar{x} \pm SD$	Length $\bar{x} \pm SD$	Weight $\bar{x} \pm SD$	BMI $\bar{x} \pm SD$	
		22.20 ± 3.91	178.65 ± 6.84	73.60 ± 5.48	23.02 ± 0.87	

BMI=Body Mass Index; CM=Central Midfielder; DM=Defensive Midfielder

In a study of 151 volunteers, Adler et al. [19] found genotypes associated with the LP phenotype in 74 (41.0%) and the frequency of the T allele of the *LCT* gene was 24.8%. Tomasz et al. [20] investigated the frequency of *LCT*-13910C>T polymorphism in 223 volunteers from Poland. The *LCT* rs4988235 T allele (lactase persistence) was found to be present in 51% of individuals sampled from the Polish population. All data from populations show the

relationship between genetic variants of lactose tolerance and lactose intolerance.

In our study, we aimed to determine the minichromosome maintenance 6 (*MCM6*) rs4988235 polymorphism in football players. None of the football players had the CC allele. It was found that 2 were in CT (10%) and 18 were in TT (90%) genotypes. C allele was found to be 2 (5%) and T allele was found to be 38 (95%) in

football players. No individual in the control group was found to have CC allele. 17 individuals had CT (26.6%) and 47 individuals had TT (73.4%) genotypes. In allelic distribution, C allele was found to be 17 (13.28%) and T allele was found to be 111 (86.72%). There was not a statistically significant difference between the two groups in terms of genotype ($p=0.122$) and allelic distribution ($p=0.149$).

In conclusion, this study addressed the combination of genetic predispositions and nutritional factors in athletes, specifically focusing on the minichromosome maintenance 6 (*MCM6*) rs4988235 polymorphism. When the genotype and allele distributions in football players were compared with the control group, no statistically significant differences were found. However, this study emphasizes that there are insufficient and diversified studies of this polymorphism in athletes in the literature and may contribute to increasing the sample size by providing a reference for future studies.

4. Conclusion

These findings highlight the importance of personalized nutrition strategies based on athletes' genetic profiles. Creating appropriate nutrition programs for athletes can help them optimize their performance. Furthermore, the increased use of genetic analyses in the sports community may contribute to the athletic performance of teams and individual athletes. Researchers may conduct additional studies, such as larger sample sizes, more comprehensive analysis of genetic and environmental factors, to better understand the results and more accurately assess the impact of genetic factors on athletic performance. This study can be considered as a fundamental step to understand the effects of genetic factors on traits such as lactose tolerance in athletes and to develop sport-specific nutritional strategies.

Article Information Form

Funding

The author (s) has no received any financial support for the research, authorship or publication of this study.

Authors' Contribution

The authors contributed equally to the study.

The Declaration of Conflict of Interest/ Common Interest

No conflict of interest or common interest has been declared by the authors.

The Declaration of Ethics Committee Approval

This study protocol was approved by the Üsküdar University Ethics Committee (61351342/ŞUBAT 2024-79) and was prepared in accordance with the guidelines of the Helsinki Declaration-2 (2015).

The Declaration of Research and Publication Ethics

The authors of the paper declare that they comply with the scientific, ethical and quotation rules of SAUJS in all processes of the paper and that they do not make any falsification on the data collected. In addition, they declare that Sakarya University Journal of Science and its editorial board have no responsibility for any ethical violations that may be encountered, and that this study has not been evaluated in any academic publication environment other than Sakarya University Journal of Science.

Copyright Statement

Authors own the copyright of their work published in the journal and their work is published under the CC BY-NC 4.0 license.

References

- [1] S. Suri, V. Kumar, R. Prased, B. Tanwar, A. Goyal, Y. Kaur, Y. Gat, A. Kumar, J. Kaur, D. Singh, "Considerations for development of lactose-free food", *Journal of Nutrition & Intermediary Metabolism*, vol. 15, p. 27-34, 2019.
- [2] T. Kleinbielen, L. Palencia-Madrid, C. Garcia-Ibarbia, F. Ortiz, J. A. Riancho, M. M. de Pancorbo, "Association of LCT-13910C>T polymorphism and hip fracture in a cohort of older adult population from Northern Spain", *Gene*, vol. 783, p. 145560, 2021.

- [3] S. B. Matthews, J. P. Waud, A. G. Roberts, A. K. Campbell, "Systemic lactose intolerance: A new perspective on an old problem", *Postgraduate Medical Journal*, vol. 81, 953, pp. 167-173, 2005.
- [4] M. B. Heyman, "Lactose intolerance in infants, children, and adolescents", *Pediatrics*, vol. 118, 3, pp. 1279-1286, 2006.
- [5] S. A. Tishkoff, F. A. Reed, A. Ranciaro, B. F. Voight, B. C. C. Babbitt, J. S. Silverman, K. Powell, H. M. Mortensen, J. B. Hirbo, M. Osman, M. Ibrahim, S. A. Omar, G. Lema, T. B. Nyambo, J. Ghorri, S. Bumpstead, J. K. Pritchard, G. A. Wray, P. Deloukas, "Convergent adaptation of human lactase persistence in Africa and Europe", *Nature Genetics*, vol. 39, 1, pp. 31-40, 2007.
- [6] M. C. E. Lomer, G. C. Parkes, J. D. Sanderson, "Review article: Lactose intolerance in clinical practice – myths and realities", *Alimentary Pharmacology & Therapeutics*, vol. 27, 2, pp. 93-103, 2008.
- [7] P. P. Apostol, M. Cristea, M. Ivan, M. Pelin, "Testing The Mcm6 13910-C/T And 22018-G/A Polymorphisms In Samples From Three Different Populations", *Journal of Hygienic Engineering and Design*, vol. 37, 2021.
- [8] E. L. Chin, L. Huang, Y. Y. Bouzid, C. P. Kirschke, B. Durbin-Johnson, L. M. Baldiviez, E. L. Bonnel, N. L. Keim, I. Korf, C. B. Stephensen, D. G. Lemay, "Association of lactase persistence genotypes (rs4988235) and ethnicity with dairy intake in a healthy US population", *Nutrients*, vol. 11, 8, p. 1860, 2019.
- [9] M. A. Arroyo, A. C. P. Lopes, V. B. Piatto, J. V. Maniglia, "Perspectives for Early Genetic Screening of Lactose Intolerance: -13910C/T Polymorphism Tracing in the MCM6 Gene", *Open Biology*, vol. 3, pp. 66-71, 2010.
- [10] C. J. Ingram, C. A. Mulcare, Y. Itan, M. G. Thomas, D. M. Swallow, "Lactose digestion and the evolutionary genetics of lactase persistence", *Human Genetics*, vol. 124, pp. 579-591, 2009.
- [11] L. C. Olds, E. Sibley, "Lactase persistence DNA variant enhances lactase promoter activity in vitro: functional role as a cis regulatory element", *Human Molecular Genetics*, vol. 12, 18, pp. 2333-2340, 2003.
- [12] O. Alharbi, A. El-Sohemy, "Lactose intolerance (LCT-13910C>T) genotype is associated with plasma 25-hydroxyvitamin D concentrations in Caucasians: a Mendelian randomization study", *The Journal of Nutrition*, vol. 147, 6, pp. 1063-1069, 2017.
- [13] R. H. Lewinsky, T. G. Jensen, J. Møller, A. Stensballe, J. Olsen, J. T. Troelsen, "T-13910 DNA variant associated with lactase persistence interacts with Oct-1 and stimulates lactase promoter activity in vitro", *Human Molecular Genetics*, vol. 14, 24, pp. 3945-3953, 2005.
- [14] B. F. Eken, H. Gezmiş, C. Sercan, S. Kapıcı, Ö. M. Chousein, D. Kırac, S. Akyüz, K. Ulucan, "Analysis of Vitamin D Receptor Gene Fok1 (Rs2228570) and Bsm1 (Rs1544410) Polymorphisms in Turkish Athletes", *Istanbul Gelisim University Journal of Health Sciences*, 6, pp. 561-572, 2018.
- [15] K. Ulucan, S. Yalcin, B. Akbas, F. Uyumaz, M. Konuk, "Analysis of Solute Carrier Family 6 Member 4 Gene promoter polymorphism in young Turkish basketball players", *The Journal of Neurobehavioral Sciences*, 1, 2, 2014.
- [16] N. S. Guest, J. Horne, S. M. Vanderhout, A. El-Sohemy, "Sport nutrigenomics: personalized nutrition for athletic performance", *Frontiers in Nutrition*, vol. 6, p. 8, 2019.
- [17] P. Ridefelt, L. D. Håkansson, "Lactose intolerance: lactose tolerance testing

versus genotyping", *Scandinavian Journal of Gastroenterology*, vol. 40, 7, pp. 822-826, 2005.

- [18] M. Raz, Y. Sharon, B. Yerushalmi, R. Birk, "Frequency of LCT-13910C/T and LCT-22018G/A single nucleotide polymorphisms associated with adult-type hypolactasia/lactase persistence among Israelis of different ethnic groups", *Gene*, vol. 519, 1, pp. 67-70, 2013.
- [19] Raz, M., Sharon, Y., Yerushalmi, B., & Birk, R. (2013). Frequency of LCT-13910C/T and LCT-22018G/A single nucleotide polymorphisms associated with adult-type hypolactasia/lactase persistence among Israelis of different ethnic groups. *Gene*, 519(1), 67–70.
- [20] T. Płoszaj, K. Jędrychowska-Dańska, H. Witas, "Frequency of lactase persistence genotype in a healthy Polish population," *Open Life Sciences*, vol. 6, 2, pp. 176-179, 2011.

Investigation of Spintronic Properties of Transition Metal Doped ZnO Thin Films Produced by Sol-Gel Spin Coating

Zafer Gültekin^{1*}, Cengiz Akay¹, Nuray Altınöçek Gültekin²

¹ Bursa Uludag University, Faculty of Science, Department of Physics, Bursa, Türkiye, zafergultekin@uludag.edu.tr, cenay@uludag.edu.tr

² Bursa Uludag University, Department of Food Technology, Bursa, Türkiye, altinolcek@uludag.edu.tr

*Corresponding Author

ARTICLE INFO

ABSTRACT

Keywords:

Sol-Gel Spin Coating
DMS Materials
Metal-Oxide Thin Films
ZnO
Contact Angle

Article History:

Received: 12.07.2024

Accepted: 24.09.2024

Online Available: 18.10.2024

Transition metal-doped diluted semiconductor materials have attracted significant interest in spintronic applications. In order to investigate the structural, optical, electrochemical, and magnetic properties of these diluted magnetic semiconductors, transition metal-doped ZnO thin films were successfully produced at room temperature using a low-cost sol-gel spin coating technique with the same molar ratios. XRD analyses revealed that all samples adopted the crystal structure of ZnO. Optical measurements indicated high transparency in the visible region for all samples, while electrical measurements confirmed that all samples were n-type semiconductors. Finally, magnetic measurements showed that pure ZnO and Al-doped ZnO exhibited diamagnetic behavior, while Ni and Co doped ZnO displayed magnetic behavior. These results show that Co and Ni-doped ZnO films can be used as diluted magnetic semiconductor materials in spintronic applications.

1. Introduction

Zinc oxide (ZnO) is an n-type semiconductor with a bandgap of 3.37 eV. Its high transparency, electron mobility, stability, and biocompatibility make ZnO suitable for electronic and photonic applications [1-12].

ZnO can be doped with transition metals to enhance its structural, morphological, magnetic, electrical, and optical properties [4,13-16]. For example, doping with elements such as Na, Mg, Fe, Cd, and Mn can alter its optical and structural properties [1, 17-21]. Transition metal doping enhances these properties of ZnO, enabling the production of higher-performance and more durable devices [22]. Under normal conditions, ZnO is diamagnetic, but when doped with Co, it exhibits room temperature ferromagnetism (RTFM) behavior, showing diluted magnetic semiconductor (DMS) characteristics [23]. The presence of RTFM in DMS was first predicted by

Dietl et al. [24]. Among all DMS materials, ZnO-based compounds have gained the most attention due to their inherent properties and wide range of applications, especially because they become ferromagnetic when doped with most transition metal elements [12, 25-28].

Additionally, DMS materials are a suitable class of materials for the production of spintronic devices such as spin valve transistors and spin organic light-emitting diodes [29, 30]. Transition metal-doped ZnO thin films have attracted significant interest due to their magnetic properties and performance in spintronic applications. These films offer ideal materials that combine semiconductor and magnetic properties, making them suitable for use in magnetic RAM (MRAM), spintronic devices, sensors, and quantum information processing systems. For example, when transition metals like Fe, Co, and Ni are doped into the ZnO matrix, they enhance the material's room

temperature ferromagnetic properties, making it suitable for such applications [31, 32].

Samanta et al. recorded weak DMS behavior at room temperature in Co and Al-doped ZnO prepared by pulsed laser deposition [33]. Nallusamy and Nammalvar reported that the saturation magnetization of ZnO films increased when Ni was added to ZnO [34]. Hadimani and colleagues observed that ZnO gained ferromagnetic properties when doped with Fe, and as the Fe content increased from 0 M to 0.2 M, the magnetic moment rose from 0.01 emu/g to 1.1 emu/g [35]. Qi et al. observed room temperature ferromagnetism in Al-doped ZnO films deposited on glass substrates after annealing in an air atmosphere [36].

Several methods can be used to synthesize ZnO films, including molecular beam epitaxy, RF magnetron sputtering, pulsed laser deposition, spray pyrolysis, chemical vapor deposition, and sol-gel spin coating [37-44]. Among these techniques, the sol-gel spin coating method has been preferred due to its low cost and ease of application [45, 46]. Spin coating is a widely preferred technique for preparing ZnO thin films and offers several advantages over other thin-film production methods. First, spin coating provides a low-cost, rapid production process and allows precise control over film thickness and uniformity. These features are especially advantageous for thin-film transistors and other microelectronic applications. Spin coating is also superior in terms of energy efficiency, as it does not require complex equipment and can be performed at room temperature [47, 48].

Other coating methods are generally performed at high temperatures and under vacuum, which increases energy consumption and production costs. Additionally, these methods can negatively affect the surface roughness and uniformity of the films. Spin coating minimizes such disadvantages and enables high-quality film production at low temperatures [48]. In this study, Al, Ni, and Co-doped ZnO thin films were coated on glass substrates using sol-gel and spin coating methods. These coatings were performed using a spin coating device that we produced ourselves [49]. Al doping improves the electrical conductivity of ZnO by increasing its electron

density. This feature is important for optoelectronic applications such as transparent conductive oxides (TCOs).

Additionally, Al doping optimizes ZnO's use in thin-film transistors and microelectronic devices by reducing surface roughness and improving crystalline structure properties [32]. Ni doping imparts magnetic properties to ZnO, resulting in materials that exhibit room temperature ferromagnetic behavior. This is critical for spintronic applications. Ni also increases the magnetic anisotropy of ZnO, thereby enhancing its potential use in magnetic data storage and sensor technologies. Furthermore, adding Ni to ZnO allows for the modification of the material's optical and magnetic properties, enabling the development of multifunctional devices [31]. Co is preferred to impart high Curie temperature and stabilized ferromagnetism to ZnO. Co-doped ZnO exhibits room temperature ferromagnetic properties, making it an ideal material for spintronic devices. Additionally, Co enhances the electronic band structure of ZnO, further improving its optical and magnetic properties, thus increasing its usability in optoelectronic applications [48].

2. General Methods

For the synthesis of transition metal-doped ZnO films, methoxyethanol was used as the solvent, monoethanolamine (MEA) as the stabilizer, and $\text{Zn}(\text{CH}_3\text{CO}_2)_2 \cdot 2\text{H}_2\text{O}$ (zinc acetate dihydrate) as the Zn source. Initially, 4.40 g of $\text{Zn}(\text{CH}_3\text{CO}_2)_2 \cdot 2\text{H}_2\text{O}$ was dissolved in 50 ml of methoxyethanol at a temperature range of 50-60°C, and stirred at 1000 rpm for 15 minutes. Subsequently, 1.22 g of MEA was added to this mixture and stirred for an additional 20 minutes.

To produce Co-doped ZnO (Co-ZnO), Ni-doped ZnO (Ni-ZnO), and Al-doped ZnO (Al-ZnO), ZnO films were doped with 0.01, 0.02, 0.03, 0.04, 0.05, and 0.1 M of cobalt acetate tetrahydrate ($(\text{CH}_3\text{COO})_2\text{Co} \cdot 4\text{H}_2\text{O}$), nickel acetate tetrahydrate ($(\text{Ni}(\text{CH}_3\text{COO})_2 \cdot 4\text{H}_2\text{O})$), and aluminum nitrate nonahydrate ($\text{Al}(\text{NO}_3)_3 \cdot 9\text{H}_2\text{O}$). The mixture was then stirred for an additional 15 minutes. A total of 12 different sol-gel solutions were obtained. These solutions were allowed to age for one day before use. After this process,

glass substrates, which were subjected to the cleaning procedure described in Figure 1, were coated with these solutions using spin coating. The coating process was carried out at a speed of 2000 rpm for a duration of 20 seconds. All obtained films were subjected to thermal annealing at 300°C. According to the examinations, the most efficient results were obtained with a doping concentration of 0.03 M.

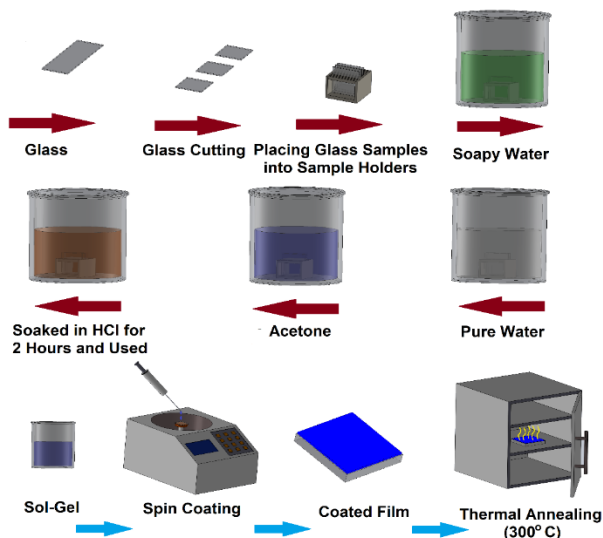


Figure 1. Steps of glass substrate cleaning and sol-gel spin coating process

3. Results and Discussion

The X-ray diffraction (XRD) patterns of ZnO, Co-ZnO, Ni-ZnO, and Al-ZnO thin films are shown in Figure 2. It can be observed that all diffraction peaks exhibit the dominant hexagonal wurtzite structure of ZnO. The diffraction peaks observed at approximately 31°, 33°, 36°, 57°, and 61° correspond to the (100), (002), (101), (102), (110), and (103) planes of ZnO, respectively. The observed diffraction patterns are consistent with the results reported in JCPDS card no: 36-1451 and [1]. The three main peaks corresponding to the (100), (002), and (101) planes of the hexagonal wurtzite structure of ZnO appear more prominent than the other peaks. No additional peaks corresponding to Co, Ni, or Al were observed in the XRD patterns. This result confirms that Co²⁺, Ni²⁺, and Al³⁺ are fully incorporated into the ZnO crystal lattice. Similar results have also been reported in [50].

Additionally, the peak position of the (002) plane of ZnO shifted to lower angles after metal doping (this was observed for all three doping metals).

This indicates that the lattice dimensions expand with doping, increasing the interplanar distance (*d*). Larger *d*-values correspond to smaller 2θ angles. The reason for this is the substitution of Zn atoms in the crystal structure of undoped ZnO with atoms of other elements (in this case, Al, Ni, and Co). The ionic radius of Zn⁺² is approximately 74 pm, while the ionic radii of Ni⁺², Al⁺³ ve Co⁺³ are 69 pm, 53.5 pm, and 61 pm, respectively. These differences lead to changes in the unit cell volume, causing angle shifts.

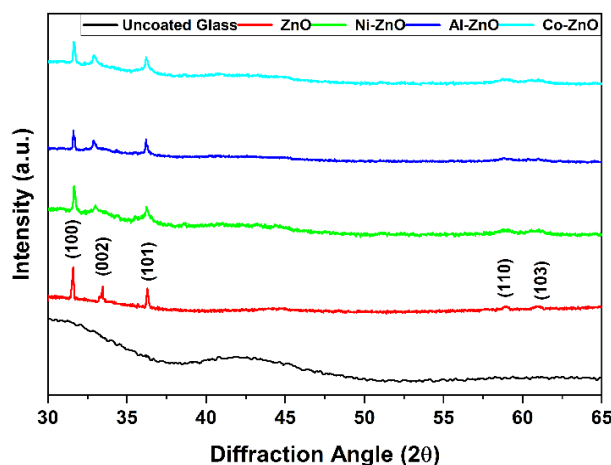


Figure 2. XRD images of uncoated glass and Co, Ni and Al doped ZnO thin films

The average crystallite sizes of the samples were calculated using the Debye-Scherrer formula (1) [1] based on the full width at half maximum (FWHM) of the peaks in the XRD patterns (Table 1).

$$D = \frac{0.9\lambda}{\beta \cos\theta} \quad (1)$$

where *D* is the crystallites size, λ is the X-ray wavelength, θ is the Bragg diffraction angle and β is the full width at half maximum.

A micro strain (ϵ) of films are calculated from Equation (2) [51, 52].

$$\epsilon = \frac{\beta \cos\theta}{4} \quad (2)$$

The dislocation density (δ) has been evaluated from Williamson and Smallman’s formula (3) [53].

$$\delta = \frac{1}{D^2} \quad (3)$$

The volume of the hexagonal unit cell (V) was calculated using Equation (4) [53].

$$V = 0.866a^2c \quad (4)$$

Furthermore, for a given plane with Miller indices (hkl) and interplanar spacing ($d_{(hkl)}$), the

lattice parameters $a=b$ and c were calculated using Equation (5) [53].

$$\frac{1}{d^2_{hkl}} = \frac{4}{3} \left(\frac{h^2 + hk + k^2}{a^2} \right) + \frac{l^2}{c^2} \quad (5)$$

Table 1. Results calculated from XRD data

Material	Lattice Parameters		D (nm)	V (Å ³)	ε (10 ⁻⁴)	δ (10 ¹⁴) (m ²)
	a=b (nm)	c (nm)				
ZnO	0.327	0.506	68	46.86	5.1	2.2
Co-ZnO	0.327	0.514	55	47.14	6.3	3.3
Ni-ZnO	0.327	0.509	58	47.32	6.0	3.0
Al-ZnO	0.327	0.511	45	47.60	7.7	4.9

SEM analysis was conducted to gain a detailed understanding of the surface morphology. Figure 3 shows the SEM images of ZnO and Co, Ni, and Al-doped ZnO thin films. The SEM image of pure ZnO (a) exhibits a quite smooth and homogeneous surface structure. The grain boundaries are distinct, and it is evident that the ZnO crystals have grown in a well-ordered manner. The grain sizes are relatively uniform and similar in shape and size, reflecting the typical orderly crystal structure of ZnO. The SEM image (b) of Al-doped ZnO reveals a significantly more homogeneous and smoother structure compared to undoped ZnO. This doping process appears to have reduced the granular features on the surface, resulting in a more compact surface formation.

The integration of aluminum atoms into the ZnO crystal lattice has led to a decrease in surface roughness, creating a more orderly structure at the microscopic level. This homogeneous surface morphology is particularly important for optoelectronic applications, as a smoother surface can enhance light propagation and improve device efficiency. The SEM image of Ni-doped ZnO (c) features a very fine and homogeneous surface structure. The grain boundaries are not as distinct as those in pure ZnO, but the surface appears smoother and finer. The addition of Ni has reduced the grain size of ZnO, leading to the formation of a finer and more uniform structure. The SEM image of Co-doped ZnO (d) has a much finer surface structure compared to ZnO and other doped films. The surface is quite smooth, and the grain boundaries

are not distinct. The lack of distinct grain boundaries indicates the presence of very small-sized crystals. This suggests that Co has integrated well into the ZnO structure without creating significant crystal defects.

The grain sizes obtained from the SEM images were added to Table 2. Overall, the results are consistent with the crystallite sizes obtained from the XRD patterns.

Figure 4 shows the contact angle (CA) plots of ZnO and Co, Ni and Al-ZnO films. These values are recorded in Table 2. Besides SEM analysis, surface morphology (roughness) can also be indirectly determined from surface contact angle measurements [54]. The variation in contact angle is greatly influenced by the morphology of the film surface, particularly its roughness [55, 56]. A contact angle of less than 90° between a liquid droplet and a solid surface indicates that the surface is hydrophilic.

When a water droplet contacts a film surface, micro- and nanoscale roughnesses and valleys on the surface play an important role. These valleys can trap air molecules and prevent the water droplet from directly contacting the surface, creating an air barrier on the surface and the surface becomes more hydrophobic [57]. ZnO film exhibits weak hydrophilic character with a surface contact angle value of 74°, while Co, Ni and Al doped ZnO films exhibit stronger hydrophilic characters with contact angle values of 17.5°, 10° and 22°, respectively. The increase or decrease in the contact angle is due to the

increase or decrease in the surface roughness of the film, respectively [58]. The results are consistent with the SEM images.

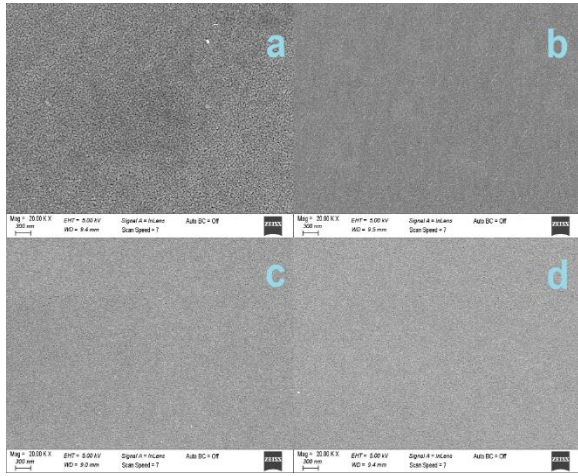


Figure 3. SEM images of thin films. a,b,c and d represent ZnO, Al-ZnO, Ni-ZnO and Co-ZnO, respectively.

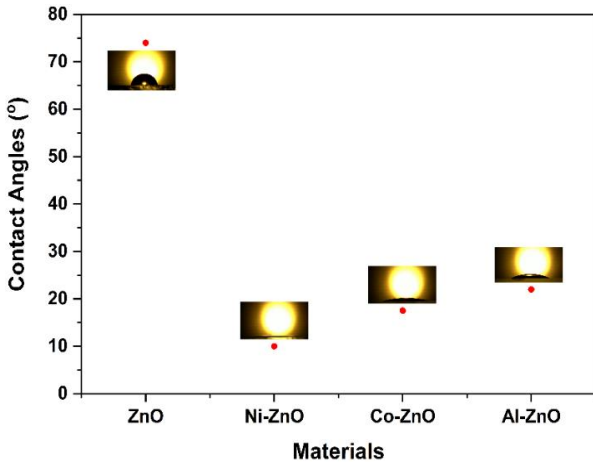


Figure 4. Contact angles of ZnO and Co, Ni and Al doped ZnO thin films

Additionally, the total surface free energies (γ_s) of all films were calculated and added to Table 2. A surface with high surface free energy enables better adhesion of the coating material and facilitates the formation of a more homogeneous coating layer. The surface free energies of Co, Ni, and Al-doped ZnO films are higher than that of undoped ZnO.

Table 2. Results from SEM and contact angle

Material	Grain Size (nm)	CA (°)	γ_s (mN/m)
ZnO	~60	74	59
Co-ZnO	<45	18	143
Ni-ZnO	<45	10	139
Al-ZnO	<45	22	135

The I-V characteristics of ZnO and Co, Ni, and Al-doped ZnO films at room temperature are illustrated in Figure 5. The linearity of the I-V graphs for all samples indicates that the films exhibit ohmic behavior. The resistivities of the films were determined using Equation (6) [51].

$$\rho = \frac{\pi t}{\ln 2} \left(\frac{V}{I} \right) \quad (6)$$

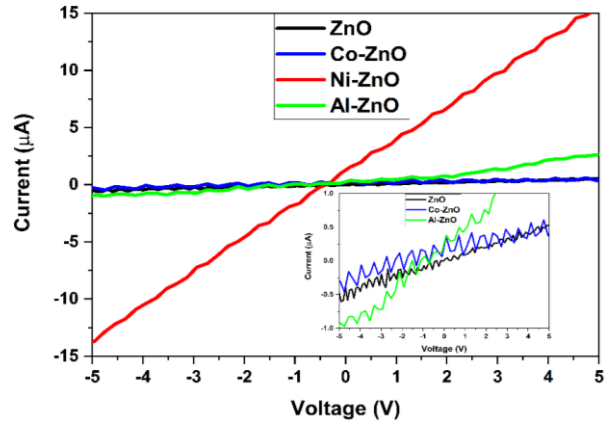


Figure 5. I-V graph of ZnO and Co, Ni and Al doped ZnO thin films

Here, t is the thickness of the thin film, and $(\pi/\ln 2) \times (V/I)$ represents the sheet resistance (R_{sh}). The calculated resistivity values (ρ) are listed in Table 3. After doping with Co, Al, and especially Ni, the conductivity increased compared to undoped ZnO. This can be attributed to the reduced presence of cracks and agglomerations on the film surfaces, which could otherwise impede electron flow. This is compatible with SEM measurements. Additionally, the increased conductivity indicates better crystallization in the doped films. The increase in carrier concentration (N_s) due to doping also contributes to the enhanced conductivity (Table 3).

Figure 6 shows the optical transmittance spectra of ZnO and Co, Ni, and Al-doped ZnO films. The optical properties of ZnO and ZnO films modified with dopants are closely related to the material's microstructural and crystallographic structure, which can be elucidated through XRD (X-ray diffraction) and SEM (scanning electron microscopy) analyses. Optical transmittance is a significant parameter that emerges during the interaction of a material with light. This property is especially critical in semiconductors like ZnO with a wide bandgap, as it determines the material's potential applications.

ZnO's wide bandgap (approximately 3.41 eV) provides high transparency in the optical transmittance spectrum, particularly in the visible light region. The XRD pattern shows that the crystal structure of ZnO is well-defined, with distinct diffraction peaks. This crystal structure maintains a wide optical bandgap, resulting in high optical transmittance. The sharp and narrow peaks observed in the XRD pattern of ZnO indicate minimal crystal defects, which allow for orderly optical transitions.

The addition of dopants such as Ni, Al, and Co to ZnO significantly alters its optical properties. In Ni-ZnO and Al-ZnO films, shifts and broadening of the peaks in the XRD patterns suggest that dopants integrate into the crystal structure, leading to phase mixtures and crystal distortions. These distortions cause the bandgap energy to narrow, resulting in red shifts in the optical spectrum. Consequently, the lower optical transmittance observed in these materials, especially in the UV region, can be attributed to increased absorption. SEM images support this observation; the irregularities and morphological disruptions seen on the surfaces of Ni-ZnO and Al-ZnO films cause increased scattering of light on the surface, reducing optical transmittance.

On the other hand, Co-ZnO films exhibit relatively sharp and well-defined peaks in XRD patterns, indicating that the crystal structure is not significantly disturbed by Co dopants, allowing ZnO to maintain its wide bandgap. SEM images of Co-ZnO films show a homogeneous and smooth surface structure, which minimizes light scattering and results in high optical transmittance. The stabilization of ZnO's crystal structure by Co dopants enables the optical bandgap to remain wide, thereby achieving high transmittance across a broad wavelength range.

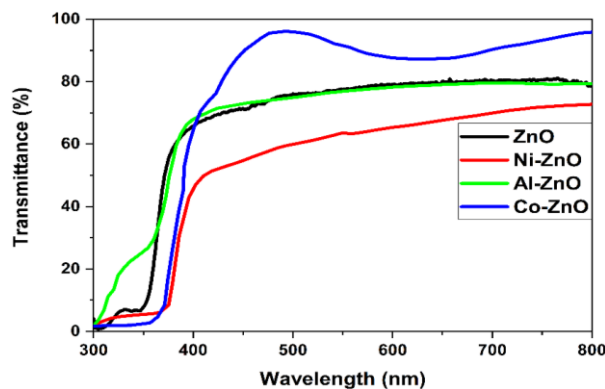


Figure 6. Optical transmittance spectrum of ZnO and Co, Ni and Al doped ZnO thin films

Table 3. Carrier density (N_s), flat band potential (V_{fb}), bandgap and resistivity of materials

Material	N_s (m^{-3})	V_{fb} (V)	Band gap (eV)	ρ ($\Omega \cdot cm$)
ZnO	1.93×10^{18}	0.38	3.41	1716
Co-ZnO	5.41×10^{18}	0.30	3.26	1320
Ni-ZnO	5.17×10^{18}	0.33	3.11	46
Al-ZnO	4.95×10^{18}	0.31	3.19	394

The optical energy range E_g of Co, Ni and Al-ZnO thin films was found using the absorption spectra defined by equation (7) and recorded Table 3:

$$\alpha h\nu = B(h\nu - E_g)^n \quad (7)$$

α is the absorption coefficient, ν is the frequency of the incident photon, B is a constant and h is Planck's constant [23]. Figure 7 summarizes the band gap obtained for ZnO and Co, Ni and Al doped ZnO thin films. It can be seen from the figure that the ZnO compound has a very large energy range, consistent with the literature [59-61]. Semiconductors like ZnO with bandgaps of this magnitude are optically transparent in the visible region, making them suitable for applications involving short-wavelength light [62].

Transition metals disrupt the structural integrity of the host ZnO cell/crystal, causing band narrowing. When the host ZnO compound is doped with transition metals, the dopant ions replace the Zn ions, changing the ZnO lattice structure. This change in the lattice structure is due to the radius difference of the dopant ions. The change of the graphs is due to the change of these lattice parameters. In the same graph, the x-axis intersection points of the slopes give the

values of the optical energy range of ZnO thin films. The energy ranges of these three ZnO films doped with transition metals correspond to the ultraviolet region.

Figure 8 shows the Mott-Schottky plots for ZnO and Co, Ni, and Al-doped ZnO films. In Mott-Schottky analysis, the slope of the plots provides insights into the carrier density of the films. A positive slope typically signifies that the films behave as n-type semiconductors, where electrons are the majority carriers.

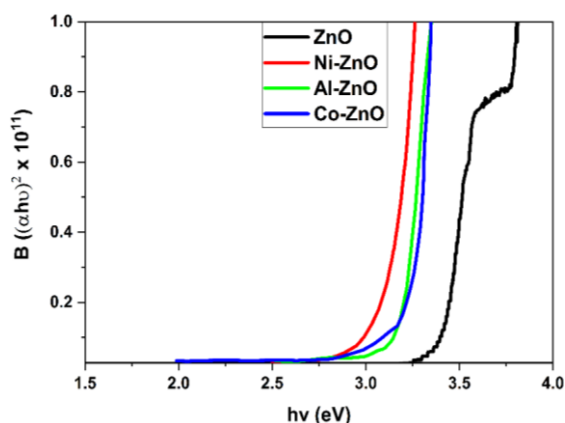


Figure 7. Band gap of ZnO and Co, Ni and Al doped ZnO thin films

Moreover, the intersection points of the Mott-Schottky curves with the x-axis yield the flat band potential (V_{fb}). The carrier densities and flat band potentials obtained from the plots were recorded in Table 3.

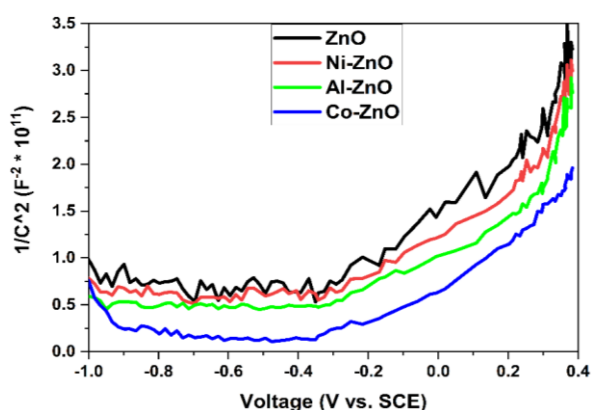


Figure 8. Mott-Schottky graph of ZnO and Co, Ni and Al doped ZnO thin films

The magnetic properties of Co, Ni, and Al-doped ZnO thin films were investigated at room temperature using a vibrating sample magnetometer (VSM). Figure 9 shows the VSM results of ZnO semiconductors doped with Al, Ni, and Co metals. The ZnO sample (inner part

in Figure 9) exhibits diamagnetic properties. The figure shows that the Al-doped ZnO semiconductor film behaves diamagnetically similar to ZnO, whereas Ni and Co-doped ZnO semiconductors acquire magnetic properties. Particularly, a rapid increase in the magnetic moment at small magnetic field values ($< \pm 100$ Oe) indicates that Ni and especially Co doped ZnO materials exhibit superparamagnetic behaviour [63]. Superparamagnetism is the condition where magnetic particles at the nanoscale exhibit random orientations without interacting with each other.

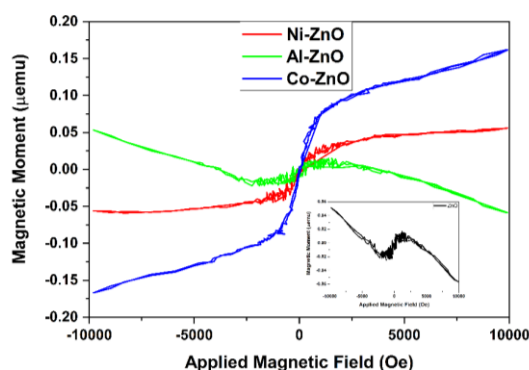


Figure 9. VSM graph of ZnO and Co, Ni and Al doped ZnO thin films

The behavior of DMS is based on the magnetic, optical, and structural changes resulting from the modification of ZnO with magnetic dopants such as Ni, Al, and Co. XRD data indicate that the ZnO matrix retains its wurtzite structure, though the dopants cause slight modifications in the crystal structure. This crystal structure provides a suitable environment for strong ferromagnetic interactions, such as RKKY (Ruderman-Kittel-Kasuya-Yosida) or Zener-type interactions. The highest magnetic moment observed in Co-ZnO on the Figure 9 suggests strong ferromagnetic interaction between dopant ions, attributed to spin alignment between Co ions.

Grain size and defects also contribute to this ferromagnetic behavior; smaller grain sizes and defects can enhance ferromagnetism by increasing the localization of free carriers. The formation of secondary phases (e.g., CoO or NiO) can also support ferromagnetic behavior, as these phases increase the carrier density within the ZnO matrix (Table 3), thereby enhancing ferromagnetic interactions. These findings indicate that ZnO-based DMS materials hold

potential for spintronic applications, with ferromagnetism in these materials being closely related to the type of dopant, carrier density, grain size, and defects.

4. Conclusion

The spin coating technique involves the uniform deposition and production of thin films by spinning the substrate and thin film solution at a certain angular speed. Using this technique, Ni, Al, and Co-doped ZnO films were produced in our laboratory. Our structural analyses revealed that all doped films adopted the crystal structure of ZnO, with no external crystalline phase observed. Optical measurements indicated that each sample exhibited high transparency in the visible region, with band gaps ranging from 3.11 to 3.41 eV. Electrical analysis demonstrated that each semiconductor was of n-type, with carrier concentrations in the range of 10^{18} m^{-3} . Magnetic measurements showed that pure ZnO and Al-doped ZnO exhibited diamagnetic properties, while Ni and Co-doped ZnO displayed superparamagnetic behaviour. Our results were generally consistent with previous studies reported in the literature. Ni and Co doped ZnO materials produced in our study could be utilized as diluted magnetic semiconductors in spintronic applications.

Article Information Form

Funding

This study was supported by Bursa Uludağ University Scientific Research Projects Commission. Project Code, FHIZ-2023-1608.

Authors' Contribution

The authors contributed equally to the study.

The Declaration of Conflict of Interest/ Common Interest

No conflict of interest or common interest has been declared by the authors.

The Declaration of Ethics Committee Approval

This study does not require ethics committee permission or any special permission.

The Declaration of Research and Publication Ethics

The authors of the paper declare that they comply with the scientific, ethical and quotation rules of SAUJS in all processes of the paper and that they do not make any falsification on the data collected. In addition, they declare that Sakarya University Journal of Science and its editorial board have no responsibility for any ethical violations that may be encountered, and that this study has not been evaluated in any academic publication environment other than Sakarya University Journal of Science.

Copyright Statement

Authors own the copyright of their work published in the journal and their work is published under the CC BY-NC 4.0 license.

References

- [1] Z. Gültekin, M. Alper, M. C. Hacıismailoğlu, C. Akay, "Effect of Mn doping on structural, optical and magnetic properties of ZnO films fabricated by sol-gel spin coating method," *Journal of Materials Science: Materials in Electronics*, vol. 34, no. 438, pp. 1-14, 2023.
- [2] C. D. Bojorge, H. R. Canepa, U. E. Gilabert, D. Silva, E. A. Dalchiele, R. E. Marotti, "Synthesis and optical characterization of ZnO and ZnO nanocrystalline films obtained by the sol-gel dip-coating process," *Journal of Materials Science: Materials in Electronics*, vol. 18, no. 10, pp. 1119-1125 2007.
- [3] M. Smirnov, C. Baban, G. I. Rusu, "Structural and optical characteristics of spin-coated ZnO thin films," *Applied Surface Science*, vol. 256, pp. 2405-2408, 2010.
- [4] N. Siregar, J. H. Panggabean, "The effect of spin coating speed on structural and optical properties of ZnO and ZnO/dye thin films synthesized by sol-gel spin coating method," *Journal of Physics: Conference Series*, Canada, 2021, pp. 1-6.

- [5] D. M. Bagnall, Y. Chen, Z. Zhu, T. T. T. Tao, S. Koyama, M. T. Shen, T. Goto, "Synthesis and optical characterization of ZnO nanocrystalline films," *Applied Physics Letters*, vol. 70, pp. 2230, 1997.
- [6] S. J. Pearton, C. R. Abernathy, M. E. Overberg, G. T. Thaler, D. P. Norton, N. Theodoropoulou, A. F. Hebard, Y. D. Park, F. Ren, J. Kim, L. A. Boatner, "ZnO thin films: Synthesis and properties," *Journal of Applied Physics*, vol. 93, no. 1, pp. 1-13, 2003.
- [7] D. C. Look, D. C. Reynolds, C. W. Litton, R. L. Zones, D. B. Eason, G. Conwell, "Structural and optical properties of ZnO films," *Applied Physics Letters*, vol. 81, pp. 1830-1832, 2002.
- [8] C. Liu, F. Yiu, H. Morkoc, "Structural and optical properties of ZnO thin films," *Journal of Materials Science: Materials in Electronics*, vol. 16, pp. 557-597, 2005.
- [9] K. Samanta, P. Bhattacharya, R. S. Katiyar, W. Iwamoto, P. G. Pagliuso, C. Rettori, "Photoluminescence properties of Cd doped ZnO films," *Physical Review B: Condensed Matter and Materials Physics*, vol. 73, pp. 245213, 2006.
- [10] P. Kumari, K. P. Misra, S. Chattopadhyay, S. Samanta, "A brief review on transition metal ion doped ZnO nanoparticles and its optoelectronic applications," *Materials Today: Proceedings*, vol. 43, pp. 3297-3302, 2021.
- [11] A. Badawi, M. G. Althobaiti, E. E. Ali, S. S. Alharthi, A. N. Alharbi, "A comparative study of the structural and optical properties of transition metals (M= Fe, Co, Mn, Ni) doped ZnO films deposited by spray-pyrolysis technique for optoelectronic applications," *Optical Materials*, vol. 124, pp. 112055-112062, 2022.
- [12] A. Murtaza, W. L. Zuo, X. Song, A. Ghani, A. Saeed, M. Yaseen, S. Yang, "Robust ferromagnetism in rare-earth and transition metal co-doped ZnO nanoparticles for spintronics applications," *Materials Letters*, vol. 310, pp. 131479, 2022.
- [13] Z. Ye, H. He, L. Jiang, "Co-doping: An effective strategy for achieving stable p-type ZnO thin films," *Nano Energy*, vol. 52, pp. 527-540, 2018.
- [14] D. Anbuselvan, S. Nilavazhagan, A. Santhanam, N. Chidhambaram, K. V. Gunavathy, T. Ahamad, S. M. Alshehri, "Room temperature ferromagnetic behavior of nickel-doped zinc oxide dilute magnetic semiconductor for spintronics applications," *Physica E*, vol. 129, pp. 114665, 2021.
- [15] A. F. Fathima, R. J. Mani, M. M. Roshan, K. Sakthipandi, "Enhancing structural and optical properties of ZnO nanoparticles induced by the double co-doping of iron and cobalt," *Materials Today: Proceedings*, vol. 49, pp. 2598-2601, 2022.
- [16] N. Ali, B. Singh, V. Ar, S. Lal, C. S. Yadav, K. Tarafder, S. Ghosh, "Ferromagnetism in Mn-doped ZnO: a joint theoretical and experimental study," *The Journal of Physical Chemistry C*, vol. 125, no. 14, pp. 7734-7745, 2021.
- [17] D. Akcan, A. Gungor, L. Arda, "Structural and optical properties of Na-doped ZnO films," *Journal of Molecular Structure*, vol. 1161, pp. 299-305, 2018.
- [18] K. Verma, B. Chaudhary, V. Kumar, V. Sharma, M. Kumar, "Investigation of structural, morphological and optical properties of Mg: ZnO thin films prepared by sol-gel spin coating method," *Vacuum*, vol. 146, pp. 524-529, 2017.
- [19] B. P. Kafle, S. Acharya, S. Thapa, S. Poudel, "Structural and optical properties of Fe-doped ZnO transparent thin films," *Ceramics International*, vol. 42, no. 1, pp. 1133-1139, 2016.
- [20] B. J. Zheng, W. Hu, "Photoluminescence properties of Cd doped ZnO films obtained

- by pulsed laser deposition," *Advanced Materials Research*, vol. 680, pp. 70-74, 2013.
- [21] H. Sun, S. C. Chen, C. H. Wang, Y. W. Lin, C. K. Wen, T. H. Chuang, M. J. Dai, "Electrical and magnetic properties of (Al, Co) co-doped ZnO films deposited by RF magnetron sputtering," *Surface and Coatings Technology*, vol. 359, pp. 390-395, 2019.
- [22] Ü. Özgür, Ya. I. Alivov, C. Liu, A. Teke, M. A. Reshchikov, S. Doğan, V. Avrutin, S.-J. Cho, H. Morkoç, "A comprehensive review of ZnO materials and devices," *Journal of Applied Physics*, vol. 98, no. 4, pp. 041301, 2005.
- [23] N. Abirami, A. M. S. Arulanantham, K. S. J. Wilson, "Structural and magnetic properties of cobalt doped ZnO thin films deposited by cost effective nebulizer spray pyrolysis technique," *Materials Research Express*, vol. 7, no. 2, pp. 2020, 2020.
- [24] T. Dietl, H. Ohno, F. Matsukura, J. Cibert, D. Ferrand, "ZnO: A ferromagnetic semiconductor," *Science*, vol. 287, pp. 1019, 2000.
- [25] K. Sato, H. Katayama-Yoshida, "Theory of room-temperature ferromagnetism in ZnO-based magnetic semiconductors," *Japanese Journal of Applied Physics*, vol. 39, pp. L555, 2000.
- [26] K. Sato, H. Katayama-Yoshida, "Theory of room-temperature ferromagnetism in ZnO-based magnetic semiconductors (II)," *Japanese Journal of Applied Physics*, vol. 40, pp. L334, 2001.
- [27] Q. Q. Gao, Q. X. Yu, K. Yuan, X. N. Fu, B. Chen, C. X. Zhu, H. Zhu, "Influence of annealing atmosphere on room temperature ferromagnetism of Mn-doped ZnO nanoparticles," *Applied Surface Science*, vol. 264, pp. 7-10, 2013.
- [28] X. Liu, F. Lin, L. Sun, W. Cheng, X. Ma, W. Shi, "Doping concentration dependence of room-temperature ferromagnetism for Ni-doped ZnO thin films prepared by pulsed-laser deposition," *Applied Physics Letters*, vol. 88, no. 6, pp. 062503, 2006.
- [29] M. Benali Kanoun, S. Goumri-Said, A. Manchon, U. Schwingenschlögl, "Ferromagnetism carried by highly delocalized hybrid states in Sc-doped ZnO thin films," *Applied Physics Letters*, vol. 100, no. 22, pp. 222504, 2012.,
- [30] D.P. Norton, S. J. Pearton, J. M. Zavada, W. M. Chen, I. A. Buyanova, "Ferromagnetism in ZnO Doped with Transition Metal Ions," First Edition, C. Jagadish, S. Pearton, Elsevier Science Ltd, 2006, pp. 555-576.
- [31] A. Janotti, C. G Van de Walle, "Fundamentals of zinc oxide as a semiconductor," *Reports on Progress in Physics*, vol. 72, no. 12, pp. 126501, 2009.
- [32] C. G. Jin, Y. Gao, X. M. Wu, M. L. Cui, L. J. Zhuge, Z. C. Chen, B. Hong, "Structural and magnetic properties of transition metal doped ZnO films," *Thin Solid Films*, vol. 518, no. 8, pp. 2152-2156, 2010.
- [33] K. Samanta, P. Bhattacharya, J. G. S. Duque, W. Iwamoto, C. Rettori, P. G. Pagliuso, R. S. Katiyar, "Optical and magnetic properties of $Zn_{0.9-x}Co_{0.1}O:Al_x$ thin films," *Solid State Communications*, vol. 147, no. 7-8, pp. 305-308, 2008.
- [34] S. Nallusamy, G. Nammalvar, "Enhancing the saturation magnetisation in Ni doped ZnO thin films by TOPO functionalization," *Journal of Magnetism and Magnetic Materials*, vol. 485, pp. 297-303, 2019.
- [35] P. L. Hadimani, S. S. Ghosh, A. Sil, "Preparation of Fe doped ZnO thin films and their structural, magnetic, electrical characterization," *Superlattices and Microstructures*, vol. 120, pp. 199-208, 2018.

- [36] Y. K. Qi, J. J. Gu, L. H. Liu, H. Y. Sun, "Annealing effects on structural and magnetic properties of Al doped ZnO thin films," *Advanced Materials Research*, vol. 239, pp. 2835-2838, 2011.
- [37] Z. Changzheng, "Effect of the oxygen pressure on the microstructure and optical properties of ZnO film prepared by laser molecular beam epitaxy," *Physica B: Condensed Matter*, vol. 404, pp. 404-408, 2009.
- [38] T. Minami, H. Nanto, S. Takata, "Optical properties of aluminum doped zinc oxide thin films prepared by RF magnetron sputtering," *Japanese Journal of Applied Physics*, vol. 24, pp. L781, 1985.
- [39] B. L. Zhu, "Low temperature annealing effects on the structure and optical properties of ZnO films grown by pulsed laser deposition," *Vacuum*, vol. 84, pp. 84-88, 2010.
- [40] T. P. Rao, M. S. Kumar, A. Safarulla, V. Ganesan, S. R. Barman, C. Sanjeeviraja, "Physical properties of ZnO thin films deposited at various substrate temperatures using spray pyrolysis," *Physica B: Condensed Matter*, vol. 405, no. 9, pp. 2226-2231, 2010.
- [41] A. George, "Microstructure and field emission characteristics of ZnO nanoneedles grown by physical vapor deposition," *Materials Chemistry and Physics*, vol. 123, Art. ID 123-123, 2010.
- [42] S. A. Kamaruddin, K. Y. Chan, H. K. Yow, M. Z. Sahdan, H. Saim, D. Knipp, "Zinc oxide films prepared by sol-gel spin coating technique," *Applied Physics A: Materials Science & Processing*, vol. 104, no. 2, pp. 263-268, 2011.
- [43] G. Demircan, S. Yalcin, K. Alivi, G. Ceyhan, M. V. Acikgoz, B. Balak, B. Aktas, R. Das, "The effect of Co and Mn Co-doping on structural and optical properties of ZnO thin films," *Optical Materials*, vol. 126, pp. 112163, 2022.
- [44] M. Abdelkrim, M. Guezoul, M. Bedrouni, M. Bouslama, A. Ouerdane, B. Kharroubi, "Effect of slight cobalt incorporation on the chemical, structural, morphological, optoelectronic, and photocatalytic properties of ZnO thin film," *Journal of Alloys and Compounds*, vol. 920, pp. 165703, 2022.
- [45] T. K. Pathak, V. Kumar, L. P. Purohit, "High quality nitrogen-doped zinc oxide thin films grown on ITO by sol-gel method," *Physica E: Low-Dimensional Systems and Nanostructures*, vol. 74, pp. 551-555, 2015.
- [46] T. K. Pathak, V. Kumar, H. C. Swart, L. P. Purohit, "Electrical and optical properties of p-type codoped ZnO thin films prepared by spin coating technique," *Physica E: Low-Dimensional Systems and Nanostructures*, vol. 77, pp. 1-6, 2016.
- [47] M. Khan, G. A. Nowsherwan, R. Ali, M. Ahmed, N. Anwar, S. Riaz, A. Farooq, S. S. Hussain, S. Naseem, J. R. Choi, "Investigation of Photoluminescence and Optoelectronics Properties of Transition Metal-Doped ZnO Thin Films," *Molecules*, vol. 28, 7963, 2023.
- [48] A. Faramawy, H. Elsayed, C. Scian, G. Mattei, "Structural, Optical, Magnetic and Electrical Properties of Sputtered ZnO and ZnO:Fe Thin Films: The Role of Deposition Power," *Ceramics*, vol. 5, pp. 1128-1153, 2022.
- [49] Z. Gültekin, M. Alper, C. Akay, M. C. Hacıismailoğlu, "Design and construction of home-made spin coater for OLED production," *International Journal of Electronic Devices and Physics*, vol. 5, pp. 0-11, 2021.
- [50] P. SivaKarthik, V. Thangaraj, S. Kumaresan, K. Vallalperuman, "Comparative study of Co and Ni substituted ZnO nanoparticles: synthesis, structural, optical and photocatalytic activity," *Journal of Materials Science:*

- Materials in Electronics, vol. 28, pp. 10582-10588, 2017.
- [51] K. Ravichandran, P. Philominathan, "Comparative Study on Structural and Optical Properties of CdS Films Fabricated by Three Different Low-Cost Techniques," *Applied Surface Science*, vol. 255, no. 11, pp. 5736-5741, 2009.
- [52] R. Karthick, M. Sundararajan, "Design and Implementation of Low Power Testing Using Advanced Razor Based Processor," *International Journal of Applied Engineering Research*, vol. 12, pp. 6384, 2017.
- [53] S. Chattopadhyay, K. P. Misra, A. Agarwala, A. Shahee, S. Jain, N. Halder, A. K. Mukhopadhyay, "Dislocations and particle size governed band gap and ferromagnetic ordering in Ni doped ZnO nanoparticles synthesized via co-precipitation," *Ceramics International*, vol. 45, no. 17, pp. 23341-23354, 2019.
- [54] A. Riaz, A. Ashraf, H. Taimoor, S. Javed, M. A. Akram, M. Islam, K. Saeed, "Photocatalytic and photostability behavior of Ag-and/or Al-Doped ZnO films in methylene blue and rhodamine B under UV-C irradiation," *Coatings*, vol. 9, no. 3, pp. 202, 2019.
- [55] Z. Bazhan, F. E. Ghodsi, J. Mazloom, "The surface wettability and improved electrochemical performance of nanostructured $\text{Co}_x\text{Fe}_{3-x}\text{O}_4$ thin film," *Surface and Coatings Technology*, vol. 309, pp. 554-562, 2017.
- [56] C. Ottone, A. Lamberti, M. Fontana, V. Cauda, "Wetting behavior of hierarchical oxide nanostructures: TiO_2 nanotubes from anodic oxidation decorated with ZnO nanostructures," *Journal of The Electrochemical Society*, vol. 161, no. 10, pp. D484, 2014.
- [57] R. Bayati, R. Molaei, A. Richmond, S. Nori, F. Wu, D. Kumar, C. L. Reynolds Jr., "Modification of properties of yttria stabilized zirconia epitaxial thin films by excimer laser annealing," *ACS Applied Materials & Interfaces*, vol. 6, no. 24, pp. 22316-22325, 2014.
- [58] G. J. Chen, S. R. Jian, J. Y. Juang, "Surface analysis and optical properties of Cu-doped ZnO thin films deposited by radio frequency magnetron sputtering," *Coatings*, vol. 8, no. 8, pp. 266, 2018.
- [59] G. Kaur, A. Mitra, K. L. Yadav, "Pulsed laser deposited Al-doped ZnO thin films for optical applications," *Progress in Natural Science: Materials International*, vol. 25, no. 1, pp. 12-21, 2015.
- [60] A. Mahroug, S. Boudjadar, S. Hamrit, L. Guerbous, "Structural, morphological and optical properties of undoped and Co-doped ZnO thin films prepared by sol-gel process," *Journal of Materials Science: Materials in Electronics*, vol. 25, pp. 4967-4974, 2014.
- [61] I. Jellal, O. Daoudi, K. Nouneh, M. Boutamart, S. Briche, M. Fahoume, J. Naja, "Comparative study on the properties of Al-and Ni-doped ZnO nanostructured thin films grown by SILAR technique: Application to solar photocatalysis," *Optical and Quantum Electronics*, vol. 55, no. 7, pp. 620, 2023.
- [62] A. F. Al Naim, A. Solieman, E. R. Shaaban, "Structural, optical, and magnetic properties of Co-doped ZnO nanocrystalline thin films for spintronic devices," *Journal of Materials Science: Materials in Electronics*, vol. 31, no. 21, pp. 3613-3621, 2020.
- [63] P. Mallick, C. Rath, A. Rath, A. Banerjee, N. C. Mishra, "Antiferro to superparamagnetic transition on Mn doping in NiO ," *Solid State Communications*, vol. 150, pp. 29-30, 2010.

New Integrated and Differentiated Sequence Spaces $\int b_p^{r,s}$ and $db_p^{r,s}$

Kübra Topal 

Çay Vocational and Technical Anatolian High School, 53020, Rize, Türkiye, kubra_topal22@erdogan.edu.tr

ARTICLE INFO	ABSTRACT
<p>Keywords: Matrix transformations Matrix domain α, β and γ –duals Matrix classes</p> <p>Article History: Received: 07.08.2024 Accepted: 19.09.2024 Online Available: 18.10.2024</p>	<p>In this work, we construct new sequence spaces by combining the integrated and differentiated sequence spaces with the binomial matrix. Firstly, we provide information about basic matters such as sequence spaces and matrix domain. Subsequently we briefly summarize some sequence spaces generated by the binomial matrix. Thereafter, we define the integrated and differentiated sequence spaces and establish the new sequence spaces. Afterwards, we examine some properties and the inclusion relations of these new sequence spaces. We also determine the α, β and γ –duals of the integrated and differentiated sequence spaces. Finally, we characterize some matrix classes associated with the new sequence spaces.</p>

1. Introduction

Let $w = \{x = (x_k) : x \in \mathbb{R} \text{ (or } \mathbb{C}), \forall k \in \mathbb{N}\}$ be a set. Under the pointwise addition and scalar multiplication w is a vector space. Each subspace of w is called a sequence space. The sequence space ℓ_p , which is absolutely p -summable sequences, is a frequently used sequence space.

A Banach sequence space is classified as a BK-space if the maps $p_n: X \rightarrow \mathbb{C}$, defined as $p_n(x) = x_n$ are continuous for all $n \in \mathbb{N}$ [1]. Therefore, we can say that the sequence space ℓ_p , with their norm defined as

$$\|x\|_p = \left(\sum_{k=1}^{\infty} |x_k|^p \right)^{\frac{1}{p}} \quad (1)$$

is a BK-space, for $1 \leq p < \infty$.

Let, $A = (a_{nk})$ be an infinite matrix of real (or complex) entries. The A -transform of the sequence x is denoted as

$$(Ax)_n = \sum_{k=0}^{\infty} a_{nk}x_k, \quad (2)$$

where the series $(Ax)_n$ is required to be convergent for every $n \in \mathbb{N}$.

Moreover, let X and Y be two sequence spaces and consider the set defined as $X_A = \{x = (x_k) \in w : Ax \in X\}$ for a given infinite matrix A . This set is referred to as the matrix domain of A on the sequence space X . Additionally, the class of all matrix transformations from X into Y is denoted by $(X:Y)$ and it is given by [2],

$$(X:Y) = \{A = (a_{nk}) : Ax \in Y \text{ for all } x \in X\}. \quad (3)$$

Let us consider the summation matrix $S = (s_{nk})$ defined as

$$s_{nk} = \begin{cases} 1, & 0 \leq k \leq n, \\ 0, & k > n, \end{cases} \quad (4)$$

where $\forall n, k \in \mathbb{N}$.

The matrix domain of S is used to define the sets $bs = (\ell_{\infty})_S$ and $cs = c_S$, which denote the sets

of all bounded and convergent series, respectively.

If the entries of an infinite matrix $A = (a_{nk})$ satisfies the conditions $a_{nn} \neq 0$ for all $n, k \in \mathbb{N}$ and $a_{nk} = 0$ for $k > n$, then this matrix is called a triangular matrix. A triangular matrix has an inverse which is also a triangular matrix.

The integrated and differentiated sequence spaces were initially introduced by Goes and Goes [3]. Recently, Kirişçi has extensively studied these sequence spaces from various perspectives [4-6].

Additionally, Binomial sequence spaces were defined by Bişgin using the matrix domain of the Binomial matrix [7, 8]. Subsequently, various sequence spaces were constructed by several authors using the matrix domain of the Binomial matrix [9, 10].

2. New Sequence Spaces

In this section, we first provide a brief overview of some previous studies. Next, we introduce new sequence spaces obtained by combining the integrated and differentiated sequence spaces with the binomial matrix. Then, we explore their respective properties.

The Binomial matrix $B^{rs} = (b_{nk}^{rs})$ is defined as follows;

$$b_{nk}^{rs} = \begin{cases} \frac{1}{(s+r)^n} \binom{n}{k} s^{n-k} r^k, & 0 \leq k \leq n \\ 0, & k > n \end{cases} \quad (5)$$

for all $n, k \in \mathbb{N}$, $r, s \in \mathbb{R}$ and $s \cdot r > 0$. (Throughout the article, we assume $s \cdot r > 0$ unless otherwise stated.)

The binomial sequence spaces were first defined by Bişgin in [7, 8] as follows;

$$b_0^{r,s} = \left\{ \lim_{n \rightarrow \infty} \frac{1}{(s+r)^n} \sum_{k=0}^n \binom{n}{k} s^{n-k} r^k x_k = 0 \right\}, \quad (6)$$

$$b_c^{r,s} = \left\{ \begin{array}{l} x = (x_k) \in w: \\ \lim_{n \rightarrow \infty} \frac{1}{(s+r)^n} \sum_{k=0}^n \binom{n}{k} s^{n-k} r^k x_k \text{ exists} \end{array} \right\}, \quad (7)$$

$$b_\infty^{r,s} = \left\{ \begin{array}{l} x = (x_k) \in w: \\ \sup_{n \in \mathbb{N}} \left| \frac{1}{(s+r)^n} \sum_{k=0}^n \binom{n}{k} s^{n-k} r^k x_k \right| < \infty \end{array} \right\} \quad (8)$$

and

$$b_p^{r,s} = \left\{ \begin{array}{l} x = (x_k) \in w: \\ \sum_n \left| \frac{1}{(s+r)^n} \sum_{k=0}^n \binom{n}{k} s^{n-k} r^k x_k \right|^p < \infty \end{array} \right\}, \quad (9)$$

where $1 \leq p < \infty$. Throughout the article, unless otherwise specified, we assume $1 \leq p < \infty$.

Subsequently, the sequence space $b_p^{r,s}(G)$, obtained from the composition of the binomial matrix with the double band matrix defined by Bişgin in [9] as follows;

$$b_p^{r,s}(G) = \left\{ \begin{array}{l} x = (x_k) \in w: \\ \sum_n \left| \frac{1}{(s+r)^n} \sum_{k=0}^n \binom{n}{k} s^{n-k} r^k (u x_k + v x_{k-1}) \right|^p < \infty \end{array} \right\}, \quad (10)$$

where double band matrix $G = (g_{nk})$ is defined by

$$g_{nk} = \begin{cases} u, & k = n \\ v, & k = n - 1 \\ 0, & \text{otherwise} \end{cases} \quad (11)$$

for all $n, k \in \mathbb{N}$ and $u, v \in \mathbb{R} \setminus \{0\}$.

Then, the sequence space $b_p^{r,s}(D)$, obtained from the combination of the binomial and triple band matrix, defined by Sönmez in [10] as follows;

$$b_p^{r,s}(D) = \left\{ \sum_n \left| \sum_{k=0}^n \binom{n}{k} \frac{1}{(s+r)^n} s^{n-k} r^k (tx_k + ux_{k-1} + vx_{k-2}) \right|^p < \infty \right\}, \quad (12)$$

where triple band matrix $D = (d_{nk})$ is defined by

$$d_{nk} = \begin{cases} t, & k = n \\ u, & k = n - 1 \\ v, & k = n - 2 \\ 0, & \text{otherwise} \end{cases} \quad (13)$$

for all $n, k \in \mathbb{N}$ and $t, u, v \in \mathbb{R} \setminus \{0\}$.

Lastly, the sequence space $b_p^{r,s}(Q)$ defined by Topal combining the binomial matrix and quadruple band matrix as follows;

$$b_p^{r,s}(Q) = \left\{ \sum_n \left| \frac{1}{(s+r)^n} \sum_{k=0}^n \binom{n}{k} s^{n-k} r^k (ox_k + tx_{k-1} + ux_{k-2} + vx_{k-3}) \right|^p < \infty \right\}, \quad (14)$$

where quadruple band matrix $Q = (q_{nk}(o, t, u, v))$ is defined as follows;

$$q_{nk}(o, t, u, v) = \begin{cases} o, & k = n \\ t, & k = n - 1 \\ u, & k = n - 2 \\ v, & k = n - 3 \\ 0, & \text{otherwise} \end{cases} \quad (15)$$

for all $n, k \in \mathbb{N}$ and $o, t, u, v \in \mathbb{R} \setminus \{0\}$.

Now, let us define the matrix $((k+1)I)$ such that;

$$(k+1)I = \begin{bmatrix} 1 & 0 & 0 & 0 & \cdots \\ 0 & 2 & 0 & 0 & \cdots \\ 0 & 0 & 3 & 0 & \cdots \\ 0 & 0 & 0 & 4 & \cdots \\ \vdots & \vdots & \vdots & \vdots & \ddots \end{bmatrix} \quad (16)$$

where $k \in \mathbb{N}_0 = \{0, 1, 2, \dots\}$. Let, X be a sequence space. Accordingly, the integrated and differentiated sequence spaces are defined by Goes and Goes [3] as follows;

$$\int X = \{x = (x_k) \in w : ((k+1)x_k) \in X\} = X_{(k+1)I} \quad (17)$$

and

$$dX = \left\{ x = (x_k) \in w : \left(\left(\frac{1}{k+1} \right) x_k \right) \in X \right\} = X_{\left(\frac{1}{k+1}\right)I}. \quad (18)$$

Here, if we take $k = 0$ we obtain $\int X = X$ and $dX = X$.

Now, we establish the new sequence spaces by combining the binomial matrix and the integrated and differentiated sequence spaces as follows;

$$\int b_p^{r,s} = (b_p^{r,s})_{(k+1)I} = \left\{ \sum_n \left| \frac{1}{(s+r)^n} \sum_{k=0}^n \binom{n}{k} s^{n-k} r^k \cdot (k+1)x_k \right|^p < \infty \right\} = [(\ell_p)_{B^{r,s}}]_{(k+1)I} \quad (19)$$

and

$$db_p^{r,s} = (b_p^{r,s})_{\left(\frac{1}{k+1}\right)I} = \left\{ \sum_n \left| \frac{1}{(s+r)^n} \sum_{k=0}^n \binom{n}{k} s^{n-k} r^k \left(\frac{1}{k+1} \right) x_k \right|^p < \infty \right\} = [(\ell_p)_{B^{r,s}}]_{\left(\frac{1}{k+1}\right)I}. \quad (20)$$

Furthermore, by constructing the matrix $T^{r,s} = (t_{nk}^{r,s}) = B^{r,s}(k+1)I$ so that;

$$t_{nk}^{r,s} = \begin{cases} \frac{1}{(s+r)^n} \binom{n}{k} s^{n-k} r^k (k+1); & 0 \leq k \leq n \\ 0 & ; k > n \end{cases}$$

for all $n, k \in \mathbb{N}$. New integrated sequence spaces can be redefined by matrix $T^{r,s} = (t_{nk}^{r,s}) = B^{r,s}(k+1)I$ as follows;

$$\int b_p^{r,s} = (\ell_p)_{T^{r,s}}. \tag{21}$$

So, for given $x = (x_k) \in w$, the $T^{r,s}$ -transform of x is defined as follows,

$$y_k = (T^{r,s}x)_k = \frac{1}{(s+r)^k} \sum_{i=0}^k \binom{k}{i} s^{k-i} r^i (i+1)x_i \tag{22}$$

for all $k \in \mathbb{N}$.

Similarly, by constructing a matrix $U^{r,s} = (u_{nk}^{r,s}) = B^{r,s} \left(\frac{1}{k+1}\right) I$ so that;

$$u_{nk}^{r,s} = \begin{cases} \frac{1}{(s+r)^n} \binom{n}{k} s^{n-k} r^k \left(\frac{1}{k+1}\right); & 0 \leq k \leq n \\ 0 & ; k > n \end{cases}$$

for all $k \in \mathbb{N}$. The new differentiated sequence spaces can be redefined by the matrix $U^{r,s} = (u_{nk}^{r,s})$ as follows;

$$db_p^{r,s} = (\ell_p)_{U^{r,s}}. \tag{23}$$

Thus, for given $x = (x_k) \in w$, the $U^{r,s}$ -transform of x is defined as follows;

$$y_k = (U^{r,s}x)_k = \frac{1}{(s+r)^k} \sum_{i=0}^k \binom{k}{i} s^{k-i} r^i \left(\frac{1}{i+1}\right) x_i \tag{24}$$

for all $k \in \mathbb{N}$.

Theorem 2.1. The sequence space $\int b_p^{r,s}$ with its norm defined as follows;

$$\|x\|_{\int b_p^{r,s}} = \|T^{r,s}x\|_p = \left(\sum_{k=0}^{\infty} |(T^{r,s}x)_k|^p \right)^{\frac{1}{p}} \tag{25}$$

is a BK - space.

Proof: $T^{r,s} = (t_{nk}^{r,s})$ is a triangular matrix and the equation (21) holds. Additionally, since the space ℓ_p with p -norm is a BK -space, according to Theorem 4.3.12 of Wilansky [2], we conclude

that the sequence space $\int b_p^{r,s}$ is also a BK -space. Thus, the proof is complete.

Theorem 2.2. The sequence space $db_p^{r,s}$ with its norm defined as follows;

$$\|x\|_{db_p^{r,s}} = \|U^{r,s}x\|_p = \left(\sum_{k=0}^{\infty} |(U^{r,s}x)_k|^p \right)^{\frac{1}{p}} \tag{26}$$

is a BK - space.

Proof: $T^{r,s} = (t_{nk}^{r,s})$ is a triangular matrix and the equation (23) holds. Therefore, the proof can be demonstrated in a similar way as shown in Theorem 2.1.

Theorem 2.3. The sequence space $\int b_p^{r,s}$ is linearly isomorphic to the sequence space ℓ_p .

Proof: Let F be a transformation defined as $F: \int b_p^{r,s} \rightarrow \ell_p, F(x) = T^{r,s}x$. It is obvious that F is linear. Also, it is clear that $x = \theta$ whenever $T^{r,s}x = \theta$. Consequently, F is injective.

Now, let us consider a sequence $y = (y_n) \in \ell_p$. We define a sequence $x = (x_n)$ for the given sequence $y = (y_n)$ such that,

$$x_n = r^{-n} \frac{1}{n+1} \sum_{k=0}^n \binom{n}{k} (-s)^{n-k} (r+s)^k y_k \tag{27}$$

for all $n \in \mathbb{N}$.

$$\begin{aligned} \left(((k+1)I)x \right)_k &= (k+1)x_k \\ &= r^{-k} \sum_{l=0}^k \binom{k}{l} (-s)^{k-l} (r+s)^l y_l. \end{aligned} \tag{28}$$

Then, we have

$$\|x\|_{\int b_p^{r,s}} = \|T^{r,s}x\|_{\ell_p} = \left(\sum_{n=0}^{\infty} |(T^{r,s}x)_n|^p \right)^{\frac{1}{p}}$$

$$\begin{aligned}
 &= \left(\sum_{n=0}^{\infty} \left| \frac{1}{(s+r)^n} \sum_{k=0}^n \binom{n}{k} s^{n-k} r^k (k+1) x_k \right|^p \right)^{\frac{1}{p}} \\
 &= \left(\sum_{n=0}^{\infty} \left| \frac{1}{(s+r)^n} \sum_{k=0}^n \binom{n}{k} s^{n-k} \sum_{l=0}^k \binom{k}{l} (-s)^{k-l} (r+s)^l y_l \right|^p \right)^{\frac{1}{p}} \\
 &= \left(\sum_{n=0}^{\infty} |y_n|^p \right)^{\frac{1}{p}} \\
 &= \|y\|_{\ell_p} \\
 &= \|F(x)\|_{\ell_p} \\
 &< \infty.
 \end{aligned} \tag{29}$$

Hence, F is norm preserving from (25) and surjective. As a result, F is an isomorphism and the proof is complete.

Theorem 2.4. The sequence space $db_p^{r,s}$ is linearly isomorphic to the sequence space ℓ_p .

Proof: Let F be a transformation defined as $F: db_p^{r,s} \rightarrow \ell_p$, $F(x) = U^{r,s}x$. Now, let us consider the sequence $x = (x_n)$ as follows;

$$x_n = r^{-n} (n+1) \sum_{k=0}^n \binom{n}{k} (-s)^{n-k} (r+s)^k y_k \tag{30}$$

for all $n \in \mathbb{N}$.

Thus, the proof is completed using the method employed in Theorem 2.3.

Theorem 2.5. The sequence space $\int b_p^{r,s}$ is not a Hilbert space under the condition $p \neq 2$.

Proof: Let us assume that $p = 2$. We know from Theorem 2.1. that the sequence space $\int b_2^{r,s}$ is a BK-space with respect to the norm defined by

$$\begin{aligned}
 \|x\|_{\int b_2^{r,s}} &= \|T^{r,s}x\|_2 \\
 &= \left(\sum_{k=0}^{\infty} |(T^{r,s}x)_k|^2 \right)^{\frac{1}{2}}.
 \end{aligned} \tag{31}$$

Therefore, this norm can be constituted in terms of the inner product as follows;

$$\|x\|_{\int b_2^{r,s}} = \langle T^{r,s}x, T^{r,s}x \rangle^{\frac{1}{2}}. \tag{32}$$

So, $\int b_2^{r,s}$ is a Hilbert space.

Conversely, let us take $p \in [1, \infty) \setminus \{2\}$. We define two sequences $y = (y_k)$ and $z = (z_k)$ as follows;

$$y_k = \left(\frac{1}{k+1} \right) \left(-\frac{s}{r} \right)^k \left(\frac{s-k(r+s)}{s} \right) \tag{33}$$

and

$$z_k = \left(\frac{1}{k+1} \right) \left(-\frac{s}{r} \right)^k \left(\frac{s+k(r+s)}{s} \right) \tag{34}$$

for all $k \in \mathbb{N}$. Then we obtain,

$$\begin{aligned}
 \|y+z\|_{\int b_p^{r,s}}^2 + \|y-z\|_{\int b_p^{r,s}}^2 &= 8 \neq 2^{p+2} \\
 &= 2 \left(\|y\|_{\int b_p^{r,s}}^2 + \|z\|_{\int b_p^{r,s}}^2 \right).
 \end{aligned} \tag{35}$$

So, the parallelogram equality is not satisfied by the norm defined in (25). As a result, if $p \neq 2$ then this norm cannot be generated by an inner product. Therefore the sequence space $\int b_p^{r,s}$ cannot be a Hilbert space. Thus, the proof is complete.

Theorem 2.6. The sequence space $db_p^{r,s}$ is not a Hilbert space under the condition $p \neq 2$.

Proof: Let us assume that $p = 2$. In this part of the proof, we utilize the norm defined Theorem 2.2. Thus, as in the previous theorem, it is shown that the sequence $db_2^{r,s}$ is a Hilbert space.

Conversely, let us take $p \in [1, \infty) \setminus \{2\}$. We define two sequence spaces $u = (u_k)$ and $v = (v_k)$ as follows;

$$u_k = (k+1) \left(-\frac{s}{r} \right)^k \left(\frac{s-k(r+s)}{s} \right) \tag{36}$$

and

$$v_k = (k + 1) \left(-\frac{s}{r}\right)^k \left(\frac{s + k(r + s)}{s}\right) \quad (37)$$

for all $k \in \mathbb{N}$. Thus, by obtaining the same results as in Theorem 2.5. Thus, the proof is complete.

Theorem 2.7. The inclusion $\int \ell_p \subset \int b_p^{r,s}$ strictly holds.

Proof: Let us consider an arbitrary sequence $x = (x_k) \in \int \ell_p$, for $1 < p < \infty$. From the definition of the sequence space $\int \ell_p$, we obtain $\sum_k |(k + 1)x_k|^p < \infty$. Therefore, by applying Hölder's inequality we can write;

$$\begin{aligned} |(T^{r,s}x)_k|^p &= \left| \frac{1}{(s+r)^k} \sum_{j=0}^k \binom{k}{j} s^{k-j} r^j (j+1)x_j \right|^p \\ &\leq \left(\frac{1}{|s+r|^k} \right)^p \left[\left(\sum_{j=0}^k \binom{k}{j} |s|^{k-j} |r|^j \right)^{p-1} \cdot \left(\sum_{j=0}^k \binom{k}{j} |s|^{k-j} |r|^j |(j+1)x_j|^p \right) \right] \\ &= \left(\frac{1}{|s+r|^k} \right)^p ((|s| + |r|)^k)^{p-1} \\ &\cdot \sum_{j=0}^k \binom{k}{j} |s|^{k-j} |r|^j |(j+1)x_j|^p \\ &= \sum_{j=0}^k \binom{k}{j} \left| \frac{s}{s+r} \right|^k \left| \frac{r}{s} \right|^j |(j+1)x_j|^p. \end{aligned}$$

Then we obtain;

$$\begin{aligned} \sum_k |(T^{r,s}x)_k|^p &\leq \sum_k \sum_{j=0}^k \binom{k}{j} \left| \frac{s}{s+r} \right|^k \left| \frac{r}{s} \right|^j |(j+1)x_j|^p \\ &= \sum_j |(j+1)x_j|^p \sum_{k=j}^{\infty} \binom{k}{j} \left| \frac{s}{s+r} \right|^k \left| \frac{r}{s} \right|^j \\ &= \left| \frac{s}{s+r} \right| \sum_j |(j+1)x_j|^p. \quad (38) \end{aligned}$$

If we consider the comparison test together with the result we have obtained, we conclude that; $T^{r,s}x \in \ell_p$. So, $x = (x_k) \in \int b_p^{r,s}$. Hence, $\int \ell_p \subset \int b_p^{r,s}$.

Now, we define a sequence $y = (y_k)$ as follows,

$$y_k = \left(-\frac{1}{k+1}\right)^k$$

for all $k \in \mathbb{N}$. From here, it is observed that $(k + 1)y = ((-1)^k) \notin \ell_p$ and $T^{r,s}y = \left(\left(\frac{s-r}{s+r}\right)^k\right) \in \ell_p$. So, $y = (y_k) \notin \int \ell_p$ and $y = (y_k) \in \int b_p^{r,s}$. Hence, $\int \ell_p \subset \int b_p^{r,s}$ is strict. Similarly, the case of $p = 1$ can be proven in a similar way. Thus, the proof is complete.

Theorem 2.8. The inclusion $d\ell_p \subset db_p^{r,s}$ strictly holds.

Proof: The proof of this theorem follows a similar method to the one used in the previous theorem. Where, using $U^{r,s}$ instead of $T^{r,s}$.

3. α, β and γ – Duals of the Spaces $\int b_p^{r,s}$ and $db_p^{r,s}$

In this part, we determine α, β and γ – duals of the differentiated and integrated sequence spaces $\int b_p^{r,s}$ and $db_p^{r,s}$. Given two sequence spaces X and Y , the multiplier space $M(X, Y)$ is defined as follows;

$$X^\alpha = M(X, \ell_1),$$

$$X^\beta = M(X, cs)$$

and

$$X^\gamma = M(X, bs).$$

Lemma 3.1. [11] Let $A = (a_{nk})$ be an infinite matrix; the following conditions hold.

i) $A = (a_{nk}) \in (\ell_1: \ell_1)$ if and only if $\sup_{k \in \mathbb{N}} \sum_n |a_{nk}| < \infty$, (39)

ii) $A = (a_{nk}) \in (\ell_1: \ell_\infty)$ if and only if $\sup_{n, k \in \mathbb{N}} |a_{nk}| < \infty$, (40)

iii) $A = (a_{nk}) \in (\ell_1: c)$ if and only if (40) holds and $\lim_{n \rightarrow \infty} a_{nk} = a_k$ for all $k \in \mathbb{N}$. (41)

Lemma 3.2. [11] Let $A = (a_{nk})$ be an infinite matrix; the following conditions hold.

i) $A = (a_{nk}) \in (\ell_p; \ell_1)$ if and only if $\sup_{K \in \mathcal{F}} \sum_k |\sum_{n \in K} a_{nk}|^q < \infty$, (42)

ii) $A = (a_{nk}) \in (\ell_p; \ell_\infty)$ if and only if $\sup_{n \in \mathbb{N}} \sum_k |a_{nk}|^p < \infty$, (43)

iii) $A = (a_{nk}) \in (\ell_p; c)$ if and only if (41) and (43) hold.

Where $1 < p < \infty$, $\frac{1}{p} + \frac{1}{q} = 1$ and \mathcal{F} is the collection of all finite subsets of \mathbb{N} .

Theorem 3.3. i) The α -dual of the integrated sequence space $\int b_p^{r,s}$ is the set,

$$\xi_1^{r,s} = \left\{ \begin{array}{l} a = (a_k) \in w: \\ \sup_{K \in \mathcal{F}} \sum_k \left| \sum_{n \in K} \frac{1}{r^n} \binom{n}{k} (-s)^{n-k} (r+s)^k a_n \right|^q < \infty \end{array} \right\} \quad (44)$$

and the α -dual of the integrated sequence space $\int b_1^{r,s}$ is the set,

$$\xi_2^{r,s} = \left\{ \begin{array}{l} a = (a_k) \in w: \\ \sup_{k \in \mathbb{N}} \sum_n \left| \frac{1}{r^n} \binom{n}{k} (-s)^{n-k} (r+s)^k a_n \right| < \infty \end{array} \right\}. \quad (45)$$

ii) The α -dual of the differentiated sequence space $db_p^{r,s}$ is the set,

$$\xi_3^{r,s} = \left\{ \begin{array}{l} a = (a_k) \in w: \\ \sup_{K \in \mathcal{F}} \sum_k \left| \sum_{n \in K} \frac{1}{r^n} \binom{n}{k} (-s)^{n-k} (r+s)^k a_n \right|^q < \infty \end{array} \right\} \quad (46)$$

and the α -dual of the differentiated sequence space $db_1^{r,s}$ is the set,

$$\xi_4^{r,s} = \left\{ \begin{array}{l} a = (a_k) \in w: \\ \sup_{k \in \mathbb{N}} \sum_n \left| \frac{1}{r^n} \binom{n}{k} (-s)^{n-k} (r+s)^k a_n \right| < \infty \end{array} \right\}. \quad (47)$$

Proof: i) Consider a sequence $x = (x_n)$ defined as,

$$x_n = \sum_{k=0}^n \left[\frac{1}{n+1} \frac{1}{r^n} \binom{n}{k} (-s)^{n-k} (r+s)^k \right] y_k \quad (48)$$

for all $n \in \mathbb{N}$. From this, we conclude that for a sequence $a = (a_n)$, we write;

$$\begin{aligned} a_n x_n &= \sum_{k=0}^n \left[\frac{1}{n+1} \frac{1}{r^n} \binom{n}{k} (-s)^{n-k} (r+s)^k a_n \right] y_k \\ &= \sum_{k=0}^n z_{nk}^{r,s} y_k \\ &= (Z^{r,s} y)_n \end{aligned}$$

for all $n \in \mathbb{N}$.

By taking into account the equality above, we observe that $ax = (a_n x_n) \in \ell_1$ whenever $x = (x_k) \in \int b_1^{r,s}$ or $x = (x_k) \in \int b_p^{r,s}$ if and only if $Z^{r,s} y \in \ell_1$ whenever $y = (y_k) \in \ell_1$ or $y = (y_k) \in \ell_p$, respectively. Where $1 < p < \infty$. So, we that $a = (a_n) \in \{\int b_1^{r,s}\}^\alpha$ or $a = (a_n) \in \{\int b_p^{r,s}\}^\alpha$ if and only if $Z^{r,s} \in (\ell_1; \ell_1)$ or $Z^{r,s} \in (\ell_p; \ell_1)$ respectively, where $1 < p < \infty$. By connecting these results, Lemma 3.1 (i) and Lemma 3.2 (i), we deduce that;

$$\begin{aligned} a = (a_n) \in \left\{ \int b_1^{r,s} \right\}^\alpha &\Leftrightarrow \\ \sup_{k \in \mathbb{N}} \sum_n \left| \frac{1}{r^n} \binom{n}{k} (-s)^{n-k} (r+s)^k \frac{1}{n+1} a_n \right| &< \infty \end{aligned} \quad (49)$$

and

$$\begin{aligned} a = (a_n) \in \left\{ \int b_p^{r,s} \right\}^\alpha &\Leftrightarrow \\ \sup_{K \in \mathcal{F}} \sum_k \left| \sum_{n \in K} \frac{1}{r^n} \binom{n}{k} (-s)^{n-k} (r+s)^k \frac{1}{n+1} a_n \right|^q &< \infty, \end{aligned} \quad (50)$$

where $1 < p < \infty$. These yield us that $\{f b_1^{r,s}\}^\alpha = \xi_2^{r,s}$ and $\{f b_p^{r,s}\}^\alpha = \xi_1^{r,s}$ Where $1 < p < \infty$. Thus, the proof is complete.

ii) The sequence $x = (x_n)$ is defined as;

$$x_n = \sum_{k=0}^n \left[(n+1) \frac{1}{r^n} \binom{n}{k} (-s)^{n-k} (r+s)^k \right] y_k \tag{51}$$

for all $n \in \mathbb{N}$. The proof is carried out in a similar method in part (i).

Theorem 3.4. i) Consider the sets $\xi_5^{r,s}$, $\xi_6^{r,s}$ and $\xi_7^{r,s}$ defined by

$$\xi_5^{r,s} = \left\{ \begin{array}{l} a = (a_k) \in w: \\ \sum_{j=k}^{\infty} \frac{1}{r^j} \binom{j}{k} (-s)^{j-k} (r+s)^k \left(\frac{1}{j+1} \right) a_j \\ \text{exists } \forall k \in \mathbb{N} \end{array} \right\}, \tag{52}$$

$$\xi_6^{r,s} = \left\{ \begin{array}{l} a = (a_k) \in w: \\ \sup_{k,n \in \mathbb{N}} \left| \sum_{j=k}^n \frac{1}{r^j} \binom{j}{k} (-s)^{j-k} \left(\frac{1}{j+1} \right) a_j \right| < \infty \end{array} \right\} \tag{53}$$

and

$$\xi_7^{r,s} = \left\{ \begin{array}{l} a = (a_k) \in w: \\ \sup_{n \in \mathbb{N}} \sum_{k=0}^n \left| \sum_{j=k}^n \frac{1}{r^j} \binom{j}{k} (-s)^{j-k} \left(\frac{1}{j+1} \right) a_j \right|^q < \infty \end{array} \right\}, \tag{54}$$

where $1 < q < \infty$. Then the following statements hold;

- I. $\{f b_1^{r,s}\}^\beta = \xi_5^{r,s} \cap \xi_6^{r,s}$,
- II. $\{f b_p^{r,s}\}^\beta = \xi_5^{r,s} \cap \xi_7^{r,s}$, $(1 < p < \infty)$
- III. $\{f b_1^{r,s}\}^\gamma = \xi_6^{r,s}$,
- IV. $\{f b_p^{r,s}\}^\gamma = \xi_7^{r,s}$. $(1 < p < \infty)$

ii) Consider the sets $\xi_8^{r,s}$, $\xi_9^{r,s}$ and $\xi_{10}^{r,s}$ defined by;

$$\xi_8^{r,s} = \left\{ \begin{array}{l} a = (a_k) \in w: \\ \sum_{j=k}^{\infty} \frac{1}{r^j} \binom{j}{k} (-s)^{j-k} (r+s)^k (j+1) a_j \\ \text{exists } \forall k \in \mathbb{N} \end{array} \right\}, \tag{55}$$

$$\xi_9^{r,s} = \left\{ \begin{array}{l} a = (a_k) \in w: \\ \sup_{k,n \in \mathbb{N}} \left| \sum_{j=k}^n \frac{1}{r^j} \binom{j}{k} (-s)^{j-k} (r+s)^k (j+1) a_j \right| < \infty \end{array} \right\} \tag{56}$$

and

$$\xi_{10}^{r,s} = \left\{ \begin{array}{l} a = (a_k) \in w: \\ \sup_{n \in \mathbb{N}} \sum_{k=0}^n \left| \sum_{j=k}^n \frac{1}{r^j} \binom{j}{k} (-s)^{j-k} (r+s)^k (j+1) a_j \right|^q < \infty \end{array} \right\}, \tag{57}$$

where $1 < q < \infty$. Then the following statements hold;

- I. $\{db_1^{r,s}\}^\beta = \xi_8^{r,s} \cap \xi_9^{r,s}$,
- II. $\{db_p^{r,s}\}^\beta = \xi_8^{r,s} \cap \xi_{10}^{r,s}$, $(1 < p < \infty)$
- III. $\{db_1^{r,s}\}^\gamma = \xi_9^{r,s}$,
- IV. $\{db_p^{r,s}\}^\gamma = \xi_{10}^{r,s}$. $(1 < p < \infty)$

Proof: Since the other parts of the proof can be done similarly, we provide the proof only for case (I) of part (i). Let us consider the sequence $x = (x_n)$ defined in (48) for an arbitrary $a = (a_n) \in w$. Then,

$$\begin{aligned} \sum_{k=0}^n a_k x_k &= \sum_{k=0}^n \left[\sum_{j=0}^k \frac{1}{r^k} \binom{k}{j} (-s)^{k-j} (r+s)^j \left(\frac{1}{k+1} \right) y_j \right] a_k \\ &= \sum_{k=0}^n \left[\sum_{j=k}^n \frac{1}{r^j} \binom{j}{k} (-s)^{j-k} (r+s)^k \left(\frac{1}{j+1} \right) a_j \right] y_k \\ &= (F^{r,s} y)_n \end{aligned} \tag{58}$$

for all $n \in \mathbb{N}$. Where the matrix $F^{r,s} = (f_{nk}^{r,s})$ is defined by,

$$f_{nk}^{r,s} = \begin{cases} \sum_{j=k}^n \frac{1}{r^j} \binom{j}{k} (-s)^{j-k} (r+s)^k \left(\frac{1}{j+1}\right) a_j, & 0 \leq k \leq n \\ 0, & k > n \end{cases} \quad (59)$$

for all $n, k \in \mathbb{N}$. So, $ax = (a_n x_n) \in cs$ whenever $x = (x_k) \in \int b_1^{r,s}$ if and only if $F^{r,s}y \in c$ whenever $y = (y_k) \in \ell_1$. This outcome makes clear that $a = (a_n) \in \{\int b_1^{r,s}\}^\beta$ if and only if $F^{r,s} \in (\ell_1 : c)$. By combining this result and Lemma 3.1. (iii), we obtain that $a = (a_n) \in \{\int b_1^{r,s}\}^\beta$ if and only if

$$\sup_{k,n \in \mathbb{N}} \left| \sum_{j=k}^n \frac{1}{r^j} \binom{j}{k} (-s)^{j-k} (r+s)^k \left(\frac{1}{j+1}\right) a_j \right| < \infty$$

and

$$\sum_{j=k}^{\infty} \frac{1}{r^j} \binom{j}{k} (-s)^{j-k} (r+s)^k \left(\frac{1}{j+1}\right) a_j$$

exists for all $k \in \mathbb{N}$.

This result shows us that $\{\int b_1^{r,s}\}^\beta = \xi_5^{r,s} \cap \xi_6^{r,s}$. Thus, the proof is complete.

4. Some Matrix Classes

In this part, we identify certain matrix classes associated with the new sequence spaces.

Now let us prefer the following sequences that we use throughout this section.

$$\rho_{nk}^{r,s} = \sum_{j=k}^{\infty} \frac{1}{r^j} \binom{j}{k} (-s)^{j-k} (r+s)^k \left(\frac{1}{j+1}\right) a_{nj} \quad (60)$$

and

$$\eta_{nk}^{r,s} = \sum_{j=k}^{\infty} \frac{1}{r^j} \binom{j}{k} (-s)^{j-k} (r+s)^k (j+1) a_{nj} \quad (61)$$

for all $n, k \in \mathbb{N}$.

Theorem 4.1. Given an infinite matrix $A = (a_{nk})$, the following statements hold.

i) $A = (a_{nk}) \in (\int b_1^{r,s} : \ell_\infty)$
if and only if $\sup_{k,n} |\rho_{nk}^{r,s}| < \infty$, (62)

ii) $A = (a_{nk}) \in (\int b_p^{r,s} : \ell_\infty)$
if and only if $\sup_{n \in \mathbb{N}} \sum_k |\rho_{nk}^{r,s}|^q < \infty$, (63)

$\{a_{nk}\}_{k \in \mathbb{N}} \in \xi_7^{r,s} \quad (1 < p < \infty)$, (64)

iii) $A = (a_{nk}) \in (db_1^{r,s} : \ell_\infty)$
if and only if $\sup_{k,n} |\eta_{nk}^{r,s}| < \infty$, (65)

iv) $A = (a_{nk}) \in (db_p^{r,s} : \ell_\infty)$
if and only if $\sup_{n \in \mathbb{N}} \sum_k |\eta_{nk}^{r,s}|^q < \infty$, (66)

$\{a_{nk}\}_{k \in \mathbb{N}} \in \xi_{10}^{r,s} \quad (1 < p < \infty)$. (67)

Proof: Since the others can be done in a similar method, we only provide the proof for (iv).

Let $1 < p < \infty$. Let us consider an arbitrary sequence $x = (x_k) \in db_p^{r,s}$ that satisfies the conditions (66) and (67). Thus, it is obtained that $\{a_{nk}\}_{k \in \mathbb{N}} \in \{db_p^{r,s}\}^\beta$. This result indicates the existence of the A -transform of x . From the relation (48), we have

$$\begin{aligned} \sum_{k=0}^m a_{nk} x_k &= \sum_{k=0}^m \left[\sum_{j=0}^k \frac{1}{r^k} \binom{k}{j} (-s)^{k-j} (r+s)^j (k+1) y_j \right] a_{nk} \\ &= \sum_{k=0}^m \left[\sum_{j=k}^m \frac{1}{r^j} \binom{j}{k} (-s)^{j-k} (r+s)^k (j+1) \right] a_{nj} y_k. \end{aligned} \quad (68)$$

By taking limit (68) side by side as $m \rightarrow \infty$, we obtain that

$$\sum_k a_{nk} x_k = \sum_k \eta_{nk}^{r,s} y_k, \quad n \in \mathbb{N}. \quad (69)$$

Then, we derive by taking ℓ_∞ -norm (69) side by side and any by applying Hölder's inequality that,

$$\|Ax\|_\infty = \sup_{n \in \mathbb{N}} \left| \sum_k \eta_{nk}^{r,s} y_k \right|$$

$$\leq \sup_{n \in \mathbb{N}} \left(\sum_k |\eta_{nk}^{r,s}|^q \right)^{\frac{1}{q}} \left(\sum_k |y_k|^p \right)^{\frac{1}{p}} < \infty. \quad (70)$$

Consequently, we conclude that $Ax \in \ell_\infty$. So, $A = (a_{nk}) \in (db_p^{r,s} : \ell_\infty)$.

Conversely, assume that $A = (a_{nk}) \in (db_p^{r,s} : \ell_\infty)$. This gives us to $\{a_{nk}\}_{k \in \mathbb{N}} \in \{db_p^{r,s}\}^\beta$ for all $n \in \mathbb{N}$. Then, it is evident that the condition (67) is necessary and that the $\{\eta_{nk}^{r,s}\}_{k,n \in \mathbb{N}}$ exists. Because of $\{a_{nk}\}_{k \in \mathbb{N}} \in \{db_p^{r,s}\}^\beta$, we can see that the condition (69) holds and the sequences $a_n = (a_{nk})_{k \in \mathbb{N}}$ define the continuous linear functionals f_n on $db_p^{r,s}$ by

$$f_n(x) = \sum_k a_{nk} x_k \quad (71)$$

for all $n \in \mathbb{N}$. Additionally, we know from the Theorem 2.4 that the $db_p^{r,s}$ is norm isomorphic to ℓ_p . By connecting this result and the condition (69), we have

$$\|f_n\| = \left\| (\eta_{nk}^{r,s})_{k \in \mathbb{N}} \right\|_q, \quad (72)$$

which yield that the functionals f_n are pointwise bounded. Moreover, we derive from the Banach-Steinhaus Theorem that the functionals f_n are uniformly bounded. So there exists a constant $M > 0$ such that;

$$\left(\sum_k |\eta_{nk}^{r,s}|^q \right)^{\frac{1}{q}} = \|f_n\| \leq M \quad (73)$$

for all $n \in \mathbb{N}$, which shows us that the condition (66) holds. Thus, the proof is completed.

Lemma 4.1. [11] Let $B = (b_{nk})$ be an infinite matrix. Then, $B = (b_{nk}) \in (\ell_1 : \ell_p)$ if and only if

$$\sup_{k \in \mathbb{N}} \sum_n |b_{nk}^{r,s}|^p < \infty,$$

where $1 < p < \infty$.

Theorem 4.2. Let an infinite matrix $B = (b_{nk})$ be given. Then,

i) $B = (b_{nk}) \in (\int b_1^{r,s} : \ell_p)$ if and only if
$$\sup_{k \in \mathbb{N}} \sum_n |\rho_{nk}^{r,s}|^p < \infty, \quad (74)$$

ii) $B = (b_{nk}) \in (db_1^{r,s} : \ell_p)$ if and only if
$$\sup_{k \in \mathbb{N}} \sum_n |\eta_{nk}^{r,s}|^p < \infty. \quad (75)$$

Proof: Let a sequence $y = (y_k) \in \int b_1^{r,s}$ be given. Assume that the condition (75) holds. Then, it is clear that $z = (z_k) \in \ell_1$ and $\{b_{nk}\}_{k \in \mathbb{N}} \in \{\int b_1^{r,s}\}^\beta$ for all $n \in \mathbb{N}$. That means B -transform of x exists. As a result of this, the series $\sum_k \rho_{nk}^{r,s} z_k$ are absolutely convergent for all $n \in \mathbb{N}$ and $z = (z_k) \in \ell_1$. Now let us consider the following equality.

$$\sum_k b_{nk} y_k = \sum_k \rho_{nk}^{r,s} z_k, n \in \mathbb{N}. \quad (76)$$

If we apply the Minkowsky inequality to equation (76), we obtain

$$\left(\sum_n |(By)_n|^p \right)^{\frac{1}{p}} \leq \sum_k |z_k| \left(\sum_n |\rho_{nk}^{r,s}|^p \right)^{\frac{1}{p}}. \quad (77)$$

Thus, it follows that $By \in \ell_p$, namely $B = (b_{nk}) \in (\int b_1^{r,s} : \ell_p)$.

Conversely, we suppose that $B = (b_{nk}) \in (\int b_1^{r,s} : \ell_p)$. Namely, $By \in \ell_p$ for all $y = (y_k) \in \int b_1^{r,s}$. So, $\{b_{nk}\}_{k \in \mathbb{N}} \in \{\int b_1^{r,s}\}^\beta$ for all $n \in \mathbb{N}$, which shows us that the relation (76) holds. These results give us that $(\rho_{nk}^{r,s}) \in (\ell_1 : \ell_p)$. By combining last result and Lemma 4.1, we obtain that the condition (74) holds.

The part (ii) can be proved by using a similar method. Thus, the proof is complete.

5. Conclusion

$T^{r,s} = (t_{nk}^{r,s})$ represents the composition of the binomial matrix and the integrated sequence space and $U^{r,s} = (u_{nk}^{r,s})$ represents the composition of the binomial matrix and the differentiated sequence space. Since $T^{r,s} = (t_{nk}^{r,s})$ and $U^{r,s} = (u_{nk}^{r,s})$ is more comprehensive

than integrated and differentiated sequence spaces, respectively, our conclusions are more general.

Article Information Form

Funding

The author (s) has no received any financial support for the research, authorship or publication of this study

The Declaration of Conflict of Interest/ Common Interest

No conflict of interest or common interest has been declared by the authors.

The Declaration of Ethics Committee Approval

This study does not require ethics committee permission or any special permission.

The Declaration of Research and Publication Ethics

The authors of the paper declare that they comply with the scientific, ethical and quotation rules of SAUJS in all processes of the paper and that they do not make any falsification on the data collected. In addition, they declare that Sakarya University Journal of Science and its editorial board have no responsibility for any ethical violations that may be encountered, and that this study has not been evaluated in any academic publication environment other than Sakarya University Journal of Science.

Copyright Statement

Authors own the copyright of their work published in the journal and their work is published under the CC BY-NC 4.0 license.

References

- [1] B. Choudhary, S. Nanda, Functional Analysis with Applications. New Delhi: Wiley, 1989.
- [2] A. Wilansky, Summability Through Functional Analysis. Amsterdam: North-Holland mathematics studies, 1984.
- [3] G. Goes, S. Goes, "Sequences of Bounded Variation and Sequences of Fourier Coefficients. I", Mathematische Zeitschrift, 118, pp. 93–102, 1970.
- [4] M. Kirişci, "Integrated and Differentiated Sequence Spaces", Journal Nonlinear Analysis and Application, 1, pp. 2-16, 2015.
- [5] M. Kirişci, "Reisz Type Integrated and Differentiated Sequence Spaces", Bulletin of Mathematical Analysis and Applications, 7, 2, pp. 14-27, 2015.
- [6] M. Kirişci, "Integrated and Differentiated Sequence Spaces and Weighted Mean", Journal of Advances in Mathematics and Computer Science, 29, 1, pp. 1-11, 2018.
- [7] M. C. Bisgin, "The Binomial Sequence Spaces of Nonabsolute Type", Journal Of Inequalities and Applications, 309, 2016.
- [8] M. C. Bisgin, "The Binomial Sequence Spaces Which Include the Spaces ℓ_p and ℓ_∞ and Geometric Properties", Journal of Inequalities and Applications, 304, 2016.
- [9] M. C. Bişgin, "A Note on the Sequence Space $b_p^{r,s}(G)$ ", Cumhuriyet Science Journal, vol. 38, 4, pp. 11-25, 2017.
- [10] A. Sönmez, "Some Notes on the New Sequence Space $b_p^{r,s}(D)$ ", Gazi University Journal of Science, vol. 33, 2, pp. 476-490, 2020.
- [11] M. Stieglitz, H. Tietz, "Matrixtransformationen von Folgenräumen Eine Ergebnisübersicht", Mathematische Zeitschrift. vol, 154, pp. 1–16, 1977.

Experimental and Theoretical Characterization, In Silico and In Vitro Studies of (E)-1-(5-Nitrothiophen-2-yl)-N-(2-(Trifluoromethyl)Phenyl)Methanimine

Seyhan Öztürk 

Ondokuz Mayıs University, Faculty of Science, Department of Chemistry, Samsun, Türkiye, sturna@omu.edu.tr

ARTICLE INFO

ABSTRACT

Keywords:
Schiff base
Crystal structure
Molecular docking
Hirshfeld surface analysis
Density Functional Theory

Article History:
Received: 14.08.204
Accepted: 01.09.2024
Online Available: 18.10.2024

The current research was conducted to assess the in silico and in vitro potential of the heterocyclic Schiff base compound (E)-1-(5-nitrothiophen-2-yl)-N-(2-(trifluoromethyl)phenyl)methanimine(N2TPM). This Schiff base was synthesized according to the reported method using ethanol as solvent, and the reaction was monitored on TLC till completion of the reaction. The compound structure was elucidated using spectroscopic techniques such as UV/Vis, FT-IR, ¹H-NMR, and ¹³C-NMR. Molecular structure was determined using a single XRD, which revealed that the compound was triclinic. Analysis of intermolecular interactions in crystalline compounds was performed using Hirshfeld surface analysis and 2D fingerprint plots. The structure of the compound was optimized using the B3LYP hybrid functional with the basis set 6-31G(d,p). The compound's theoretical and experimental parameters (bond length, bond angle, molecular orbital energies, electronic transitions, and vibration frequencies) were compared with each other which are in close agreement. R² values were found to be 0.9914 for bond lengths and 0.9859 for bond angles. In vitro, esterase potential of the synthesized compound was checked using a spectrophotometric model, while in silico molecular docking studies were performed with Auto-dock against two enzymes of the esterase family. The docking studies and in vitro assessment predicted that such molecules could be used as enzyme inhibitors against tested enzymes; acetylcholine esterase (AChE) and butyrylcholine esterase (BChE). the compound showed a binding score of -10.4159, a binding energy of -10.2743 with AChE, a binding score of -10.3378 and a binding energy of -9.8889 with BChE.

1. Introduction

Schiff bases are synthesized by reacting aldehydes/ketones and amines in a suitable medium. These compounds have exhibited numerous valuable pharmacological applications, such as the inhibition of acetylcholine and butyrylcholine esterase enzymes, which are responsible for Alzheimer's disease [1–3]. Schiff bases also behave as ligands, coordinating with metals through imine nitrogen [4]. They possess exceptional properties, including stability, selectivity, and sensitivity. Researchers are continually creating different Schiff bases with varied structural attributes for significant applications [5, 6]. Schiff bases find broad application across

various fields, biochemistry, separation processes, decarboxylation reactions, including catalysis, materials science, and enzymatic aldolization [7, 8].

Heterocyclic cores represent a major class of organic compounds characterized by the presence of at least one non-carbon atom (heteroatom) within the ring structure. These compounds acquire different properties due to their compressed structure, such as anti-corrosion, anti-oxidant, and anti-wear properties. Heterocyclic compounds play a fundamental role in the cells of living organisms, exhibiting vast dimensional applications in different fields, including veterinary products, pharmaceuticals, and agrochemicals [9, 10]. These compounds are

also utilized in various applications, including as dyes, antioxidants, sanitizers, copolymers developers, and corrosion inhibitors [11, 12].

Molecular docking has become an essential tool in drug discovery, allowing researchers to model the interactions between a small ligand molecule and a protein at the atomic level [13]. With this method, the optimal ligand orientation that binds most effectively to a particular protein is determined and information about the intermolecular structure of the complex formed between multiple molecules is obtained [14]. The binding site's knowledge enhances docking study efficiency [15].

In this study, we have synthesized Schiff base following our previous work [16], determined their structures with single-crystal X-ray diffraction, performed computational studies with Gaussian, and carried out biological potential assessments using an in-silico docking model.

2. General Methods

2.1. Chemicals and instruments

All chemicals used for synthesis and purification were obtained from Merck. UV-Vis absorption spectrum was measured from 200 to 900 nm in ethyl alcohol using a Thermo Evolution Array UV-Vis spectrophotometer. The IR spectra of the synthesized compounds were recorded with a Perkin Elmer Spectrum Two FT-IR spectrophotometer equipped with an ATR module, covering a range of 4000-400 cm^{-1} . NMR spectra were obtained in DMSO-d_6 with a Bruker Avance III 400 MHz NMR Spectrometer.

2.2. Synthesis of (E)-1-(5-nitrothiophen-2-yl)-N-(2-(trifluoromethyl)phenyl) methanimine (N2TPM)

The title compound was synthesized following a protocol previously established by our research group [1,16]. Schiff base formed by an equimolar reaction of 5-nitro-2-thiophenecarboxaldehyde and 2-(trifluoromethyl)aniline in ethanol, with the reaction mixture refluxed for 36 hours (Figure 1). The reaction was monitored by TLC. At the end of the reaction, a burgundy product

was obtained and filtered. Crystallization was carried out slowly in ethyl alcohol at room temperature.

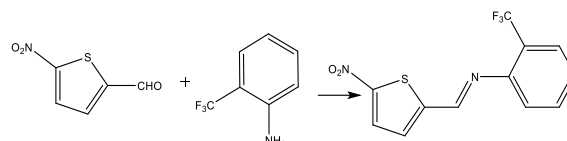


Figure 1. Synthesis scheme of N2TPM

2.3. Crystal structure analysis

Data were collected with the STOE IPDS 2 [17] diffractometer. The structure was determined using the SHELXT program [18] and the SHELXL program [19]. X-Area was used for unit cell optimization. Molecular geometry calculations were made with WinGX [20].

2.4. Computational studies

The geometric optimization, theoretical UV-Vis spectrum, theoretical infrared spectrum, molecular orbital energies, and electronic transitions for the compound were obtained by Gaussian 09 software [21, 22]. GaussSum 3.0 was also used for visualization [23, 24]. Harmonic vibration frequencies and wavenumbers for the optimized structure were calculated using a scale factor of 0.962 [25]. Additionally, the theoretical vibrational spectrum of the synthesized compound was analyzed using Potential Energy Distribution (PED) with the assistance of the VEDA 4 program [26]. Gaussian 09, B3LYP method, and 6-31G(d,p) set were used in DFT studies [27, 28]. Results from DFT studies, including natural bond orbitals (NBO), the density of states (DOS), frontier molecular orbitals (FMO), and global reactivity parameters were analyzed using GaussView 5.0. Input files for optimization are derived from the crystal structure to ensure the best possible alignment with the data [1, 29].

2.5. Hirshfeld surfaces analysis

A Hirshfeld surface represents the outer contour of the space occupied by a molecule or an atom within a crystalline environment. In this study, Hirshfeld surfaces and 2D fingerprint plots were generated using the Crystal Explorer 17.5

program, which incorporates the TONTO software [30]. The normalized contact distance d_{norm} , based on both the external distance d_e and internal distance d_i , was calculated using a standard equation [1, 31].

2.6. In silico and In vitro assessments toward Esterases

In vitro evaluation, a spectrophotometric method was used. Docking studies of the resulting compound were carried out using the free online docking program AutoDock [1, 32]. Acetylcholinesterase (AChE) and butyrylcholinesterase (BChE) crystal structures were used for docking simulations. The results were visualized graphically using Discovery Studio Visualize.

3. Results and Discussion

3.1. Spectroscopic studies

The compound was characterized using X-ray diffraction and spectroscopic techniques. The compound depicted 257 nm and 355 nm in UV-Vis spectroscopy (Figure 2). In UV-Vis spectroscopy, the band below 290 nm was assigned to the $\pi-\pi^*$ transition, while the band above 290 nm was attributed to the $n-\pi^*$ transitions [33].

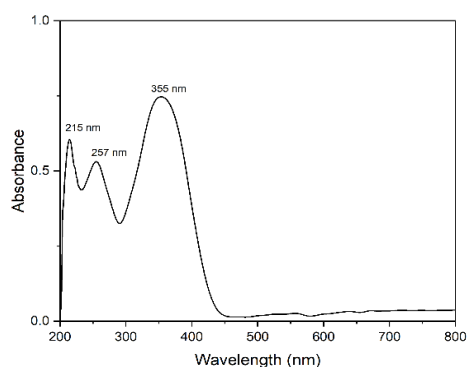


Figure 2. UV-Vis spectrum of N2TPM

Several informative bands appeared in the FT-IR spectrum in the $4000-650\text{ cm}^{-1}$ range. The absorption band observed between $1695-1595\text{ cm}^{-1}$ is characteristic of the C=N group in N2TPM [34, 35]. In FT-IR spectra of compound a strong bands appeared at 1578 cm^{-1} due to azomethine linkage. The appearance of these bands provided preliminary indications about the

targeted products. Additionally, it was observed that the presence of the fluorine (F) group in the compound caused the C=N group to shift to 1578 cm^{-1} . The C=C IR band at 1535 cm^{-1} is seen in Figure 3.

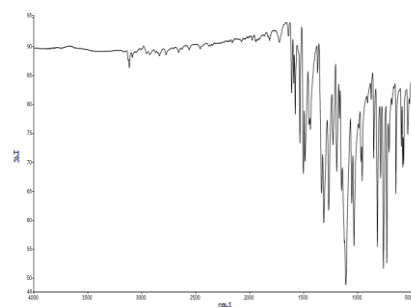


Figure 3. FT-IR spectrum of N2TPM

NMR spectra were recorded in DMSO- d_6 using a Bruker Avance III 400 MHz NMR Spectrometer. The disappearance of NH_2 and appearance of a new singlet peak in $^1\text{H-NMR}$ was assigned to HC=N at δ 8.89 which confirmed the synthesis of the targeted compound [36]. The doublet peaks at 8.20 and 7.80 correspond to protons in the thiophene ring in the compound. The signal for Ar-H was observed in the range δ 7.80-7.43 Figure 4. $^{13}\text{C-NMR}$ of the compound showed twelve signals from 158.14 to 14.63 ppm Fig. 5.

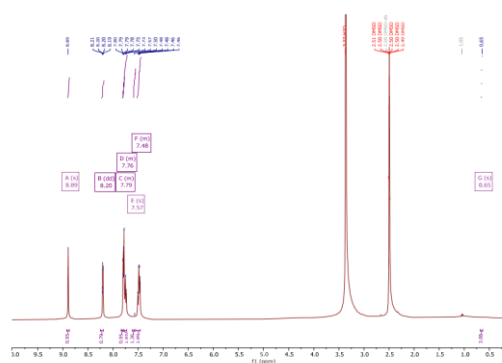


Figure 4. $^1\text{H-NMR}$ spectrum of N2TPM

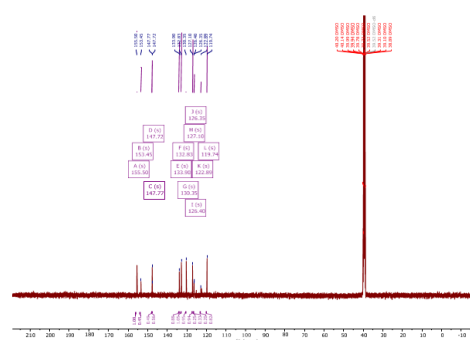


Figure 5. $^{13}\text{C-NMR}$ spectrum of N2TPM

Yield: 89%; m.p.: 161 °C; λ_{max} : 257 nm and 355 nm; IR: 3117 (C–H, arom.), 1578 (HC=N), 1575 (C–NO₂), 1535 (C=C), 1109 (C–O), 817 (C–S) cm⁻¹; ¹H-NMR (400 MHz, DMSO-d₆): δ 8.89 (s, 1H), 8.20 (dd, J = 4.0, 1.8 Hz, 1H), 7.82 – 7.77 (m, 1H), 7.80 – 7.71 (m, 2H), 7.53 – 7.43 (m, 2H); ¹³C NMR (100 MHz, DMSO-d₆): δ 155.50 (C2), 153.45 (C6), 147.77 (C5), 147.72 (C8), 133.90 (C10), 132.83 (C4), 130.35 (C3), 127.10 (C11), 126.40 (C9), 126.35 (C12), 122.89 (C13), 119.74 (C15).

3.2. XRD Analysis

The structure of the compound was further confirmed by single-crystal X-ray analysis. Table 1 summarizes the data. Figure 6 illustrates the asymmetric unit of the compound. The

compound contains two independent organic molecules and are not planar. The corresponding angles for C7–C12 and C20–C25 fluorobenzene rings are 37.22(12)° and 31.752(10)° in compound, respectively. The molecule is linked by C6–H6···O3 (–x+1, –y+1, –z+1), C19–H19···O1 (–x+1, –y+1, –z+2) and C11–H11···O4 (–x+1, –y+2, –z+1) hydrogen bonds (Figure 6 and Table 2). The C6–N1 and C19–N2 bond lengths are typical of double bonds. The N–O bond lengths [1.221(5), 1.210(5), and 1.212(5) Å] in the nitro group are close to the values observed for related compounds reported in the literature. In addition, C–F bond lengths [1.329–1.342 Å] in the trifluoromethyl group are similar to a work by Ilmi et al. [37]. Crystal packing of N2TPM is given in Figure 7.

Table 1. Crystal data and structure refinement of N2TPM

Crystal data	Compound
CCDC	2067648
Empirical formula	C ₁₂ H ₇ F ₃ N ₂ O ₂ S
Formula weight	300.263
Temperature/K	296
Crystal system	triclinic
Space group	P-1
a/Å	7.5965(5)
b/Å	11.0021(7)
c/Å	15.9138(10)
α /°	91.351(5)
β /°	94.741(5)
γ /°	105.750(5)
Volume/Å ³	1274.25(15)
Z	4
ρ_{calc} /g/cm ³	1.565
μ /mm ⁻¹	0.293
F(000)	608.9
Crystal size/mm ³	0.45 × 0.27 × 0.14
Radiation	Mo K α (λ = 0.71073)
2 θ range for data collection/°	3.86 to 52
Index ranges	-11 ≤ h ≤ 11, -16 ≤ k ≤ 16, -24 ≤ l ≤ 22
Reflections collected	26313
Independent reflections	5021 [R_{int} = 0.1075, R_{sigma} = 0.1192]
Data/restraints/parameters	5021/0/361
Goodness-of-fit on F ²	1.003
Final R indexes [$I \geq 2\sigma(I)$]	R_1 = 0.0769, wR_2 = 0.1799
Final R indexes [all data]	R_1 = 0.1249, wR_2 = 0.2057
Largest diff. peak/hole / e Å ⁻³	0.85/-0.59

Table 2. Hydrogen-bond geometries for N2TPM (Å, °)

D–H···A	D–H	H···A	D···A	D–H···A
C6–H6···O3i	0.93	2.53	3.313(6)	142
C19–H19···O1ii	0.93	2.43	3.277(5)	151
C11–H11···O4iii	0.93	2.53	3.2189(6)	131

Symmetry codes: (i) $-x+1, -y+1, -z+1$; (ii) $-x+1, -y+1, -z+2$; (iii) $-x+1, -y+2, -z+1$. (Cg2: C6–C11 ring center)

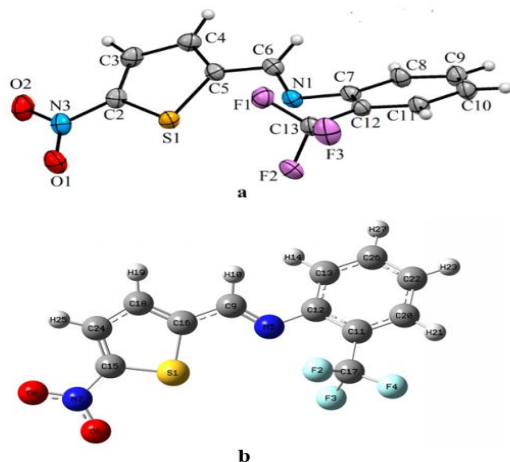


Figure 6. (a) Crystal unit; (b) Optimized structure of N2TPM (Atomic numbering used for PED analysis)

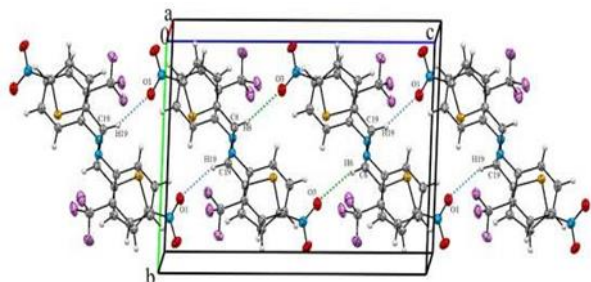


Figure 7. Crystal packing of N2TPM

3.3. Computational Studies

3.3.1. UV–Vis spectrum

Three absorption bands were observed in the experimental electronic spectrum of the compound in ethanol. The absorption observed at $\lambda = 214$ nm in the absorption spectrum corresponds to π - π^* electronic transitions resulting from the delocalization of electrons in aromatic thiophene and benzene rings.

The absorption at $\lambda = 256$ nm, visible as the second peak detected in the experimental spectrum, is attributed to the π - π^* transition in the benzene ring, thiophene, and azomethine ($-\text{HC}=\text{N}-$) moieties. The electronic transitions found in the calculated UV-Vis spectra between 272-339 nm are observed to occur through the

benzene ring towards the thiophene ring, whereas the transitions at higher wavelengths are monitored to occur through the imine group.

The peak observed as a broad band at $\lambda = 352$ nm is the characteristic n - π^* transition of the azomethine ($\text{C}=\text{N}$) group. This same transition was theoretically observed nearly at $\lambda = 426$ nm. It has been identified that the results of the experimental and theoretical studies are in good agreement with previous studies [38-42].

The calculated UV-Vis spectrum and the frontier molecular orbitals were examined utilizing Gauss-View and GaussSum and given with experimental spectrum in Figure 8. Table 3 lists the wavelengths of the experimental and calculated electronic transitions and the corresponding transitions, the energy of the transitions, the oscillator intensity, and the contribution of the orbitals to the electronic transitions.

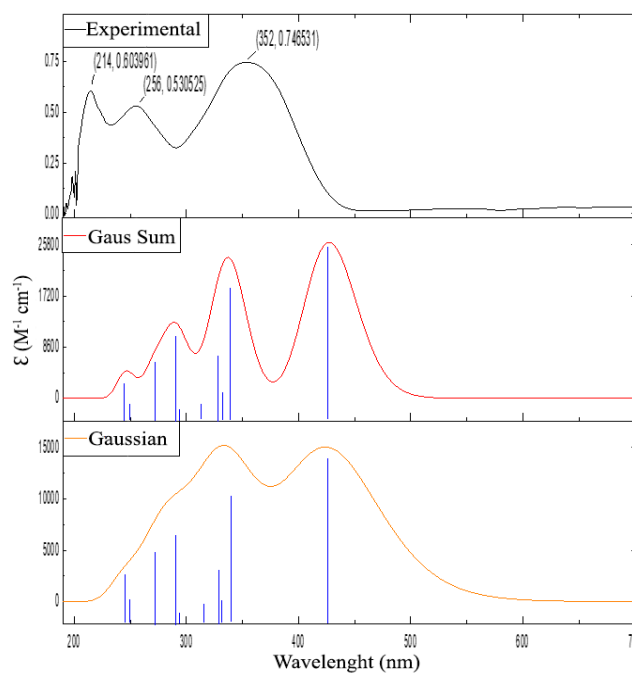


Figure 8. Experimental and calculated UV-Vis absorption spectra of N2TPM

Table 3. Assignments, energies, and wavelengths of the experimental and major theoretical transitions of N2TPM

λ exp (nm)	λ calc. (nm)	Assignment	Energy (eV)	Oscillator strengths	Major Contribution (%)
214	250.73	π - π^*	4.9449	0.0159	HOMO \rightarrow L+2 (45%) H-1 \rightarrow L+1 (33%) H-2 \rightarrow L+1 (14%)
	244.77	π - π^*	5.0654	0.0503	H-1 \rightarrow L+1 (41%) H-2 \rightarrow L+1 (37%)
	339.71	π - π^*	3.6497	0.2446	H-1 \rightarrow LUMO (75%) H-4 \rightarrow LUMO (12%)
256	331.08	π - π^*	3.7449	0.0228	H-5 \rightarrow LUMO (65%) H-4 \rightarrow LUMO (11%) H-1 \rightarrow LUMO (13%)
	328.91	π - π^*	3.7696	0.0718	H-2 \rightarrow LUMO (91%)
	314.91	π - π^*	3.9371	0.0184	H-3 \rightarrow LUMO (95%)
	293.57	π - π^*	4.2233	0.0048	H-6 \rightarrow LUMO (88%)
	290.63	π - π^*	4.2660	0.1517	HOMO \rightarrow L+1 (53%) H-4 \rightarrow LUMO (25%)
	272.04	π - π^*	4.5576	0.0843	H-4 \rightarrow LUMO (45%) H-5 \rightarrow LUMO (10%) HOMO \rightarrow L+1 (37%)
352	426.84	π - π^*	2.9047	0.3621	HOMO \rightarrow LUMO (94%)

3.3.2. Vibration spectral analysis

The experimental and theoretical FT-IR spectra of the compound are presented in Figure 9. In Table 4 the experimental and calculated values of the wave numbers of the vibrations in the molecule are provided along with the % PED values. The experimental aromatic C-H stretching vibrations of the thiophene and benzene rings in the structure of the compound were observed in the range of 3126 to 3046 cm^{-1} [43]. The theoretical wavelengths corresponding to these vibrations were calculated as 3140, 3110, 3102, 3090, 3082, and 3068 cm^{-1} , respectively.

The C-H stretching vibration of the imine group was found experimentally at 2927 cm^{-1} and was found to be in good agreement with the theoretical value of 2928 cm^{-1} . In previous studies, it has been reported that the stretching frequencies for C=C bonds in the aromatic ring are typically observed between 1625 and 1430 cm^{-1} [44, 45]. The experimental vibrations for C=C bonds were recorded at 1592, 1578, and 1488 cm^{-1} , while the theoretical vibrations were recorded at 1585, 1568, and 1472 cm^{-1} , respectively. Furthermore, the vibrational frequency of the C=C bond in the thiophene ring was determined experimentally at 1503 cm^{-1} and found computationally at 1523 cm^{-1} .

The calculated value for the azomethine $\nu(\text{C}=\text{N})$ vibration of the N2TPM is 1627 cm^{-1} , while the observed experimental value is 1592 cm^{-1} . The experimental observation determined the asymmetric vibration of the N-O bond at a frequency of 1535 cm^{-1} , which is different from the calculated value of 1564 cm^{-1} . Similarly, the symmetric stretching of $\nu(\text{N}-\text{O})$ was experimentally detected at 1334 cm^{-1} and is almost identical to the calculated value of 1335 cm^{-1} .

The symmetric vibration of the $\nu(\text{SC})$ bond was detected experimentally at 1149 cm^{-1} and theoretically at 1153 cm^{-1} . The bending vibrations of the C-S bond were found at 708 cm^{-1} in the experimental spectrum and 713 cm^{-1} in the calculation method.

The stretching vibrations of the symmetric and antisymmetric CF_3 groups typically occur between 1290-1235 cm^{-1} and 1226-1200 cm^{-1} , respectively [46]. For this compound, these stretching vibrations were observed experimentally between 1268-1149 cm^{-1} and theoretically between 1285-1153 cm^{-1} .

The correlation plots in Figure 10 obtained using the experimental and theoretical wavenumbers were analyzed and it was found that plot B had a

stronger R^2 value than plot A, indicating a better agreement of the experimental data with the scaled theoretical frequencies.

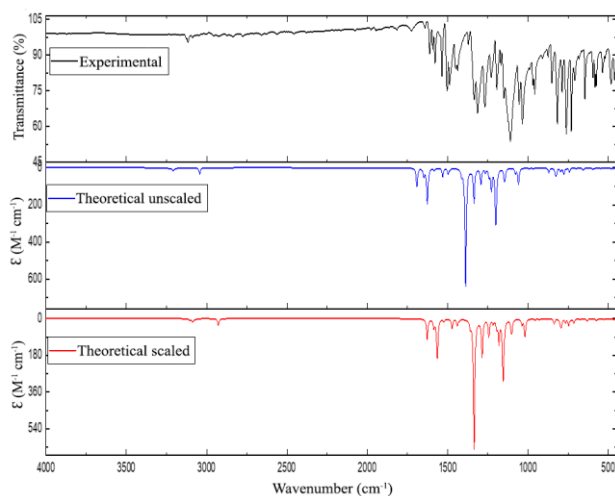


Figure 9. Comparative illustration of experimental and theoretical spectrum of N2TPM

3.3.3. Molecular orbitals

The bond lengths and angles of the resulting compound were analyzed by comparing them with theoretical density functional theory results and experimental X-ray diffraction data. The comparison showed a close agreement between the experimental and theoretical studies, as detailed in Tables 5, and 6. The R^2 values were 0.9914 for bond lengths and 0.9859 for bond angles, as shown in Figures 11 and 12. These high R^2 values indicate a strong agreement between the experimental and theoretical structural parameters, with values close to 1.0.

Small differences in bond angles may be attributed to the distinction between gaseous phase calculations in DFT and solid phase measurements in XRD studies. DFT calculations were also used to determine the compound's

Table 4. Experimental and theoretical wavenumbers and PED analysis of N2TPM.

Experimental (cm ⁻¹)	Calculated (unscaled) (cm ⁻¹)	Calculated (scaled with 0.962) (cm ⁻¹)	Vibration source	Assignment (PED%) Atom number
3126	3264	3140	Tiophene moiety	ν CH (97) \rightarrow C ₂₄ H ₂₅
3117	3234	3110	Benzene moiety	ν CH (91) \rightarrow C ₂₀ H ₂₁
3076	3213	3090	Benzene moiety	ν CH (91) \rightarrow C ₁₃ H ₁₄ + C ₂₂ H ₂₃ + C ₂₆ H ₂₇
3061	3204	3082	Benzene moiety	ν CH (95) \rightarrow C ₁₃ H ₁₄ + C ₂₂ H ₂₃
3046	3190	3068	Benzene moiety	ν CH (97) \rightarrow C ₁₃ H ₁₄ + C ₂₂ H ₂₃ + C ₂₆ H ₂₇
2927	3044	2928	Imine moiety	ν CH (100) \rightarrow C ₉ H ₁₀
1612	1691	1627	Imine moiety	ν NC (69) \rightarrow N ₅ C ₉
1592	1649	1585	Benzene moiety	ν CC (59) \rightarrow C ₁₁ C ₂₀ + C ₁₃ C ₂₆ + C ₂₀ C ₂₂ + C ₁₂ C ₁₃
1578	1630	1568	Benzene moiety	ν CC (41) \rightarrow C ₂₂ C ₂₆
1535	1626	1564	NO ₂ moiety	ν NO (89) \rightarrow N ₇ O ₆ + N ₇ O ₈
1503	1584	1523	Tiophene moiety	ν CC (58) \rightarrow C ₁₅ C ₂₄ + C ₁₆ C ₁₈
1488	1531	1472	Benzene moiety	β CCC (23) \rightarrow C ₁₂ C ₁₃ C ₂₆ + C ₁₃ C ₂₆ C ₂₂ + C ₂₀ C ₂₂ C ₂₆ β HCC (15) \rightarrow H ₂₁ C ₂₀ C ₂₂ β HCC (25) \rightarrow H ₁₄ C ₁₃ C ₂₆ + H ₂₃ C ₂₂ C ₂₆
1334	1388	1335	NO ₂ moiety	ν NO (75) \rightarrow N ₇ O ₆ + N ₇ O ₈

Table 4. Experimental and theoretical wavenumbers and PED analysis of N2TPM (Continue)

Experimental (cm ⁻¹)	Calculated (unscaled) (cm ⁻¹)	Calculated (scaled with 0.962) (cm ⁻¹)	Vibration source	Assignment (PED%) Atom number
1228	1293	1243	CF ₃ moiety	ν FC(11) → F ₂ C ₁₇ + F ₃ C ₁₇
1168	1202	1156	CF ₃ moiety	ν FC (60) → F ₃ C ₁₇ + F ₄ C ₁₇
1149	1199	1153	CF ₃ moiety	ν FC (61) → F ₂ C ₁₇ + F ₃ C ₁₇
1109	1148	1104	Tiophene moiety	ν SC (60) → S ₁ C ₁₅
817	823	792	NO ₂ moiety	β ONO(58) → O ₈ N ₇ O ₆
729	742	713	NO ₂ moiety	γ OCON(85) → O ₈ C ₁₅ O ₆ N ₇
708	689	674	Tiophene moiety	β SCC (41) → S ₁ C ₁₅ C ₂₄

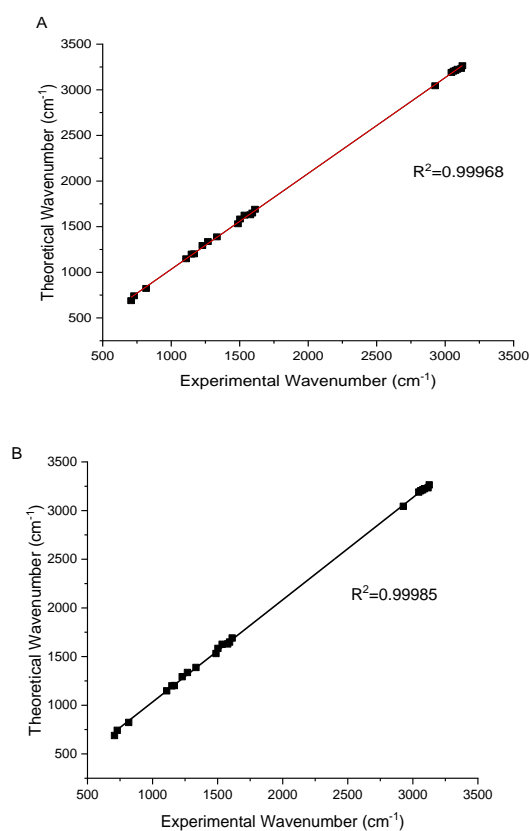


Figure 10. Correlation graphs of (A) experimental wavenumber-theoretical wavenumber (not scaled), (B) experimental wavenumber-theoretical wavenumber (scaled with 0.962)

HOMO and LUMO orbitals as well as different inter-orbital energy gaps. An energy difference of 4.724 eV was found between HOMO and LUMO, and an energy difference of 7.676 eV was found between HOMO-1 and LUMO+1 (Figure 13). This energy difference between HOMO and LUMO suggests that the molecule is relatively stabilized [47].

Table 5. Bond lengths of N2TPM

Atom	Atom	Length/Å	
		XRD	DFT
S1	C2	1.710(4)	1.72936
S1	C5	1.716(4)	1.73687
F1	C13	1.333(6)	1.35189
F2	C13	1.342(6)	1.35187
F3	C13	1.336(5)	1.34760
N1	C6	1.271(5)	1.27440
N1	C7	1.413(6)	1.39868
O1	N3	1.221(5)	1.22695
N3	O2	1.221(5)	1.22909
N3	C2	1.430(6)	1.43827
C12	C7	1.402(6)	1.40857
C12	C13	1.483(6)	1.50831
C12	C11	1.385(6)	1.38926
C6	C5	1.447(6)	1.44633
C2	C3	1.354(6)	1.36932
C7	C8	1.416(6)	1.39972
C8	C9	1.352(7)	1.38845
C5	C4	1.371(6)	1.38083
C4	C3	1.400(7)	1.40720
C10	C11	1.372(6)	1.39097
C10	C9	1.383(7)	1.38884

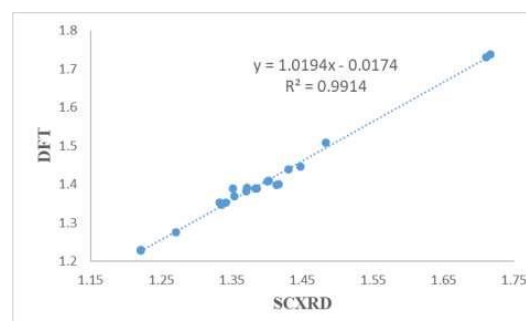


Figure 11. Correlation of bond length between DFT and SCXRD of N2TPM

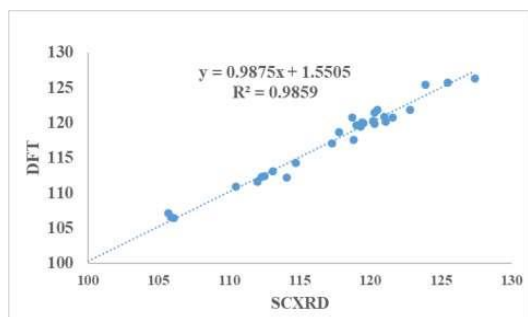


Figure 12. Correlation of bond angle between DFT and SCXRD of N2TPM

Table 6. Bond angles of N2TPM

Atom	Atom	Atom	Length/Å	
			XRD	DFT
C5	S1	C2	89.4(2)	89.38666
C6	C5	S1	120.3(3)	121.42081
C10	C9	C8	121.1(4)	120.15856
C7	N1	C6	118.7(4)	120.70378
O2	N3	O1	123.9(5)	125.39812
C2	N3	O1	117.3(4)	117.07657
C2	N3	O2	118.8(4)	117.52528
F3	C13	F2	105.7(4)	107.09661
C12	C13	F1	114.1(4)	112.24987
C12	C13	F2	112.5(4)	112.41674
C12	C13	F3	112.0(4)	111.63392
C13	C12	C7	120.2(4)	120.20031
C11	C12	C7	119.5(4)	119.95297
C11	C12	C13	120.3(4)	119.84233
C5	C6	N1	120.5(4)	121.86881
C4	C5	S1	112.3(4)	112.31070
C4	C5	C6	127.4(4)	126.26849
F2	C13	F1	105.9(4)	106.57544
F3	C13	F1	106.1(4)	106.47915
C3	C2	S1	114.7(4)	114.28557
C3	C2	N3	125.9(4)	125.71288
N3	C2	S1	119.4(3)	120.00154
C3	C4	C5	113.1(4)	113.06748
C9	C10	C11	119.0(5)	119.63679
C4	C3	C2	110.5(4)	110.94952
C10	C11	C12	121.6(4)	120.72574
C12	C7	N1	119.3(4)	119.41970
C8	C7	N1	122.8(4)	121.81181
C8	C7	C12	117.8(4)	118.67699
C9	C8	C7	121.0(4)	120.82674

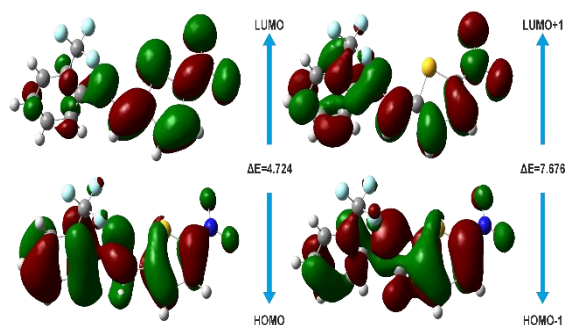


Figure 13. HOMO and LUMO of N2TPM

3.3.4. Natural bond orbitals

Gaussian software was used to calculate the Natural Bond Orbitals of the resulting compound. NBO analysis provides information about individual bonds in the molecule and the associated energies of lone pair and bond pair electrons, which helps understand atomic interactions. This analysis allows for the prediction of the behavior of donor and acceptor atoms within the molecule.

The NBO data for the compound, as listed in Table 7, show that the highest energy interaction is between C12-C13 and C11-C12, with an energy of 4.48 kcal/mol. The lowest energy interaction is between S1-C16 and C18, with an energy of 2.12 kcal/mol, where F2 acts as the donor and C17 as the acceptor.

Table 7. NBO of the N2TPM

Donor (i)	Acceptor (j)	E(2) [Kcal/mol]	E(j)E(i) (a.u)	F(I,J) (a.u)
S1-C15	C16	0.59	1.70	0.028
S1-C16	C18	0.53	1.37	0.024
N5-C9	C11-C12	1.95	1.47	0.048
O6-N7	C15	1.92	2.00	0.056
N7-C15	O6	1.57	1.97	0.050
C9-H10	N5	0.56	1.60	0.027
C11-C17	C20	1.36	1.77	0.044
C12-C13	C11-C12	4.48	1.27	0.070
F2	C17	2.12	25.08	0.207
O8	N7	0.97	15.21	0.199

3.3.5. Density of state

The density of states (DOS) for the synthesized compound was computed from the optimized and calculated using GaussSum software. This analysis is crucial for determining the various energy states or levels within the molecule, which is essential for understanding electron excitation from the ground state.

As depicted in Figure 14, the DOS spectra reveal that the energy difference between HOMO-1 and LUMO+1 varies between compounds. The net energy difference among the frontier molecular orbitals (FMOs) is 2.952 eV.

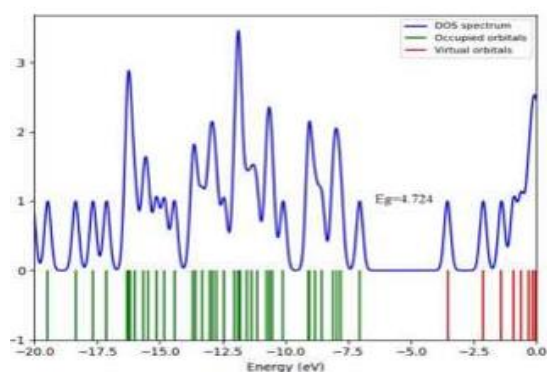


Figure 14. DOS spectra of the N2TPM

3.3.6. Global reactivity parameters

The compound shows high electronegativity due to fluorine atoms. The compound's electron affinity and ionization potential are 4.777 eV and 9.499 eV, respectively (Table 8). The chemical potential and chemical hardness values indicate favorable kinetic stability for the compound.

Table 8. Global reactivity parameters of the N2TPM

χ	μ	η	IP	EA	$1/2\eta$	ω
7.138	-	2.362	9.499	4.777	0.211	10.786
	7.138					

3.4. Hirshfeld Surface Analysis

Hirshfeld surface analysis (HS) is primarily used to study intermolecular interactions in crystalline compounds that contribute to crystal stabilization. The parameters d_e (distance to the nearest outer nucleus) and d_i (distance to the nearest inner nucleus) are taken into account with respect to the van der Waals radius. HS is visualized with red, blue, and white colors representing different distances relative to the total radius [16, 48].

Hirshfeld surfaces for the compound were generated with high surface resolution, mapped over the ranges -0.55 to 1.0 Å for d_{norm} , shape index from -0.10 to 1.0 Å, and curvature over the ranges -0.40 to 4.0 Å. The surfaces were made transparent to show the molecular environment around them clearly.

To identify close contacts, the d_{norm} surface was analyzed with values ranging from negative to positive. Negative values represent shorter contacts compared to van der Waals radii, while positive values represent longer contacts. Red

areas on the surface indicate closer contacts at negative d_{norm} values, blue areas indicate longer contacts at positive d_{norm} values, and white areas indicate distances at zero (Figure 15)

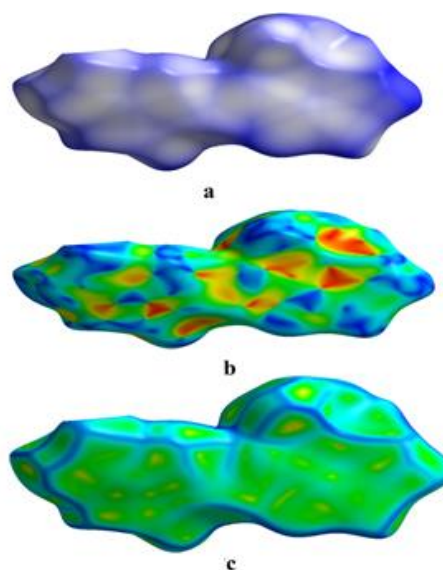


Figure 15. Hirshfeld surfaces are mapped at three views; (a) d_{norm} , (b) shape index, and (c) curvature.

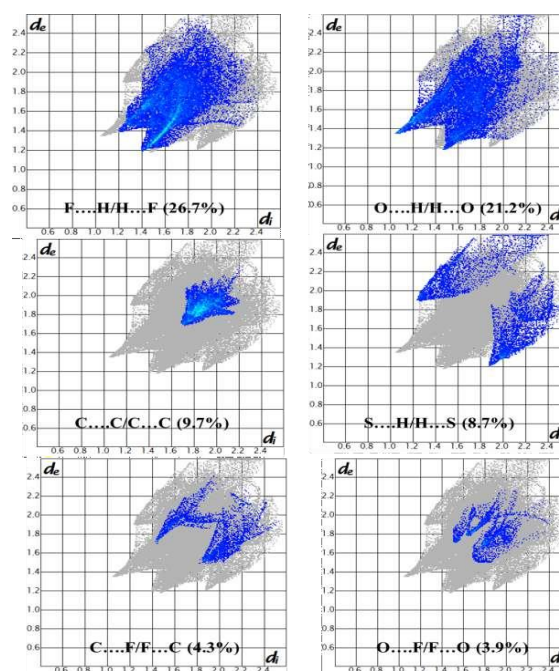


Figure 16. Fingerprint plots of contacts along with relative contributions for N2TPM

2 D fingerprint plots of under studied compound were mapped to check the connections between atoms as shown in Figure 16. It was observed from contacts that H...F/F...H (26.7%). Interactions are major contributors to compound. O...H/H...O (21.2%) are the second major contributing contacts in compound. The

compound has depicted contacts C...C (9.7%), S...H/H...S (8.7%), C...F/F...C (4.3%), and O...F/F...O (3.9%).

3.5. In silico and in vitro enzyme inhibition

The esterase family, which includes enzymes such as acetylcholinesterase (AChE) and butyrylcholinesterase (BChE), plays an important role in Alzheimer's disease. Table 9 details the in vitro potential of the synthesized compound. Docking studies using energy-based scoring functions help determine the optimal conformation of a ligand when binding to a target protein [15]. In general, lower energy scores indicate better binding affinity between protein and ligand [49], making it very important to identify ligand binding modes with the lowest energy values [50].

The results indicate that the compound can act as an enzyme inhibitor, exhibiting significant docking scores and binding energies (Table 9). Specifically, the compound showed a docking score of -10.4159, a binding energy of -10.2743 with AChE, a docking score of -10.3378, and a binding energy of -9.8889 with BChE.

The phenyl ring of the compound displayed π - π interactions with Trp279 and Trp334, while the thiophene moiety showed similar interactions with Phe330. The fluorine atom within the molecule formed strong hydrogen bonds with Phe288 on AChE. Additionally, the residues Phe331 and His440, located at the active sites, interacted with the compound, helping to anchor it at the active site of AChE (Figure 17).

Similarly, the compound showed firm binding with various amino acid residues at the active site of BChE, including Trp82, Glu443, and Gly155, through strong hydrogen bonding interactions involving the fluorine atom and the nitro group's oxygen. The compound also exhibited π -alkyl and π - π interactions between the five-membered ring of the N2TPM and the phenyl ring of Trp82, along with Ala328 and Leu450 (Figure 18).

Table 9. Docking Results of the N2TPM

Docking Score (Kcal/mol)		Enzyme Inhibition (%age)	
AChE	BChE	AChE	BChE
-10.4159	-10.3378	66.42 ± 1.1	65.20 ± 1.0

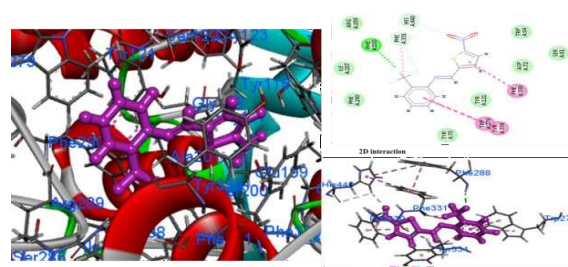


Figure 17. 3D Interactions of N2TPM on active sites of AChE

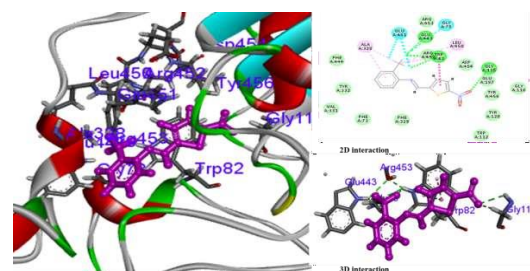


Figure 18. 3D Interactions of N2TPM on active sites of BChE

4. Conclusion

In organic chemistry, new bioactive molecules are constantly being developed for human health. Schiff bases show significant potential and active effects in the treatment of many diseases. In this study, a Schiff base containing heterocyclic components was synthesized and its structure was elucidated by spectroscopic techniques. The crystal structure of the compound was analyzed using 2D and 3D plots, which showed the crystal stability due to various interactions through Hirshfeld surface analysis.

The crystal structure was optimized using Gaussian software and the results were compared with X-ray diffraction (XRD) data, which showed a close agreement in bond angles and lengths. Gaussian calculations have shown that the molecule has remarkable kinetic stability, providing information on various structural parameters such as chemical potential, chemical hardness, electronegativity, and electron affinity.

The biological activity of the synthesized Schiff base was assessed through enzyme inhibition assays targeting acetylcholinesterase (AChE) and butyrylcholinesterase (BChE), enzymes linked to neurodegenerative disorders such as Alzheimer's disease. Both in vitro and in silico studies demonstrated strong inhibitory activity against AChE and BChE, suggesting that the compound possesses significant potential as a

therapeutic agent. Molecular docking studies further supported these findings, revealing favorable binding interactions within the active sites of the target enzymes.

Article Information Form

Acknowledgments

The author would like to thank Dr. Taşkın Basılı for his contributions.

Funding

The author has not received any financial support for this study's research, authorship or publication.

The Declaration of Conflict of Interest/ Common Interest

No conflict of interest or common interest has been declared by the authors.

The Declaration of Ethics Committee Approval

This study does not require ethics committee permission or any special permission.

The Declaration of Research and Publication Ethics

The authors of the paper declare that they comply with the scientific, ethical and quotation rules of SAUJS in all processes of the paper and that they do not make any falsification on the data collected. In addition, they declare that Sakarya University Journal of Science and its editorial board have no responsibility for any ethical violations that may be encountered, and that this study has not been evaluated in any academic publication environment other than Sakarya University Journal of Science.

Copyright Statement

Authors own the copyright of their work published in the journal and their work is published under the CC BY-NC 4.0 license

References

- [1] M. A. Raza, N. Dege, O. E. Dogan, T. Agar, S. H. Sumrra, "Synthesis of two new Schiff bases; crystal structure, Hirshfeld surface analysis, density functional theory and molecular docking," *Journal of Molecular Structure*, vol. 1226, p. 129330, 02/15/ 2021.
- [2] R. Kataria, D. Vashisht, P. Rani, J. Sindhu, S. Kumar, S. Sharma, S. C. Sahoo, V. Kumar, S. Kumar Mehta, "Experimental and Computational Validation of Structural Features and BSA Binding Tendency of 5-Hydroxy5trifluoromethyl3arylpyrazolines," *Chemistry Select*, vol. 6, no. 38, pp. 10324-10335, 2021.
- [3] N. Dege, M. A. Raza, O. E. Doğan, T. Açar, M. W. Mumtaz, "Theoretical and experimental approaches of new Schiff bases: efficient synthesis, X-ray structures, DFT, molecular modeling and ADMET studies," *Journal of the Iranian Chemical Society*, vol. 18, no. 9, pp. 2345-2368, 09/01/ 2021.
- [4] M. Shakir, N. Shahid, N. Sami, M. Azam, A. U. Khan, "Synthesis, spectroscopic characterization and comparative DNA binding studies of Schiff base complexes derived from L-leucine and glyoxal," (in eng), *Spectrochim Acta A Mol Biomol Spectrosc*, vol. 82, no. 1, pp. 31-36, 2011.
- [5] S. Zolezzi, E. Spodine, A. Decinti, "Electrochemical studies of copper(II) complexes with Schiff-base ligands," *Polyhedron*, vol. 21, no. 1, pp. 55-59, 01/15/ 2002.
- [6] P. G. Cozzi, "Metal–Salen Schiff base complexes in catalysis: practical aspects," *Chemical Society Reviews*, vol. 33, no. 7, pp. 410-421, 2004.
- [7] H. Zafar, A. Ahmad, A. U. Khan, T. A. Khan, "Synthesis, characterization and antimicrobial studies of Schiff base complexes," *Journal of Molecular Structure*, vol. 1097, pp. 129-135, 10/05/ 2015.
- [8] P. Arora, V. Arora, H. Lamba, D. Wadhwa, "Importance of heterocyclic chemistry: A review," *International Journal of*

- Pharmaceutical Sciences and Research, vol. 3, no. 9, p. 2947, 2012.
- [9] T. Kunied, H. Mutsanga, "The chemistry of heterocyclic compounds," Palmer (B), vol. 175, 2002.
- [10] M. S. Saini, A. Kumar, J. Dwivedi, R. Singh, "A review: biological significances of heterocyclic compounds," International Journal of Pharma Sciences and Research, vol. 4, no. 3, pp. 66-77, 2013.
- [11] J. Zhang, W. Liu, Q. Xue, "The effect of molecular structure of heterocyclic compounds containing N, O and S on their tribological performance," Wear, vol. 231, no. 1, pp. 65-70, 1999.
- [12] A. W. Czarnik, "Guest Editorial," Accounts of Chemical Research, vol. 29, no. 3, pp. 112-113, 03/13/1996.
- [13] B. J. McConkey, V. Sobolev, M. Edelman, "The performance of current methods in ligand-protein docking," Current Science, vol. 83, pp. 845-856, 2002.
- [14] N. K. Sharma, K. Jha, "Molecular docking: an overview," Journal of Advanced Scientific Research, vol. 1, no. 1, pp. 67-72, 2010.
- [15] A. Vijesh, A. M. Isloor, S. Telkar, T. Arulmoli, H.-K. Fun, "Molecular docking studies of some new imidazole derivatives for antimicrobial properties," Arabian Journal of Chemistry, vol. 6, no. 2, pp. 197-204, 2013.
- [16] Raza, M. A., Farwa, U., Danish, M., Ozturk, S., Agar, A. A., Dege, N., Rehman, S. U., Al-Sehemi, A. G., "Computational modeling of imines based anti-oxidant and anti-esterases compounds: Synthesis, single crystal and In-vitro assessment," Computational Biology and Chemistry, vol. 104, p. 107880, 06/01/2023.
- [17] C. Stoe, "X-area (version 1.18) and X-red32 (version 1.04)," Stoe & Cie, Darmstadt, Germany, 2002.
- [18] G. M. Sheldrick, "SHELXT—Integrated space-group and crystal-structure determination," Acta Crystallographica Section A: Foundations and Advances, vol. 71, no. 1, pp. 3-8, 2015.
- [19] G. M. Sheldrick, "Crystal structure refinement with SHELXL," Acta Crystallographica Section C: Structural Chemistry, vol. 71, no. 1, pp. 3-8, 2015.
- [20] L. J. Farrugia, "WinGX suite for small-molecule single-crystal crystallography," journal of Applied Crystallography, vol. 32, no. 4, pp. 837-838, 1999.
- [21] A. D. Becke, "Density-functional exchange-energy approximation with correct asymptotic behavior," Physical review A, vol. 38, no. 6, p. 3098, 1988.
- [22] C. Lee, W. Yang, R. G. Parr, "Development of the Colle-Salvetti correlation-energy formula into a functional of the electron density," Physical review B, vol. 37, no. 2, p. 785, 1988.
- [23] R. Dennington, T. Keith, J. Millam, "GaussView, Version 4.1. 2," Semichem Inc., Shawnee Mission, KS, 2007.
- [24] N. M. O'boyle, A. L. Tenderholt, K. M. Langner, "Cclib: a library for package-independent computational chemistry algorithms," Journal of computational chemistry, vol. 29, no. 5, pp. 839-845, 2008.
- [25] M. P. Andersson, P. Uvdal, "New scale factors for harmonic vibrational frequencies using the B3LYP density functional method with the triple- ζ basis set 6-311+ G (d, p)," The Journal of Physical Chemistry A, vol. 109, no. 12, pp. 2937-2941, 2005.

- [26] M. H. Jamróz, "Vibrational energy distribution analysis (VEDA): scopes and limitations," *Spectrochimica Acta Part A: Molecular and Biomolecular Spectroscopy*, vol. 114, pp. 220-230, 2013.
- [27] A. D. Becke, "Density-functional thermochemistry. I. The effect of the exchange-only gradient correction," *The Journal of chemical physics*, vol. 96, no. 3, pp. 2155-2160, 1992.
- [28] M. J. Frisch, G. W. Trucks, H. B. Schlegel, G. E. Scuseria, M. A. Robb, J. R. Cheeseman, G. Scalmani, V. Barone, B. Mennucci, G. A. Petersson, H. Nakatsuji, M. Caricato, X. Li, H. P. Hratchian, A. F. Izmaylov, J. Bloino, G. Zheng, J. L. Sonnenberg, M. Hada, M. Ehara, K. Toyota, R. Fukuda, J. Hasegawa, M. Ishida, T. Nakajima, Y. Honda, O. Kitao, H. Nakai, T. Vreven, J. A. Montgomery, Jr., J. E. Peralta, F. Ogliaro, M. Bearpark, J. J. Heyd, E. Brothers, K. N. Kudin, V. N. Staroverov, R. Kobayashi, J. Normand, K. Raghavachari, A. Rendell, J. C. Burant, S. S. Iyengar, J. Tomasi, M. Cossi, N. Rega, J. M. Millam, M. Klene, J. E. Knox, J. B. Cross, V. Bakken, C. Adamo, J. Jaramillo, R. Gomperts, R. E. Stratmann, O. Yazyev, A. J. Austin, R. Cammi, C. Pomelli, J. W. Ochterski, R. L. Martin, K. Morokuma, V. G. Zakrzewski, G. A. Voth, P. Salvador, J. J. Dannenberg, S. Dapprich, A. D. Daniels, Ö. Farkas, J. B. Foresman, J. V. Ortiz, J. Cioslowski, D. J. Fox, *Gaussian 09* (Gaussian, Inc., Wallingford CT, 2009), vol. 121, pp. 150-166, 2009.
- [29] M. Danish, A. Bibi, K. Gilani, M. Asam Raza, M. Ashfaq, M. Nadeem Arshad, A. M. Asiri, K. Ayub, "Antiradical, antimicrobial and enzyme inhibition evaluation of sulfonamide derived esters; synthesis, X-Ray analysis and DFT studies," *Journal of Molecular Structure*, vol. 1175, pp. 379-388, 2019.
- [30] S. Wolff, D. Grimwood, J. McKinnon, M. Turner, D. Jayatilaka, M. Spackman, "Crystal explorer," ed: University of Western Australia Perth, 2012.
- [31] K. Azouzi, B. Hamdi, R. Zouari, A. b. Salah, "Synthesis, structure and Hirshfeld surface analysis, vibrational and DFT investigation of (4-pyridine carboxylic acid) tetrachlorocuprate (II) monohydrate," *Bulletin of Materials Science*, vol. 40, pp. 289-299, 2017.
- [32] M. A. Raza, K. Fatima, Z. Saqib, J. K. Maurin, A. Budzianowski, "Designing of diamino based esterases inhibitors; synthesis, characterization, density functional theory and molecular modeling," *Journal of Molecular Structure*, vol. 1195, pp. 712-722, 2019.
- [33] Z. H. Chohan, M. Hanif, "Design, synthesis, and biological properties of triazole derived compounds and their transition metal complexes," *Journal of Enzyme Inhibition and Medicinal Chemistry*, vol. 25, no. 5, pp. 737-749, 10/01/2010.
- [34] É. Tozzo, S. Romera, M. P. dos Santos, M. Muraro, R. H. de A. Santos, L.M. Lião, L. Vizotto, E. R. Dockal, "Synthesis, spectral studies and X-ray crystal structure of N,N'-(±)-trans-1,2-cyclohexylenebis(3-ethoxysalicylideneamine) H₂(t-3-EtOsalcHxn)," *Journal of Molecular Structure*, vol. 876, no. 1, pp. 110-120, 03/30/2008.
- [35] A. Bartyzel, "Synthesis, thermal study and some properties of N₂O₄—donor Schiff base and its Mn(III), Co(II), Ni(II), Cu(II) and Zn(II) complexes," *Journal of Thermal Analysis and Calorimetry*, vol. 127, pp. 2133-2147, 2017.
- [36] A. U. Hassan, S. H. Sumrra, M. A. Raza, M. Zubair, M. N. Zafar, E. U. Mughal, M. F. Nazar, A. Irfan, M. Imran, M.A. Assiri, "Design, facile synthesis, spectroscopic characterization, and medicinal probing of metal-based new sulfonamide drugs: A theoretical and spectral study," *Applied Organometallic Chemistry*, vol. 35, no. 1, p. e6054, 2021.

- [37] R. Ilmi, S. Kansız, N. K. Al-Rasbi, N. Dege, P. R. Raithby, M. S. Khan, "Towards white light emission from a hybrid thin film of a self-assembled ternary samarium (III) complex," *New Journal of Chemistry*, vol. 44, no. 15, pp. 5673-5683, 2020.
- [38] A. Bashir, I. Siraj, "Synthesis, Characterization and Antimicrobial Studies of Schiff Base Derived from the Reaction of 2-Thiophenecarboxaldehyde and Ethylenediamine and its Metal (II) Complexes," *ChemSearch Journal*, vol. 12, no. 1, pp. 143-148, 2021.
- [39] E. Ermiş, K. Durmuş, "Novel thiophene-benzothiazole derivative azomethine and amine compounds: Microwave assisted synthesis, spectroscopic characterization, solvent effects on UV-Vis absorption and DFT studies," *Journal of Molecular Structure*, vol. 1217, p. 128354, 2020.
- [40] M. I. Jaafar, R. K. Ahmed, A.J. M. Al-Karawi, Al. Bariz OmarAli, S.Kansız, Y. Sert, N. Dege, "Synthesis, structural studies, Hirshfeld surface analysis, and molecular docking studies of a thiophene-based Schiff base compound," *Journal of Molecular Structure*, vol. 1265, p. 133477, 2022.
- [41] M. Shakir, A. Abbasi, M. Azam, A. U. Khan, "Synthesis, spectroscopic studies and crystal structure of the Schiff base ligand L derived from condensation of 2-thiophenecarboxaldehyde and 3, 3'-diaminobenzidine and its complexes with Co (II), Ni (II), Cu (II), Cd (II) and Hg (II): Comparative DNA binding studies of L and its Co (II), Ni (II) and Cu (II) complexes," *Spectrochimica Acta Part A: Molecular and Biomolecular Spectroscopy*, vol. 79, no. 5, pp. 1866-1875, 2011.
- [42] M. N. Uddin, D. A. Chowdhury, M. M. Rony, M. E. Halim, "Metal complexes of Schiff bases derived from 2-thiophenecarboxaldehyde and mono/diamine as the antibacterial agents," *Modern Chemistry*, vol. 2, no. 2, pp. 6-14, 2014.
- [43] C. N. R. Rao, "Chemical applications of infrared spectroscopy," in *Chemical applications of infrared spectroscopy*, 1963, pp. 681-681.
- [44] S.-J. Koyambo-Konzapa, R. Premkumar, R. V. Berthelot Saïd Duvalier, M. K. Gilbert Yvon, M. Nsangou, A. M. F. Benial, "Electronic, spectroscopic, molecular docking and molecular dynamics studies of neutral and zwitterionic forms of 3, 4-dihydroxy-l-phenylalanine: A novel lung cancer drug," *Journal of Molecular Structure*, vol. 1260, p. 132844, 07/15/2022.
- [45] V. K. Rastogi, M. A. Palafox, R. P. Tanwar, L. Mittal, "3,5-Difluorobenzonitrile: ab initio calculations, FTIR and Raman spectra," *Spectrochimica Acta Part A: Molecular and Biomolecular Spectroscopy*, vol. 58, no. 9, pp. 1987-2004, 07/01/2002.
- [46] D. G. Iraiadian, S. J. Vedhagiri, M. Govindarajan, K. Parimala, "Molecular Dynamic Simulation Studies of 4-(Trifluoromethyl) phenylacetonitrile," *Bulgarian Journal of Physics*, vol. 48, no. 4, 2021.
- [47] D. Li Ping, F. H. Zhang, Y. S. Zhu, C. Lu, X. Yu Kuang, J. LvPeng Shao, "Understanding the structural transformation, stability of medium-sized neutral and charged silicon clusters," (in eng), *Scientific Reports*, vol. 5, p. 15951, Nov 3 2015.
- [48] T. Hökelek, S. Özkaya, H. Necefoğlu, "Crystal structure and Hirshfeld surface analysis of aqua-bis-(nicotinamide-κN(1))bis-(2,4,6-tri-methyl-benzoato-κ(2)O,O')cadmium(II)," (in eng), *Acta Crystallogr E Crystallogr Commun*, vol. 74, no. Pt 2, pp. 246-251, Feb 1 2018.
- [49] R. Thomsen, M. H. Christensen, "MolDock: A New Technique for High-

Accuracy Molecular Docking," Journal of Medicinal Chemistry, vol. 49, no. 11, pp. 3315-3321, 06/01/2006.

- [50] D. S. Goodsell, A. J. Olson, "Automated docking of substrates to proteins by simulated annealing," (in eng), Proteins, vol. 8, no. 3, pp. 195-202, 1990.

Air Fixation and AFM: A Comparative Study of Nanoparticle-Induced Topographical Changes in Lung Cells

Gamze Yeşilay^{1,2} 

¹ University of Health Sciences, Experimental Medicine Application & Research Center, Validebag Research Park, Türkiye, gamze.yesilay@sbu.edu.tr

² Department of Molecular Biology and Genetics, Hamidiye Institute of Health Sciences, University of Health Sciences, Türkiye

ARTICLE INFO

ABSTRACT

Keywords:
Desiccation
Sample preparation
Membrane roughness



Article History:
Received: 21.06.2024
Accepted: 14.10.2022
Online Available: 23.10.2024

Gold nanoparticles (AuNPs) have emerged as promising agents in biomedical applications due to their unique physicochemical properties. This study investigates the cellular interactions of AuNPs with A549 (non-small cell lung adenocarcinoma) and BEAS-2B (normal bronchial epithelial) cell lines. AuNPs were synthesized via the citrate reduction method, resulting in 20, 50, and 70 nm particles.

Cells were incubated with AuNPs for increasing durations (30 minutes, 4 hours, and 24 hours). Post-incubation, cells were washed with PBS, air-fixed, and subsequently analyzed using Atomic Force Microscopy (AFM) to obtain detailed topographical maps. AFM imaging revealed distinct interactions between AuNPs and the two cell lines.

A549 cells displayed darker regions on the cell surface, indicative of topographical depressions likely resulting from nanoparticle-induced membrane collapse. In contrast, BEAS-2B cells did not exhibit such depressions, which is consistent with the literature that suggests cancer cells are mechanically softer than normal cells.

The surface roughness analysis results indicated that the preservation of surface integrity post-fixation validates the air-fixation methodology for obtaining reliable mechanical data from AFM analyses.

1. Introduction

Atomic Force Microscopy (AFM) has emerged as a critical tool for cellular imaging, providing high-resolution topographic maps of cell surfaces and offering significant insights into cellular morphology, mechanical properties, and surface roughness [1, 2]. The ability of this technique to capture nanometer-scale features makes it indispensable for understanding cellular processes and interactions, particularly in cancer research, as cancer cells exhibit unique mechanical properties, such as reduced stiffness and altered surface topography, compared to their normal counterparts [3]. Gaining insight on these subtle changes is essential for understanding cancer progression and developing new diagnostic approaches. At this

point, sample preparation step for AFM is critical. Among various sample preparation methods, air fixation of cells offers unique advantages over conventional chemical fixation and live-cell AFM imaging in terms of preserving surface integrity and reducing artifacts [4, 5].

Chemical fixation methods, such as formaldehyde or glutaraldehyde, are commonly used to stabilize cellular structures for AFM imaging. These fixatives cross-link proteins and other cellular components, "freezing" the cells in a state closely resembling their natural conditions. However, chemical fixation can create artifacts due to potential over-fixation or uneven penetration, which may alter the natural topography of the cell surface [6]. Additionally,

residual chemicals can sometimes interfere with subsequent AFM imaging and analysis.

On the other hand, live-cell AFM imaging allows the real-time observation of dynamic cellular processes. This method provides valuable insights into cell mechanics and behaviors under physiological conditions. However, maintaining cell viability during imaging can be challenging and requires complex environmental control systems to maintain optimal temperature, CO₂ levels, and humidity [7]. Moreover, live-cell imaging is sensitive to thermal drift and noise, which can compromise the resolution needed to detect fine topographical changes, such as membrane roughness or indentation patterns induced by nanoparticles.

Air fixation, a less invasive and artifact-free alternative, has shown promise in preserving cellular structures while enabling high-resolution AFM imaging. This method avoids the chemical distortions introduced by traditional fixation techniques and provides stable samples suitable for detailed surface roughness and topography analyses [4, 5]. Given that membrane roughness is a critical indicator of cellular mechanical properties, particularly in distinguishing cancerous cells from normal ones, there is a need for more accurate and non-invasive fixation methods that can retain the native surface characteristics of cells.

Gold nanoparticles (AuNPs) are increasingly recognized for their potential in biomedical applications, particularly in cancer diagnosis and treatment, due to their unique physicochemical properties. The cellular interactions of AuNPs, especially their impact on the cell membrane's mechanical properties, remain a key area of research [8]. Specifically, understanding how AuNPs induce topographical and roughness changes in cancerous versus normal cells can provide valuable insights into cancer cell behavior, as cancer cells are known to be mechanically softer than their normal counterparts [3].

In this study, the applicability of air fixation as a method for preserving the native membrane structures of both cancerous and normal lung cells was explored, with the aim of assessing its

potential to enable precise AFM measurements of surface roughness and topographical changes. Specifically, the effects of AuNPs of increasing diameter sizes (20 nm, 50 nm, and 70 nm) on A549 (non-small cell lung adenocarcinoma) and BEAS-2B (normal bronchial epithelial) cell lines.

The hypothesis is that the surface roughness changes induced by AuNPs will differ between cancerous and normal cells, with more pronounced changes in A549 cells due to their altered membrane mechanics. It was also aimed to determine whether air fixation can effectively reveal these subtle surface alterations and differential AuNP uptake between the two cell lines. The cell lines were incubated with AuNPs for different time points (30 minutes, 4 hours, and 24 hours), air-fixed, and then analyzed using AFM. The time-dependent topographic changes caused by increasing AuNP diameter sizes in air-fixed cell samples were evaluated.

2. General Methods

2.1. AuNP synthesis

AuNPs were synthesized using the citrate reduction method [9]. Initially, for the synthesis of 20 nm AuNPs, 10 mg of HAuCl₄·3H₂O was dissolved in 100 mL of deionized water. Upon the solution reaching a boil, 2 mL of a 1% sodium citrate (w/v) solution was rapidly added while stirring. The solution was continuously stirred at boiling temperature until a deep red color was observed. To synthesize larger AuNPs, the amount added from sodium citrate (1%, w/v) was adjusted to 0.8 mL for 50 nm AuNPs and 0.6 mL for 70 nm AuNPs. UV-Visible spectroscopy (Shimadzu, UV3600i Plus) was used to confirm the characteristic plasmon resonance peaks of the synthesized AuNPs. Dynamic Light Scattering (DLS) (Malvern, ZetaSizer Ultra) was used to verify the size and distribution of AuNPs.

2.2. Cell culture

BEAS-2B cell line was cultured in Dulbecco's Modified Eagle Medium (DMEM), while A549 cells were cultured in DMEM-F12 medium. Both media were supplemented with 10% fetal bovine serum (FBS) and 1% penicillin-streptomycin.

Cells were maintained at 37°C in a humid atmosphere with 5% CO₂.

For A549 cell line, 7500 cells were seeded on each round coverslip, and for the BEAS-2B cell line, 5000 cells were seeded on each coverslip. The coverslips were placed in 24-well plates and allowed to grow until they reached 80% confluency. All experiments were performed in triplicate. Cells were incubated with AuNPs at a concentration of 50 µg/mL for three different time points: 30 minutes, 4 hours, and 24 hours. Post-incubation, cells were thoroughly washed with PBS to remove uninternalized AuNPs and air-fixed in a desiccator for 24 hours. The next day, dried cells were washed with deionized water to remove salts from PBS and then re-dried for AFM imaging.

2.3. AFM imaging

Fixed cells were imaged using a Nanosurf CoreAFM. Imaging was conducted with a PPP-NCLR (Nanosurf) cantilever in tapping mode to obtain detailed topographic maps of cell surfaces. Each scan consisted of 512 points per line at a scan rate of 1 line per second. Three 100×100 µm² areas were scanned for each sample.

2.4. Surface roughness analysis

Surface roughness parameters and standard deviation parameters were calculated using Gwyddion 2.66 open-source software. Pre-processing steps applied to the AFM images included leveling data by mean plane subtraction, polynomial row alignment, measurement range normalization, and image sharpening using Laplacian filtering.

3. Results and Discussion

3.1. AuNP characterization

UV-Visible spectra and DLS results of the AuNPs confirm that the synthesis achieved the targeted sizes (Figure 1).

The synthesized AuNPs match the size-absorbance peak results reported in the literature (Figure 1A) [10]. Additionally, the hydrodynamic diameter measurements obtained

using DLS confirm that the targeted AuNP sizes were achieved (Figure 1B).

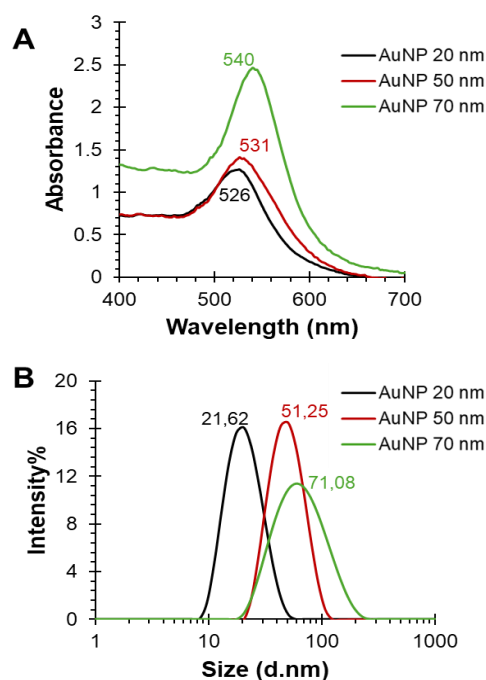


Figure 1. AuNP characterization results. (A) UV-Visible spectra and absorbance peaks. (B) DLS distribution and hydrodynamic diameter results.

3.2. AFM imaging

AFM topography images were obtained after the interaction of AuNPs with increasing diameters with both cell lines at increasing time points (Figures 2 and 3).

Figure 2 presents the AFM images of A549 cells incubated with AuNPs of increasing diameters and varying time points. Panel (A) shows the control sample without AuNP treatment, providing a baseline reference for cellular surface topography. Panels (B-D) display the topographical changes after 30 minutes of incubation with 20 nm, 50 nm, and 70 nm AuNPs, respectively, while panels (E-G) and (H-J) depict the topographical changes after 4 hours and 24 hours of incubation. The darker regions observed in A549 cell line represent topographical changes and cellular responses resulting from the interaction of nanoparticles with the cell surface (Figure 2).

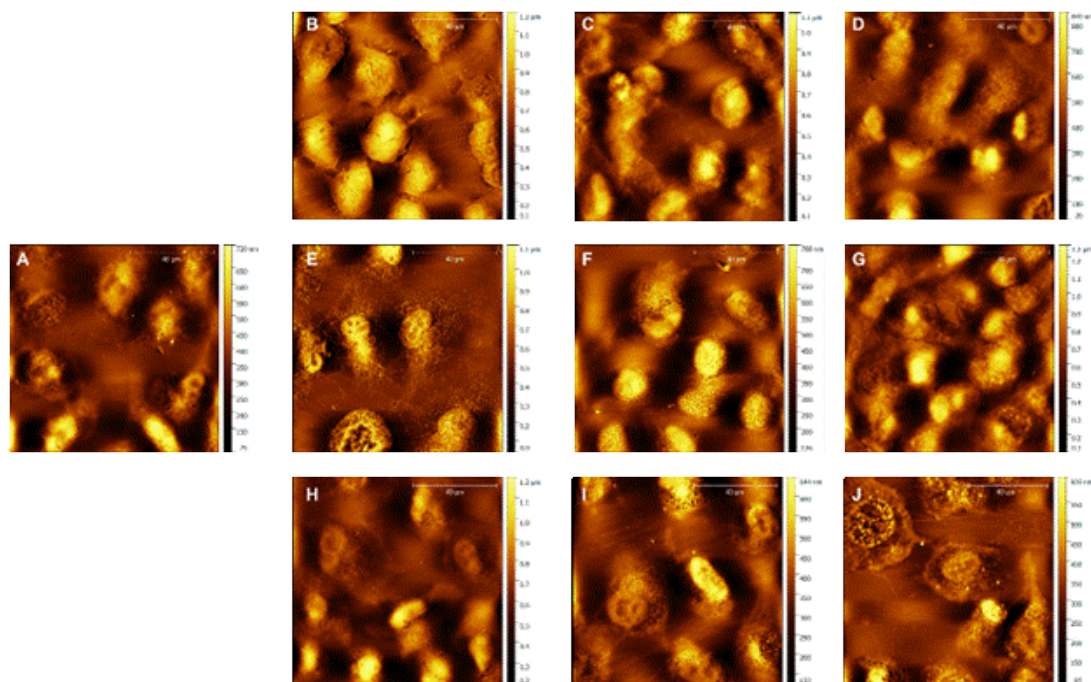


Figure 2. AFM images obtained for A549 cell line based on increasing AuNP diameters and incubation times. (A) Control sample not treated with AuNP. (B-D) Images obtained after incubation with AuNP for 30 minutes, (E-G) 4 hours, and (H-J) 24 hours. Images for samples incubated with (B, E, H) 20 nm AuNPs, (C, F, I) 50 nm AuNPs, and (D, G, J) 70 nm AuNPs. Scale bars are 40 μm .

The membrane structure observed in the BEAS-2B cell line in the control group and other samples shows significant differences compared to A549 cell line (Figure 3). As indicated in the literature, cancer cells have a mechanically "softer" structure compared to normal cells,

leading to indentations in A549 cell line, while such topographical changes are not observed in BEAS-2B cell line [11].

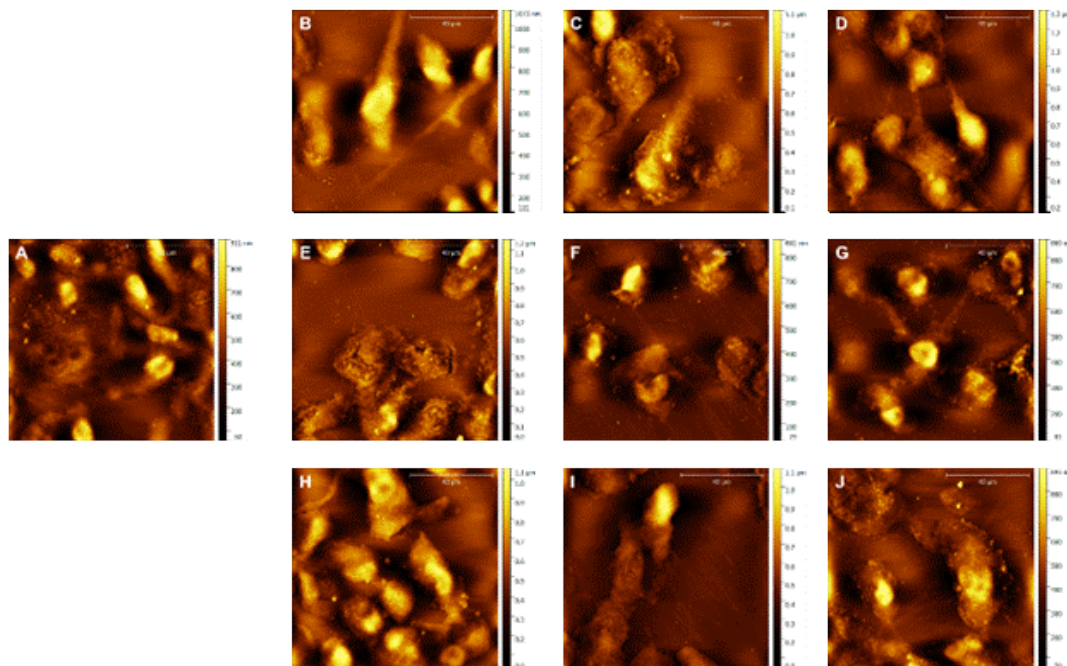


Figure 3. AFM images obtained for the BEAS-2B cell line based on increasing AuNP diameters and incubation times. (A) Control sample not treated with AuNP. (B-D) Images obtained after incubation with AuNP for 30 minutes, (E-G) 4 hours, and (H-J) 24 hours. Images for samples incubated with (B, E, H) 20 nm AuNPs, (C, F, I) 50 nm AuNPs, and (D, G, J) 70 nm AuNPs. Scale bars are 40 μm .

For both cell lines, the data shows that when AuNPs bind to or are internalized by the cell surface, they cause indentations or flattening in specific areas of the cell membrane. The presence of nanoparticles on the cell surface can induce morphological changes such as resorption, making certain areas of the cell membrane appear thinner or collapsed [12]. These effects are observed as darker regions in AFM images (Figure 2B-J, Figure 3B-J) representing topographical depressions or lower elevations, which are most likely caused by nanoparticle-induced membrane deformation. These depressions are more pronounced in samples incubated with 20 nm AuNPs (panels B, E, H), which aligns with the hypothesis that smaller nanoparticles induce more significant surface alterations due to higher cellular uptake. As incubation time increases (panels H-J), the topographical features become less pronounced, suggesting that the nanoparticles are being internalized, leading to a reduction in surface roughness. This temporal trend supports the notion that AuNP interactions with the cell membrane evolve over time, causing initial membrane deformation followed by nanoparticle uptake.

As seen in the figures, the surface integrity of the samples examined after air fixation was preserved and suitable for obtaining mechanical information.

3.3. AFM roughness analysis

The effect of AuNPs on the surface roughness of A549 and BEAS-2B cell lines was investigated using three important roughness parameters: arithmetic mean roughness (Ra), root mean square roughness (Rq), and maximum profile height (Rt). The results provide detailed information on the topographical changes caused by increasing AuNP sizes (20 nm, 50 nm, and 70 nm) over increasing incubation times (30 minutes, 4 hours, and 24 hours) (Table 1).

The basic roughness parameters of the control samples not treated with AuNPs (CtrlA and CtrlB) reveal inherent differences in surface topography between cancerous and non-cancerous cells. BEAS-2B cell line (CtrlB) exhibits higher basic roughness compared to

A549 cell line (CtrlA), indicating that normal lung epithelial cells have a more irregular surface. This could be attributed to the altered membrane properties of cancer cells, which may facilitate higher interaction or uptake rates of AuNPs in A549 cell line. In contrast, BEAS-2B cell line shows more variability in roughness parameters with larger AuNPs and longer incubation times, reflecting different interaction dynamics.

Table 1. Ra, Rq, and Rt values obtained from AFM measurements. (Ctrl: sample not treated with AuNP, other groups' names represent the incubation time (30 min, 4 h, 24 h), AuNP diameter (20, 50, 70 nm), and cell line (A549, BEAS-2B) respectively.)

	Ra	Rq	Rt
CtrlA	70.53±27.73	91.08±34.87	358.3±116.6
3020A	116.4±37.55	151.4±50.97	674.3±203.8
0420A	130.1±57.85	174.8±62.12	828±318.7
2420A	105.9±53.95	141.1±59.8	538.8±240.6
3050A	117.7±41.27	148.6±48.58	609.8±162.2
0450A	92.29±33.5	117.1±35.81	481.9±141
2450A	63.37±27.19	83.59±31.56	336.5±133.5
3070A	74.86±24.71	97.78±30.3	410.6±118.6
0470A	121.8±29.81	152±36.36	611.5±129.7
2470A	43.7±12.96	60.66±21.52	317.1±97.7
CtrlB	79.72±34.26	105.4±45.27	424.5±158
3020B	85.17±48.15	117.5±51.14	404.7±220.6
0420B	115.2±51.89	156.8±67.98	763.9±314.2
2420B	113.4±23	138.4±25.65	528.6±98.17
3050B	89.36±47.46	126.4±57.13	506.1±271.7
0450B	77.98±43.5	111.1±46.69	421.6±247.7
2450B	97.94±59.99	135.9±85.43	472.6±240.7
3070B	102.5±64.98	144.2±76.27	509.5±277.1
0470B	93.44±52.49	126.7±56.69	444.2±234.2
2470B	69.14±23.63	92.43±31.82	419.4±145.1

Small AuNPs (20 nm) caused the most significant changes in surface roughness for both cell lines. In A549 cell line, Ra, Rq, and Rt values significantly increased after 4 hours of incubation, indicating a high density of AuNPs on the cell membrane surface. This trend is also observed in BEAS-2B cell line, where roughness parameters peak at 4 hours, reflecting similar membrane interactions. At longer incubation times (24 hours), a decrease in roughness is observed in both cell lines, indicating AuNP internalization and a subsequent reduction in surface irregularities.

Larger AuNPs (50 nm and 70 nm) exhibit a similar roughness change pattern, with initial increases peaking at 4 hours. However, the

magnitude of the change is less pronounced compared to 20 nm AuNPs. Subsequently, a decrease in roughness is observed at 24 hours, indicating AuNP internalization. Notably, 70 nm AuNPs show a significant reduction in roughness at 24 hours, suggesting that cellular adaptation or AuNP agglomeration may reduce the effective interaction of particles with the cell surface.

The temporal dynamics of AuNP interaction reveal peak surface roughness at intermediate incubation times (around 4 hours), indicating optimal surface interaction and maximal membrane residence time. As the incubation time extends to 24 hours, roughness decreases, aligning with the AuNP internalization process [13]. This trend highlights a general mechanism across both cell lines and AuNP sizes: AuNPs initially reside on the cell membrane, increasing surface roughness, and later internalize, reducing surface irregularities. In A549 cells, roughness values peak at 4 hours of incubation, suggesting that the maximum nanoparticle-membrane interaction occurs within this window, likely due to the higher uptake efficiency of smaller, more flexible cancerous cells. In contrast, BEAS-2B cells show less dramatic changes in roughness, possibly due to their stiffer, more structurally stable membrane.

In this study, it was confirmed that cancerous cells, due to their distinct mechanical properties, exhibit more pronounced topographical changes upon interaction with AuNPs, which can be effectively captured through air-fixated AFM imaging. Importantly, these findings reinforce the potential of air fixation as an ideal preparation method for AFM studies, particularly when investigating membrane dynamics and surface roughness in cancer research. The compatibility of air fixation with AFM broadens its applicability in nanomedicine, providing a reliable alternative to more traditional preparation methods.

4. Conclusion

This study effectively demonstrates that interactions between AuNPs and cell membranes lead to significant topographical changes. Initially, surface roughness increases due to the presence of AuNPs on the cell membrane, and later decreases as internalization occurs. These

findings provide valuable insights into the behavior of AuNPs in biological environments, emphasizing the importance of controlling AuNP size and exposure duration to achieve desired cellular interactions.

Additionally, the results highlight the compatibility and advantages of air fixation for AFM sample preparation. Air fixation offers a balance of structural preservation and measurement stability, enabling precise topographical evaluation of AuNP interactions. This presents the potential for air fixation to become a valuable method for AFM studies, particularly in contexts where high-resolution, artifact-free imaging is critical.

Article Information Form

Acknowledgments

The author would like to thank University of Health Sciences, Experimental Medicine Application & Research Center, Validebag Research Park for Access to research infrastructure.

Funding

The author has not received any financial support for the research, authorship or publication of this study.

Author's Contribution

The author designed and conducted the experiments, wrote the original draft and the final version of the manuscript.

The Declaration of Conflict of Interest/ Common Interest

No conflict of interest or common interest has been declared by the author.

The Declaration of Ethics Committee Approval

This study does not require ethics committee permission or any special permission.

The Declaration of Research and Publication Ethics

The author of the paper declare that they comply with the scientific, ethical and quotation rules of SAUJS in all processes of the paper and that she does not make any falsification on the data collected. In addition, she declares that Sakarya

University Journal of Science and its editorial board have no responsibility for any ethical violations that may be encountered, and that this study has not been evaluated in any academic publication environment other than Sakarya University Journal of Science.

Copyright Statement

Author owns the copyright of her work published in the journal and her work is published under the CC BY-NC 4.0 license.

References

- [1] X. Deng, F. Xiong, X. Li, B. Xiang, Z. Li, X. Wu, C. Guo, X. Li, Y. Li, G. Li, W. Xiong, Z. Zeng, "Application of atomic force microscopy in cancer research," *Journal of Nanobiotechnology*, vol. 16, p. 102, 2018.
- [2] F. Xia, K. Youcef-Toumi, "Review: Advanced Atomic Force Microscopy Modes for Biomedical Research," *Biosensors*, vol. 12, Art. no. 12, 2022.
- [3] A. Massey, J. Stewart, C. Smith, C. Parvini, M. McCormick, K. Do & A. X. Cartagena-Rivera, "Mechanical properties of human tumour tissues and their implications for cancer development," *Nature Reviews Physics*, vol. 6, p. 269-282, 2024.
- [4] S. O. Konorov, H. G. Schulze, J. M. Piret, R. F. B. Turner, M. W. Blades, "Evidence of marked glycogen variations in the characteristic Raman signatures of human embryonic stem cells," *Journal of Raman Spectroscopy*, vol. 42, pp. 1135–1141, 2011.
- [5] M. M. Mariani, P. Lampen, J. Popp, B. R. Wood, V. Deckert, "Impact of fixation on in vitro cell culture lines monitored with Raman spectroscopy," *Analyst*, vol. 134, pp. 1154–1161, 2009.
- [6] B. Q. Huang, E. C. Yeung, "Chemical and Physical Fixation of Cells and Tissues: An Overview," in *Plant Microtechniques and Protocols*, E. C. T. Yeung, C. Stasolla, M. J. Sumner, B. Q. Huang, Eds., Cham: Springer International Publishing, 2015, pp. 23–43.
- [7] L. Andolfi, E. Bourkoula, E. Migliorini, A. Palma, A. Pucer, M. Skrap, G. Scoles, A.P. Beltrami, D. Cesselli, M. Lazzarino, "Investigation of Adhesion and Mechanical Properties of Human Glioma Cells by Single Cell Force Spectroscopy and Atomic Force Microscopy," *PLOS ONE*, vol. 9, p. e112582, 2014.
- [8] C. Huang, T. Ozdemir, L. C. Xu, P. J. Butler, C. A. Siedlecki, J. L. Brown & S. Zhang, "The role of substrate topography on the cellular uptake of nanoparticles," *Journal of Biomedical Materials Research Part B: Applied Biomaterials*, vol. 104, pp. 488-495, 2016.
- [9] J. Turkevich, P. C. Stevenson, J. Hillier, "A study of the nucleation and growth processes in the synthesis of colloidal gold," *Discussions of the Faraday Society*, vol. 11, pp. 55–75, 1951.
- [10] W. Haiss, N. T. K. Thanh, J. Aveyard, D. G. Fernig, "Determination of Size and Concentration of Gold Nanoparticles from UV–Vis Spectra," *Analytical Chemistry*, vol. 79, pp. 4215–4221, 007.
- [11] S. Suresh, "Biomechanics and biophysics of cancer cells," *Acta Biomaterialia*, vol. 3, pp. 413–438, 2007.
- [12] C. Lara-Cruz, J. J. Salazar, E. Ramón-Gallegos, P. Damian-Matsumura, N. Batina, "Increasing roughness of the human breast cancer cell membrane through incorporation of gold nanoparticles," *International Journal of Nanoscience*, vol. 11, pp. 5149–5161, 2016.
- [13] B. D. Chithrani, A. A. Ghazani, W. C. W. Chan, "Determining the Size and Shape Dependence of Gold Nanoparticle Uptake into Mammalian Cells," *Nano Letters*, vol. 6, pp. 662–668, 2006.



A Study of q -Deformed Bosons, and Their Implications to Quantum Optics

Mustafa Senay 

Bartın University, Vocational School of Health Services, Department of Medical Services and Techniques, Bartın, Türkiye, msenay@bartin.edu.tr

ARTICLE INFO

ABSTRACT

Keywords:
 q -deformed boson
Quantum statistics
Quantum optics
Thermodynamics

Article History:

Received: 26.07.2024

Accepted: 14.10.2024

Online Available: 23.10.2024

In this study, we investigate three types of q -deformed boson oscillators, focusing on their mathematical frameworks and thermodynamic properties. We calculate key thermodynamic quantities, such as internal energy and entropy, as functions of the deformation parameter q . Our results reveal that these oscillators are eigenstates of specific deformed boson annihilation operators. We also analyze their unique characteristics and implications in deformed quantum optics. Furthermore, we examine the impact of q -deformation on qutrit logic gates, including cycle, self-shift, controlled cycle, controlled self-shift, Feynman, ternary Toffoli, and Fredkin gates, highlighting their altered computational properties. This research contributes to a deeper understanding of q -deformed systems and their applications in quantum computing. Overall, it opens new avenues for exploring the interplay between deformation parameters and quantum information processing.

1. Introduction

The spin-statistics theorem is a fundamental principle in quantum field theory that bridges quantum mechanics and statistical mechanics [1]. It establishes an important connection between the symmetry of particles (especially their spin) and the statistical behavior they exhibit in many-body systems. This theorem states that particles with integer spin (bosons) have symmetric wave functions, allowing multiple particles to occupy the same quantum state simultaneously. In contrast, particles with half-integer spin (fermions) have antisymmetric wave functions, enforcing the Pauli exclusion principle that no two fermions can occupy the same quantum state. These symmetrization or antisymmetrization requirements are expressed through commutation or anticommutation relations in the second quantization framework, which govern how the creation and annihilation operators work for bosons and fermions, respectively. This distinction in quantum statistical behavior directly affects the number of possible states a system can use; It affects the

collective statistical mechanical description of the system by determining the set of occupancy numbers and thus shaping macroscopic properties such as thermal conductivity and specific heat capacity.

In recent years, there has been increasing research into quantum statistics, which departs from the traditional classifications of bosons and fermions. Building on the fundamental contributions of Gentile and Green [2, 3], researchers have developed various extensions beyond these standard statistics. These include parastatistics, fractional statistics, quon statistics, anion statistics, and quantum group theory, which have attracted great attention due to their potential applications in various fields of physics. In condensed matter physics, these statistics have proven vital in elucidating phenomena such as the fractional quantum Hall effect and the behavior of anionic particles that are neither fermions nor bosons, but exhibit unique statistical properties [4].

There are two important approaches to investigate the statistics and thermodynamics of intermediate states, each offering unique perspectives and methodologies: One method uses Tsallis' non-extensive statistics [5] and generalized entropies. Tsallis statistics generalize standard Boltzmann-Gibbs statistics by introducing a parameter q that modifies the entropy formula [6]. The second method involves the use of deformed quantum algebras [7-14], leading to deformed thermostatics functions [15-39]. Deformed quantum algebras, such as quantum groups or q -deformed algebras, introduce modifications to the standard commutation relations of quantum mechanics. These changes affect the formulation of statistical mechanics, changing the distribution functions and thermodynamic properties of the particles.

In recent work, q -deformed theory has found applications in a wide range of physics disciplines and has contributed to various fields such as: In ref [15], generalized thermodynamics with q -deformed bosons and fermions has been used to describe systems with non-trivial quantum deformations, which are conventional has worked in ways that extend beyond statistical mechanics, Ref. [16]; q -deformed theory has been applied to study Bose-Einstein condensation, offering new insights into the behavior of particles at extreme temperatures and densities; Ref. [17], investigations into the thermodynamic geometry of deformed bosons and fermions have provided geometric insights into the statistical properties of quantum systems and phase transitions; Ref. [20] used thermosize effects in models of q -deformed fermion gases, investigating how quantum deformations affect the thermodynamic properties and size scaling of fermionic systems. Moreover, it has been studied a two-parameter deformed boson gas model based on commuting Fibonacci oscillators, leading to a generalized Fibonacci energy spectrum in [23,24]. Friedmann equations and Einstein field equations incorporating the deformation parameter q were derived in [25,26]. A quantum Otto cycle was analyzed using q -deformed oscillators as the working substance alongside classical thermal baths in [29]. Further, q -deformed harmonic oscillators were utilized to construct qubits and quantum gates in [30,31].

Investigations into a single particle's q -deformed harmonic oscillator have focused on how deformation influences statistical complexity, including Shannon information entropy and disequilibrium in [32]. A modified cosmological scenario was proposed, featuring q -deformed Friedmann and Raychaudhuri equations that introduce effective dark energy components in [33].

On the other hand, q -deformed qubits are generalizations of traditional qubits in which the algebra governing quantum states is replaced by a deformation parameter q derived from quantum groups [30,31]. These generalized states introduce a deformation that changes how quantum states interact and evolve. This leads to changes in the energy spectra, quantum gate operations, and overall dynamics of the qubits. Such changes can create new avenues for quantum state manipulation and lead to more generalized forms of quantum systems with potential applications in fields such as quantum optics and condensed matter physics. In quantum information theory, q -deformed qubits can be used as a tool to better understand non-standard entanglement properties and quantum correlations.

Our aim in this work is to perform an analysis of quantum algebraic properties associated with three types of q -deformed boson oscillator algebra models: the Arik-Coon (AC) model, the Biedenharn-Macfarlane (BM) model, and the Quesne model. These models represent different mathematical formulations that incorporate quantum deformations into the standard bosonic oscillator algebra. We will also examine some thermostatic properties of AC and BM models. This will include the study of statistical mechanics aspects such as their partition functions, entropy formulations and thermodynamic behavior. Understanding these properties is crucial for applications in various physical systems where quantum deformations play an important role. As an application, we will investigate the effect of the Quesne model in quantum optics. Quantum optics deals with the interaction of light and matter at the quantum level [40-42]. For instance, in Ref. [40], photonic structural designs have been emphasized to enhance light-matter interaction in two

dimensional material based optoelectronic devices.

Moreover, understanding how q -deformed patterns affect photon statistics, coherence properties, and other optical phenomena can provide valuable information about new regimes of light-matter interactions. For example, in Ref. [43], it was focused on the study of a multi-level atom excited by a laser pulse in the form of a q -deformed hyperbolic function. The dynamic properties of a two-level system excited by a q -deformed laser beam were analyzed. Also, the optical properties of a three-level atom system interacting with two electromagnetic fields were investigated.

2. AC-type Oscillators Model

In this section, we investigate the quantum statistical mechanical properties of q -deformed boson oscillators, focusing specifically on Arik-Coon (AC)-oscillators. The algebraic framework of quantum AC-oscillators are characterized by the q -deformed Heisenberg algebra, where the creation and destruction operators are denoted a^* and a , respectively. The q -deformed Heisenberg algebra associated with AC-oscillators is expressed as [7, 44]

$$aa^* - qa^*a = 1$$

$$[\hat{N}, a^*] = a^*, \quad [\hat{N}, a] = -a, \quad (2.1)$$

where \hat{N} is the total number operator and q is the deformation parameter. Also, the basic number is given as

$$[x] = \frac{q^x - 1}{q - 1}. \quad (2.2)$$

Furthermore, the Jackson derivative (JD) operator for the AC-oscillators is expressed as

$$\partial_x^{(q)} f(x) = \frac{1}{x} \left[\frac{f(qx) - f(x)}{q - 1} \right], \quad (2.3)$$

which reduces to the ordinary derivative when q goes to unity. The mean occupation number of AC oscillators is defined as [44]

$$n_i = \frac{1}{\log q} \ln \left(\frac{z^{-1} e^{\beta \epsilon_i} - 1}{z^{-1} e^{\beta \epsilon_i} - q} \right) \quad (2.4)$$

where $z = \exp(\mu/k_B T)$ is the fugacity and $\beta = 1/k_B T$. Following the standard procedure [45], one can easily find

$$\frac{P}{k_B T} = \frac{1}{\lambda^3} h_{5/2}(z, q), \quad (2.5)$$

$$\frac{N}{V} = \frac{1}{\lambda^3} h_{3/2}(z, q), \quad (2.6)$$

where $\lambda = h/(2\pi m k_B T)^{1/2}$ is the thermal wavelength and the generalized Bose Einstein functions $h_n(z, q)$ are defined as

$$h_n(z, q) = \frac{1}{\log q} \left[\sum_{l=1}^{\infty} \frac{(zq)^l}{l^{n+1}} - \sum_{l=1}^{\infty} \frac{(z)^l}{l^{n+1}} \right]. \quad (2.7)$$

The internal energy and the entropy of the AC-oscillators gas can be found as [44]

$$U = \frac{3}{2} \frac{k_B T V}{\lambda^3} h_{5/2}(z, q). \quad (2.8)$$

and

$$\frac{S}{N k_B} = \frac{5}{2} \frac{h_{5/2}(z, q)}{h_{3/2}(z, q)} - \log z. \quad (2.9)$$

respectively. Also, from the thermodynamic relation $F = \mu N - PV$, the Helmholtz free energy can be derived as

$$F = N k_B T \left[\log z - \frac{h_{5/2}(z, q)}{h_{3/2}(z, q)} \right]. \quad (2.10)$$

3. BM-type Oscillators Model

The symmetric q -deformed algebraic structure of BM-type oscillators is characterized by the q -deformed Heisenberg algebra, with the creation operator c^* , the annihilation operator and c , and the total number operator \hat{N} playing central roles. In this framework, the BM-oscillators algebra is defined as [8, 9, 15]

$$cc^* - qc^*c = q^{-N}$$

$$[\hat{N}, c^*] = c^*, \quad [\hat{N}, c] = -c, \quad (3.1)$$

where q is the real deformation parameter. Also, the operators have the following relations [15]

$$c^*c = [\hat{N}], \quad c^*c = [1 + \hat{N}]. \quad (3.2)$$

The basic q -deformed quantum number is defined as

$$[x] = \frac{q^x - q^{-x}}{q - q^{-1}}. \quad (3.3)$$

Moreover, the Jackson derivative (JD) operator for the system is given as

$$D_x^{(q)} f(x) = \frac{1}{x} \left[\frac{f(qx) - f(q^{-1}x)}{q - q^{-1}} \right], \quad (3.4)$$

for any function $f(x)$.

To investigate the high-temperature properties of the BM-oscillators model, we examine the logarithm of grand partition function:

$$\ln Z = - \sum_i \ln(1 - ze^{-\beta \epsilon_i}) \quad (3.5)$$

The mean occupation number is expressed by the following form

$$n_i = \frac{1}{q - q^{-1}} \ln \left(\frac{z^{-1} e^{\beta \epsilon_i} - q^{-1}}{z^{-1} e^{\beta \epsilon_i} - q} \right). \quad (3.6)$$

The pressure of the BM-oscillators model is given as

$$P = \frac{k_B T}{V} \sum_i \ln(1 - ze^{-\beta \epsilon_i}). \quad (3.7)$$

This relation can be written by using Eq. (3.4)

$$\frac{P}{k_B T} = \frac{1}{\lambda^3} g_{5/2}(z, q), \quad (3.8)$$

where q -deformed $h_n(z, q)$ function is defined as

$$g_n(z, q) = \frac{1}{q - q^{-1}} \left[\sum_{l=1}^{\infty} \frac{(zq)^l}{[n+1]} - \sum_{l=1}^{\infty} \frac{(zq^{-1})^l}{[n+1]} \right]. \quad (3.9)$$

One can also derive the following thermodynamic functions for a gas of BM-oscillators: the particle density, internal energy, and entropy, respectively

$$\frac{N}{V} = \frac{1}{\lambda^3} g_{3/2}(z, q), \quad (3.10)$$

$$U = \frac{3 k_B T V}{2 \lambda^3} g_{5/2}(z, q), \quad (3.11)$$

$$\frac{S}{N k_B} = \frac{5 g_{5/2}(z, q)}{2 g_{3/2}(z, q)} - \ln z. \quad (3.12)$$

4. Quesne-type Oscillators Model

Quesne-oscillators algebra is defined as [46, 47]

$$q a_q a_q^* - a_q^* a_q = I, \quad a_q a_q^* - a_q^* a_q = q^{-N-1}. \quad (4.1)$$

where a_q^* and a_q are deformed creation and annihilation operators, respectively, and they satisfy in the following forms

$$a_q |n\rangle = \sqrt{[n]} |n-1\rangle, \quad (4.2)$$

$$a_q^* |n\rangle = \sqrt{[n+1]} |n+1\rangle, \quad (4.3)$$

where $a_q |0\rangle = 0$ and the q -basic number is given as

$$[x] = \frac{1 - q^{-x}}{q - 1}. \quad (4.4)$$

Moreover, q -deformed coherent states are expressed as

$$|z\rangle = [E_q((1 - q)q|z|^2)]^{-1/2} \sum_{n=0}^{\infty} \frac{z^n}{\sqrt{[n]!}} \sqrt{[n]} |n\rangle \quad (4.5)$$

where q -exponentials are $E_q(z) = \prod_{k=0}^{\infty} (1 + q^k z)$.

Now, we investigate the geometric and physical properties of the new q -deformable coherent state $|z\rangle$. To achieve this, we need to compute the expectation values of various Hermitian monomials involving the boson creation and annihilation operators a^* and a . These expectation values can be expressed in terms of derivatives of the function $\mathcal{N}_q(x)$ [25]

$$\langle (a^*)^r a^r \rangle = \frac{x^r}{\mathcal{N}_q(x)} \frac{d^r \mathcal{N}_q(x)}{dx^r}, \quad r=0,1,2,\dots \quad (4.6)$$

The last equation can be rewritten as

$$\langle (a^*)^r a^r \rangle = (z^*)^p z^r S_q^{(p,r)}(x) \quad (4.7)$$

where

$$S_q^{(p,r)}(x) = \frac{1}{\mathcal{N}_q(x)} \sum_{n=0}^{\infty} \left(\frac{(n+p)!(n+r)!}{[n+p]![n+r]!} \right)^{1/2} \frac{x^n}{n!} \quad (4.8)$$

with $r, p = 0, 1, 2, \dots$

Moreover, in two dimensional surface, the metric factor can be defined as [25]

$$w_q(x) = \frac{d}{dx} \langle N \rangle = \left(\frac{x \mathcal{N}_q(x)}{\mathcal{N}_q(x)} \right)' \quad (4.9)$$

where primes indicate the number of times differentiation is performed with respect to the variable x . For $x \ll 1$, one can easily reach

$$w_q(x) \approx q \left[1 - \frac{2q(1-q)}{1+q} x + \dots \right]. \quad (4.10)$$

On the other hand, the variance of the number operator N is equal to its mean, which can be evaluated using deviations from the Poisson statistics [46]

$$Q_q(x) = \frac{(\Delta N)_q^2 - \langle N \rangle_q}{\langle N \rangle_q}. \quad (4.11)$$

From Eq. (4.6), it can be found

$$Q_q(x) = x \left(\frac{\mathcal{N}_q''(x)}{\mathcal{N}_q'(x)} - \frac{\mathcal{N}_q'(x)}{\mathcal{N}_q(x)} \right). \quad (4.12)$$

For $x \ll 1$, we reach

$$Q_q(x) \approx -\frac{q(1-q)}{1+q} x + \dots. \quad (4.13)$$

5. Possible application of Quesne-type Oscillators Model to Quantum Optics

Unlike binary systems, ternary logic gates offer more information carrying capacity in quantum computing. Qutrits (three-level systems) can encode more information than classical qubits, which makes quantum circuits more efficient. In quantum computers and quantum optics, qutrit systems offer advantages such as lower error rates, lower energy consumption, and more efficient use of physical resources. In addition, qutrit logic and ternary gates are an innovative research area in quantum information processing and are less studied in the current literature.

Therefore, the study of ternary gates within the scope of the article is important for the advancement of quantum technologies, both theoretically and practically. In particular,

studying the effects of q -deformation on such systems can lead to new discoveries.

In this section, we follow the Ref. [31] to investigate the impact of q -deformation on qutrit logic gates such as cycle, self-shift, controlled cycle, controlled self-shift, Feynman, ternary Toffoli, and Fredkin gates. These gates can be expressed in the framework of angular momentum states, where their operations correspond to transformations in a quantum system characterized by total angular momentum. For example, the cycle gate effectively permutes the qutrit states, while the self-shift gate applies a shifting operation. Utilizing the Schwinger representation allows us to depict these gates in terms of ladder operators acting on the angular momentum states. This perspective provides valuable insights into how q -deformation alters the algebraic structure and functional properties of these gates.

These gates can be represented in the context of angular momentum states as

$$\mathbf{C}_n |i\rangle = |n+i\rangle \quad (5.1)$$

$$\mathbf{S}_n |i\rangle = |2i+n\rangle \quad (5.2)$$

$$\mathbf{CC}_n |ij\rangle = \frac{i(i-1)}{2} |ij+n\rangle + \frac{(2-i)(i+1)}{2} |ij\rangle \quad (5.3)$$

$$\mathbf{CS}_n |ij\rangle = \frac{i(i-1)}{2} |i2j+n\rangle + \frac{(2-i)(i+1)}{2} |ij\rangle \quad (5.4)$$

$$\mathbf{FG} |ij\rangle = |i+i+j\rangle \quad (5.5)$$

$$\mathbf{TTG} |ijk\rangle = |ij+i.j+k\rangle \quad (5.6)$$

$$\mathbf{TFG} |ijk\rangle = \frac{i(3-i)}{2} |ijk\rangle + \frac{(2-i)(i-1)}{2} |ijk\rangle \quad (5.7)$$

In the context of qubits, quantum gates are represented as unitary transformations acting on a three-dimensional Hilbert space. A qutrit is a quantum system with three possible states, and can be represented $|0\rangle$, $|1\rangle$ and $|2\rangle$. The operators on the left side of equations (5.1) – (5.7) above operate on these three quantum states to reach a different quantum state. Also, $|ij\rangle$ represents a two-qutrit state, which can be expressed as $|ij\rangle = |i\rangle |j\rangle$. The connection between q -deformed operators and conventional operators is specified as

$$a_q = a \sqrt{\frac{\phi_1 - q^{-N} \phi_2}{N(q-1)}} \quad (5.5)$$

$$a_q^* = \sqrt{\frac{\phi_1 - q^{-N} \phi_2}{N(q-1)}} a^* \quad (5.6)$$

where ϕ_1 and ϕ_2 represent arbitrary constants, a and a^* indicate the standard annihilation and creation operators, respectively. To create a qutrit, the total angular momentum number j must be equal to $j = 1$. Therefore, since $m = -j, \dots, 0, \dots, +j$, there are three different possible states ($|1 - 1 \rangle = |0 \rangle$, ($|10 \rangle = |1 \rangle$, ($|11 \rangle = |2 \rangle$). So, the q -deformed qutrit states can be expressed using the creation operators from the q -deformed algebra

$$|0 \rangle_q = \frac{(a_2^*)_q}{\sqrt{[2]!}} |\tilde{0}_1 \tilde{0}_2 \rangle \quad (5.7)$$

$$|1 \rangle_q = \frac{(a_1^*)_q (a_1^*)_q}{\sqrt{[1]!}} |\tilde{0}_1 \tilde{0}_2 \rangle \quad (5.8)$$

$$|2 \rangle_q = \frac{(a_1^*)_q^2}{\sqrt{[2]!}} |\tilde{0}_1 \tilde{0}_2 \rangle \quad (5.9)$$

where $\tilde{0}_1$ and $\tilde{0}_2$ are ground states of j and m , respectively, and $[n]! = [1][2] \dots [n]$. A general formulation of q -deformed qutrits is

$$|x \rangle_q = \frac{(a_1^*)_q^x (a_2^*)_q^{(2-x)}}{\sqrt{[x]! [(2-x)]!}} |\tilde{0}_1 \tilde{0}_2 \rangle \quad (5.10)$$

Using Eq. (5.6), Eq. (5.10) can be re-written as

$$|x \rangle_q = \left(\sqrt{\frac{\phi_1 - q^{-N_1} \phi_2}{N_1(q-1)}} a_1^* \right)^x \left(\sqrt{\frac{\phi_3 - q^{-N_2} \phi_4}{N_2(q-1)}} a_2^* \right)^{(2-x)} \frac{1}{\sqrt{[x]! [(2-x)]!}} |\tilde{0}_1 \tilde{0}_2 \rangle \quad (5.11)$$

Eqs. (5.1)-(5.7) can be re-derived by using Eq. (5.11). To meet the requirements of these expressions, it's essential to establish the arbitrary parameters. Let's demonstrate how to find these parameters using an example

$$C_1 |0 \rangle_q = |1 \rangle_q \quad (5.12)$$

In Eq. (5.11), if we put $x = 0$ to find $|0 \rangle_q$ and $x = 1$ to find $|1 \rangle_q$, we reach

$$C_1 \left(\sqrt{\frac{\phi_3 - q^{-N_2} \phi_4}{N_2(q-1)}} a_2^* \right) \left(\sqrt{\frac{\phi_1 - q^{-N_1} \phi_2}{N_1(q-1)}} a_1^* \right) \frac{1}{\sqrt{[2]!}} |\tilde{0}_1 \tilde{0}_2 \rangle =$$

$$\left(\sqrt{\frac{\phi_1 - q^{-N_1} \phi_2}{N_1(q-1)}} a_1^* \right) \left(\sqrt{\frac{\phi_3 - q^{-N_2} \phi_4}{N_2(q-1)}} a_2^* \right) |\tilde{0}_1 \tilde{0}_2 \rangle \quad (5.13)$$

From the relation $a^* |n \rangle = \sqrt{n+1} |n+1 \rangle$, one can find $\phi_1 = \phi_2 = \phi_3 = \phi_4$. Similarly, arbitrary parameters can be obtained using Eqs. (5.2)-(5.7) for other gates.

Following Ref. [30], it can be determined qutrit gates by utilizing q -deformed three-level quantum states

$$C_{nq} = \sum_{j=0}^2 |n+j \rangle_q \langle j| \quad (5.14)$$

$$S_{nq} = \sum_{j=0}^2 |2j+n \rangle_q \langle j| \quad (5.15)$$

$$CC_{nq} = \sum_{i,j=0}^2 \frac{i(i-1)}{2} |ij+n \rangle_q \langle j|i| + \sum_{i,j=0}^2 \frac{(2-i)(i+1)}{2} |ij \rangle_q \langle i|j| \quad (5.16)$$

$$CS_{nq} = \sum_{i,j=0}^2 \frac{i(i-1)}{2} |i2j+n \rangle_q \langle j|i| + \sum_{i,j=0}^2 \frac{(2-i)(i+1)}{2} |ij \rangle_q \langle i|j| \quad (5.17)$$

$$FG_q = \sum_{i,j=0}^2 |iij \rangle_q \langle j|i| \quad (5.18)$$

$$TTG_q = \sum_{i,j=0}^2 |ijij+k \rangle_q \langle kj|i| \quad (5.19)$$

$$TFG_q = \sum_{i,j=0}^2 \frac{i(3-i)}{2} |ikj \rangle_q \langle kj|i| + \sum_{i,j=0}^2 \frac{(2-i)(i-1)}{2} |ijk \rangle_q \langle k|j|i| \quad (5.20)$$

To build the q -deformed quantum ternary gates, we must identify the parameters ϕ . In the Eq. (5.14), if we take $n = 1$, we get

$$C_{1q} = |1 \rangle_q \langle 0| + |2 \rangle_q \langle 1| + q|0 \rangle_q \langle 2| \quad (5.21)$$

where we use the orthogonality relation $\langle j|i \rangle = \delta_{ij}$. Now, we consider that C_{1q} act on the state $|1 \rangle_q$, such that

$$C_{1q} |1 \rangle_q = |2 \rangle_q \quad (5.22)$$

Based on the orthogonality relation, it becomes clear that the only remaining term is the second term of Eq. (5.21). Thus, the parameters can be obtained from the orthogonality condition

$$\begin{aligned}
& {}_q \langle 1|1 \rangle_q = \langle \tilde{0}_1 \tilde{0}_2 | a_2 \left(\sqrt{\frac{\phi_7 - q^{-N_2} \phi_8}{N_2(q-1)}} \right) \\
& a_1 \left(\sqrt{\frac{\phi_5 - q^{-N_1} \phi_6}{N_1(q-1)}} \right) \\
& \left(\sqrt{\frac{\phi_1 - q^{-N_1} \phi_2}{N_1(q-1)}} \right) a_1^* \left(\sqrt{\frac{\phi_3 - q^{-N_2} \phi_4}{N_2(q-1)}} \right) a_2^* | \tilde{0}_1 \tilde{0}_2 \rangle \quad (5.23)
\end{aligned}$$

In the last Eq., one can find $\phi_1 = \phi_2$, $\phi_3 = \phi_4$, $\phi_5 = \phi_6$, and $\phi_7 = \phi_8$. Similary, for cases $\mathcal{C}_{1q}|2 \rangle_q = |0 \rangle_q$ and $\mathcal{C}_{1q}|0 \rangle_q = |1 \rangle_q$, ${}_q \langle 2|2 \rangle_q$ and ${}_q \langle 0|0 \rangle_q$ can be obtained.

5. Conclusion

In this article, we present a comprehensive analysis of q -deformed boson oscillator algebras, focusing particularly on their thermo-statistical properties and their relationship to quantum optics. In the second section, we examine AC oscillator algebras. This analysis examines the thermo-statistical properties of these algebras in detail and investigates how these algebras modify the thermal behavior of quantum systems. In this context, we provide a comprehensive assessment of how thermo-statistical parameters are modified by these algebras, examining how different thermal properties and temperature-related behaviors of quantum systems are affected. In the third section, we focus on the BM oscillator model.

This section examines the thermo-statistical properties of the BM model in detail. In this context, we delve into various thermo-statistical quantities, such as internal energy and entropy, and investigate how these quantities differ from classical systems. The fourth section is devoted to Quesne oscillator algebras, which have not received sufficient attention in the literature. In this section, we discuss the theoretical framework and practical applications of Quesne algebras, especially in the context of quantum optics. We discuss the mathematical properties of Quesne algebras, their effects on quantum states, and their potential applications in quantum optical systems. We also evaluate possible application scenarios on how these algebras can be used in quantum optics and innovative approaches in this field. In the last section, we construct q -deformed qubits by exploiting q -deformed angular momentum states, which

allows us to investigate their distinct characteristics. We study the effects of logical qubit gates on these q -deformed qubits to understand how their deformation influences the performance of quantum operations.

Although there are similarities in structure between the arbitrary parameters obtained with Reference 31 and the parameters obtained in Section 5, the main difference lies in the deformation algebra used. The arbitrary parameters obtained in Section 5 depend on the q -deformation parameter and the properties of these parameters differ from the parameters obtained in Reference 31. This difference arises due to the use of quantum algebraic properties of the Quesne oscillator system in our work. However, in Reference 31, different deformed quantum algebra is used. Our findings aim to contribute to the broader landscape of quantum information processing, offering new pathways for enhancing computational efficiency and enabling innovative quantum technologies.

Article Information Form

Funding

The author has no received any financial support for the research, authorship or publication of this study.

The Declaration of Conflict of Interest/ Common Interest

No conflict of interest or common interest has been declared by the authors.

The Declaration of Ethics Committee Approval

This study does not require ethics committee permission or any special permission.

The Declaration of Research and Publication Ethics

The authors of the paper declare that they comply with the scientific, ethical and quotation rules of SAUJS in all processes of the paper and that they do not make any falsification on the data collected. In addition, they declare that Sakarya University Journal of Science and its editorial board have no responsibility for any ethical violations that may be encountered, and that this study has not been evaluated in any academic

publication environment other than Sakarya University Journal of Science.

Copyright Statement

Authors own the copyright of their work published in the journal and their work is published under the CC BY-NC 4.0 license.

References

- [1] A. Blum, "From the Necessary to the Possible the Genesis of the Spin-Statistics Theorem," *The European Physical Journal H*, vol. 39, pp. 543-574, 2014.
- [2] G. Gentile, M. Hechinger, "Osservazioni sopra le statistiche intermedie", *Nuovo Cimento*, vol. 17, pp. 493-497, 1940.
- [3] H. S. Green, "A Generalized Method of Field Quantization," *Physical Review*, vol. 90, pp. 270, 1953.
- [4] F. Wilczek, "Fractional Statistics and Anion Superconductivity," *World Scientific*, Singapore, 1990.
- [5] C. Tsallis, "Possible generalization of Boltzmann-Gibbs statistics," *Journal of Statistical Physics*, vol. 52, pp. 479-487, 1988.
- [6] M. Masi, "A step beyond Tsallis and Rényi entropies," *Physics Letters A*, vol. 338, pp. 217-224, 2005.
- [7] M. Arik, D. D. Coon, "Hilbert spaces of analytic functions and generalized coherent states," *Journal of Mathematical Physics*, vol. 17, pp. 524-527, 1976.
- [8] L. C. Biedenharn, "The quantum group $SU_q(2)$ and a q -analogue of the boson operators," *Journal of Physics A: Mathematical and General*, vol. 22, pp. L873-L878, 1989.
- [9] A. J. Macfarlane, "On q -analogues of the quantum harmonic oscillator and the quantum group $SU_q(2)$," *Journal of Physics A: Mathematical and General*, vol. 22, pp. 4581-4588, 1989.
- [10] K. S. Viswanathan, R. Parthasarathy, R. Jagannathan, "Generalized q -fermion oscillators and q -coherent states," *Journal of Physics A: Mathematical and General*, vol. 25, pp. L335-L339, 1992.
- [11] M. Chaichian, R. Gonzalez Felipe, C. Montonen, "Statistics of q -oscillators quons and relations to fractional statistics," *Journal of Physics A: Mathematical and General*, vol. 26, pp. 4017-4034, 1993.
- [12] Y. J. Ng, "Comment on the q -analogues of the harmonic oscillator," *Journal of Physics A: Mathematical and Theoretical*, vol. 23, no. 6, pp. 1023-1027, 1990.
- [13] C. R. Lee, J. P. Yu, "On q -analogues of the statistical distribution," *Physics Letters A*, vol. 150, no. 2, pp. 63-66, 1990.
- [14] H. S. Song, S. X. Ding, I. An, "Statistical mechanical properties of the q -oscillator system," *Journal of Physics A: Mathematical and Theoretical*, vol. 26, no. 20, pp. 5197-5205, 1993.
- [15] A. Lavagno, P. Narayana Swamy, "Generalized thermodynamics of q -deformed bosons and fermions," *Physical Review E*, vol. 65, pp. 036101-1-036101-5, 2002.
- [16] G. Su, S. Cai, H. Chen, "Bose-Einstein condensation of a relativistic q -deformed Bose gas," *Journal of Physics A: Mathematical and Theoretical*, vol. 41, pp. 045007, 2008.
- [17] B. Mirza, H. Mohammadzadeh, "Thermodynamic geometry of deformed bosons and fermions," *Journal of Physics A: Mathematical and Theoretical*, vol. 44, pp. 0475003, 2011.
- [18] A. A. Marinho, F. A. Brito, C. Chesman, "Thermal properties of a solid through q -deformed algebra," *Physica A*, vol. 391, pp. 3424-3434, 2012.

- [19] E. Dil, "Q-Deformed Einstein equations," *Canadian Journal of Physics*, vol. 93, no. 11, pp. 1274-1278, 2015.
- [20] M. Senay, S. Kibaroğlu, "Thermosize effects in a q -deformed fermion gas model," *Modern Physics Letters B*, vol. 32, no. 20, pp. 1850230-1-1850230-9, 2018.
- [21] A. Lavagno, P. Narayana Swamy, "Deformed Quantum Statistics in Two Dimensions," *International Journal of Modern Physics B*, vol. 23, no. 2, pp. 235-250, 2009.
- [22] M. Senay, "High temperature thermostatical properties of deformed quantum gas in two dimensions," *Sakarya University Journal of Science*, vol. 23, pp. 1273-1278, 2019.
- [23] A. Algin, A. S. Arikan, "Thermostatical properties of the blackbody radiation and Debye crystal model through Fibonacci oscillators," *The European Physical Journal Plus*, vol. 137, pp. 1230, 2022.
- [24] A. Algin, A. S. Arikan, E. Dil, "High temperature thermostatics of fermionic Fibonacci oscillators with intermediate statistics," *Physica A: Statistical Mechanics and its Applications*, vol. 416, pp. 499-517, 2014.
- [25] M. Senay, "Entropic gravity corrected by q -statistics, and its implications to cosmology," *Physics Letters B*, vol. 820, pp. 136536, 2021.
- [26] M. Senay, S. Kibaroğlu, " q -deformed Einstein equations from entropic force," *International Journal of Modern Physics A*, vol. 33, pp. 1850218, 2018.
- [27] A. Algin, M. Senay, "Fermionic - deformation and its connection to thermal effective mass of a quasiparticle," *Physica A: Statistical Mechanics and its Applications*, vol. 447, pp. 232-246, 2016.
- [28] A. Algin, M. Senay, "High-temperature behavior of a deformed Fermi gas obeying interpolating statistics," *Physical Review E*, vol. 85, pp. 041123, 2012.
- [29] F. Ozaydin, O. E. Mustecaplıoğlu, T. Hakioglu "Powering quantum Otto engines only with q -deformation of the working substance," *Physical Review E*, vol. 108, pp. 054103, 2023.
- [30] A. A. Altintas, F. Ozaydin, C. Yesilyurt, S. Bugu, M. Arik, "Constructing quantum logic gates using q -deformed harmonic oscillator algebras," *Quantum Information Processing*, vol. 13, pp. 1035-1044, 2014.
- [31] A. A. Altintas, F. Ozaydin, C. Bayındır, " q -Deformed three-level quantum logic," *Quantum Information Processing*, vol. 19, No. 247, 2020.
- [32] F. Nutku, K. D. Sen, E. Aydiner, "Complexity study of q -deformed quantum harmonic oscillator," *Physica A: Statistical Mechanics and its Applications*, vol. 533, pp. 122041, 2019.
- [33] S. Jalalzadeh, H. Moradpour, P. V. Moniz, "Modified cosmology from quantum deformed entropy," *Physics of the Dark Universe*, vol. 42, pp. 101320, 2023.
- [34] A. Guha, J. Selvaganapathy, P. K. Das, " q -deformed statistics and the role of light fermionic dark matter in SN1987A cooling," *Physical Review D*, vol. 95, pp. 015001, 2017.
- [35] X. Y. Hou, H. Yan, G. Guo, "Thermostatics of a q -deformed relativistic ideal Fermi gas," *Journal of Statistical Mechanics: Theory and Experiment*, vol. 2020, pp. 113402, 2020.
- [36] A. Boumali, A. Bouzenada, S. Zare, H. Hassanabadi, "Thermal properties of the q -deformed spin-one DKP oscillator," *Physica A: Statistical Mechanics and its Applications*, vol. 628, pp. 129134, 2023.
- [37] A. M. Gavrilik, I. I. Kachurik, Yu. A. Mishchenko, "Quasibosons composed of two q -fermions: realization by deformed

- oscillators,” *Journal of Physics A: Mathematical and Theoretical*, vol. 44, pp. 475303, 2011.
- [38] M. Maleki, Z. Ebadi, H. Mohammadzadeh, “ q -deformed Bose statistics and the Gross-Pitaevskii equation,” *International Journal of Geometric Methods in Modern Physics*, vol. 21, pp. 2450121, 2024.
- [39] H. Mohammadzadeh, Y. A. Kalandaragh, N. Cheraghpour, F. Adli, “Thermodynamic geometry, condensation and Debye model of two-parameter deformed statistics,” *Journal of Statistical Mechanics: Theory and Experiment*, vol. 2017, pp. 083104, 2017.
- [40] L. Tao, Z. Chen, Z. Li, J. Wang, X. Xu, J. B. Xu, “Enhancing light-matter interaction in 2D materials by optical micro/nano architectures for high-performance optoelectronic devices,” *Infomat*, vol. 3, pp. 36-60, 2021.
- [41] M. Fleischhauer, A. Imamoglu, J. P. Marangos, “Electromagnetically induced transparency: Optics in coherent media,” *Reviews of Modern Physics*, vol. 77, pp. 633, 2005.
- [42] Y. Ashida, A. İmamoğlu, E. Demler, “Cavity Quantum Electrodynamics at Arbitrary Light-Matter Coupling Strengths,” *Physical Review Letters*, vol. 126, pp. 153603, 2021.
- [43] N. Boutabba, S. Grira, H. Eleuch, “Analysis of a q -deformed hyperbolic short laser pulse in a multi-level atomic system,” *Scientific Reports*, vol. 12, pp. 9308, 2022.
- [44] A. Lavagno, P. Narayana Swamy, “Thermostatistics of a q -deformed boson gas,” *Physical Review E*, vol. 61, pp. 1218-1226, 2000.
- [45] K. Huang, “Statistical Mechanics,” John Wiley and Sons, New York 1987.
- [46] C. Quesne, “New q -deformed coherent states with an explicitly known resolution of unity,” *Journal of Physics A: Mathematical and General*, vol.35, pp.9213-9226, (2002).
- [47] M. N. Hounkonnou, E. B. Ngompe Nkouankam, “New $(p, q; \mu, \nu, f)$ -deformed states,” *Journal of Physics A: Mathematical and Theoretical*, vol.40, pp.12113-12130, (2007).

Shear Capacity Prediction of Extremely-Loaded Box Culvert on Elastic Soil Using Artificial Neural Network

Yesim Tuskan^{*iD}, Dilay Yıldırım Uncu^{iD}

Manisa Celal Bayar University, Faculty of Engineering and Natural sciences, Department of Civil Engineering, Manisa, Türkiye, yesim.tuskan@cbu.edu.tr, dilay.yildirim@cbu.edu.tr

*Corresponding Author

ARTICLE INFO

ABSTRACT

Keywords:

Box culvert
Beam on elastic foundation
Traffic load
Artificial neural network
Winkler method



Article History:

Received: 11.04.2023
Accepted: 12.10.2024
Online Available: 23.10.2024

A box culvert, buried at shallow depths beneath roadways, may experience deflections caused by the dynamic impact of traffic loading and the vertical pressure exerted by the soil fill. A computational model commonly employed used to various engineering issues, including those in geotechnical applications, is the beam-on-elastic-foundation model. In this context, the Moment Distribution Method (MDM) must be applied to account for the elastic foundation. To achieve this, the internal forces acting on the ends of both exterior and interior walls are transferred to the beam-like bottom slab of the culvert, which rests on an elastic soil bed. Subsequently, the secondary internal forces are determined by refining the structural parameters, taking into account the characteristics of the elastic soil bed. This study presents the development and application of an Artificial Neural Network (ANN) model to predict the shear capacity of box culverts on elastic soil under traffic loading conditions. The proposed model is trained and validated using a comprehensive database of beam on elastic foundation solutions. The input parameters include the geometrical and mechanical properties of the culvert and the soil, as well as the loading conditions. The results of the ANN model show R^2 values of 0.9633 and 0.9581 for the training and testing sets, respectively, indicating the model's excellent accuracy. These findings suggest that the ANN model can reliably predict the shear capacity of culverts.

1. Introduction

Box culvert installation is a commonly used methods on roadways to provide drainage across roads. According to the literature, there are various procedures for installing reinforced concrete box culverts. Embankment culverts are often the focus of initial finite element analyses and are typically characterized by their installation process. These culverts are usually positioned on pre-existing or constructed soil and then covered with backfill material [1]. A box culvert buried at shallow depths beneath roadways can experience deflections due to the dynamic impact of traffic loading and the vertical pressure exerted by the soil fill. The model, configuration, and magnitude of the traffic load

affect the culvert's response. Vertical soil stress increment, horizontal soil pressure, the culvert's self-weight, and wheel load are the major forces encountered in a culvert.

Yankelevsky [2] examined the behavior of a rigid box culvert when buried in a non-linear medium, exploring various factors. The research focuses on design aspects such as compressibility, stiffness, settlement, displacement due to trench wall slope, and depth-related stress variations. Kim and Yoo [3] indicated that sloping soils excavated for trench installation maintain higher resulting pressure than those with vertical walls. Beaver et al. [4] utilized a quantitative method to evaluate the structural and hydraulic performance of over 47,000 culverts installed

and managed by the Utah Department of Transportation. Their culvert inspections primarily included metal, concrete, and plastic culverts up to five feet in diameter, with numeric performance ratings determined. Pimentel et al. [5] investigated the pressure distribution on the top slab of culverts and observed a significant reduction due to soil-structure interaction. Bennett et al. [6] concluded that the geometry of the structure affected the pressure on the culvert under a high embankment. Abolmaali and Garg [7] conducted an assessment on the shear capacity of precast reinforced concrete box culverts.

The study involved subjecting six full-scale 2.4 m (8 ft) span box culverts to failure under the AASHTO HS-20 wheel load. Each culvert underwent incremental loading until failure, with crack initiation and propagation meticulously identified and recorded at each load stage. In some specimens, the absence of top slab compression distribution steel during fabrication was noted; however, experimental evidence suggested that this factor had a insignificant impact on the culvert's performance.

3D numerical analyses of culverts conducted by Petersen [8] showed that the pavement spread the load and shielded the culvert. Wood et al. [9] compared measured demands with predicted values using analytical tools during load testing of box culverts and found that pavement stiffness plays an important role in reducing live loads on the culvert's roof. The effect of the wheel loads from traffic is a significant factor in the performance of culverts installed at shallow depths. Additionally, the live load carrying rating must be determined to assess the culvert's load capacity. Three major factors influence load capacity: culvert load capacity, dead load demand, and live load demand for moment and shear [10]. Wood et al. [11] studied both a 2D direct-stiffness structural-frame model and a 2D linear-elastic finite element soil-structure interaction model.

The culvert structure is designed as a rigid frame using the Moment Distribution Method (MDM), a well-known method to determine the final distributed moments based on the relative stiffness of the slab and vertical walls [12]. MDM

calculations, which involve successive cycles of computation, can be stopped after several iterations, providing a very accurate approximate analysis. In this method, each element of rigid box-type culvert, such as the top and bottom slabs, and the interior and exterior walls is treated as a beam-like element, with the corners of the box clamped.

The MDM requires the fixed-end moments at the top slab of the culvert from the uniform surcharge load, referred to as critical vertical pressure, the fixed-end moments at the bottom slab from uniform vertical earth pressure, and the fixed-end moments on the exterior walls from lateral earth pressure due to cohesionless soil. These moments are then distributed and carried over accordingly [13].

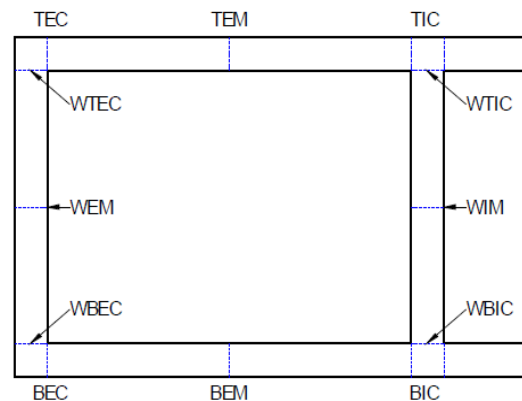


Figure 1. Internal forces at the corners and mid-spans of each elements of culvert

The primary internal forces related to the wall top interior corner (WTIC), top exterior corner (TEC), top interior corner (TIC), top exterior mid-span (TEM), and wall top exterior corner (WTEC) are calculated by considering the fixed-end moments and external loads (Figure 1). Finally, the diagrams for normal forces (kN), shear forces (kN) and moments (kN.m) are determined at the corners and mid-spans of each elements of the culvert.

2. Shear Capacity Prediction of a Box Culvert Under Critical Live Load as per Beams on Elastic Foundation Approach Using Artificial Neural Network

The computational model of a beam on an elastic foundation is frequently used to solve various engineering problems, particularly in geotechnical applications. In this case, the MDM

results need to be adapted to the elastic foundation. For this aim, the internal forces at the ends of the exterior and interior walls are applied to the beam-like bottom slab of the culvert resting on an elastic soil bed. The secondary internal forces are calculated by refining the structural factors, taking into account the elastic soil bed.

2.1. Vertical pressure calculation by Boussinesq Method on top slab of box culvert subjected to traffic load

Boussinesq [14] solved the problem of tension arising from a single load on the surface in a linear, elastic, homogeneous, isotropic, and semi-infinite medium. According to this solution, the vertical stress at any depth below the earth's surface due to a single surface load is expressed follows:

$$\sigma_z = \frac{3}{2\pi} \frac{1}{[1+(r/z)^2]^{5/2}} \cdot \frac{P}{z^2} \quad (1)$$

where P is the point wheel load (Truck geometry: H₃₀-S₂₄, W_{truck}=300 kN, wheel loads; P_{front}=3 tons, P_{rear}=P_{middle}=12 tons, s=75 cm, t=34 cm), r is radial distance from point wheel load and z: soil depth above the box culvert.

For practical purposes, it can be assumed that the stress approaches zero at a finite depth. A grid system was established on the platform, and the stress at the considered depth for each grid point was determined by applying the superposition of wheel loads from trucks travelling in the two different directional lanes on the same platform roadway. This was done by integrating the equation for a line load over a uniformly loaded rectangular area. The following equation provides the desired stress superposition [15].

$$\begin{aligned} \sigma_z &= q_0 \left(\frac{1}{4\pi} \right) \left[\frac{2mn\sqrt{(m^2+n^2+1)}}{(m^2+n^2+1+m^2n^2)} \frac{(m^2+n^2+2)}{(m^2+n^2+1)} \right. \\ &\quad \left. + \arctan \frac{2mn\sqrt{(m^2+n^2+1)}}{(m^2+n^2+1-m^2n^2)} \right] \quad (2) \end{aligned}$$

Where σ_z ; superposition of vertical pressure subjected to each wheel load at the considered depth z, q_0 ; the contact stress at the surface {P/(s.t)}, $m=x/z$, $n=y/z$, x-y; length and width of

the uniformly loaded area and z; depth from surface to point where stress increase is desired [16].

2.2. Lateral earth pressure acting on side walls of box culvert

According to Coulomb's theory, the active coefficient factor of active lateral earth pressure in cohesionless soil were calculated by using Eq 3a and 3b:

$$K_A = \frac{\sin^2(\beta+\phi)}{\sin^2\beta \sin(\beta-\delta) \left[1 + \sqrt{\frac{\sin(\phi+\delta) \sin(\phi-\alpha)}{\sin(\beta-\delta) \sin(\alpha+\beta)}} \right]^2} \quad (3a)$$

$$\sigma_h = K_A \gamma_s (z+h_{eq}) \quad (3b)$$

Then the increase in horizontal pressure due to live load was obtained from Eq 4:

$$\Delta P = K_A h \gamma_s h_{eq} \quad \{\Delta P = \sigma_z\} \quad (4)$$

where K_A ; active lateral earth pressure coefficient, δ is angle of internal friction of soil, ϕ ; batter angle of wall; β is angle of friction between the wall and the cushion, α ; slope of the cushion top surface, γ_s ; unit weight of soil, z; depth below the surface of earth at pressure surface (h_{eq} should be added to the original soil depth z in case of surcharge loads). σ_z ; vertical pressure due to surcharge load, ΔP ; constant horizontal earth pressure due to live load surcharge and h_{eq} ; equivalent height of soil for traffic load.

2.3 Elastic soil under box culvert

The Winkler method [17] assumes that the reaction forces at each point of the foundation under external loads are proportional to the deflection of the beam at that point, following Hooke's law (Figure 2).

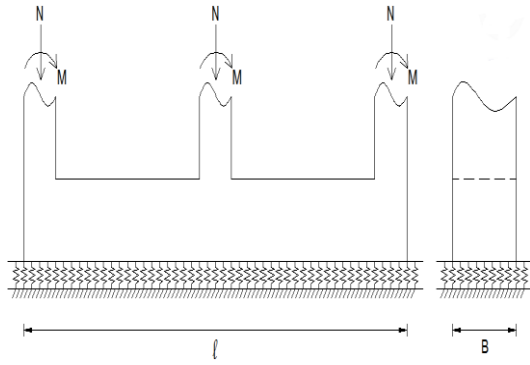


Figure 2. Beam on elastic foundation

The elasticity of the foundation, characterized by Winkler's constant, K which includes the effect of the width of the beam, the force called the modulus of the foundation K_o . λ are described by the following equations 5 and 6 [18]:

$$K = K_o \cdot B \tag{5}$$

$$\lambda = \sqrt[4]{\frac{K}{4EI}} \tag{6}$$

In this study, internal forces such as moments and shear forces at the lower ends of the baffle and side walls are calculated by using the Moment Distribution Method (MDM) and are subsequently applied to the unit width of the lower slab over elastic soil bed, in accordance with the following equations.

Moments and shear forces equations of unit width beam-like slab on elastic foundation for concentrated load can be expressed as:

$$M_{(x)} = \frac{1}{2\lambda} \beta_{MP}^{(x)} \frac{1}{(\sinh^2 \lambda l - \sin^2 \lambda l)} \{2 \sinh \lambda x \cdot \sin \lambda x (\sinh \lambda l \cdot \cos \lambda a \cdot \cosh \lambda b - \sin \lambda l \cdot \cosh \lambda a \cdot \cos \lambda b) + (\cosh \lambda x \cdot \sin \lambda x - \sinh \lambda x \cdot \cos \lambda x) \cdot [\sinh \lambda l (\sin \lambda a \cdot \cosh \lambda b - \cos \lambda a \cdot \sinh \lambda b) + \sin \lambda l (\sinh \lambda a \cdot \cosh \lambda b - \cosh \lambda a \cdot \sin \lambda b)]\} \tag{7}$$

$$Q_{(x)} = P \beta_{QP}^{(x)} \frac{1}{\sinh^2 \lambda l - \sin^2 \lambda l} \{(\cosh \lambda x \cdot \sin \lambda x + \sinh \lambda x \cdot \cos \lambda x) (\sinh \lambda l \cdot \cos \lambda a \cdot \cosh \lambda b - \sin \lambda l \cdot \cosh \lambda a \cdot \cos \lambda b) + \sinh \lambda x \cdot \sin \lambda x [\sinh \lambda l (\sin \lambda a \cdot \cosh \lambda b - \cos \lambda a \cdot \sinh \lambda b) + \sin \lambda l (\sinh \lambda a \cdot \cosh \lambda b - \cosh \lambda a \cdot \sin \lambda b)]\} \tag{8}$$

Moments and shear forces equations of unit width beam-like slab on elastic foundation for concentrated moment can be expressed as:

$$M_{(x)M} = -M \delta_{MM}^{(x)} = -M \frac{1}{(\sinh^2 \lambda l - \sin^2 \lambda l)} \{ \sinh \lambda x \cdot \sin \lambda x [\sinh \lambda l (\cosh \lambda b \cdot \sin \lambda a + \sinh \lambda b \cdot \cos \lambda a) + \sinh \lambda l (\sinh \lambda a \cdot \cos \lambda b + \cosh \lambda a \cdot \sin \lambda b)] - [(\cosh \lambda x \cdot \sin \lambda x - \sinh \lambda x \cdot \cos \lambda x) (\sin \lambda l \cdot \cos \lambda b \cdot \cosh \lambda a + \sin \lambda l \cdot \cosh \lambda b \cdot \cos \lambda a)] \} \tag{9}$$

$$Q_{(x)M} = -\lambda M \beta_{QM}^{(x)} = \frac{M}{e} \lambda \frac{1}{(\sinh^2 \lambda l - \sin^2 \lambda l)} \{(\cosh \lambda x \cdot \sin \lambda x + \sinh \lambda x \cdot \cos \lambda x) [\sinh \lambda l (\cosh \lambda b \cdot \sin \lambda a + \sinh \lambda b \cdot \cos \lambda a) + \sin \lambda l (\sinh \lambda a \cdot \cos \lambda b + \cosh \lambda a \cdot \sin \lambda b)] - 2 \sinh \lambda x \cdot \sin \lambda x (\sin \lambda l \cdot \cos \lambda b \cdot \cosh \lambda a + \sin \lambda l \cdot \cosh \lambda b \cdot \cos \lambda a)\} \tag{10}$$

Concentrated load and concentrated moment in accordance with integral of a beam on an elastic foundation are described by the following equations:

$$M_{(x)} = -M \delta_{MM}^{(x)} \tag{11}$$

$$Q_{(x)} = -\lambda \beta_{QM}^{(x)} = -\frac{\lambda l}{l} M \beta_{QM}^{(x)} = -M \delta_{QM}^{(x)} \tag{12}$$

$$M_{(x)} = PL \frac{1}{\lambda l} \beta_{MP}^{(x)} = Pl \delta_{MP}^{(x)} \tag{13}$$

$$Q_{(x)} = P \beta_{QP}^{(x)} = P \delta_{QP}^{(x)} \tag{14}$$

3. Case Study

The observed rigid two-cell box-shaped culvert is aligned perpendicularly to the two-lane highway. The cushion material lies under a 250 mm asphalt concrete pavement.

A parametric study is conducted to assess the effect of the soil parameters, burial depth, box culvert dimensions (mm), and traffic load (kN) (Figure 3).

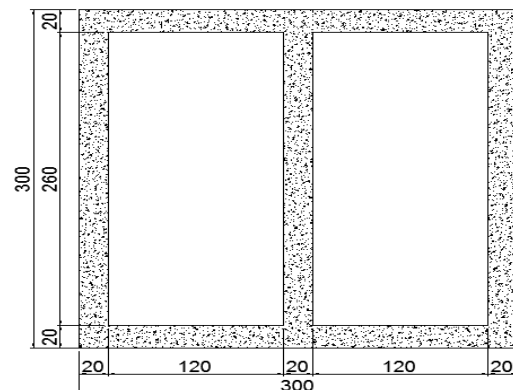


Figure 3. The cross-section of the box culvert

The culvert extends under the sloping embankment area on each side of the road. The embankment has a dry unit weight of about 18 kN/m^3 , a saturated unit weight of 21 kN/m^3 and shear strength parameter of $\phi=40^\circ$, $c=5 \text{ kN/m}^2$, with $K_0=50000$, $E=3 \times 10^7 \text{ kN/m}^2$, and $I=6.6 \times 10^{-4} \text{ m}^4$. The wheel spacing of design vehicle (Figure 4) was 1.8 m. (6 ft.) according to H₃₀-S₂₄ truck axle loads. Since truck types with long rear axle distances are generally more common, the distance between the rear axles was chosen to be long.

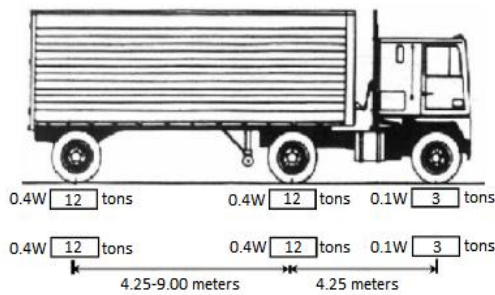


Figure 4. H₃₀-S₂₄ truck axle loads

3.1. Critical vertical pressure subjected to wheel load and uniform surcharge load

Although the front axial load is much lower than those of rear axles, its contribution is included in calculating the superposition of all wheel loads of two design trucks by Boussinesq's [14] equation.

In this study, a 300 kN-load per wheel is considered for two design trucks with three axles each, traveling in opposing directions. It was determined that the second case has the highest vertical pressure. Therefore, the maximum pressure over the culvert is calculated as 2.27 kN/m^2 and is taken as uniform surcharge load in design (Figure 5).

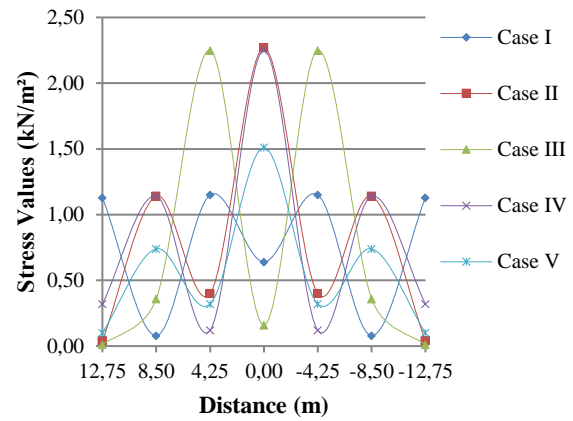


Figure 5. Stress distributions on the axis according to the loading conditions

To determine the extreme loading conditions for tridem-trucks traveling simultaneously in two lanes, five possible passing scenarios are considered as Case I: The front axles overlapped at one line, Case II: The middle axles overlapped at one line, Case III: The mid-spans of trailer lengths overlapped at one line, Case IV: The rear axles overlapped at one line and Case V: The cross axles overlapping (Figure 6).

The critical vertical pressure can be calculated using Eq 2. The vertical pressure combinations from the wheel loads were evaluated for the five possible passing conditions of trucks (Figure 6). The different distributions of wheel load recommended by proposed scenarios caused the vertical pressure concentration affecting the top slab shear resistance of the culvert. For the highest wheel load concentration, the stress was greatest between the edge and the center, as shown in Figure 6.

An analytical solution to the beam problem on an elastic foundation is investigated to obtain the improved final bending moments and shear forces from the secondary structural analysis, as presented in Figure 7.

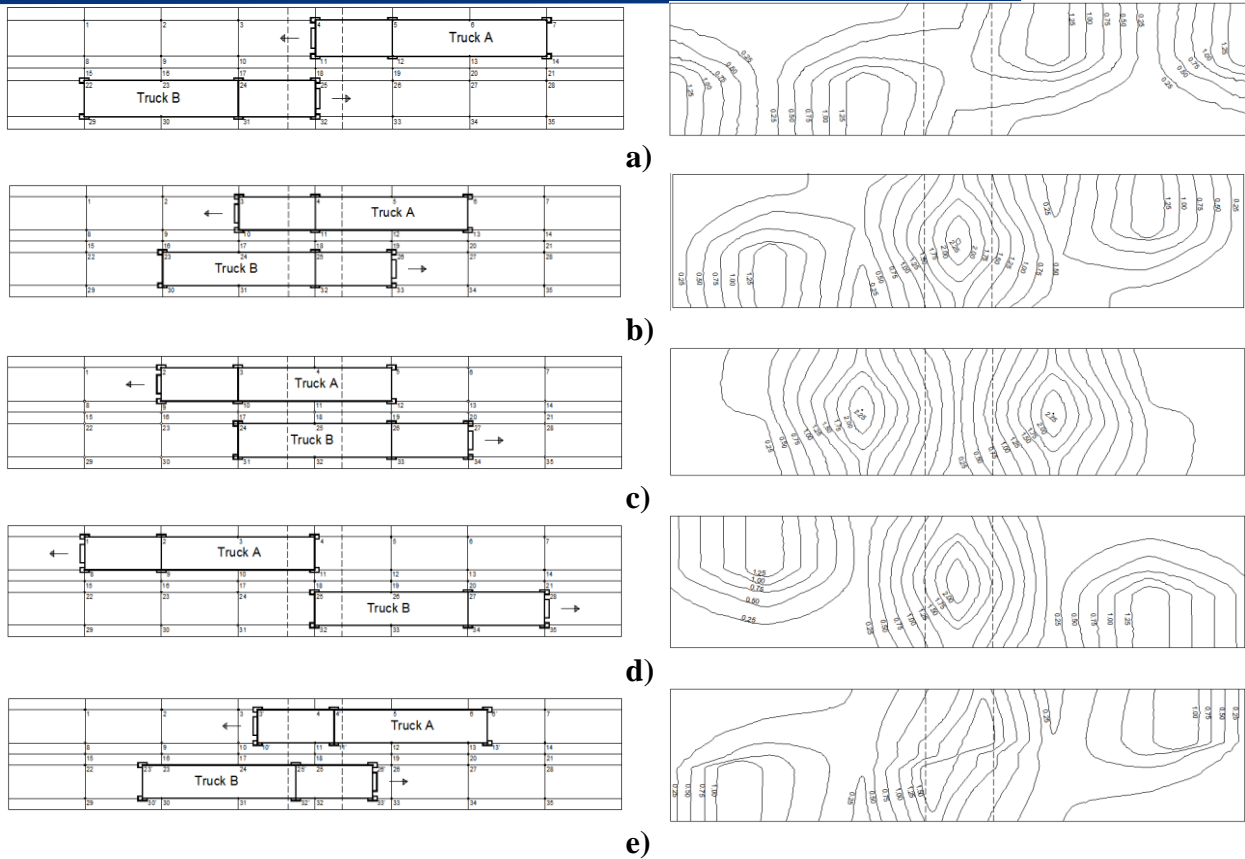


Figure 6 The situations of the truck passing positions and relevant stress distribution: a) Case I: The front axles overlapped at one line, b) Case II: The middle axles overlapped at one line, c) Case III: The mid-spans of trailer lengths overlapped at one line, d) Case IV: The rear axles overlapped at one line and e) Case V: The cross axles overlapping

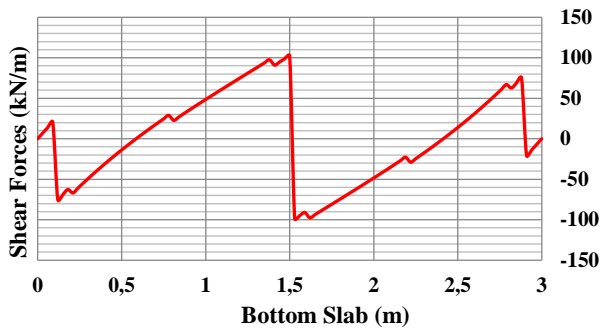
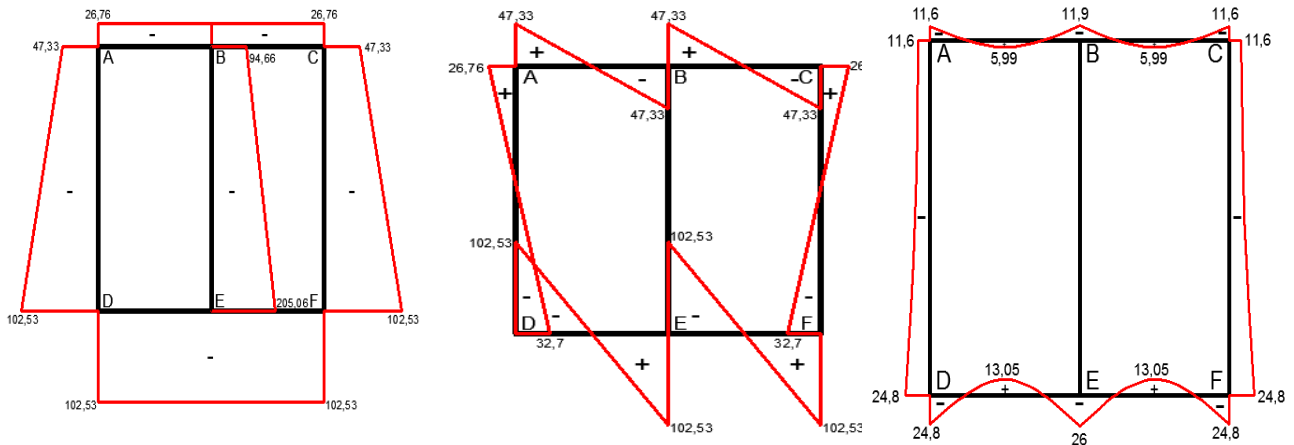


Figure 7. Shear diagram of box culvert as beam on elastic foundation

The diagrams for normal forces (kN), shear forces (kN) and moments (kN.m) are presented in Figure 8 (a, b, c) respectively.

The overall results for the beam on elastic foundation analysis, including the input parameters such as the geometrical and mechanical properties of the culvert and soil, as well as the loading conditions, along with the output parameter of the shear capacity of the top slab, are summarized in Table 1.



(a) **(b)** **(c)**
Figure 8. (a) The normal forces (kN), **(b)** shear forces (kN) and **(c)** moments (kN.m)

Table 1. Results of shear capacity on box culvert used for training and testing set

	Data Number	Depth of cushion (hr) (mm)	Height of culvert (H) (mm)	Width of culvert (B) (mm)	Thickness of top slab (t _{ts}) (mm)	Soil friction angle (φ)	Soil unit weight (γ)	Wheel load (WL) (kN)	FS _{shear}
Training Set	1	700	1100	1100	110	30	18	30	1.08
	2	750	1100	1100	110	30	18	30	1.17
	3	800	1100	1100	110	30	18	30	1.259
	4	850	1100	1100	110	30	18	30	1.345
	5	900	1100	1100	110	30	18	30	1.428
	6	950	1100	1100	110	30	18	30	1.507
	7	1000	1100	1100	110	30	18	30	1.582
	8	700	1200	1200	120	30	18	30	1.115
	9	750	1200	1200	120	30	18	30	1.208
	10	800	1200	1200	120	30	18	30	1.299
⋮									
	112	950	1100	1100	110	40	19	40	1.447
Testing Set	113	800	2000	2000	200	40	19	40	1.315
	114	850	2000	2000	200	40	19	40	1.404
	115	900	2000	2000	200	40	19	40	1.489
	116	950	2000	2000	200	40	19	40	1.57
	117	1000	2000	2000	200	40	19	40	1.645
	118	700	3000	3000	300	40	19	40	1.125
	119	750	3000	3000	300	30	19	40	1.218
	120	800	2000	2000	200	30	19	40	1.315
	121	850	2000	2000	200	30	19	40	1.404
	122	900	2000	2000	200	30	19	40	1.489
⋮									
	140	1000	3000	3000	300	40	19	40	1.655

4. Artificial Neural Networks

Artificial Neural Networks (ANNs) are sophisticated computational models inspired by the behavior of the human brain and nervous system. Emerging artificial intelligence techniques have shown great sensitivity in predicting actual values without lengthy observational processes [19,20].

At this point, artificial neural networks (ANNs) have clear advantages in addressing complex non-linear problems in the field of civil the optimum weight combination of these neurons of feed-forward neural networks with various combinations of network and training parameters, including number of hidden layers is the back-propagation (BP) algorithm [27] Feed-

engineering [21,22]. These complex relationships are estimated by artificial neural networks with high accuracy [23-26]. In this regard, ANNs offer several advantages over more conventional computing techniques.

A typical ANN architecture is constitutes by layers including an input layer, one or more hidden layer(s) and an output layer. Each layer basically contains a number of neurons working as an independent processing element and densely interconnected with each other. The method most commonly used for finding

forward neural network is trained by a fastest BP algorithm called Levenberg-Marquardt [27] Levenberg-Marquardt was used to improve the speed and general performance of BP [27]. An activation function governs a summing process

by multiply inputs by its weights. Training process terminates its cycles with a minimal sum squared error.

ANNs have a natural property for storing experiential knowledge of data and making it available for use of the problem solving as an interconnected group of artificial neurons [27]. According to above mentioned definitions, an ANN is considered one of the most powerful techniques inspired by the human-brain information process in soft computation method [28].

The assignment of the ANN architecture is difficult task to obtain. Currently, there is no analytical way of defining the network structure as a function of the complexity of the problem to achieve the desired accuracy.

An optimal ANN architecture is considered as the one yielding the best performance in terms of error minimization, while retaining a simple and compact structure [27]. Specifying the network architecture and detecting the optimal values for the connection weights of a training algorithm constitutes two main issues concerning the implementation of the ANN. The architecture arranged in a sequence of layers, one for the input, one for hidden layer and one for the output was used for ANN model (Figure 9).

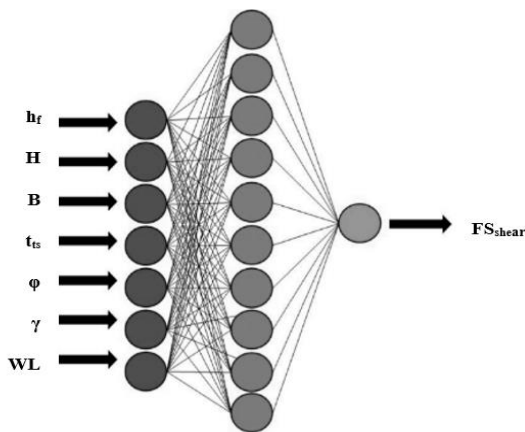


Figure 9. The ANN's architecture

Data from several scenarios were determined by utilizing an ANN architecture consisting of one input layer, one hidden layer, and one output layer. The data derived from the several shear capacity calculations have identified that, even by using one hidden layer, any complex function in a network can be solved [29]. Thus, one hidden

layer was selected in the ANN model using 10 hidden neurons provides the most accurate and minimum error.

Developing an optimum ANN architecture is a time-consuming operation because of the insufficient nonlinear relationship between input and output layers of the small structures [30]. However, a large structure provides a complex problem and requires a significant amount of time to train without well generalization. The literature shows that the number of neurons in the hidden layer (N_{hn}) has a significant effect on the system's nonlinearity [31]. Thus, N_{hn} is the key factor for a proper mapping in which data flows between the input and output layers, resulting in good predicting using ANN.

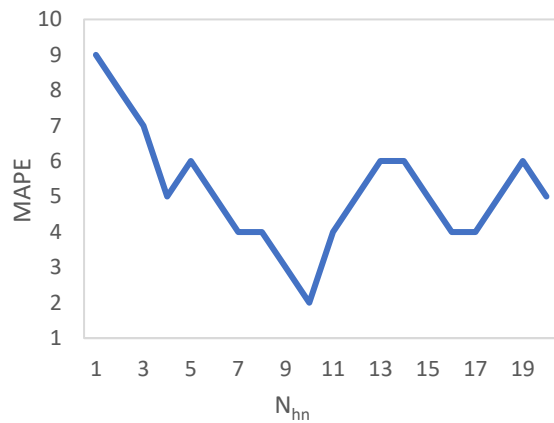


Figure 10. MAPE- N_{hn} relation of the ANN architecture.

The prediction performance and the influence of the N_{hn} has been evaluated using mean absolute percentage error (MAPE). The minimum MAPE has been reached in the combination with $N_{hm} = 10$, showing the optimum architecture (Figure 10).

Table 2. Details of the parameters used for the ANN model

Data Type	Model Parameters	Minimum Value	Maximum Value	Mean Value
Input	Depth of cushion (h_f) (mm)	700	1000	850
	Height of culvert (H) (mm)	1100	3000	1754.29
	Width of culvert (B) (mm)	1100	3000	1754.29

Thickness of top slab (t_{ts}) (mm)	110	300	175.43	
Soil friction angle (ϕ)	30	40	35	
Soil unit weight (γ)	18	19	18.50	
Wheel load (WL) (kN)	30	40	35	
Output	FS_{shear}	1.03	1.72	1.38

Subsequently, the data classification of the ANN model is based on the use of 80% of the data for training and 20% for testing, as suggested by Shahin et al. [32]. The network capacity is characterized by testing phase results emphasizing data generalization. In the model, LM algorithm is utilized to assemble the ANN model, while applying log sigmoid as the transfer function. The details of the parameters examined throughout the ANN analysis are dedicated in Table 2 for proposed scenarios.

5. Results and Discussion

Based on different scenarios of extreme loading of reinforced concrete culvert with different geometries and soil conditions, the ANN values modeled by multi-layer perception were shown in Figs. 11 and 12. An overall good agreement between ANN model and conventional results of beam on elastic foundation has been found.

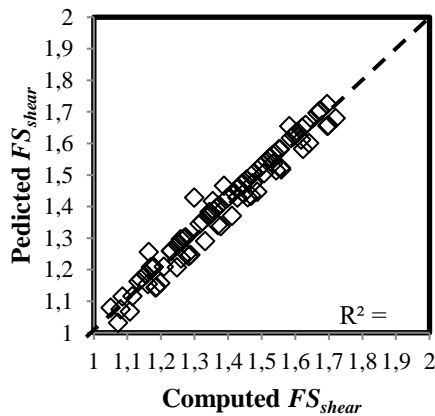


Figure 11. The comparison of the computed FS_{shear} of top slab values with the predicted FS_{shear} of top slab values from the ANN model for training samples

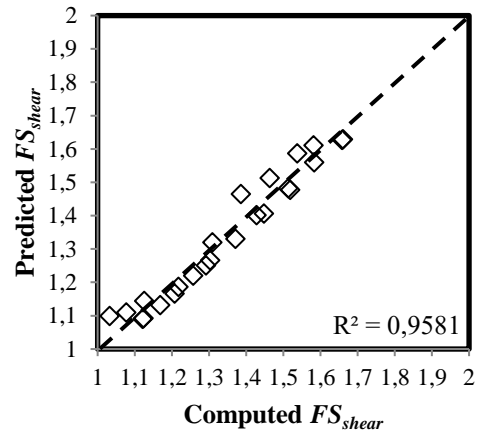


Figure 12. The comparison of the computed FS_{shear} of top slab values with the predicted FS_{shear} of top slab values from the ANN model for testing samples

Subsequently, the performance of the ANN was evaluated in Table 3 with four factors: coefficient of determination (R^2), mean absolute error (MAE), variance accounted for (VAF) and mean square error (RMSE) to predict the accuracy of the proposed ANN model. The suitability of the model was verified with the ranges of performance indices.

Table 3. Performance indices (R^2 , RMSE, MAE and VAF) of the ANN and model

Model	Data	R^2	RMS E	MA E	VA F
ANN	Trainin g set	96.3	0.82	0.43	95.2
	Testin g set	95.8	1.23	0.76	94.7
	Trainin g set	96.3	0.82	0.43	95.2
	Testin g set	95.8	1.23	0.76	94.7

It is noted from the results of the ANN model has the R^2 value of 0.9633 and 0.9581 for training and testing set, respectively indicating a perfect accuracy of the proposed model in this study.

6. Conclusion

In this study, the efficiency of the ANN model to predict the shear capacity of top slab (FS_{shear}) has been investigated and compared. To achieve this, the FS_{shear} values were computed by changing the applied wheel load, soil friction angle, box culvert geometry and fill conditions from road level and utilized in the simulation of the ANN model. The input parameters used in the ANN model are five geotechnical parameters containing geometry component of box culvert (H , B , and t_{ts}), soil condition (ϕ and γ_{soil}) and

traffic condition (wheel load, WL) with depth of cushion (h_f). The output parameter of the model is the computed shear capacity of top slab (FS_{shear}) by using beam on elastic foundation approach.

It can be concluded that the ANN model developed in this study can be used for the estimation of the FS_{shear} value and so for the determination of the top slab shear capacity of extremely loaded reinforced concrete culvert on elastic soil.

In conclusion, the suitability of the model has been rigorously evaluated through comprehensive performance index evaluations, and the findings confirm the model's outstanding accuracy, demonstrating its potential as a reliable method for the chosen rear axle distance. However, for future research efforts, it would be appropriate to investigate comparative analyses with different axle distances using various soft-computing methodologies.

Article Information Form

Funding

The author(s) has no received any financial support for the research, authorship or publication of this study.

Authors' Contribution

The authors contributed equally to the study.

The Declaration of Conflict of Interest/ Common Interest

No conflict of interest or common interest has been declared by the authors.

The Declaration of Ethics Committee Approval

This study does not require ethics committee permission or any special permission.

The Declaration of Research and Publication Ethics

The authors of the paper declare that they comply with the scientific, ethical and quotation rules of SAUJS in all processes of the paper and that they do not make any falsification on the data collected. In addition, they declare that Sakarya University Journal of Science and its editorial

board have no responsibility for any ethical violations that may be encountered, and that this study has not been evaluated in any academic publication environment other than Sakarya University Journal of Science.

Copyright Statement

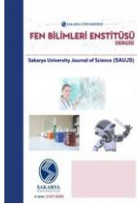
Authors own the copyright of their work published in the journal and their work is published under the CC BY-NC 4.0 license.

References

- [1] W. D. Lawson, T. A. Wood, C. D. Newhouse, P. W. Jayawickrama, "Evaluating Existing Culvert for Load Capacity Allowing for Soil Structure Interaction". *Multidisciplinary Research in Transportation*, 2010.
- [2] David Z. Yankelevsky., "Loads on Rigid Box Buried in Nonlinear Medium", *Journal of Transportation Engineering*, Vol. 115, No. 5, September, 1989. @asce, ISSN 0733-947X/89/0005-0461. Paper No. 23870.
- [3] K. Kim, C. Yoo, "Design Loading for Deeply Buried Box Culverts", *Highway Research Center, Auburn University*, 2002.
- [4] J. L. Beaver, T. J. McGrath, B. Leonard, "Condition Assessment of Utah Highway Culverts and Determination of Culvert Performance Measures", In *Critical Transitions in Water and Environmental Resources Management*, 2004, pp. 1-10.
- [5] M. Pimentel, P. Costa, C. Félix, J. Figueiras, "Behavior of reinforced concrete box culverts under high embankments", *Journal of Structural Engineering*, vol.135, no.4, pp.366-375, 2009.
- [6] R. M. Bennett, S. M. Wood, E. C. Drumm, N. R. Rainwater, "Vertical loads on concrete box culverts under high embankments", *Journal of Bridge Engineering*, vol. 10, no. 6, pp. 643-649, 2005.

- [7] A. Abolmaali, A. K. Garg, "Effect of Wheel live load on Shear Behaviour of Precast Reinforced Concrete Box Culverts." *Journal of Bridge Engineering*, Vol. 13, No.1, January 1, 2008, @ ASCE, ISSN 1084-0702/200/1-93-99.
- [8] D. L. Petersen, "Recommended design specifications for live load distribution to buried structures", *Transportation Research Board*, vol. 647, 2010.
- [9] T. A. Wood, W. D. Lawson, P. W., Jayawickrama, C. D. Newhouse, "Evaluation of production models for load rating reinforced concrete box culverts", *Journal of Bridge Engineering*, vol. 20, no.1, 04014057, 2015.
- [10] W. D. Lawson, T. A. Wood, C. D. Newhouse, P. W. Jayawickrama, "Evaluating existing culverts for load capacity allowing for soil structure interaction", Texas DOT, Austin, TX, 2010.
- [11] T. A. Wood, W. D. Lawson, P. W. Jayawickrama, "Newhouse, Evaluation of Production Models for Load Rating Reinforced Concrete Box Culverts", *The Journal of Bridge Engineering*, pp.1-12, 2014.
- [12] N. Kolate, M. Mathew, S. Mali, "Analysis and Design of RCC Box Culvert", *International Journal of Scientific & Engineering Research*, 5(12), 2014.
- [13] W. F. Chen, J. Y. Liew, "The Civil Engineering Handbook", Second Edition, National University of Singapore, CRC Press. 2003.
- [14] J. Boussinesq, "Application des potentiels à l'étude de l'équilibre et du mouvement des solides élastiques: Principalement au calcul des déformations et des pressions que produisent, dans ces solides, des efforts quelconques exercés sur une petite partie de leur surface ou de leur intérieur; mémoire suivi de notes étendues sur divers points de physique mathématique et d'analyse", Gauthier-Villars, 1885.
- [15] R. A. Cook, D. Bloomquist, "Report on Evaluation of Precast Box Culvert Systems: Part 2-Design Live Loads on Box Culverts", Department of Civil Engineering, University of Florida, Project No. 4910 4504 857 12. 2002.
- [16] ASCE, "Standard Practice for Direct Design of Buried Precast Concrete Pipe Using Standard Installations (SIDD)", (ASCE 15-98), American Society of Civil Engineers, Reston, Virginia. 2000.
- [17] E. Winkler, "Die Lehre Von Elasticität Und Festigkeit". 1st Edn., H. Dominicus, Prague, 1867.
- [18] M. Hetenyi, "Beams on elastic foundation, Waverly press, Baltimore, 1946.
- [19] S. Lee, J. H. Ryu, I. S. Kim, "Landslide susceptibility analysis and its verification using likelihood ratio, logistic regression, and artificial neural network models: Case study of Youngin, Korea", *Landslides*, vol. 4, pp. 327-338. 2007.
- [20] S. Karimi, O. Kisi, J. Shiri, O. Makarynsky, "Neuro-fuzzy and neural network techniques for forecasting sea level in Darwin Harbor, Australia", *Computers and Geosciences*, vol. 52, pp. 50-59, 2013.
- [21] Y. Erzin, Y. Tuskan, "Prediction of standard penetration test (SPT) value in Izmir, Turkey using radial basis neural network", *Celal Bayar University Journal of Science*, vol.13, no.2, pp.433-439, 2017.
- [22] S. A. Yildizel, Y. Tuskan, G. Kaplan, "Prediction of skid resistance value of glass fiber-reinforced tiling materials", *Advances in Civil Engineering*, 2017.
- [23] B. Y. Dagli, Y. Tuskan, D. Uncu, "Artificial Neural Networks For Hydraulic Systems", *Research and Reviews In Engineering*–Summer, 2019, 85.

- [24] Y. Tuskan, B. Y. Dagli, D. Uncu, "The Use Of Artificial Neural Networks (Anns) In Geotechnics", *Research and Reviews In Engineering–Summer*, 2019, 225.
- [25] Y. Erzin, Y. Tuskan, "Prediction of Standard Penetration Test (SPT) Value in Izmir, Turkey using General Regression Neural Network", In *International Conference on Agricultural, Civil and Environmental Engineering (ACEE-16) April 2016*, pp. 18-19.
- [26] Y. Erzin, Y. Tuskan, "The use of neural networks for predicting the factor of safety of soil against liquefaction", *Scientia Iranica*, vol.26, no.5, pp. 2615-2623, 2019.
- [27] H. Sonmez, C. Gokceoglu, H. A. Nefeslioglu, A. Kayabasi, "Estimation of rock modulus: For intact rocks with an artificial neural network and for rock masses with a new empirical equation". *International Journal of Rock Mechanics and Mining Sciences*, vol. 43, no.2, pp.224-235, 2006.
- [28] N. Q. Hung, M. S. Babel, S. Weesakul, N. K. Tripathi, "An artificial neural network model for rainfall forecasting in Bangkok, Thailand", *Hydrology and Earth System Sciences*, vol. 13, no.8, pp.1413-1425, 2009.
- [29] E. Ebrahimi, M. Monjezi, M. R. Khalesi, D. J. Armaghani, "Prediction and optimization of back-break and rock fragmentation using an artificial neural network and a bee colony algorithm", *Bulletin of Engineering Geology and the Environment*, vol. 75, pp. 27-36, 2016.
- [30] T. K. Gupta, K. Raza, "Optimization of ANN architecture: a review on nature-inspired techniques". *Machine learning in bio-signal analysis and diagnostic imaging*, pp.159-182, 2019.
- [31] N. Singh, A. Singh, M. Tripathy, "Selection of hidden layer neurons and best training method for ffnn in application of long-term load forecasting". *Journal of electrical engineering*, vol.63, no.3, pp.153-161, 2012.
- [32] M. A. Shahin, H. R. Maier, M. B. Jaksa, "Data division for developing neural networks applied to geotechnical engineering". *Journal of Computing in Civil Engineering*, vol.18, no.2, pp.105-114, 2004.



A Review of Structural Systems to be Built on Planets

Serra Çelik Kıratlı* , Ali Osman Kuruşçu 

Yıldız Technical University, Faculty of Architecture, Department of Architecture, İstanbul, Türkiye, serracelikkiratli@gmail.com, okuruscu@yildiz.edu.tr

*Corresponding Author

ARTICLE INFO

ABSTRACT

Keywords:

Planets
Structural Systems
Pneumatic Systems
Space
Multi-criteria decision making

The architectural construction process on planets is an architectural issue that develops day by day due to extreme environmental conditions and uncertainties. Architectural design needs structural systems to survive. Structural systems on planets encounter load factors that are different from the load factors on Earth. Choosing the optimum structural system is important for the structures planned to be built on planets to survive under the effects and loads of the environment and to adapt to human physiology. Some of the different types of structural systems used on Earth are featured in the literature for building a structure on planets. An evaluation system has been created to determine the correct system type for the first settlements on planets among the prominent structural system types and to narrow down the selection area of these system features. In line with this evaluation system in this study, a structural system model that stands up to harsh environmental conditions and protects human health is proposed for the first settlements on the planets. It is aimed that the evaluation system will be developed in the light of research emerging from developing technologies and can be used in future studies.

Article History:

Received: 02.03.2024

Accepted: 20.09.2024

Online Available: 18.10.2024

1. Introduction

Due to the rapid depletion of Earth's resources and advancements in technology, the search for life on other planets has introduced the concept of planetary architecture. Planetary architecture, which encompasses the design and construction of structures, aims to enable livings to work and live healthily on planets for extended periods.

On Earth, structures protect living beings from potential environmental effects. However, planetary environmental conditions are significantly harsher and more unusual than those on Earth. The goal is to shield the occupants of buildings constructed in these harsh conditions from environmental impacts.

The extreme environments of planets profoundly influence the architecture and structural systems of buildings. While on Earth, structural systems

are designed with conventional factors such as dead and live loads in mind, on other planets, factors such as gravity, radiation, pressure, dust, temperature, and cost are critical in selecting the structural system.

There are numerous studies being updated daily on the types of structural systems that can withstand the harsh environmental conditions of planets and the materials that compose these systems. With continually advancing technological developments, discussions about the selection of structural systems suitable for planetary conditions will persist. Creating an evaluation system to determine the optimal structural system for planetary structures accelerates the decision-making process among options, facilitates understanding the behavior of structural systems under environmental influences, and highlights the superiority of different systems.

2. Harsh Environmental Conditions of Planets

While Mars, where life is predicted to exist, is on average millions of kilometers away from Earth, the Moon is on average 384,400 kilometers away from Earth (Figure 1) [1, 2]. Transporting materials, workers, and equipment over these vast distances is quite costly [3]. When determining the structural system for planned constructions, it is important that the structural elements transported from Earth to these planets are small in volume and light in weight. Additionally, it is crucial that the materials used in the construction are locally sourced.

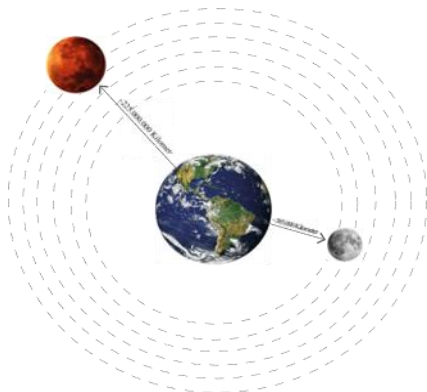


Figure 1. Distance between Earth and planets

The gravitational force, which is considered constant on Earth at an average value of 9.80665 m/s^2 , varies on other planetary surfaces [4]. On the Moon, this value is one-sixth of Earth's gravitational acceleration (1.62 m/s^2), while on Mars, it is one-third of Earth's acceleration [5, 6]. Structural system design in different gravity environments is a concept for which knowledge and experience are limited on Earth. However, with decreasing gravity, the weight of structures built on other planets will be less than those built on Earth (Figure 2). Consequently, much thinner and lighter structures can be designed, and larger spans can be achieved [7]. This is because the load-bearing capacity of structures will be greater than on Earth [6]. As the load-bearing capacity increases with decreasing gravity, the materials used in the design of structural systems do not need to be as high-strength as those used on Earth [8].

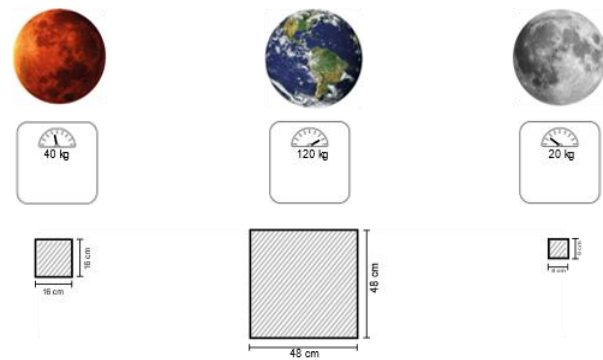


Figure 2. Comparing the gravity of planets

Radiation that harms human health and electronic equipment is limited on Earth by the atmospheric layer. However, since the atmospheric layers surrounding other planets are very thin or non-existent, they cannot limit these harmful rays. There is no atmospheric layer on the Moon, while Mars has a very thin atmosphere (Figure 3) [5, 9]. To build a livable structure in a planetary environment that cannot limit harmful radiation, the radiation effect on the building's structural system must be mitigated. Although radiation does not create a direct load on structural systems, radiation protective layers added to structures for human health can create an additional load [5].

In various studies carried out for planets, the shielding method is used to provide protection from radiation [10]. Different materials are considered for shielding to protect the building from radiation. Regolith, the soil covering the surface of planets, is the local material considered for radiation protection [11]. To provide radiation protection equivalent to Earth's atmosphere, the structural system must be covered with a 5-meter thick layer of regolith [12]. Another material planned for shielding on planets is water. Water is considered an effective radiation shield due to its chemical properties. For protection equivalent to Earth's atmospheric standards, a 10-meter thick water column is required [8].

The temperature factor, which is evaluated in structural system design on Earth, is crucial in the high temperature difference environments on other planets.

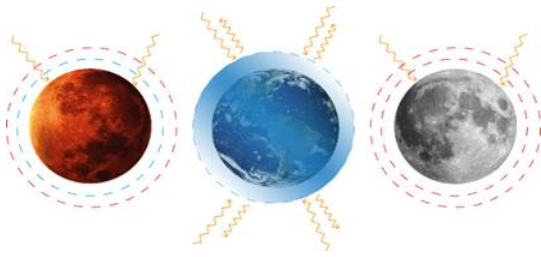


Figure 3. Radiation effect on Earth and Planets

On the Moon, where life is predicted to exist, the temperature varies between -310°F (-190°C) and $+279^{\circ}\text{F}$ (137°C), while on Mars it ranges between -89°C and -31°C (Figure 4) [13]. Such extreme temperature differences can cause effects on structural systems such as thermal stress, expansion, contraction, and fatigue, impacting the strength and durability of the structure. Therefore, various precautions must be taken during and after the construction phase. Large temperature differences also affect the material selection and form of the structural system. For this reason, in selecting materials for the structural system, it is important to use materials that have low thermal expansion properties, do not exhibit deterioration, shrinkage, or expansion within a certain temperature range, and can adapt to large temperature changes. This is essential for building habitable structures on planets [8, 13].

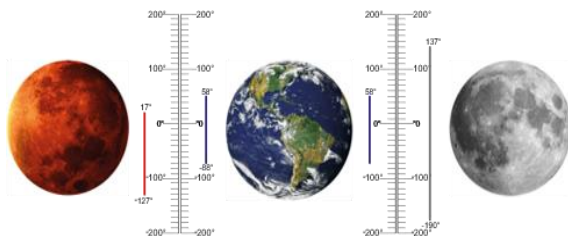


Figure 4. Temperature values of the Earth and planets

The pressurized environment required for livings to survive is maintained on Earth by the influence of the atmospheric layer [14]. However, the open air pressure on Mars and the Moon, where habitable structures are planned, is significantly lower [15]. To avoid the negative effects of low pressure on humans and to establish long-term living habitats on these planets, pressurized living spaces (Pressure Vessels) must be created. These structures will need to maintain a sea-level pressure of 101.3 kPa [16]. In pressurized structures, tensile forces will occur on the outer surface due to the internal pressure (Figure 5) [17].

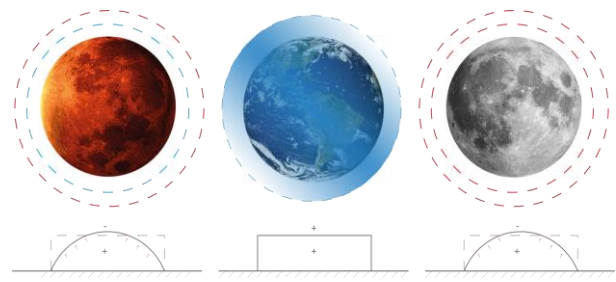


Figure 5. Pressure effect on Earth and planets

Unlike the Earth's environment, the surface of planets has a layer of fine particles. These fine particles adhere to surfaces, causing permanent damage to construction equipment and exposed surfaces [6]. They accumulate on the surface and lead to the corrosion of structural system elements and electronic equipment [8, 18]. This factor is crucial in determining the form of the structural system. As the surface area of the structure increases, the impact surface of these particles also increases [19]. Circular forms that reduce the accumulation of dust particles on the surface can be utilized in planetary structures [20].

3. Structural Systems Planning on Planets

To establish long-term settlements in the harsh environmental conditions of planets, the structures must ensure the safety of their users and create healthy environments. To determine the structural system of these structures, various suggestions have emerged that can adapt to the challenging variables of planetary conditions.

3.1. Steel systems

Steel, which is used on Earth as a high-performance, lightweight, ductile building material that can span large spans, can also be used for the structural systems of structures on planets. Iron-nickel (FeNi) meteorites found on Mars remain on the surface of Mars without oxidation due to the existence of an atmosphere consisting of carbon dioxide (CO_2) and the absence of water [21]. Studies on the use of steel systems with high tensile strength under planetary conditions continue.

Research continues to ensure that steel systems with high tensile strength can be used under planetary conditions. It is important how steel, which can be produced from local resources on Mars, responds to the planet's environmental

conditions. Steel production on the Moon is also an issue that needs to be investigated. Designed by ABIBOO Studio (A global design company) and SONet (The Sustainable Offworld Research Network), the Mars City named “NÜWA”, which is planned to be built in 2054, is a self-sufficient sustainable city. This city is intended to be built using steel obtained by processing iron-nickel meteorites, the local material on Mars, with carbon dioxide. Steel will be the main material in the structure to be built with the lava tube system (Figure 6-7) [22, 23].



Figure 6. Nüwa City [22]



Figure 7. Nüwa City [23]

3.2. Concrete, regolith and reinforced concrete systems

Concrete consists of mineral materials such as aggregate and gravel combined with cement and water as binders. Reinforced concrete systems are created by reinforcing concrete, known for its high resistance to compression, low cost, and proven methods, with steel elements. To be used as a building material in harsh planetary conditions, concrete requires special modifications to maintain its bearing strength under extreme conditions. The durability, continuity, vapor permeability, tensile and compressive strength, thermal expansion, and UV resistance of a habitable structure built with concrete on planets must be evaluated and designed for these harsh conditions [8].

The low gravitational force of planets affects the load on the structural system. High temperature fluctuations increase the thermal stress on the concrete, and the high radiation environment complicates construction conditions and may affect the integrity of the structure. Harsh environmental conditions will require rethinking processes such as pouring, curing, and compaction of concrete [24].

To produce concrete in planetary environments, it is important to utilize local materials found on planets. For standard concrete to be produced, aggregate, water, and cement must be sourced or manufactured. Producing waterless concrete is crucial to ensure that the concrete made from local resources is not affected by temperature differences [8]. Three types of concrete stand out for use on planets.

Sulfur concrete (Figure 8) is a type of concrete made from sulfur aggregates and plastic, without water and cement [25, 26]. Compared to standard concrete, it offers “Fast curing time, waste management, recycling opportunities, high resistance to acids and radiation, the possibility of concreting at sub-zero ambient temperatures, fast setting time, low electrical and thermal conductivity, water resistance, high freezing resistance, and high wear resistance” [27]. Since Mars and the Moon are rich in sulfur, the use of sulfur concrete is recommended. Sulfur concrete is twice as strong as standard concrete and has a much shorter curing time [3]. However, like standard concrete, sulfur concrete has weak tensile strength. The use of elements that can absorb the tensile force of concrete under planetary conditions, which is reinforced with steel elements for tensile strength on Earth, has yet to be discovered.

Magnesium concrete is not widely preferred as a structural system material on Earth due to its high cost. However, it can be used on planets. It is suitable for the extreme conditions of planets due to its properties of not conducting heat, cold, or electricity [26].



Figure 8. Sulfur concrete [28]

Polymer concrete (Figure 9) uses polymer materials as binders. "Polymer concrete materials are used in various applications due to their superior properties such as fast curing, high compressive strength, high rigidity and strength, resistance to chemicals and corrosion, ability to form complex shapes, and high vibration damping properties" [25, 29]. It has 2-4 times the compressive strength and 3-6 times the tensile strength compared to conventional concrete [25]. However, to produce this concrete on planets, polymer materials would need to be transported from Earth [8].



Figure 9. Polymer Concrete [30]

3.3 3. D printed systems

The 3D printing system creates three-dimensional shapes from a malleable material [31]. Applications using 3D printing systems take less time than traditional methods. Structures created with these systems have no restrictions on span or length, allowing for unlimited building forms. Since robots construct the structure in this system, the need for labor decreases significantly. However, this technology is still evolving. Although material and labor costs are low with 3D printing, the equipment is costly. By using this developing system with concrete materials, the 3D concrete printing (3DCP) method has emerged [20, 31]. In structures built with the 3D printing system, vertical elements are created by spraying

concrete material with the help of a pump and layering the material.

Different studies have been carried out to build habitable structures on planets with the 3D printing system. Designed by AI SpaceFactory (A company developing manufacturing technologies for space exploration), "Marsha" is planned to be built on Mars with 3D printing systems. The structure, rising in an egg-like vertical form, is printed with printing material derived from natural materials (Figure 10) [32, 33]. A different study, the "Mars Ice House" project, which envisions creating a habitable structure by printing water ice with 3D printing systems, was designed by SEARch+ (Space Exploration Architecture) and Clouds Architecture Office (Figure 11) [34].



Figure 10. Marsha [32]



Figure 11. Mars Ice House [34]

3.4. Pneumatic (Inflatable) systems

Pneumatic (Inflatable) systems are created by using membrane materials to absorb tensile forces on the structure, which are then inflated with air supports. The basic working mechanism of this system relies on the membrane material becoming structural through the pressure difference on its surfaces. To withstand the stress on the membrane material, it is additionally supported by different structural systems such as columns and cables [35].

Considering the harsh environmental conditions of planets, pneumatic structural systems are

suitable for transportation from Earth to planetary environments due to their low mass-to-volume ratio and foldable feature [36]. They are resistant to the tensile forces that occur when the structure is pressurized in low-pressure environments [37]. This system, which is suitable for spherical geometric forms, can also be configured into free forms such as cylinders, cones, and tori [36].

It is crucial that the membrane material, the main element of pneumatic systems, is suitable for the

harsh conditions of the planet and has the strength to carry the loads imposed on it. Simple membrane fabrics are not suitable for use in planetary conditions, so layered or composite solutions are preferred [8]. Organic polymer materials are lightweight and can be easily shaped [38]. Aramid fabrics composed of organic polymers are used in aerospace applications [39]. Different types of aramid fabrics, known for their high strength, lightness, durability, and heat resistance under planetary conditions, are listed in Table 1 along with their properties.

Table 1. Characteristics of Different [40-43]

	<i>Kevlar</i>	<i>Vectran</i>	<i>Nomex</i>	<i>Twaron</i>
Temperature Resistance	-40°/429°	-40°/330°	-40°/250°	-40°/300°
Thermal expansion	Low	Low	Low	Low
UV Resistance	Available	Available	Not available	Available
Tensile Strength(MPA)	2800-4100	1100-3200	400-500	2500-3500

In the studies carried out, there are suggestions for structures with pneumatic structural systems that are intended to be used on planets. A cylindrical structure with a pneumatic system was designed by Kriss Kennedy and his team [35]. The "Space Nomad" project, created from three-layer membrane materials, was designed for Mars [44]. The "Mars Ice Home" project was created with pneumatic systems and was achieved by filling the pockets of the membrane material with water (Figure 12) [45]



Figure 12. Mars Ice Home [45]

3.5. Mixed systems

The systems intended to build structures against the harsh environmental conditions of planets have both advantages and disadvantages. To mitigate these disadvantages, hybrid systems

have been developed, combining rigid and flexible systems for planetary construction. Flexible structures are vulnerable to environmental effects such as meteorite impacts and radiation. While rigid structures are more effective against these environmental effects, flexible structures are more resistant to the loads created by internal pressure compared to rigid structures [46]. By combining these systems, which have complementary strengths and weaknesses, mixed structural systems for buildings can be created.

Different design suggestions have emerged to create livable spaces on planets for buildings with mixed structural systems. "TransHab", which is one of the examples of mixed structural system buildings, is a design model with an inflatable outer shell and a rigid core inside [47]. Another mixed structural system structure proposed for planetary settlements is the "Hive Mars" project. It is formed by pressurizing an egg-shaped pneumatic system into the outer shell built with 3D systems (Figure 13) [48, 49]. The "Lunar Habitation ESA" project, which is planned to be built on the lunar surface and designed by Foster and Partners, was created by adding the regolith layer on top of the dome-shaped pneumatic system with 3D printing systems (Figure 14) [50, 51]. Another

construction proposal using hybrid systems "Mars X-House V1", was created by covering two pneumatic (Inflatable) systems in the inner center with a 3D-printed protective radiation shield (Figure 15) [52, 53].



Figure 13. Hive Mars [48]



Figure 14. Lunar Habitation ESA [50]



Figure 15. Mars X-House V1 [53]

4. Evaluation of structural systems

To determine the structural system of a structure to be built on planets, a building material that can safely carry loads, withstand environmental conditions, is cost-effective, has a suitable modular geometric form, and possesses high strength with low thermal expansion is needed [17]. Understanding the different environmental conditions of planets is essential to creating a suitable environment for users. When determining the structural system of buildings, important variables include the structure's function, geometry, loads, material, and cost.

Using a scoring system to choose a structural system in planetary environments, where there are various variables and alternatives with respective advantages and disadvantages, facilitates the decision-making process. This evaluation system aims to select an appropriate system by assessing numerous sub-variables to decide on the structural system suitable for planetary conditions. As information about planets is continually developed and updated, the structural system alternatives and factors in the scoring system will evolve over time. In the scoring system, structural system types are compared against factors affecting their selection, and as a result of the comparison, the systems are rated from 1 to 5. A rating of 5 indicates that the structural system is efficient and preferable against the factor, while a rating of 1 indicates that it is weak and not advisable. Ratings of 2, 3, and 4 are intermediate evaluation scores. These scores for the factors will be explained specifically for each structural system.

4.1. Cost of the structure

Various variables affect the cost of a structure planned to be built on planets. Transporting building materials from Earth to the planetary environment and the construction process on the planet itself significantly impact the cost. The types of structural systems prominent for use on planets are evaluated according to the factors shown in Figure 16.

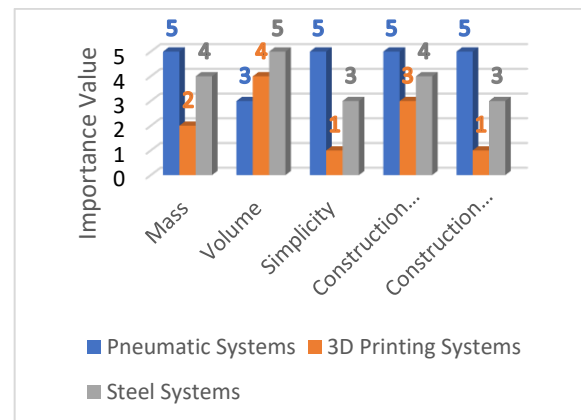


Figure 16. Evaluation of structural systems according to cost factor

- Mass: Pneumatic systems are the lightest (5 points). Steel systems carry less material from Earth (4 points). 3D printing systems are rated intermediate (2

points) due to the size of the equipment that must be transported to the planets (Figure 16).

- **Volume:** 3D printing systems can create unlimited volumes (5 points). Steel systems can span large areas (4 points). The volumes that pneumatic systems can create are limited (3 points) (Figure 16).
- **Simplicity:** Pneumatic systems are the simplest in construction (5 points). Steel systems are more complex than pneumatic systems in terms of material production (3 points), and our experience with them is limited. 3D printing systems are the most challenging (1 point) (Figure 16).
- **Construction Time:** Pneumatic systems arrive from Earth to the planets almost ready (5 points). 3D printing systems, built through robots, are faster than steel systems (4 points). Steel systems are slower (3 points) (Figure 16).
- **Construction Equipment:** Pneumatic systems can be constructed almost without the aid of equipment (5 points). Steel systems require equipment for material production (3 points). Bringing 3D printing system robots from Earth is challenging (1 point) (Figure 16).

4.2. Loads of the structure

Loads refer to the forces acting on a structure. A building withstands these loads thanks to its structural system. The environmental conditions of planets affect the load characteristics acting on the structure.

The durability of structural systems depends on environmental conditions, structural loads, and material properties. When choosing a structural system, the differences in environmental conditions between Earth and other planets affect the loads on the structures. For example, wind formation is not very common on the Moon and Mars due to the lack of a significant atmosphere [9]. Therefore, wind load can be ignored when

creating structures on these planets. However, dust storms that affect the structure similarly to wind are a significant consideration. This dust load is important for ensuring resistance to external influences. Dust should not accumulate on the structure, and designs that protect structural system elements should be considered. The form of the building and any indentations on the structure influence the structural system's exposure to dust load. Additionally, the durability of habitable structures is crucial to prevent them from being affected by the dust load. Rigid structural systems are more resistant to this load compared to flexible systems.

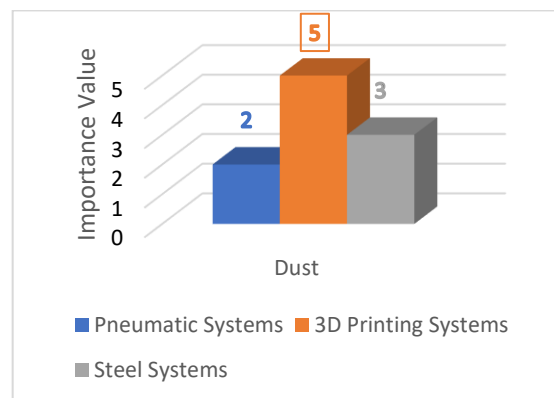


Figure 17. Evaluation of structural systems according to dust load factor

- **Dust:** Since 3D printing systems are rigid systems, they are resistant to wear (5p). Since steel systems are rigid systems (3p). It is more durable compared to pneumatic systems (2p) (Figure 17).

Gravity load, which determines the amount of dead load on the structure on Earth, dominates the choice of structural system. Unlike on Earth, on planets, the pressure load is the determining factor, not the gravitational load. Tensile forces occur on the surface of the structure, which must be pressurized in order to create a healthy environment for its users.

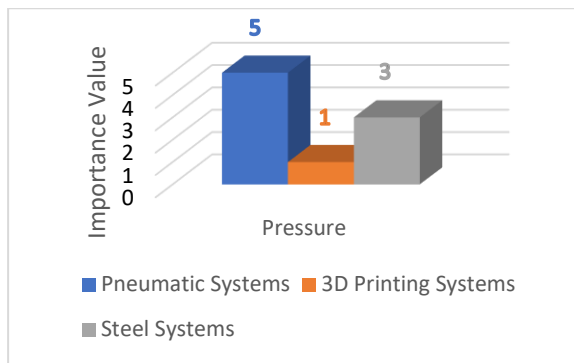


Figure 18. Evaluation of structural systems according to pressure load factor

- Pressure: It is usable because it is resistant to the tensile forces of pneumatic systems (5p). The steel material used in steel systems is resistant to tensile (3p), however, 3D printing systems are not efficient without additional supports (1p) (Figure 18).

Flexible structural systems are more affected by radiation compared to rigid structural systems. Proposed methods of protection from radiation on planets will create an additional load mass on the structure [16]. It is important that the structures to be built can bear this load.

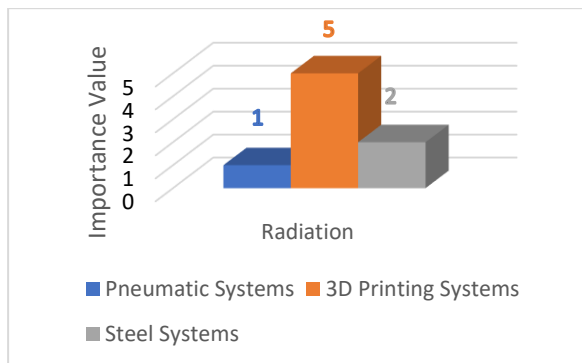


Figure 19. Evaluation of structural systems according to radiation load factor

- Radiation: 3D printing systems carry the incoming load to protect from radiation (5p). The strength of steel systems without coating with additional coatings is low (2p). Pneumatic systems cannot handle the shielding load even without support elements (1p) (Figure 19).

4.3. Material of the structure

It is important to determine the structural system before considering system materials on planets.

The evaluation system used to propose a structure for the first settlements on planets suggests that economical (inflatable) flexible systems are advantageous according to cost and load factors. However, it will be important to compare this system with the ready-made capsule systems sent from Earth to planets for construction. The different effects of these two systems have been evaluated.

- Cost: Capsule systems (2p), created with high technological possibilities, are much more costly to produce compared to pneumatic structural systems (5p) (Figure 20).

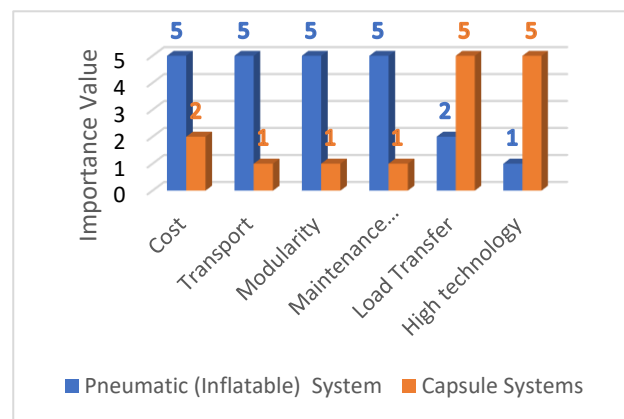


Figure 20. Comparison of Pneumatic Systems and Capsule Systems

- Transport: Transport and installation of capsule systems (1), which are planned to be sent ready-made from Earth to the planetary environment, are quite difficult and costly compared to pneumatic systems (4p). According to Dr. İbrahim Güven, an associate professor in the Department of Mechanical and Nuclear Engineering in the VCU College of Engineering, the cost of transporting 1 pound of weight to the moon is currently around \$100,000 (Figure 20).
- Modularity: In the planetary environment, which is quite open to developments and changes, capsule systems (1p) are closed to adaptations compared to pneumatic systems (5p) (Figure 20).
- Maintenance and repair: Repair and maintenance of high-tech capsule

systems (1p) are quite complicated compared to pneumatic systems (5p) (Figure 20).

- Load Transfer: Capsule systems (5p) are advantageous compared to pneumatic systems (2p) in carrying heavy loads (Figure 20).
- High Technology: Capsule systems (5p), produced with advanced technological systems, are more resistant to harsh conditions compared to pneumatic systems (1p) (Figure 20).

- UV degradation: Kevlar, Vectran and Twaron (4p), a membrane with uv degradation resistance. Nomex that does not have this resistance is rated as (1p) (Figure 21).
- Tensile strength: Kevlar (2800-4100 mpa) has the highest tensile strength of the membrane fabrics that become structural by pressurization (5p). Tensile strength value respectively twaron (2500-3500 mpa) (4p). vectran (1100-3200 mpa) (3p). nomex is rated as (400-500 mpa) (2p) (Figure 21).

As a result of the evaluation, pneumatic systems are advantageous compared to capsule systems. In this regard, when material selection is made, it is important that the membrane material, which is the structural element, is selected in accordance with the environmental conditions of the planet. Studies have shown that aramid fabrics consisting of organic polymers are used on planets [54]. Aramid fabrics recommended for use were also evaluated. (Figure 21).

In addition to making the membrane fabrics of structures with pneumatic structural systems resistant to radiation, it is important to provide shielding around the structure to ensure the health of living things and the resistance of the structure. In order to provide shielding on planets, the materials that have been highlighted in the research carried out so far have been evaluated (Figure 22).

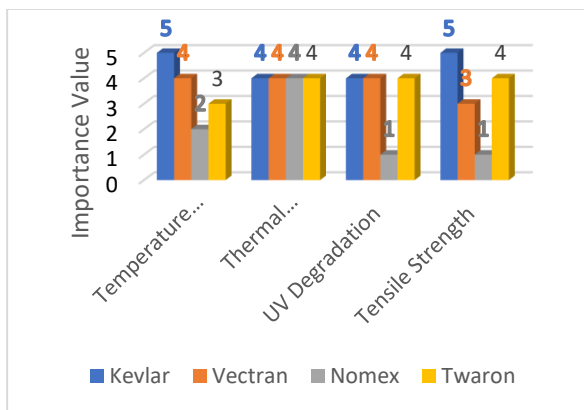


Figure 21. Evaluation of the properties of materials

- Temperature resistance: Kevlar fabric material has the widest temperature range (5p) as it can withstand $-40^{\circ}/429^{\circ}$. Vectran (4p) based on $-40^{\circ}/330^{\circ}$ range respectively. Twaron (3p) based on $-40^{\circ}/300^{\circ}$ range. Nomex (2p) is rated based on the $-40^{\circ}/250^{\circ}$ range (Figure 21).
- Thermal expansion: Since the thermal expansion feature of the membrane fabrics intended to be used is at a low level (4p), they are scored equally (Figure 21).

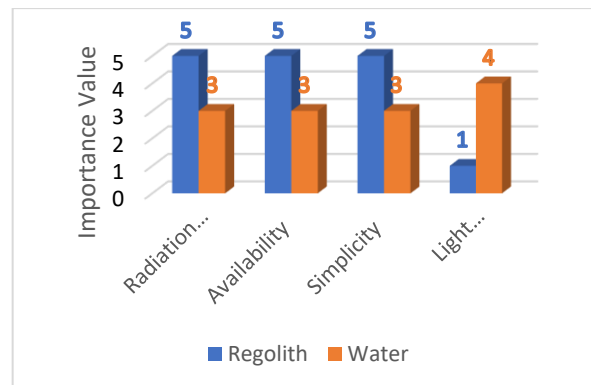


Figure 22. Evaluation of the properties of radiation protective materials

- Radiation protection: regolith requires a depth of 5m to provide protection equivalent to the Earth's atmosphere (5p). The water must be 10m deep to provide protection from there (3p) (Figure 22).
- Availability: since the surface layer of the planets is covered with its native material, regolith (5p). Water is not directly present on the surface (3p) (Figure 22).
- Simplicity: regolith found on the surface of planets can be used directly (5p). In

order to use water, its form must be transformed into ice (3p) (Figure 22).

- Light transmittance: Water is a material that transmits light (5p). The regolith does not allow light into the structure (1p) (Figure 22).

4.4. Geometry of the structure

Geometric form is an important factor in determining a structural system. The harsh conditions of the planets are effective in the formation of the geometric form of the structure. Straight or arch geometries are used in the openings we will pass through to create structures in these harsh environments. Crossing the opening straight is not as effective as arch geometry in terms of load transfer. As seen in the Figure 23, arches are more resistant to tensile and pressure forces than straight opening transitions.

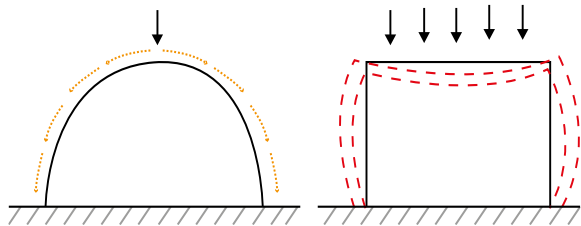


Figure 23. Arches and straight opening transitions

There are different geometric forms proposed to build structures in the harsh environmental conditions of the planets. Rectangular, spherical, cylindrical and conical forms intended to be used on planets are evaluated according to their various features in the figure 24.

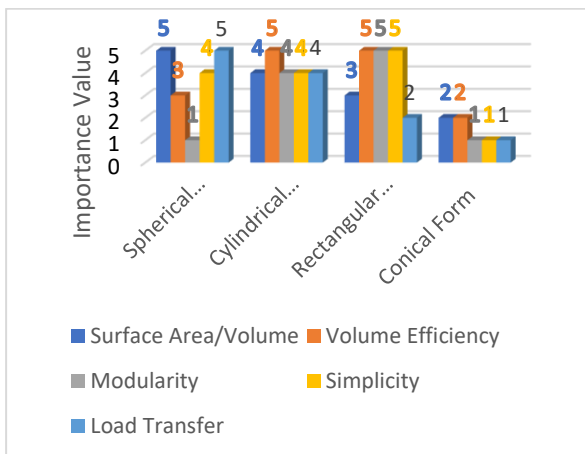


Figure 24. Evaluation of building forms

- Spherical form: although its surface area is small, it is large in volume (5p). It is difficult to use this large volume efficiently (3p). It is relatively easy to produce a tested geometry form (4p). It transfers the loads acting on it to the ground evenly (5p). Also, the form is not a good choice when considering modular additions (1p) (Figure 24).

- Cylindrical form: the surface area it covers is quite small compared to the volume (4p). It is very efficient in terms of volume (5p). It distributes the loads acting on it equally (5p). It is a geometric form (4p) suitable for modular additions. It is relatively easy to produce a tested geometry form (4p) (Figure 24).

- Rectangular form: surface area to volume ratio is inefficient compared to other forms (3p). It allows efficient use of the volume it creates (5p). Suitable for modular additions (5p). They are simple because they form symmetrical geometries (5p). Considering spherical forms, charge transfer is incomplete (2p) (Figure 24).

- Conical form: the volume narrows as it rises, making it difficult to use it efficiently (2p). To obtain large volumes, the surface area must increase considerably (2p). It does not allow modular additions (1p). It is a complex structural form (1p). It cannot transfer the load to the ground efficiently (1p) (Figure 24).

4.5. Building proposal

As a result of the evaluation, it is important to be able to build fast, simple, and functional structures in the first settlements on planets. The types of structural systems envisaged for use in these initial settlements were evaluated according to cost, load, material, and geometric form criteria. The evaluation concluded that mixed (hybrid) systems, which incorporate 3D systems, would be more appropriate for use in the settlement phase after the first planetary

settlements. Transporting capsule structures, planned to be built on Earth using high technological means and then transported to the planet's surface, is very costly. Studies have determined that the cost of transporting 1 pound (0.45359237 kilograms) of weight to the moon is currently around \$100,000, and sending it to Mars will cost much more [55].

Therefore, pneumatic (inflatable) structural systems, which are light, foldable, and can be built very quickly, were deemed suitable for the first settlements on planets. These systems will be transported to planets by folding them into small volumes and built on the planet's surface.

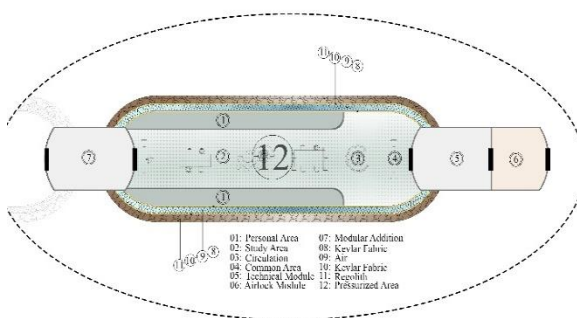


Figure 25. Building proposal plan

When evaluating aramid fiber fabrics, which are the main material of pneumatic structural systems, Kevlar Aramid Fiber and Twaron Aramid Fiber, intended for use in the planetary environment, received close scores. To make an evaluation between these two options, their costs were compared, and Kevlar Aramid fabric was deemed appropriate due to its affordable cost [56, 57]. It is recommended to use a hybrid form created with cable support elements to benefit from the advantages of both spherical and cylindrical geometries, which yielded close results in the scoring of the geometric form of the structure.

It is deemed appropriate to cover the Kevlar aramid fabric, which meets the tensile stresses that will occur when the pneumatic system is pressurized to sea level pressure (1013.25 millibars), with a layer of regolith, the surface material of planets, to protect against the negative effects of radiation, meteorites, and temperature. Studies have shown that a three-meter deep regolith layer provides the protection equivalent to Earth's atmosphere [58].

Additionally, the protective regolith layer added to the structural system also creates thermal comfort within the building. The regolith layer surrounding the structural system can keep the temperature inside the structure constant at ± 2 degrees [28]. The floor of the structure created with a pneumatic system will be separated from the planet's surface thanks to its air layer feature. There should be a regolith layer on the upper layer of air, providing good insulation with low thermal conductivity, as on all other surfaces of the building. This regolith layer separates the ground of the structural system from the planet's surface.

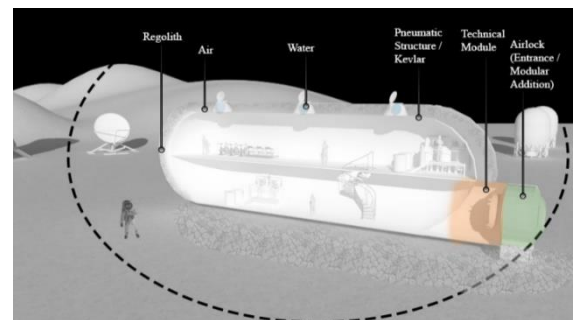


Figure 26. Building proposal section

Light does not penetrate the structure covered with regolith, the surface material of planets. To protect the psychological and physical health of users, they need surfaces that allow light transmission. In this building proposal, aimed for use in the first settlements on planets, the regolith layer will be pierced with air-locked systems to allow natural light into the volume. To create a skylight that transmits light while maintaining pressure and radiation control, the space between the double-layered transparent PVC membrane material will be filled with water, which has radiation protection properties, acting as a cushion and sealing the openings [59]. To allow modular joints and increase research on planets, it is recommended to use input and output elements designed specifically for pneumatic systems, ensuring they do not disrupt the pressurization within the structure (Figure 25, 26, 27).



Figure 27. Building proposal

5. Conclusion

In this study, which aims to create a structural proposal for the first settlements on planets, a scoring system was developed to select and compare criteria. This scoring system aims to mathematically grade all stages in the structural system selection process. Based on this system, it was determined that the primary system to be used in the first settlements should be Pneumatic (Inflatable) systems, transported from Earth to planets. To increase the usable volume area, the proposed structure, combining cylindrical and spherical forms, should be supported with cable elements to bear the loads. It is recommended to cover the structure with regolith to protect the main structural system and living organisms from the damaging effects of the planetary environment.

The building model proposed as a result of the evaluation is still at the conceptual stage. With advancing technological steps, planetary environments need to be tested in more detail. The evaluation system is designed to keep pace with developing technology. Based on further studies, additional criteria can be added to this evaluation system, or obsolete criteria can be removed.

This research simplifies and objectifies the process of determining the structural system for the frameworks of structures to be built on the planets where we plan to travel and settle permanently in the near future. It is intended that this evaluation system can serve as a foundation for future studies on structural system selection on planets.

Article Information Form

Funding

The author (s) has no received any financial support for the research, authorship or publication of this study.

Authors' Contribution

The authors contributed equally to the study.

The Declaration of Conflict of Interest/ Common Interest

No conflict of interest or common interest has been declared by the authors.

The Declaration of Ethics Committee Approval

This study does not require ethics committee permission or any special permission.

The Declaration of Research and Publication Ethics

The authors of the paper declare that they comply with the scientific, ethical and quotation rules of SAUJS in all processes of the paper and that they do not make any falsification on the data collected. In addition, they declare that Sakarya University Journal of Science and its editorial board have no responsibility for any ethical violations that may be encountered, and that this study has not been evaluated in any academic publication environment other than Sakarya University Journal of Science.

Copyright Statement

Authors own the copyright of their work published in the journal and their work is published under the CC BY-NC 4.0 license.

References

- [1] T. Gangale, "MarsSat: Assured Communication with Mars," *Annals of the New York Academy of Sciences*, vol. 1065, no. 1, pp. 296–310, 2005.
- [2] J. Huang, G. Huadong, L. Guang, S. Guozhuang, Y. Hanlin, Y. Deng, R. Dong "Spatio-Temporal Characteristics for Moon-Based Earth Observations," *Remote Sensing*, vol. 12, no. 17, p. 2848, 2020.

- [3] N. Savage, "Home, sweet martian home," *C&EN Global Enterp*, vol. 96, no. 1, pp. 16–18, 2018.
- [4] D. B. Newell, E. Tiesinga, "The international system of units (SI):: 2019 edition," National Institute of Standards and Technology, Gaithersburg, MD, NIST SP 330-2019, 2019.
- [5] Y. C. Toklu, "Optimum lunar and martian structures and their construction," in *Proceedings of 2nd International Conference on Recent Advances in Space Technologies*, 2005. RAST 2005., Istanbul, Turkey: IEEE, 2005, pp. 260–264.
- [6] H. Benaroya, "An Overview of Lunar Base Structures: Past and Future," in *AIAA Space Architecture Symposium*, Houston, Texas: American Institute of Aeronautics and Astronautics, 2002.
- [7] O. Doule, "Ground Control: Space Architecture as Defined by Variable Gravity: Ground Control: Space Architecture as Defined by Variable Gravity," *Archit. Design*, vol. 84, no. 6, pp. 90–95, 2014.
- [8] S. Ulubeyli, "Lunar shelter construction issues: The state-of-the-art towards 3D printing technologies," *Acta Astronautica*, vol. 195, pp. 318–343, 2022.
- [9] G. Petrov, J. Ochsendorf, "Building on Mars," *Civ. Eng.*, vol. 75, no. 10, pp. 46–53, 2005.
- [10] H. Benaroya, L. Bernold, K. M. Chua, "Engineering, Design and Construction of Lunar Bases," p. 13, 2002.
- [11] H. J. Llamas, K. L. Aplin, L. Berthoud, "Effectiveness of Martian regolith as a radiation shield," *Planetary and Space Science*, vol. 218, p. 105517, 2022.
- [12] H. Benaroya, "Lunar habitats: A brief overview of issues and concepts," *REACH*, vol. 7–8, pp. 14–33, 2017.
- [13] J. Edmunson, M. R. Fiske1, R. P. Mueller, H. S. Alkhateb, A. K. Akhnoukh, H. C. Morris, I. I. Townsend, J. C. Fikes, M. M. Johnston "Additive Construction with Mobile Emplacement: Multifaceted Planetary Construction Materials Development," in *Earth and Space 2018*, Cleveland, Ohio: American Society of Civil Engineers, 2018, pp. 782–792.
- [14] "How the atmosphere sustains life on Earth | OpenLearn - Open University." Accessed: Feb. 20, 2024. [Online]. Available: <https://www.open.edu/openlearn/science-maths-technology/across-the-sciences/how-the-atmosphere-sustains-life-on-earth>
- [15] J. Kozicki, J. Kozicka, "Human friendly architectural design for a small Martian base," *Advances in Space Research*, vol. 48, no. 12, pp. 1997–2004, 2011.
- [16] N. Järvistråt, C. Toklu, "Design and Construction for Self-sufficiency in a Lunar Colony," 2004.
- [17] W. Z. Sadeh, J. E. Abarbanel, M. E. Criswell, "A Generic Inflatable Structure for a Lunar/Martian Base," presented at the *International Conference On Environmental Systems*, 1996, p. 961399.
- [18] O. Bannova, L. Bell, "Radiation shielding design strategies for lunar minimal functionality habitability element," *Acta Astronautica*, vol. 67, no. 9–10, pp. 1103–1109, 2010.
- [19] N. Leach, "Space Architecture: The New Frontier for Design Research," *Architectural Design*, vol. 84, no. 6, pp. 8–15, 2014.
- [20] Y.-S. Lee, C. Keys, S. Terreno, "3D Printed Martian Habitats and Challenges to Overcome," *RRJoSST*, 2022.
- [21] G. A. Landis, "Meteoritic steel as a construction resource on Mars," *Acta Astronautica*, vol. 64, no. 2–3, pp. 183–187, 2009.

- [22] “Nüwa, the first sustainable city on Mars • ABIBOO Studio.” Accessed: Feb. 20, 2024. [Online]. Available: <https://abiboo.com/projects/nuwa/>
- [23] “Abiboo envisions cliff face city as ‘future capital of Mars.’” Accessed: Feb. 20, 2024. [Online]. Available: <https://www.dezeen.com/2021/04/07/nuwa-mars-city-cliffside-abiboo/>
- [24] Y. Reches, “Concrete on Mars: Options, challenges, and solutions for binder-based construction on the Red Planet,” *Cement and Concrete Composites*, vol. 104, p. 103349, 2019.
- [25] M. Z. Naser, “Extraterrestrial construction materials,” *Progress in Materials Science*, vol. 105, p. 100577, 2019.
- [26] A. Kumar, T. Sharma, “Study of In-Situ Construction Materials on Mars,” p. 12, 2020.
- [27] R. Fediuk, Y. H. Mugahed Amran, M. A. Mosaberpanah, A. Danish, M. El-Zeadani, S. Klyuev, N. Vatin, “A Critical Review on the Properties and Applications of Sulfur-Based Concrete,” *Materials*, vol. 13, no. 21, p. 4712, 2020.
- [28] L. Wan, R. Wendner, G. Cusatis, “A novel material for in situ construction on Mars: experiments and numerical simulations,” *Construction and Building Materials*, vol. 120, pp. 222–231, 2016.
- [29] R. Bedi, R. Chandra, S. P. Singh, “Mechanical Properties of Polymer Concrete,” *Journal of Composites*, vol. 2013, pp. 1–12, 2013.
- [30] “3 KEY THINGS TO KNOW ABOUT POLYMER OVERLAY.” Accessed: Feb. 20, 2024. [Online]. Available: <https://www.carolinaconcrete.com/3-key-things-to-know-about-polymer-overlay>
- [31] N. Nadarajah, “Development of concrete 3D printing,” 2018.
- [32] “MARSHA,” AI Spacefactory. Accessed: Feb. 20, 2024. [Online]. Available: <https://spacefactory.ai/marsha>
- [33] “AI SpaceFactory Wins NASA’s 3D-Printed Mars Habitat Challenge,” *ArchDaily*. Accessed: Feb. 20, 2024. [Online]. Available: <https://www.archdaily.com/916888/ai-spacefactory-wins-nasas-3d-printed-mars-habitat-challenge>
- [34] “Mars Ice House,” *Space Exploration Architecture*. Accessed: Feb. 20, 2024. [Online]. Available: <http://www.spacearch.com/mars-ice-house>
- [35] Y. Bal, “Geçmişten Günümüze Dünya’da ve Türkiye’de Pnömatik Sistemlerin İncelenmesi ve Değerlendirilmesi,” 2022.
- [36] A. K. Dhumad, “The Impact of using the Pneumatic Structures on the Sustainability of Iraqi Cities During Religious Events,” *IOP Conf. Ser.: Mater. Sci. Eng.*, vol. 1094, no. 1, p. 012094, 2021.
- [37] L. Pernigoni, A. M. Grande, “Development of a supramolecular polymer based self-healing multilayer system for inflatable structures,” *Acta Astronautica*, vol. 177, pp. 697–706, 2020.
- [38] C. H. M. Jenkins, “Gossamer Spacecraft: Membrane And Inflatable Structures Technology For Space Applications,” Reston ,VA: American Institute of Aeronautics and Astronautics, 2001.
- [39] Y. Xu, H. Zhang, G. Huang, “Review on the mechanical deterioration mechanism of aramid fabric under harsh environmental conditions,” *Polymer Testing*, vol. 128, p. 108227, 2023.
- [40] F. B. International, “All About Kevlar®,” *Fiber Brokers International, LLC*. Accessed: Feb. 20, 2024. [Online]. Available: <https://fiberbrokers.com/body-armor-disposal/all-about-kevlar/>

- [41] “Tensile Properties,” Kuraray Vectran. Accessed: Feb. 20, 2024. [Online]. Available: <https://www.vectranfiber.com/properties/tensile-properties/>
- [42] “Kevlar® Elyaf | DuPont.” Accessed: Feb. 20, 2024. [Online]. Available: <https://www.dupont.com.tr/products/dupont-kevlar-fiber.html>
- [43] “Twaron®,” FibrXL. Accessed: Feb. 20, 2024. [Online]. Available: <https://fibrxl.com/fibrxl-performance/fibers/twaron/>
- [44] “A simple inflatable Mars Habitat,” Space Settlement Progress. Accessed: Apr. 27, 2024. [Online]. Available: <https://spacesettlementprogress.com/a-simple-inflatable-mars-habitat/>
- [45] “MARS ICE HOME — Clouds Architecture Office.” Accessed: Feb. 20, 2024. [Online]. Available: <https://cloudsao.com/MARS-ICE-HOME>
- [46] C. Zhou, R.Chen, J. Xu, L. Ding, H. Luo, J.Fan, E. Chen, L.Cai, T. Bin, “In-situ construction method for lunar habitation: Chinese Super Mason,” *Automation in Construction*, vol. 104, pp. 66–79, 2019.
- [47] K. Kennedy, “Lessons from TransHAB: An Architect’s Experience,” in *AIAA Space Architecture Symposium*, Houston, Texas: American Institute of Aeronautics and Astronautics, 2002.
- [48] “Hive Mars - Hybrid-scalable settlement on Mars,” C A G E Architecture. Accessed: Feb. 20, 2024. [Online]. Available: <https://archicage.com/portfolio/hive-mars/>
- [49] Paola, “Hive Mars: A project of a human settlement on Mars,” Universe. Accessed: Feb. 20, 2024. [Online]. Available: <https://universe.wiki/2023/09/27/hive-mars-a-project-of-a-human-settlement-of-mars/>
- [50] “Foster + Partners To 3D Print Structures on the Moon,” ArchDaily. Accessed: Feb. 20, 2024. [Online]. Available: <https://www.archdaily.com/326429/foster-partners-to-3d-print-structures-on-the-moon>
- [51] “Lunar Habitation | Architecture Projects.” Accessed: Feb. 20, 2024. [Online]. Available: <https://www.fosterandpartners.com/projects/lunar-habitation>
- [52] M. Yashar, C. Ciardullo, M. Morris, R. Pailes-Friedman, “Mars X-House: Design Principles for an Autonomously 3D-Printed ISRU Surface Habitat,” p. 20, 2019.
- [53] “Mars X-House V1 — Space Exploration Architecture.” Accessed: Apr. 27, 2024. [Online]. Available: <https://www.spacexarch.com/marsxhouse-v1>
- [54] E. Orndoff, “Resurrecting NASA Historical Fabrics to Meet the Thermal Challenges of Landing in the South Pole of the Moon,” 2023.
- [55] R. J. of Engineering, “Advanced materials for missions to the moon — and beyond,” VCU News. Accessed: Sep. 01, 2024. [Online]. Available: <https://news.vcu.edu/article/2022/03/advanced-materials-for-missions-to-the-moon-and-beyond>
- [56] “170 g/m2 Plain Kevlar/Carbon Fabric, 120 cm width,” Castro Composites. Accessed: Feb. 20, 2024. [Online]. Available: <https://www.castrocompositesshop.com/en/fibre-reinforcements/1612-165-gm2-plain-kevlarcarbon-fabric-100-cm-width.html>
- [57] “170 g/m2 Twaron Aramid Woven Fabric Twill 2x2 STYLE 282.” Accessed: Feb. 20, 2024. [Online]. Available: <https://www.castrocompositesshop.com/en/fibre-reinforcements/2367-170-gm2->

twaron-aramid-woven-fabric-twill-2x2-
style-282.html

- [58] V. Dayal, “Conceptual Design of Pressurized Shelters on the Lunar Surface,” *J. Aerosp. Eng.*, vol. 27, no. 1, pp. 33–39, 2014.
- [59] N. A. Maziad, M. S. Sayed, E. A. Hegazy, “Use of radiation grafted PVC–acrylamide membranes in radioactive waste treatment,” *Polymer International*, vol. 51, no. 2, pp. 150–155, 2002.